Supercritical Microfluidics for understanding CO2 / water systems under pressure and temperature : Application to the sustainable management of the anthropogenic CO2

Na Liu

THÈSE

PRÉSENTÉE A

L'UNIVERSITÉ BORDEAUX 1

ÉCOLE DOCTORALE DES SCIENCES CHIMIQUES

Par Na LIU

POUR OBTENIR LE GRADE DE

DOCTEUR

SPÉCIALITÉ : Physico-Chimie de la Matière Condensée

Microfluidique supercritique pour la compréhension des systèmes CO_2 / eau sous pression et en température : Application à la gestion durable de la filière CO_2

Sous la direction de : Samuel MARRE et Yves GARRABOS

Soutenue le : 22 Novembre 2013

Devant la commission d'examen formée de :

M. Mario MAGLIONE	Directeur de Recherche, ICMCB-CNRS, Pessac	Président
M. Ryan L. HARTMAN	Professeur, University of Alabama, Tuscaloosa, USA	Rapporteur
Dr. Jean DUBESSY	Directeur de Recherche, Géoressources, Vandoeuvre	Rapporteur
Dr. Mohammed AZAROUAL	Responsable scientifique de programme, BRGM, Orléans	Examinateur
Dr. Yves GARRABOS	Directeur de Recherche, ICMCB-CNRS, Pessac	Examinateur
Dr. Samuel MARRE	Chargé de Recherche, ICMCB-CNRS, Pessac	Examinateur

Acknowledgements

I would like to thank my advisors, Samuel MARRE and Yves GARRABOS for guiding and supporting me during these past three years. Without their constant advice and efforts, this thesis would not have been completed. It has been an honor to be their Ph.D. student. Sam is an enthusiastic and energetic advisor and one of the smartest people I know. He taught me how good experimental chemist is done. Yves has been supportive and provided insightful theoretical discussions in the research. I appreciate his support and contributions of time and ideas over these three years. Thank you!

I would like to acknowledge Dr. Mario MAGLIONE, the ICMCB-director for hosting me in the *Institut de Chimie de la Matière Condensée de Bordeaux*, and agreed to chair the thesis committee.

I wish to express my gratitude to the members of the jury who were willing take their time to judge the work. For the dissertation I would like to thank my rapporteurs, Prof. Jean DUBESSY and Dr. Ryan L. HARTMAN for their time, interest and helpful comments.

I am also very grateful to Cyril AYMONIER, the director of Group 7, for his scientific advice and knowledge and many insightful discussions and suggestions. I especially want to thank Carole LECOUTRE for her kindness and supportive. Thank Jalil OUAZZANI for numerical simulations performed for understanding of our systems. Thank you very much.

I would also like thank my friends and peers in Group 7, present and past, for their good advice and collaboration, as well as moral support and friendships. They have helped me keep things in perspective during some of the most difficult times over the past three years.

I gratefully acknowledge the funding sources that made my Ph.D. work possible, especially the ANR support through the 2012 SEED Project “CGSμLab” and the

CNES support through the ICMCB-CNES R&T projects. I was funded by the BQR of University of Bordeaux for my 3 years. I was also supported by the China Scholarship Council (CSC).

Last, but not least, I would like to thank my family and all my friends for their tremendous love and support.

Thèse de Na LIU

Université Bordeaux 1

Soutenue le 22 Novembre 2013

Résumé en français

La gestion durable de la filière CO_2 est au cœur des problématiques liées aux changements climatiques dus à l'effet de serre. A ce jour, la quantité de $C0_2$ rejetée dans l'atmosphère atteint des masses considérables, evaluées à plus de 36 Gt/an en 2013, en augmentation sensible ces dernières années. Parmi les solutions de remédiation proposées et compatibles avec la gestion de telles quantités de CO_2, seul le stockage géologique dans les aquifères salins apparaît comme une voie prometteuse et réaliste au vu des volumes et des sites de stockage potentiels. Toutefois, les aquifères salins ne bénéficient pas toujours d'une description géologique détaillée, contrairement aux sites déjà exploités et donc mieux connus, comme les anciens bassins pétrolifères ou les bassins miniers de charbon. Malheureusement, ces dernières formations géologiques offrent des volumes de stockage très insuffisants. Le stockage profond du CO_2 dans les aquifères salins nécessite donc d'acquérir des connaissances scientifiques suffisantes et avérées pour définir les futurs scénarios d'injection, pour estimer la rentabilité et capacité de stockage du réservoir et pour, finalement, évaluer les risques de fuite avec la certitude nécessaire pour une acceptation sociétale du procédé.

Il est communément admis que quatre principaux mécanismes de piégeage du CO_2 se produisent pendant et après son injection dans les aquifères salins: (i) le piégeage structurel du CO_2 sous une roche de couverture à très faible perméabilité, (ii) le piégeage résiduel ou « capillaire » qui correspond au CO_2 essentiellement piégé par effet capillaire dans le milieux poreux, (iii) la solubilisation du CO_2 dans la saumure et enfin (iv) la minéralisation qui constitue le mode ultime de stockage le plus sécurisé à très long terme. Depuis trois décennies, de nombreuses études ont été réalisées sur ces différents mécanismes, comprenant à la fois la modélisation théorique et la simulation numérique, associées à la mise en oeuvre de démonstrateurs pilotes représentatifs des technologies à déployer pour la capture, le transport et le stockage profond du CO_2. Mais en raison des grandes échelles spatiales et temporelles à considérer pour le stockage, les études à l'échelle du réservoir géologique révèlent de nombreuses lacunes dans notre connaissance, notamment à l'échelle du pore, pour évaluer avec certitude la réelle capacité de stockage et l'effet de la séquestration du CO_2 dans des aquifères salins.

Très récemment, des stratégies complémentaires se sont donc développées pour tenter de répondre à ces limitations. En particulier, les approches utilisant des micromodèles ont contribué à des progrès spectaculaires dans la compréhension des écoulements diphasiques en milieu poreux et ont apporté de précieuses informations sur les comportements à l'échelle porale. Toutefois, la plupart des études actuelles se limitent à des conditions de pression et de température proches des conditions ambiantes de température et de pression (*i.e.* 25°C – 1 atm).

L'objectif principal de ce travail de thèse a été de démontrer la fiabilité et la capacité des micromodèles fonctionnant à haute pression et haute température - c'est-à-dire dans les conditions réelles de stockage - pour étudier, à l'échelle des pores, l'influence des principaux paramètres clés liés au stockage géologique du CO_2. Ce travail de thèse a donc été focalisé sur la mise en oeuvre d'outils et de techniques de mesures permettant l'accès à la connaissance de cinq paramètres

spécifiques qui contrôlent les différents mécanismes du piégeage profond du CO_2 et dont le rôle est essentiel pour les développements des futures technologies à déployer dans la gestion durable de la filière CO_2.

1. **La perméabilité relative** : comment le CO_2 se déplace au sein de la saumure ?
   ➔ Objectif : comprendre le comportement de migration de fluides modèles dans le réservoir.

2. **La pression capillaire** : combien de CO_2 est piégé par les forces capillaires ?
   ➔ Objectif : prédire la distribution et le comportement des fluides dans les milieux poreux.

3. **La saturation**: quelle fraction de l'espace poreux est remplie de CO_2 ?
   ➔ Objectif : prédire la capacité de stockage du CO_2 sous la roche de couverture.

4. **La solubilité** : combien et à quelle vitesse (i) le CO_2 se dissout dans la saumure et (ii) l'eau se dissout dans phase riche en CO_2 ?
   ➔ Objectif : analyser les données d'inclusions fluides, la précipitation des carbonates et le piégeage résiduel du CO_2.

5. **La précipitation des carbonates** : comment le CO_2 précipite pour former des carbonates et quels sont les taux de précipitation ?
   ➔ Objectif : prédire la sécurité d'un site de stockage de CO_2.

La thèse est divisée en quatre chapitres :

Le chapitre introductif présente les motivations de ce travail de thèse et traite de l'examen des méthodes possibles pour une gestion durable de la production de CO_2 anthropique, où le stockage géologique profond du CO_2 dans les aquifères salins est une solution proposée. Une partie bibliographique sur les travaux de recherche antérieurs ou actuels concernant les études des mécanismes de drainage / imbibition / solubilisation du CO_2 dans les milieux poreux aqueux est ensuite réalisée. Il en ressort qu'une connaissance scientifique expérimentale adéquate à l'échelle du laboratoire est nécessaire pour mieux comprendre les mécanismes de stockage dans les formations géologiques. L'observation des écoulements diphasiques en milieu poreux peut en effet apporter de précieuses informations sur les études du stockage du CO_2 dans des aquifères salins profonds et à l'échelle porale.

Le chapitre 2 présente un examen approfondi de la technologie microfluidique à haute pression, en particulier concernant la conception des micro-réseaux de pores, les matériaux utilisés, les procédés de fabrication, la visualisation et la caractérisation, et leurs applications dans les études de déplacement de CO_2. Les réseaux poreux 2D (micromodèles) sont fabriqués sur la base de la technologie silicium / Pyrex pour reproduire les conditions du réservoir et faire varier les propriétés de mouillabilité. Ces derniers peuvent être couplés à diverses techniques de caractérisation *in situ* (observation visuelles, spectroscopie Raman et UV) et sont capables de mimer les conditions de stockage réelles rencontrées dans les réservoirs de stockage.

Le chapitre 3 - dont les résultats ont été publiés (N. Liu *et al.*, *Chem. Phys. Lett.*, **2012**, 551, 139-143) - décrit une méthode nouvelle et rapide pour déterminer la solubilité du CO_2 dans l'eau ou la saumure en couplant les micromodèles haute pression avec la spectroscopie Raman confocale. Les courbes d'étalonnage pour la solubilité du CO_2 dans l'eau et la saumure ont été tracées dans une large gamme de température, de pression et de la salinité. Cette étude a prouvé que l'utilisation de microréacteurs sous pression combinée à la technique de spectroscopie Raman peut être étendue à

une grande gamme de concentration de CO_2. Mais plus important encore, cette méthode réduit considérablement le temps de l'expérience.

Enfin, la dernière partie de ce mémoire met l'accent sur le processus de drainage et de réactions CO_2 - saumure - minéraux au sein d'un réseau poreux 2D dans les conditions de stockage. Les effets de la composition de la saumure, de la porosité, de la pression, de la température, de rapport de viscosité ($M=\eta_{CO2}/\eta_{H20}$), du nombre capillaire et de la mouillabilité ont été étudiés. La figure 1, où les deux images supérieures correspondent à la saturation initiale en eau (ou saumure) de réseaux de pores mouillants et non-mouillants à l'eau (T=40°C ; p=8MPa), illustre les captures optiques sous microscope des différents mécanismes de déplacements et/ou de piégeage, comme:

- Le drainage où le CO_2 percole à travers le réseau de pores et occupe un certain nombre d'espaces poraux.
- La séparation de phase où des gouttelettes d'eau peuvent précipiter de la phase de CO_2 dans certaines conditions de température et de pression correspondant à une faible solubilité de l'eau dans le CO_2.
- La précipitation des carbonates dans le cas des systèmes CO_2 / saumure contenant des cations métalliques (Ca^{2+} ici). Ce mécanisme se produit généralement avant que le CO_2 ne pénètre dans le réseau de pores, par réaction entre les ions carbonates et les cations métalliques. Cette réaction est très dépendante du pH de la saumure.
- Le séchage où, au cours du temps, l'eau résiduelle se solubilise dans le flux de CO_2, pour finir par une saturation complète en CO_2, en considérant ici un flux constant de CO_2 « sec ».

Sur la base de ces premières observations « géologiques » uniques à l'échelle du pore, nous avons noté que la chute de pression le long du microsystème est déterminée par le rapport des viscosités et la vitesse d'injection. Elle est également fortement influencée par la taille des pores et la variation des conditions de mouillage dans le milieu poreux : une plus grande taille de pore génère une plus faible pression d'entrée et une percolation plus rapide du CO_2, tandis qu'un mouillage au CO_2 est favorable à une meilleure saturation en CO_2. Nous avons également établi que la saturation en eau résiduelle se traduit par différentes configurations (piscines, ponts, domes, gouttes isolées) de l'écoulement diphasique, tandis que la saturation en CO_2 augmente lorsque le nombre capillaire et le rapport de viscosité augmentent (digitation visqueuse et capillaire).

En conclusion, cette thèse constitue les premières études basées sur l'utilisation des microsystèmes géologiques sur puce pour simuler l'injection de CO_2 dans des aquifères salins profonds à l'échelle porale dans des conditions de stockage géologiques réelles (pression et température). Les études présentées dans cette thèse ont permis de valider le concept de « Geological Lab on Chip » (GLoC) en utilisant des micromodèles silicium / Pyrex pour capturer les principaux mécanismes d'invasion du CO_2 liés au stockage souterrain, impliquant la solubilisation du CO_2, les processus de drainage du CO_2, et la précipitation des carbonates.

Les innovations principales de cette thèse portent sur:

1- Le développement d'une méthode nouvelle et rapide pour mesurer la solubilité du CO_2 dans l'eau et de la saumure à l'aide de microréacteurs silicium-Pyrex couplés à la spectroscopie Raman confocale.
2- Les premières études de caractérisation des principaux mécanismes d'invasion du CO_2 dans un milieu poreux en conditions réelles de température et de pression.

En perspectives, cette thèse ouvre de nouvelles voies d'études basées sur des modèles plus réalistes de milieux poreux sous pression, en intégrant des hétérogénéités de perméabilité et/ou de

mouillabilité, en simulant des fissures, etc. De même, le couplage final entre des milieux poreux 3D reconstitués et la technique d'analyse en microtomographie X devrait permettre d'examiner les hétérogénéités 3D de la matrice poreuse. Les GLoCs offrent donc de nouvelles potentialités pour améliorer notre compréhension de la séquestration du CO_2 dans des aquifères salins profonds et contribuer ainsi aux futurs développements technologiques pour une gestion durable de la production de CO_2 par l'homme dans les années à venir.

Mécanismes de déplacement	Micromodèles hydrophiles	Micromodèles hydrophobes
Saturation initiale en saumure	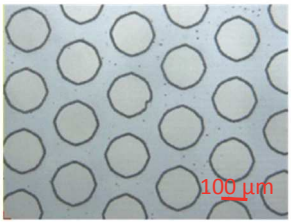	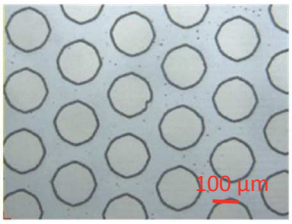
Drainage	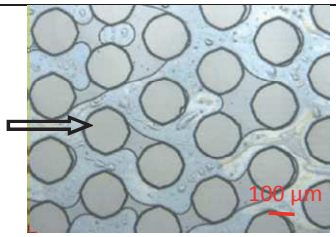	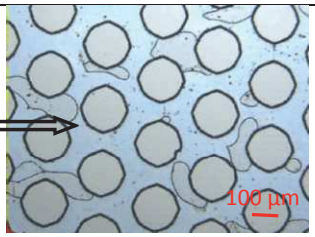
Séparation de phase	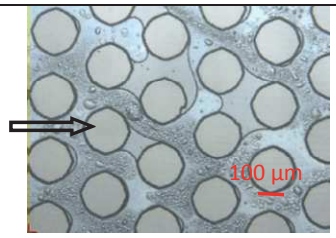	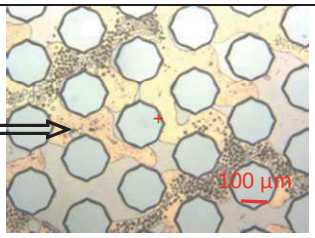
Précipitation de carbonates	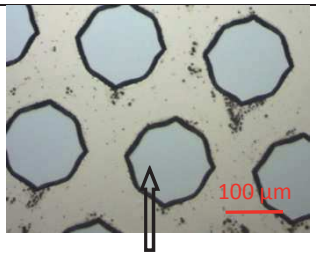	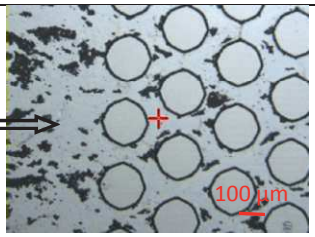
Séchage	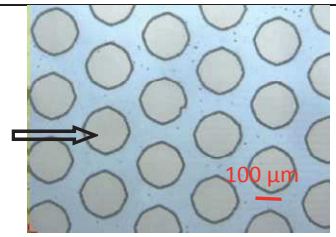	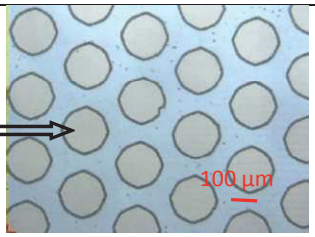

Figure 1 : *Mécanismes de déplacement observés durant les invasions de CO_2 dans les GLoCs 2D (mouillants ou non-mouillants à l'eau). La direction des flux de CO_2 est indiquée par les flèches noires.*

General Table of Content

General Introduction

The sustainable management of the gigantic CO_2 production by the industry and other human activities is currently a key factor for preventing climate changes due to the greenhouse effect. Among the proposed remediation solutions is CO_2 deep underground geological storage in deep saline aquifers. Such a storage required adequate scientific knowledge to evaluate injection scenarios, estimate reservoir capacity and assess leakage risks.

Mainly four different trapping mechanisms are thought to occur during and after CO_2 injection into the deep subsurface water formation: structural trapping, solubilization, mineralization and residual trapping. To investigate these different mechanisms, which understanding will drive the future of the carbon storage technologies, researchers generally focus on the study of (at least) five specific essential parameters:

1. Relative permeability: how the dissolved and immiscible CO_2 travels (moves) with brine? ➔ *Required for accurate modelling fluid migration behavior in the reservoir.*

2. Capillary pressure: how much CO_2 is trapped by capillary forces?
   ➔ *Required to predict fluid distribution and behavior in porous media.*

3. Saturation: what fraction of the pore space is filled with CO_2?
   ➔ *Required to predict the storage capacity of CO_2 stored underneath the caprock.*

4. Solubility: how much and how quickly CO_2 dissolves in brine and water dissolves in rich CO_2 phase?

   ➔ *Required to analyze fluid inclusion data, carbonate precipitation and residual CO_2 trapping.*

5. Carbonate precipitation: how CO_2 precipitates as new minerals and precipitation rates?

   ➔ *Required to predict the safety of a CO_2 storage site.*

Many studies have been performed on these problems quite recently, including both theoretical modelling and numerical simulation. Due to the large spatial extent and long time scale, core and field scale studies face limitations to assess the effect of CO_2 sequestration in saline aquifers. Meanwhile, micromodels have provided spectacular advances in the understanding of two phase flow in porous media and have brought valuable insight into pore-scale studies.

In this context, the overall objective of this thesis dissertation is to demonstrate the capability of high pressure (p) /high temperature (T) micromodels to investigate key parameters related to CO_2 geological storage at pore scale. The obtained experimental data could later feed the numerous numerical modeling works done in this field. The fabricated 2D porous networks are created in silicon/Pyrex microsystems to replicate the (p, T) conditions of the reservoir and to account for the key rocks properties. These, which can be coupled to various *in situ* characterization techniques, are able to mimic the actual storage conditions encountered in real storage reservoirs. Such an approach is proved viable in the laboratory, and can be used to simulate and analyze various CO_2 underground storage issues.

The dissertation is divided into four chapters (Fig. 1).

The first presents the motivations for selecting deep saline aquifers for geologic sequestration of CO_2 and contains a review on the previous research approaches of CO_2 displacement in porous media.

Chapter 2 presents an extensive review of high pressure microfluidics, pore network designs and micromodels materials, manufacturing processes, visualization and characterization, and their applications in CO_2 displacement studies.

Chapter 3 describes a novel and fast method to determine the CO_2 solubility in water or saltwater by using pressurized micromodels coupled to Raman spectroscopy.

The last chapter of the dissertation emphasizes a first approach of the drainage process and CO_2-brine-mineral reactions within a two dimension pore network micromodel under (p, T) storage conditions. Here the 2-D limitation introduced by the pore network will be used to overcome the difficulties of measuring the flow velocity field, thus introducing the direct observation of some key mechanisms of the CO_2/brine phase distribution. In this first capture of the pore-scale phenomena in p,T storage conditions, the effects of porosity, pressure, temperature, capillary number, wettability and brine composition were investigated.

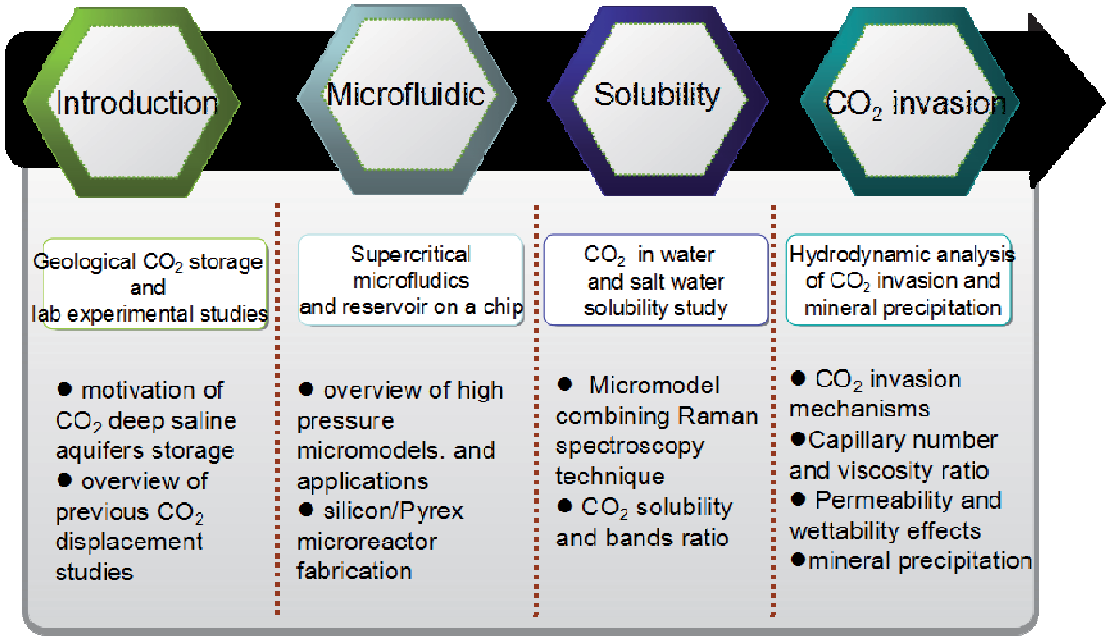

Fig. 1 *Scheme of the PhD manuscript organization.*

Chapter 1

CO_2 geological storage in Aquifers: Background, Key processes and Investigation strategies at small scale

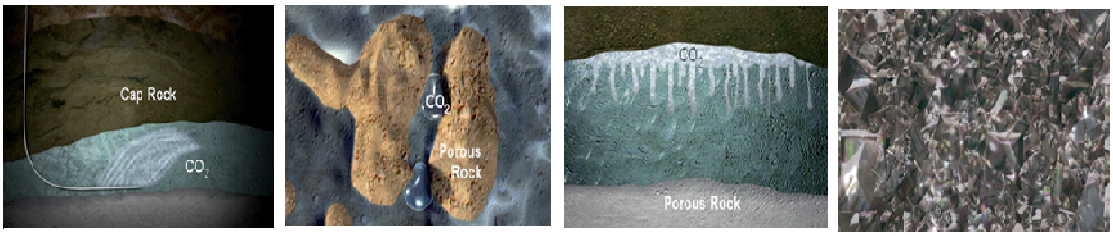

1. Introduction

The atmospheric concentrations of greenhouse gases, including carbon dioxide (CO_2), methane (CH_4), or nitrous oxide (N_2O), are increasing and have raised concerns over the last few decades (Fig. 1-1). The atmospheric concentration of CO_2 has increased in the atmosphere by 31% percent, CH_4 increased by 151% and N_2O increased by 17% during the Industrial Era and keeps increasing [1].

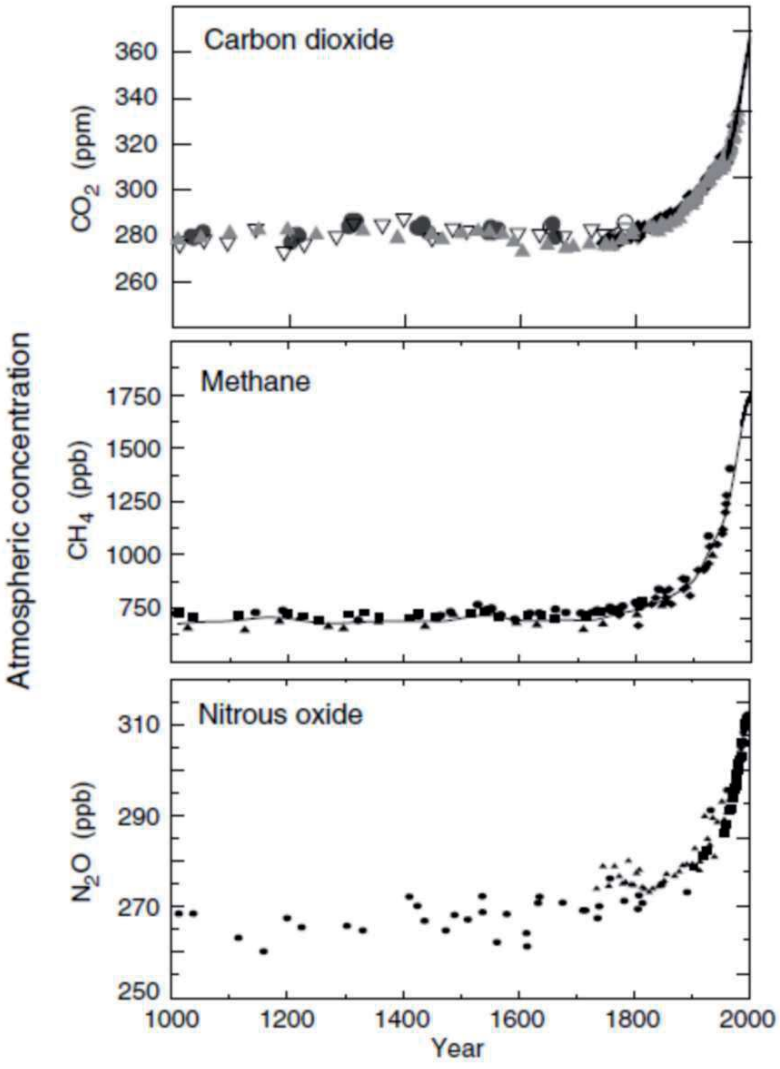

Fig. 1-1 *The sharp increase of three greenhouse gases (CO_2, CH_4, N_2O) concentrations in atmosphere during the Industrial Era [1].*

These greenhouse gases can absorb the infrared radiations of sunlight and trap the heat in the atmosphere, which results in the temperature of Earth's surface increasing. Radiative Forcing refers to the capacity of a gas contributing to climate change. As shown in Fig. 1-2, greenhouse gases result to the positive radiative forcing and ultimately lead to warming. Among all the greenhouse gases, CO_2 is the most important one in concentration. Methane (CH_4) is the second most prevalent greenhouse gas, which is oxidized to produce CO_2. Global warming studies suggest that the Earth's climate has warmed over the last century [2-3]. The overuse of fossil fuels (natural gas, oil, and coal) leads to the problem of rising anthropogenic CO_2 concentrations, which is considered as the major contributor to global warming.

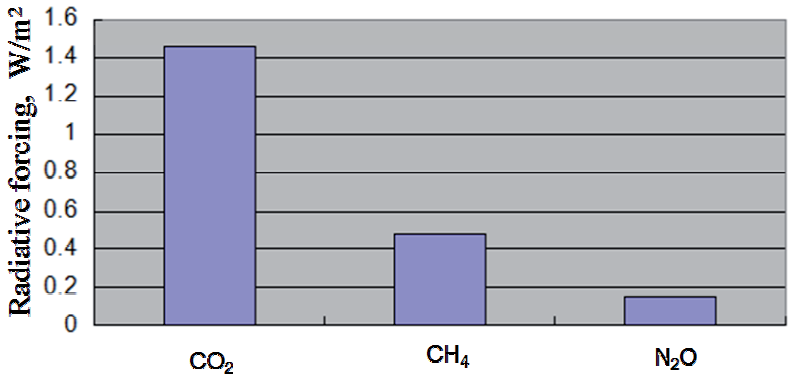

Fig. 1-2 *Radiative Forcing of greenhouse gases from 1750 to 2000 (data from IPCC 2001 [1]).*

2. CO_2 Emissions

The human-caused origin (anthropogenic) of CO_2 emissions is a cornerstone for the sharp increase rate of CO_2 concentration in the atmosphere [4]. In absolute terms, anthropogenic CO_2 emissions have strong links with human overuse of fossil fuels. Among the largest CO_2 emitters USA and China contributed most to this increase from fossil fuels combustion (Fig. 1-3).

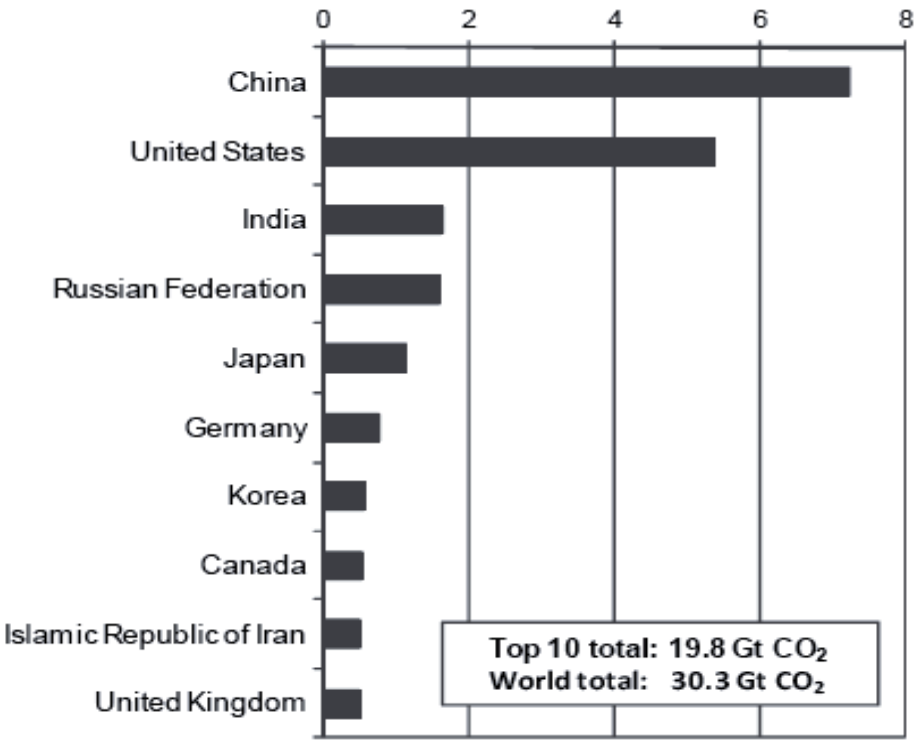

Fig. 1-3 *The top 10 countries by CO_2 emissions from fossil-fuel combustion in 2010 [5].*

The warming effect of CO_2 has been forecast to lead to an increase in global temperature of 1.8 - 4.0 ^{o}C by 2050 if current trends persist [6]. It is widely believed that the global warming effects will introduce dramatic environmental consequences, such as a rise of sea levels, a loss of fragile ecosystems, and a probable expansion of subtropical deserts [7]. Thus, a massive effort must be undertaken to slow down the buildup of CO_2 concentration in the atmosphere, which hopefully can control a stabilization concentration to no more than double of the pre-industrial level at around 550 ppm.

3. Strategies for Reducing CO_2 Emissions

Growing concern about the human-induced CO_2 emissions in the atmosphere is driving technology developments to slow down the buildup rate. There are four key prospective solutions to reduce emissions using current technologies: (a) switching to

hydrogen-rich fuels, such as natural gas, instead of carbon rich fuels; (b) decarbonizing fossil fuels to hydrogen; (c) switching to renewable energy sources (biomass, wind and solar); (d) Carbon capture and storage (CCS) [8,9]. Among all these options, CCS is the only way to reduce the carbon concentration in the atmosphere to solve the already serious climate change problem.

CCS refers to a family of technologies that enable the separation of CO_2 either pre- or post-combustion from major industrial sources, the transport of CO_2 *via* ships or pipelines, and its safe and permanent storage deep underground. Fig. 1-4 shows that capture is the largest cost component in a CCS system.

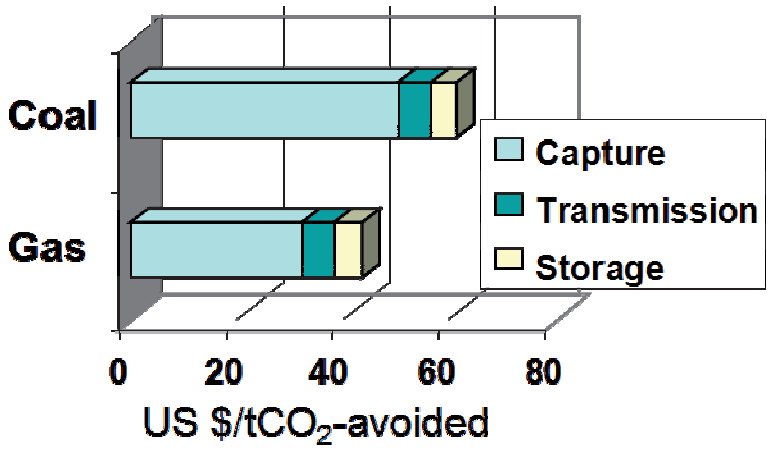

Fig. 1-4 *Costs of CCS systems from newly built, large-scale fossil fuel-based power plants (coal and gas) [6].*

CO_2 capture, the first step of the CCS chain, currently has three main approaches (Fig. 1-5) [10]: (a) Post-combustion systems separate CO_2 from the combustion gases flow; (b) Oxy-fuel combustion uses pure oxygen instead of air for combustion; (c) Pre-combustion systems transform the high-carbon fuel to H_2, which can be used as a fuel and CO_2 for storage.

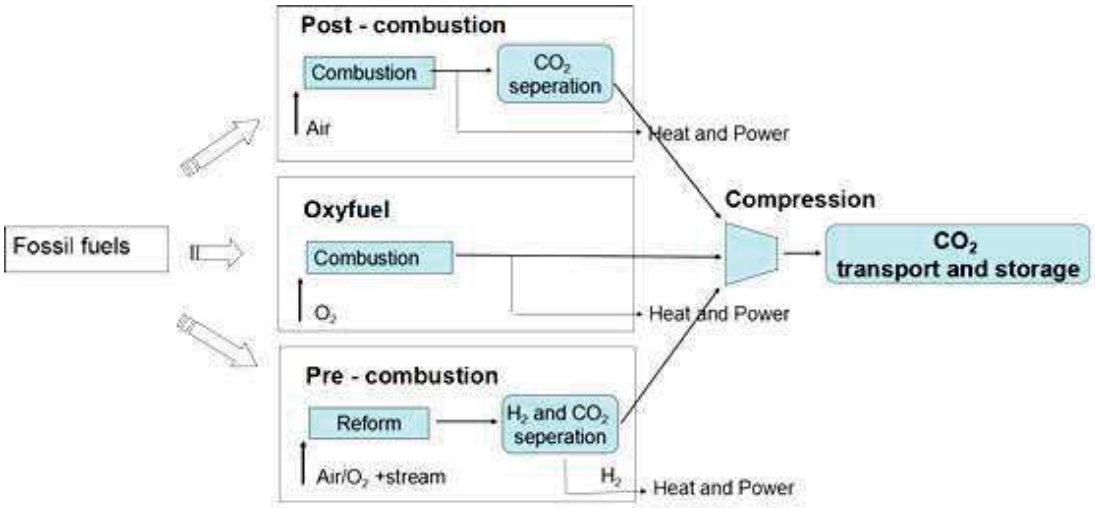

Fig. 1-5 *Schematic representation of three capture systems [1].*

Transport is the link step between CO_2 capture and storage sites. For the transport convenience, the captured CO_2 gas is generally first compressed to increase its density and reduce its volume. The compressed CO_2 can be delivered *via* pipelines, ships, and tanker trucks for industries of Enhanced Oil Recovery (EOR) and other storage sites. Concerned for public safety, transport pipelines are laid in extremely remote areas, like deserts, mountain ranges, seas and oceans down to 2200 m in depth [10].

The pressurized CO_2 is injected into suitable deep sedimentary formations. Various physical and geochemical trapping mechanisms would sequestrate it for millions of years.

CCS has been proved as a promising way to reduce the CO_2 emission from the large and centralized CO_2 sources including fossil-fuel and biomass energy facilities, natural gas production plants, synthetic fuel plants [11]. All technologies along the CCS chain have been operated in various industries for decades, although at relatively small scale. It is reported by Intergovernmental Panel on Climate Change (IPCC) that approximately 90% of emissions produced by the fuel plants can be captured and stored [12]. From the perspectives of both atmospheric stabilization and long-term sustainable development, CCS must capture and store around 25 Gt of carbon underground by 2050 [13].

4. Underground geological storage

We will now focus on the last step of the CCS chain: injection of CO_2 into deep underground. Since the 80's, millions of tons of CO_2 have been safely pumped into oil-producing formations for enhanced oil recovery (EOR), which indicates that geologic sequestration can be widely used as a CO_2 mitigation option [14]. Given the safety of CO_2 sequestration, a well structured, permeable reservoir is needed to contain CO_2 for millions of years.

4.1 Potential CO_2 Sequestration Sites

As discussed in the previous section, the overall task of CO_2 storage is to safely sequestrate CO_2 for a long time. This requires the following criteria for the candidate sites:

1) sufficient pore volume to store a significant portion of CO_2 emissions,

2) satisfactory sealing caprocks to prevent CO_2 from escaping out of the storage sites,

3) sufficiently stable storage environments: most of the injected CO_2 should be retained for 10 -30000 years,

4) location near the major CO_2 emissions sources to reduce the transport cost [15].

CO_2 is an odourless, colourless gas at normal temperature and pressure encountered in the atmosphere and turns supercritical when temperatures are higher than 31.1 °C and pressures greater than 7.38 MPa (critical point) (see Fig. 1-6 (a)). Supercritical CO_2 behaves like a gas, but has a much higher density that varies from less than 200 kg/m^3 to more than 900 kg/m^3 depending on pressure and temperature conditions, around 300 times volume reduction relative to gas (Fig. 1-6 (b)) [16]. As reported in IPCC, if 90 % of world total CO_2 emissions in 2010 could be captured, this would lead to a huge volume of CO_2 gas, which could cover the land area of France with a heigh of 2.7 m (for ρ_{CO2} = 1.98 kg/m^3). Therefore, for an efficient utilization of the underground storage space in the pores, the targeted injection formations should be

below 800 m, where the high pressure can condense CO_2 gas to supercritical fluid phase at higher density, therefore reducing its global volume (Fig. 1-6 (c)) [11].

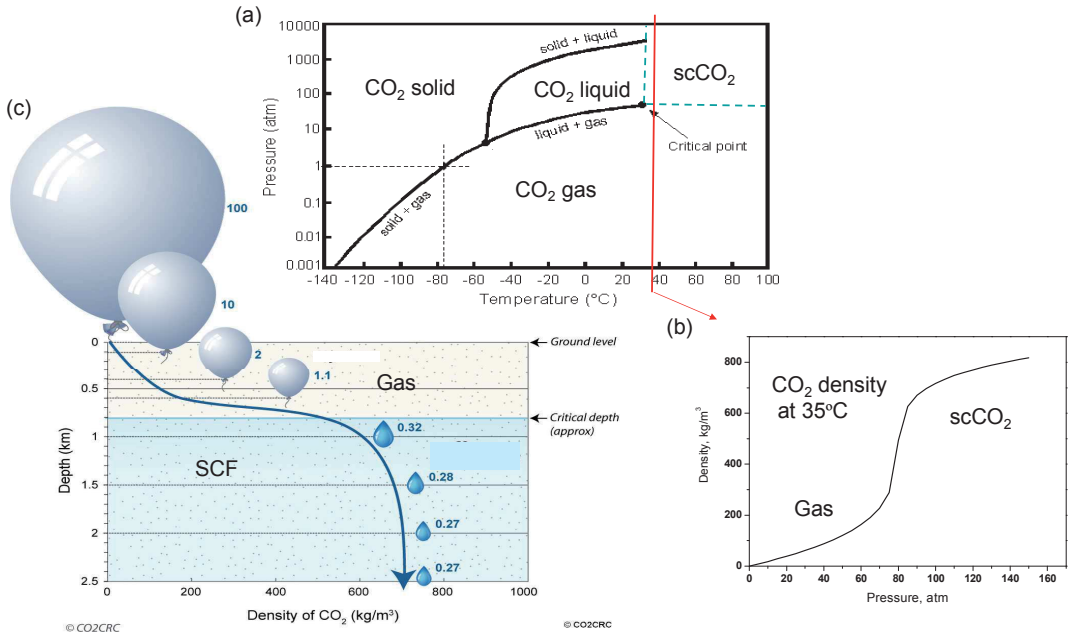

Fig. 1-6 *(a) CO_2 phase digram; (b) CO_2 density digram with pressure at 35 ºC; (c) CO_2 density increases with depth and becomes a supercritical fluid below 800 m (image from CO2CRC).*

Three different types of geological formations can fulfill the requirements for CO_2 storage (Fig. 1-7), as they already securely hold fluids such as oil, natural gas or brine often for millions of years: 1) depleted oil and gas reservoirs; 2) deep unminable coal formations; 3) deep saline formations.

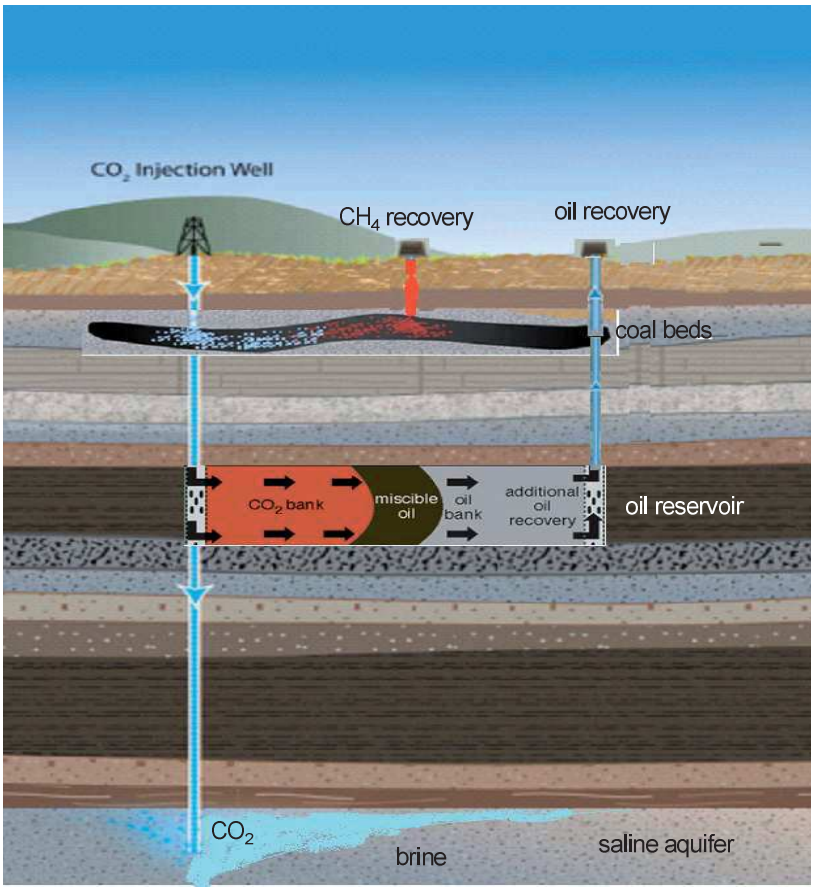

Fig. 1-7 *Options for storing CO_2 in deep underground geological formations (images Sources: CO2CRC).*

4.1.1 Depleted oil and/or gas reservoirs

Since the 90's, oil and gas reservoirs have been considered as attractive options for CO_2 sequestration. The injected CO_2 acts as a solvent to extract trapped oil, meanwhile, a significant portion of CO_2 remains in the reservoir. It is reported that 30 to 60 percent or more of the reservoir's original oil can be extracted *via* this method [17], and about 900 Gt of CO_2 could be eventually stored in depleted oil reservoirs [18]. By 2010, there have been over 2 billion cubic feet of CO_2 injected and over 280,000 BOPD (barrels of oil per day) produced in U.S through this method [19].

4.1.2 Deep unminable coal formations

Similarly, injecting CO_2 into coal beds can enhance CH_4 production, at the same time as CO_2 is immobilized by absorption in coal beds [20-21]. This produced Coalbed Methane (CBM) used as feedstock production of H_2 or petrochemicals, which can be used instead of coal as a much cleaner fuel. At the Allison Field ECBM project (San Juan Basin), 3:1 ratio of CO_2 and N_2 has been injected and increased methane production by ~77 % to ~95 % [22].

A huge economic benefit can be produced by EOR and CBM, while storing CO_2 in the subsurface (see Fig. 1-7). However, these sites often not have a well-defined structural-stratigraphic barrier for long term storage. These oil and gas extraction wells can also act as CO_2 leakage pathways. The significant pressure change due to reduplicative extraction and injection can cause fractures in the geologic framework.

4.1.3 Deep saline Aquifers

A saline aquifer consists of an underground layer of permeable rock filled with high salinity water and capped by a non-porous rock. The injected CO_2 can be trapped by a low permeability cap rock, by dissolution in the pore brine, and by reactions with minerals to finally form carbonate minerals. The Europe's longest-operating on-shore CO_2 storage site, Ketzin CO2SINK project, started in April 2004. Up to the middle of 2013, about 65.000 tons of CO_2 were successfully stored into this deep saline aquifer [23].

4.2 Why Saline Aquifers*?*

Unlike oil and gas reservoirs or coal bed with economic return, deep saline aquifers are considered as viable options for suitable injection due to their largest potential capacity [24-28].

Saline aquifers are permeable, geological formations typically located within sedimentary basins at depths below 800 m. It is evident that deep saline aquifers can

provide the largest potential storage volume because they exist extensively. It is estimated to ～ 70×10^6 km^3 of the total pore volume contained in saline aquifer formations worldwide [25]. The estimates for global capacity of CO_2 sequestration in saline aquifers vary from 100 to 200,000 Gt CO_2 because of the poorly constrained criterion [5]. They contain very salty water from 25 g/L to more than 225 g/L [29], which have little other economic interest at such high salinity. The high pressures encountered in this geologic layer framework indicate that they can withstand CO_2 injection and trap CO_2 at supercritical conditions [30].

The suitability of sedimentary basins for CO_2 storage depends partly on their location. To reduce the transport cost, the distance between the capture points and the storage sites must be within 300 km [31]. Fortunately, many fossil-fuel fired power plants suitable for CO_2 capture are located on coastal regions, where deep aquifers also widely exist. Therefore, a number of sedimentary basins distributed widely on- and off-shore are available for CO_2 storage.

In regard to the safety of saline aquifers, the well-developed pore structure and suitable top seal provide the excellent evidence to CO_2 retention as immobile phase for long-term CO_2 storage. Caprock, a confining shale or evaporite rock layer, will contain CO_2 in the reservoir. Fig. 1-8 shows that the sandstone and/or carbonate rocks of the porous media influences the internal movement of the injected CO_2 and react with the saturated CO_2-brine solution to precipitate carbonate, which will eventually eliminate the potential of leakage. Such aquifers offer the opportunity to contain CO_2 permanently.

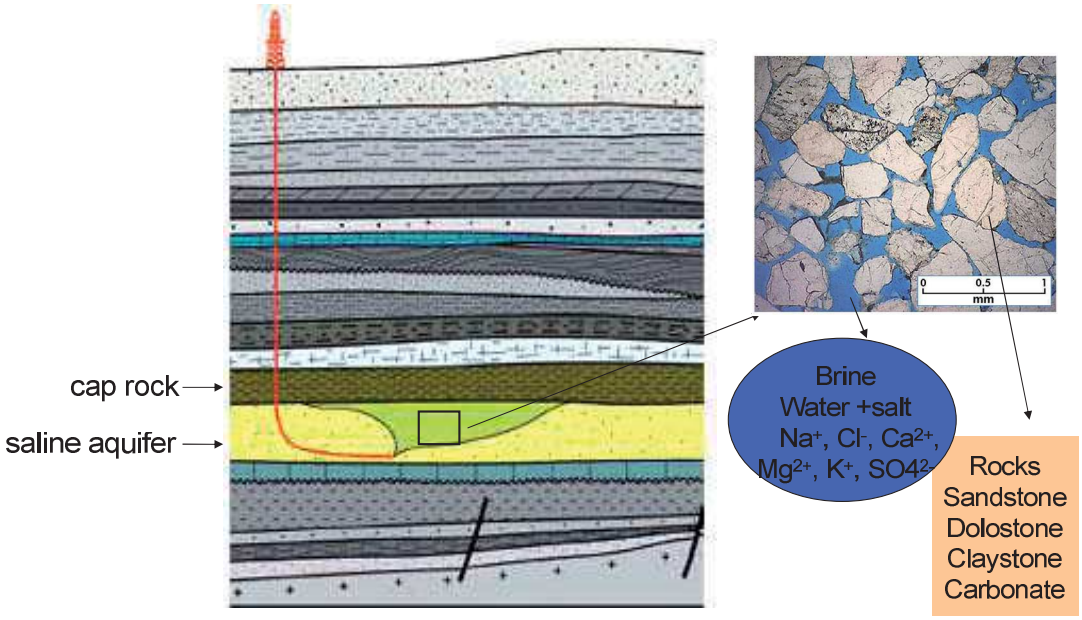

Fig. 1-8 *Injection CO_2 into deep saline aquifer (Image Source: CO2CRC and IFP).*

To present the general characteristics of a deep saline aquifer, we will focus on the example of the Ketzin storage site in Germany. Ketzin CO2SINK located at Ketzin, north-eastern Germany (Fig. 1-9 (a)), is the first on-shore CO_2 storage site in Europe aiming at understanding the geological CO_2 storage in saline aquifers. The Ketzin site was used as a gas storage facility in Lower Jurassic strata at about 280 m depth until 2000. Thus, the existing data and characteristics from site structural and stratigraphic features make it as a potential CO_2 injection aquifer. As shown in Fig. 1-9 (b), the target reservoir for the CO_2 injection has a total thickness of 70-80 m, lithologically heterogeneous Stuttgart Formation sandstones aquifer. The sandstones have an average porosity of 23 % and the permeability varies in the range of 500-1000 mD (millidarcy, 10^{-15} m^2). Temperatures measured at a depth between 600 and 700 m are 33-36 ºC and formation pressure at 700 m depth range from 7 to 7.5 MPa. Upper Triassic playa-type rocks of the Weser and Arnstadt Formations formed an approximately 160 m thick caprock sections. The porosities of the cap rock range from 13 % to 26 % and the average permeability is 0.1 mD. Brine in the target reservoir consists of 250-321 g/L dissolved solids.

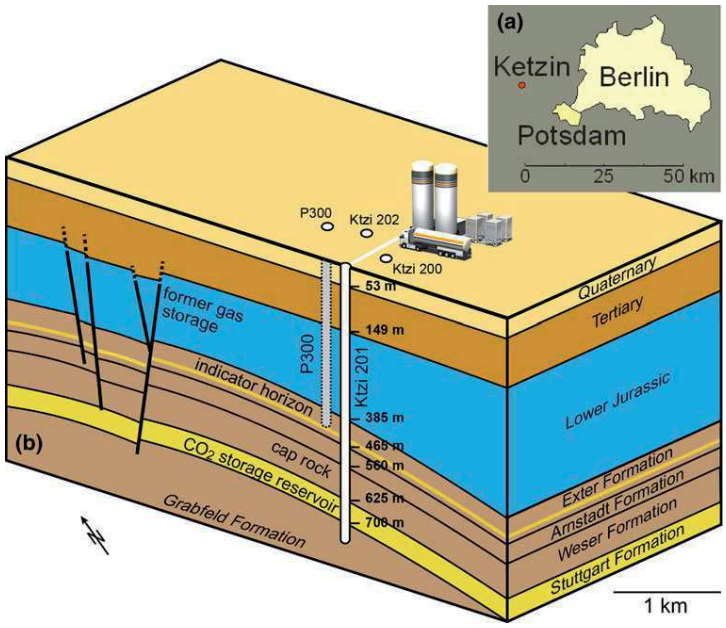

Fig. 1-9 *(a) Location of the Ketzin pilot site, (b) schematic block diagram of the Ketzin anticline from [32].*

Table 1-1 shows the composition of the brine. One injection well and two observation wells have been drilled to a depth of about 800 m into the target Stuttgart formation aiming at providing operational field experience to aid in the development of harmonized regulatory frameworks and standards for CO_2 geological storage [33-34].

Table 1-1 *Chemical Composition of brine from Stuttgart formation .*

Ions	Ca^{2+}	K^{+}	Mg^{2+}	Na^{+}	Cl^{-}	SO_4^{2-}	HCO_3^{-}
Concentrations ($mg \cdot L^{-1}$)	1760	430	1270	90,100	143,300	3600	40

4.3 Trapping mechanisms at large scale

When CO_2 is injected into a deep saline aquifer, a number of physics-chemical mechanisms cause it to remain trapped from free-phase CO_2 to CO_2 dissolved in water to CO_2 forming minerals over thousands of years [35-37] (Fig. 1-10). Once injected, the supercritical CO_2 will be sealed by a barrier of non-porous rock. This is

called “structural or stratigraphic trapping”, typical of hydrocarbon accumulations. While CO_2 plumes rise upward through the rock, an amount of CO_2 can dissolve into the groundwater, referred to as a “solubility trapping”. “Residual trapping” occurs when a small amount of CO_2 is trapped by surface tension in the porous rock. The capillary pressure shears off the tail of CO_2 plume as tiny bubbles trapped in the pore while CO_2 flows through the porous media, also called “capillary trapping” [38]. Eventually, “mineral trapping” reactions take hundreds to thousands of years or more, where the CO_2 precipitates as new carbonate minerals.

According to CO_2 injection numerical modelings [39-40], CO_2 can exist in three different phases along the injection site. Nearest the injection site the single CO_2 phase almost fully saturates the pore space. In this zone, the CO_2 rich phase can concentrate brine and precipitate salts out from brine due to the solubility of water in CO_2 (drying mechanism). The middle zone contains mixed brine phase with CO_2 (aq) and the CO_2 rich free phase. The outer zone only contains a small amount of aqueous CO_2 dissolved in brine. As shown in Fig1-10, initially, most CO_2 is physically trapped below low-permeability caprocks. Over time, the contributions of geochemical processes of solubility trapping and mineral trapping increase.

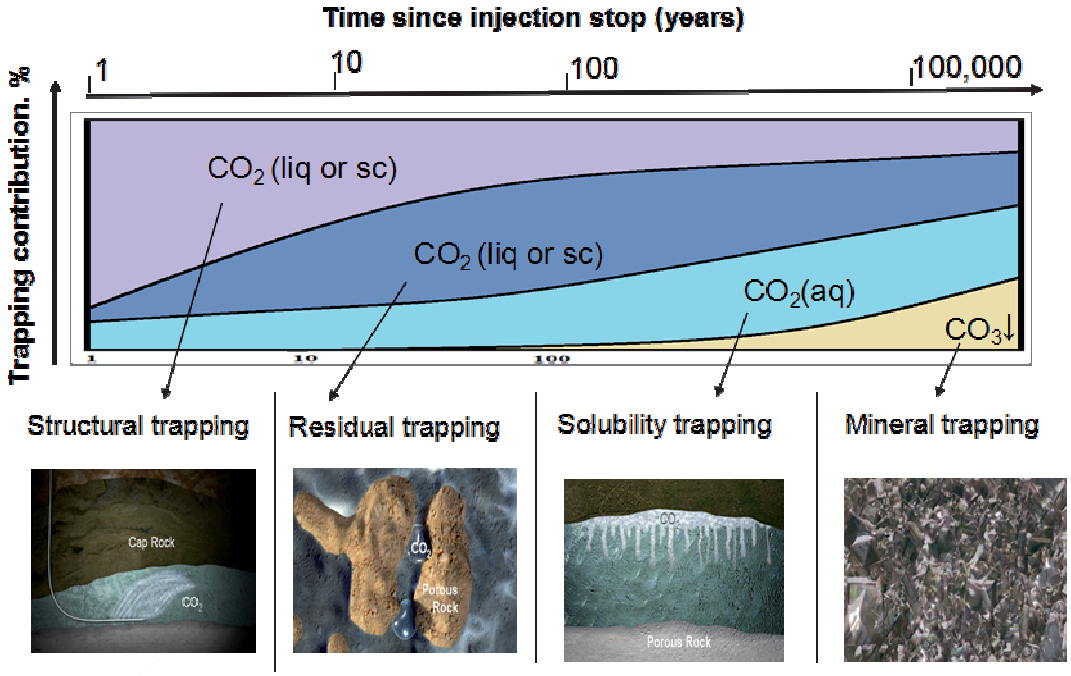

Fig. 1-10 *Four trapping mechanisms and storage safety over time (images from CO_2 Capture Project).*

Once CO_2 is injected into deep saline aquifers, these trapping mechanisms will trap CO_2 in the porous aquifers, and prevent it to escape to the surface. Thus, CO_2 storage capacity and safety are mainly determined by the trapping mechanisms parameters. In the next section, we will detail each trapping mechanism and expose the current approaches available for their studies.

5. Stratigraphic and structural trapping

5.1 Definition

The structural trapping is a type of physical trap that blocks the upward migration of the free CO_2 and formation fluid (e.g. water for Deep Saline Aquifers). It is the principal mean to store CO_2 in geological formations at short time scales (see Fig. 1-10). When CO_2 is injected into the deep saline formation, the supercritical CO_2 displaces and partly dissolves in the pore fluid. The free CO_2 phase is more buoyant than other liquids (CO_2 is 15-20 times less viscous than brine at 1000 m). Therefore, the influence forces of CO_2 migration away from the injection well involve both gravity and buoyancy force. The plume percolates up until reaching the caprock impermeable layer, and then spreads out laterally. The impermeable caprock in the form of a closed dome or anticlines can stop the upward flow and lateral escape, which is the key factor of safe storage through this trapping mechanism.

Structural trapping is effective but unreliable, as the CO_2 remains mobile. Indeed, pre-existing wells, faults or fractures in the sedimentary basins could act as leakage points [41]. Hence, the injection rate and time must be carefully taken into account not to exceed the allowable bearing pressure.

5.2 Experimental means

The major challenge in this trapping mechanism is the potential leakage of CO_2. Although typical caprock layers are nearly impermeable and often quite thick (160 m in the Ketzin site), faults and fractures or human-made wellbores that penetrate the confining layer are the main pathways for CO_2 leakage. Thus, understanding and predicting the CO_2 flow mechanisms in fractured media is important for designing methods to prevent CO_2 escape to the surface and remediate the confining layers.

Zhao et al. [42] performed a detailed study to analyze the effects of fractures for oil recovery in an artificial consolidated sandstone core with permeability heterogeneity at a typical reservoir temperature and pressure condition (70 ºC and 15 MPa). Nuclear magnetic resonance imaging (MRI) provides *in situ* analysis to characterize fractures and flow distributions in porous media. Fig. 1-11 (a) shows the artificial fractured sandstone core (15 mm in diameter and 40 mm in length).

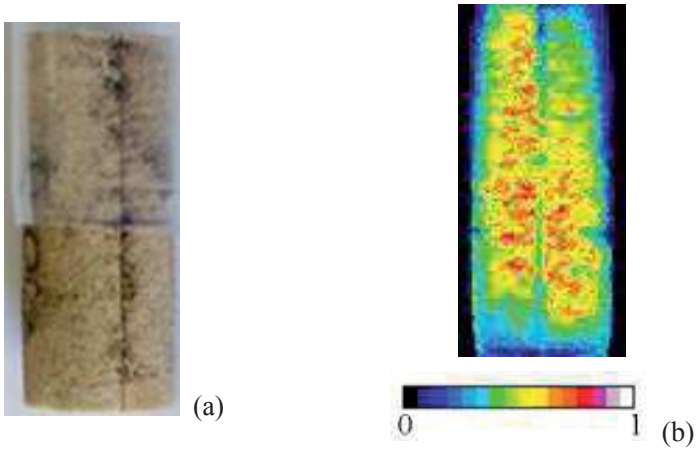

Fig. 1-11 *(a) Photo of artificial consolidated sandstone core (middle is fracture); (b) MRI signal intensity distribution image after water and subsequent supercritical CO_2 injection for 1 h.*

Besides the experiments conducted at core scale, some researchers also focused on investigations at pore scale. *Er et al*. [43] investigated the pore-scale behavior of the CO_2-oil interaction within a glass homogeneous fractured micromodel (Fig. 1-12).

This study observed at pore scale the miscibility, the CO_2 breakthrough, and the oil/CO_2 transfer between the matrix and fracture.

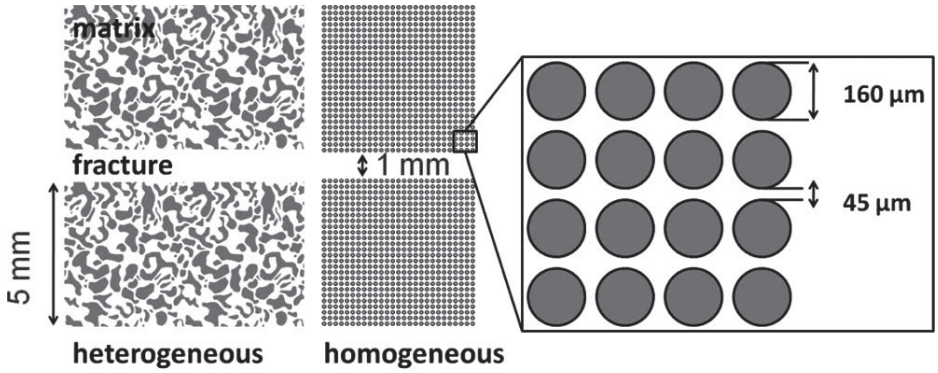

Fig. 1-12 *Pore patterns of the homogeneous fractured micromodel.*

In a fractured system, the displacement process tends to occur in the highly permeable fractures (Fig. 1-11 (b)). The fractures in the core often cause early breakthrough and poor sweep efficiency in the matrix. Especially for CO_2 driving oil recovery, a large portion of heavier components of oil is left behind in the matrix, and make it harder for CO_2 to diffuse inside.

Compared to core holder, microfluidic devices can provide substantial visualization information and enables us to monitor the process at the pore scale.

6. Capillary trapping at small and intermediate scales

When CO_2 plume migrates through the porous rock, the trailing edge may be isolated leading to immobilized blobs trapped in pore spaces due to capillary forces. Residual trapping is determined by the capillary pressure and often occurs in the heterogeneous porous rock with mixed pore sizes and low vertical permeability. In a heterogeneous storage formation, the capillary pressure of the rock is correlated with interfacial tension, contact angle and pore sizes, which is also one of the important

research objectives related to CO_2 displacement and will be discussed in detail below. Capillary trapping is an ideal mechanism for the geological storage of CO_2 as it increases storage capacity and containment safety. These residual trapped CO_2 bubbles are immobile, and will gradually dissolve into the brine, greatly decreasing the risk of leakage [44-45]. From Fig. 1-10, capillary trapping sustains the whole history of CO_2 migration in aquifers, from injection to the last long time sequestration. This is also the most studied aspect in CO_2 geological storage studies, from local trapping mechanisms to global capacity measurements.

6.1 Research approaches on capillary trapping and pore invasion

CO_2 physical displacement has already been studied on many levels including both integrated experimental investigations and numerical simulations to address fundamental issues. The interaction and iteration among these approaches are shown Fig. 1-13. Multi-phase flow experiments are being carried out to investigate the fundamental processes that underpin these questions. Computer simulations have attempted to model the propagation of CO_2 in the aquifer over thousands of years and provide the theoretical basis and research orientations for the experimental studies [46]. Flow theory offers theoretical foundations for observing the CO_2 plume flows in the porous media with combined influence of gravity, capillarity and flowrate. The three-dimensional mapping of porosity, permeability and *in situ* capillary pressure in trapping reservoir is obtained from the detailed petrophysical analysis. Rock properties provide insight into the influence of heterogeneity on the multi-phase flows in the cores [47].

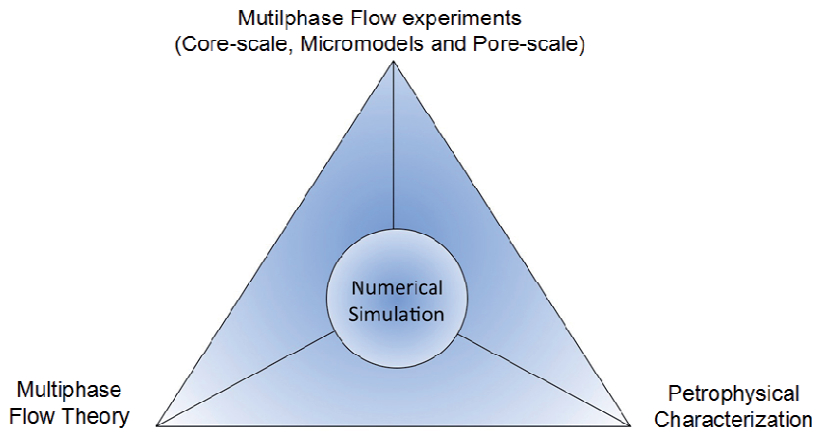

Fig. 1-13 *Illustration of the interrelated components used to study multiphase flow and trapping of CO_2 [48].*

6.2 Numerical simulation

TOUGH2, a general numerical simulator for multicomponent and multiphase fluid flow, has been widely used to replicate laboratory experiments or real storage conditions to model fluid injection and propagation through the rock core. Recently, a large number of works have been published to cover all aspects of CO_2 storage studies. *Burton et al*. [49] evaluated the injectivity of CO_2 into a homogeneous aquifer with a model based on Darcy's Law and Buckley–Lewerett frontal flow theory. *Pruess and Müller* [50-51] have studied the effect of the drying-out and salt precipitation during CO_2 injection. *Kopp et al*. [52-53] have reported the gravity, viscous and capillary effects on storage capacity of reservoirs, qualitatively. *Kuuskraa et al*. [54] simulated the CO_2 injection reservoir with different permeability sandstone layers, which showed that CO_2 preferentially breaks through the high permeability layers. *Marini et al*. [55] demonstrated that clay minerals and carbonates can lead to pore space geometry changes in a relatively short time. Finally, *Busch et al*. [56] consequently reported that clay minerals and carbonates can change the surface layer chemistry, which affects the wettability and the relative permeability. Numerical simulations are vital for predicting the storage capacity and safety. These are available

at various scales from micro- [57], core- [58], to reservoir- [59] scales with reasonable accuracy. The governing equations and dominating processes may vary with scale [60].

6.2.1 Reservoir scale model

The reservoir scale model focuses on the effect of flow processes and *in situ* parameters on injectivity and storage capacity of CO_2 in saline aquifers, such as, capillary pressure on CO_2 injectivity, dissolution and salinity on storage capacity, and the *in situ* thermodynamic conditions on dominating reservoir forces.

The governing equations are described as follow [61]:

$$\frac{d}{dt}\int_V M\,dV = \int_\Gamma F n d\Phi + \int_V Q dV \qquad \text{Eq. 1-1}$$

$$F = -K\frac{k_r}{\mu}\rho(\nabla P - \rho g) \qquad \text{Eq. 1-2}$$

$$k_{rw} = (S_h)^4 \qquad \text{Eq. 1-3}$$

$$k_{rn} = (1-S_h)^2(1-S_c) \qquad \text{Eq. 1-4}$$

$$p_c = p_0\left((S_c)^{-1/\lambda-1} - 1\right)^{(1-\lambda)} \qquad \text{Eq. 1-5}$$

where $S_h = (S - S_{wr})/(1 - S_{wr} - S_{nr})$ and $S_c = (S - S_{wr})/(1 - S_{wr})$. M, F and Q are the accumulation term, flux, and sink/source volumetric rate, successively. V, is an arbitrary sub-domain, Φ, is the closed bounded surface. The mass flux term F, is the determined by Darcy's Law. K is the absolutely permeability, k_r is relative permeability, which is obtained using the Corey model [62] by effective saturations, S_h, S_c. p_c is capillary pressure and can be obtained using the van-Genuchten model [63], which is determined by the entry pressure p_0, saturation S_c, and heterogonous distribution index, λ.

Alkan et al. [59] used TOUGH2 simulator to investigate the combined effects of capillary pressure, salinity and *in situ* thermodynamic conditions on the

CO_2-brine-rock interactions (Fig. 1-14). The target saline aquifer is a radial axis-symmetric model of 10,000 m in radius, 100 m in thickness, initially saturated with water. CO_2 is injected at a constant flow rate of 30 $kg \cdot s^{-1}$. The porosity and horizontal permeability of the aquifer are assumed to be 0.15 and 100 mD, respectively. The porosity and permeability of the upper cap rock are set at 0.02 and 0.001 mD, respectively. The reservoir temperature and pressure are 55 ºC and 12 MPa, respectively. They demonstrated the effects of capillary pressure, solubility, salinity, drying out and precipitation on CO_2 injectivity and storage capacity on a saline aquifer over a timescale of 100 years.

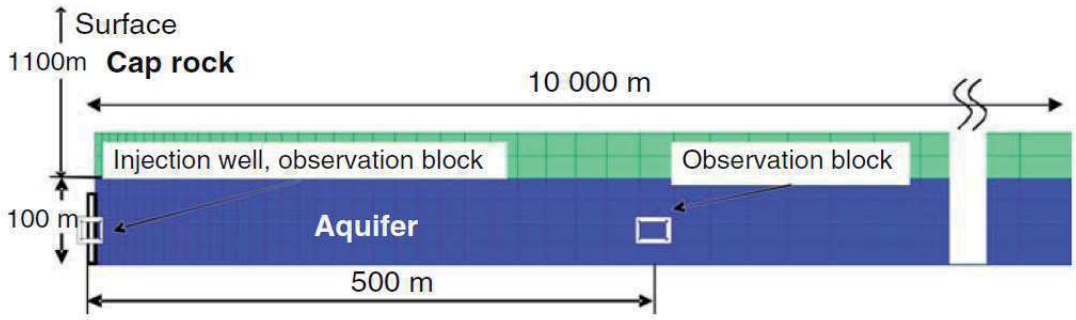

Fig. 1-14 *Schematic view of the model geometry at reservoir scale [59].*

6.2.2 Core scale model

Core scale model is usually conducted to simulate the displacement parameters of fluids during CO_2 injection: relative permeability and capillary pressure. They used the similar governing equations as reservoir scale model. However, core scale model chooses a rock core instead of the whole saline aquifer.

Perrin et al. [60] used the TOUGH2 MP simulator with the ECO2N fluid property module to qualitatively reproduce their lab experiments and correlate the porosity, saturation and capillary pressure. Rock sample is a 8.3 cm long Berea sandstone, which permeability is assumed to be 50 mD and porosity is 18.2%. The reservoir conditions are set at 63ºC and a pressure of 12.4 MPa. The brine solution is composed

of 6 $g \cdot L^{-1}$ NaCl and 0.5 $g \cdot L^{-1}$ $CaCl_2$. Fig. 1-15 shows that the saturation distributions are calculated with TOUGH2 MP to correct some of the important features in the core-flood experiments.

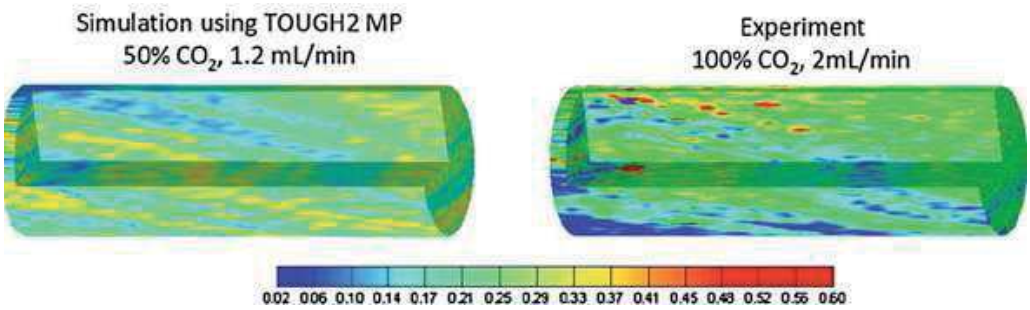

Fig. 1-15 *Comparison between simulation and experimental saturation map from [60].*

6.2.3 Pore Network Models

Pore Network Models (PNMs) are used to predict a detailed displacement mechanisms of CO_2. These models are used to assess the variability in relative permeability and capillary pressure for a long time. Recently, there has been an explosion of interest concerning the effects of wettability, capillary force and viscous force, hysteresis, and mass transfer between phases. A major challenge for accurate predictions of pore-scale modeling is the detail of the pore space geometry. As shown in Fig. 1-16, for pores with angular cross-sections, the non-wetting phase occupies the center of the pore space, while the wetting phase may occupy the crevices [64].

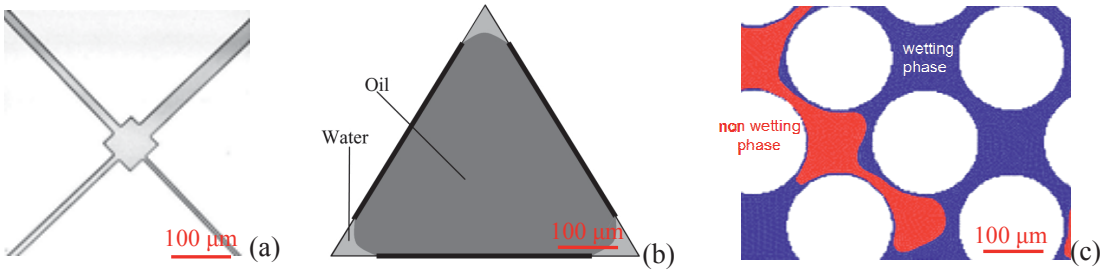

Fig. 1-16 *Different types of pore shape, wetting phase may occupy the corners while non-wetting phase occupies the pore center. (a) pore throat and squire pore body [49]; (b) pores with an angular cross-section [65]; (c) Pore shape formed by the intersection of four spherical grains*

[66].

Bandara et al. [66] used a pore scale model to investigate the effects of gravitational, viscous, and capillary forces on pore-scale displacement and capillary trapping mechanisms. In this study, the displacement flow of each fluid phase is described by the combination of the continuity equation and the momentum conservation equation:

$$\frac{d\rho}{dt} = -\rho(\nabla \cdot v) \qquad \text{Eq. 1-6}$$

$$\rho \frac{dv}{dt} = -(\nabla p) + \nabla \cdot \left[\mu\left(\nabla v + \nabla v^{T}\right)\right] + \rho g \qquad \text{Eq. 1-7}$$

$$p_c = \frac{2\gamma \cos\theta}{R} \qquad \text{Eq. 1-8}$$

where v is the velocity vector ($m \cdot s^{-1}$); ρ is the density ($kg \cdot m^{-3}$); p is the pressure (Pa); μ is the dynamic viscosity (Pa·s); g is the gravitational acceleration ($m \cdot s^{-2}$). p_c is calculated using the Young-Laplace Law.

Even though the numerical simulation has accurately modeled CO_2 injection into a saline aquifer, experimental methods are required to prove the simulation results and to calibrate the models.

6.3 Experimental approaches

Usually, flow experiments in porous media are also carried on three different length scales: micro-, core-, and reservoir- scales (Fig. 1-17). The research of upscaling can provide relatively reliable results. At lab scale, core- and pore- scale experiments can be performed. These are needed to predict the storage capacity and the effectiveness of capillary trapping, depending on the considered geological formation characteristics.

Core-scale experiments have been conducted to measure the relative permeability, capillary pressure and capillary heterogeneity as CO_2 migrates subjected to buoyancy

forces at representative reservoir pressure and temperatures. CO_2 and brine are co-injected into the core holder at a range of fractional flows and a number of different total flow rates. X-ray Computed Tomography is used to map CO_2 saturation and porosity of the porous media while relative permeability and capillary pressure are measured through Darcy's law during drainage and imbibition.

Micro-scale experiments are used to visualize and study the micro-scale complex flow behaviors in two-dimensional micromodels. Pore networks are etched into different materials such as silicon, glass, or can be molded in polydimethylsiloxane (PDMS). Micromodel displacements studies provide fundamental insights into the trapping mechanisms at pore scale, and quantitive analysis of the capillary heterogeneity, wettability, interfacial tension, core permeability, and effects of capillary and viscous forces [67,43].

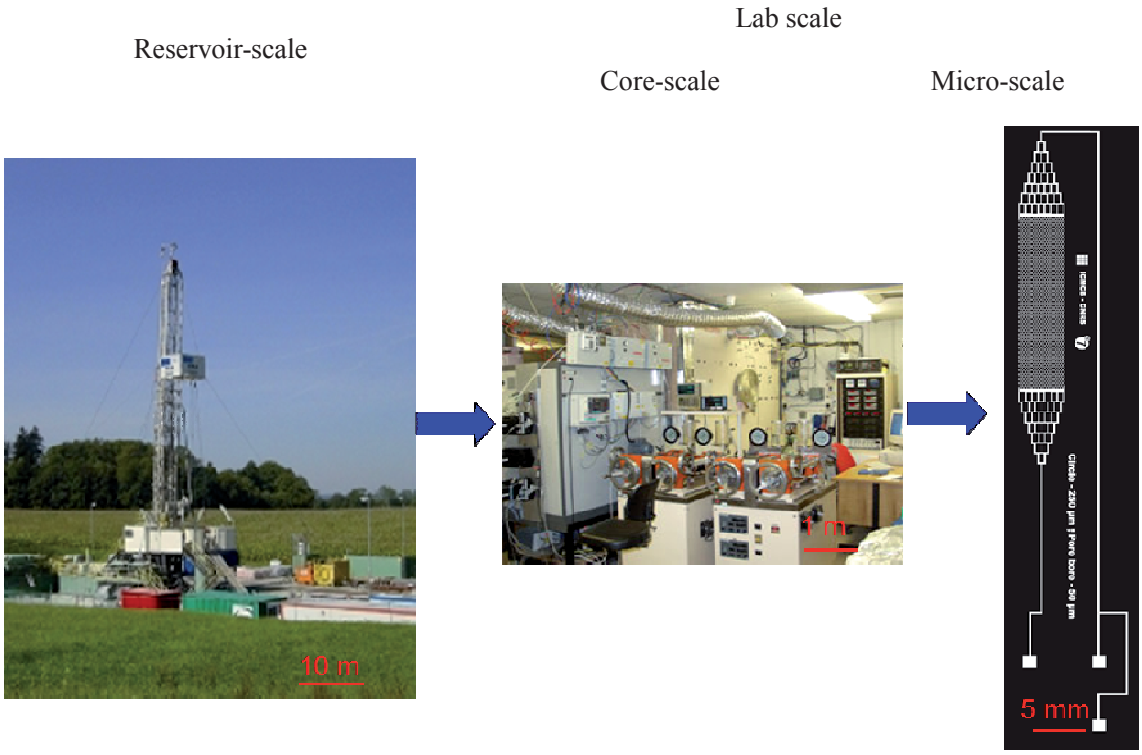

Fig. 1-17 *Three different scale experiments: reservoir scale, lab core scale, micro scale (from left to right).*

In brief, in parallel to a growing capability of the numerical simulations to predict the storage capacity and safety, the number of experimental investigations to characterize the displacement has also increased. Here, we overview the published lab experimental works at micro- and core- scale.

6.3.1 Core scale experiments

The core scale experiments used to investigate the drainage process of CO_2 in brine are usually conducted in a Hassler-type core holder loaded with a rock sample, and using X-ray Tomography to scan CO_2 and brine saturations (Fig. 1-18). A fixed ratio of the two phases is driven at a constant flow rate through a porous medium until the saturation and the differential pressure along the sample become constant [68].

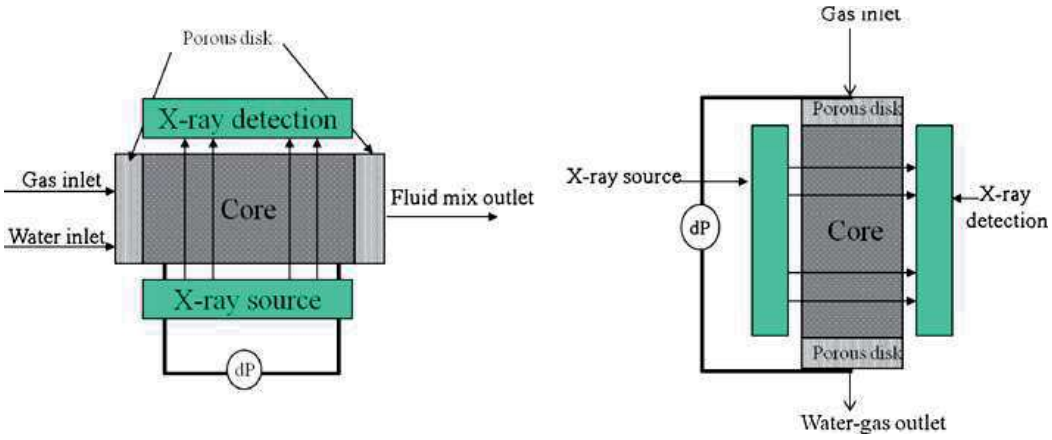

Fig. 1-18 *Scheme of typical core scale experiment set up [69].*

6.3.1.1 Relative permeability

In the CO_2/brine migration process, the CO_2 plume travels upward through the porous medium by gravity and buoyancy forces. As a result of the drainage at the top and the imbibition at the tail, a part of the CO_2 is trapped due to relative permeability hysteresis [70]. The relative permeability values k_{ri}, is proportional to the flow rate Q_i ($m^3 \cdot s^{-1}$) and the viscosity μ_i (Pa·s), and in inverse proportion to the absolute

permeability K (m^2), the cross-section area of the porous media A (m^2), and the pressure gradient dP/dx ($Pa \cdot m^{-1}$):

$$k_{ri} = \frac{Q_i \mu_i}{AK} \left(\frac{dx}{dP} \right) \quad \text{Eq. 1-9}$$

The relative permeability curve as a function of the saturation is needed to predict the storage capacity and to ensure the accuracy of modelling of the fluid migration behaviour in the reservoir.

Benson et al. [58,71-72] used the traditional steady state experiments setup, an aluminum core holder loaded with two different rocks (sandstone from the Otway Basin/Australia and fired Berea sandstone) to observe the behavior of exsolved CO_2 under a wide range of depressurization. The core is initially saturated with brine. 3-D porosity maps can be constructed by the images taken by X-ray Computed Tomography scanner along the length of the core. The temperature was maintained constant at 50 °C. Brine and CO_2 were co-injected into the core holder at a certain fractional flowrate and pressure. The CO_2 pumps were cooled down to 5 ºC by a surrounded cooling fluid to ensure a constant mass injection rate. At the outlet of the core, brine and CO_2 were in constant contact to each other to reach thermodynamic equilibrium, then separated by gravity in a high pressure separator.

During the experiments, the pressure drop across the core was measured with pressure transducers at the inlet and outlet of the core. After the system was stabilized, CO_2 saturation were recorded by X-ray Computed Tomography to create 2-D saturation maps along the length of the core, then the 2-D images were attached together along the third dimension to construct the 3-D saturation maps (Fig. 1-19). This process was repeated with sequentially higher fractional flows until fully saturation of CO_2.

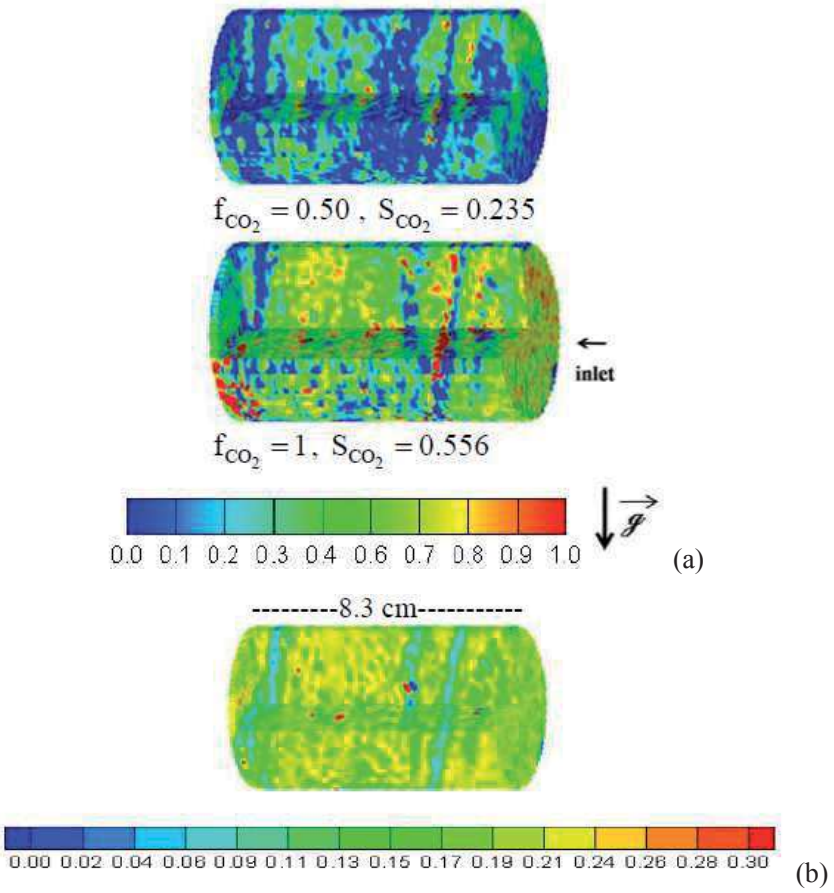

Fig. 1-19 *(a) Three dimensional porosity map and (b) Saturation map of CO_2-brine core flooding of Otway Basin sandstone [75].*

The CO_2 saturation is calculated according to the brine saturated images, the CO_2 saturated images and the experimental images at steady state:

$$S_{CO2} = \frac{CT_{\exp} - CT_{brine}^{sat}}{CT_{CO_2}^{sat} - CT_{brine}^{sat}} \qquad \text{Eq. 1-10}$$

where CT is a numerical value converted from the X-ray attenuation coefficients. The complete relative permeability curve was obtained by the saturation at each given flow rate. The experimental results showed that the incomplete fluid displacement is heavily influenced by the sample heterogeneity and the horizontal setup with long cores.

6.3.1.2 Capillary pressure

Capillary forces have significant effects on the migration and trapping of the injected CO_2. The drainage capillary pressure traps CO_2 into the pore until it reaches the threshold pressure. The interfacial interactions (interfacial tension, wettability) play important roles on fluid distribution and behaviour in porous media. Therefore, estimating interfacial interactions between CO_2, brine and reservoir rocks are crucial information for determining the effectiveness of CO_2 storage operation.

The laboratory studies at core scale have also focused on measuring the capillary pressure curves with CO_2 saturation and on elucidating the role of textural heterogeneity on CO_2 displacement mechanisms by using various techniques to characterize phase distributions in porous media.

Pentland et al. [73] performed the experiments in a core holder constituted of Berea sandstones to measure primary drainage capillary pressure and the relationship between initial and residual CO_2 saturation. A modified semipermeable disk was placed at the ends of the rock sample to vary the capillary pressure and saturation. The primary drainage time was inversely related to the capillary pressure. The longest drainage time was 166 hours.

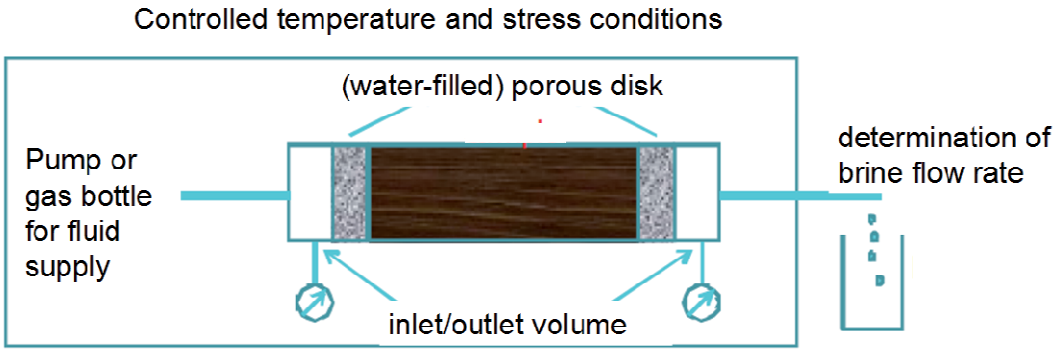

Fig. 1-20 *Schematic drawing of capillary threshold pressure set up [74].*

Pini et al. [75-76] presented a relative faster method to measure drainage capillary pressure curves and heterogeneity effects using the traditional steady state relative permeability experimental equipments. CO_2/water drainage capillary pressure curves

have been measured in less than two days. Two sandstone rock cores were used to quantify the capillary pressure heterogeneities at the sub-core scale: a homogeneous Berea sandstone and an Arqov formation core sample. CO_2 and water were first pre-equilibrated for at least 12 h at the experimental conditions by circulation in a closed loop.

Experiments were carried at two temperatures (25 and 50 °C); the core has a differential radial stress of about 3 MPa. The imposed CO_2 flow rate ranged from 0.5 up to 50 ml·min^{-1} to cover a sufficiently large portion of the capillary pressure curve. After reaching a stable reading of the pressure drop, a X-ray Computed Tomography scan was taken to get the core sample porosity and CO_2 saturation (see Fig. 1-21 (a)). The capillary pressure curves are then calculated using the pressure drop and the slice-averaged saturations (Fig. 1-21 (b)). This study quantified capillary pressure heterogeneities at the sub-core scale, which played an important role in controlling saturation distributions during multiphase flow.

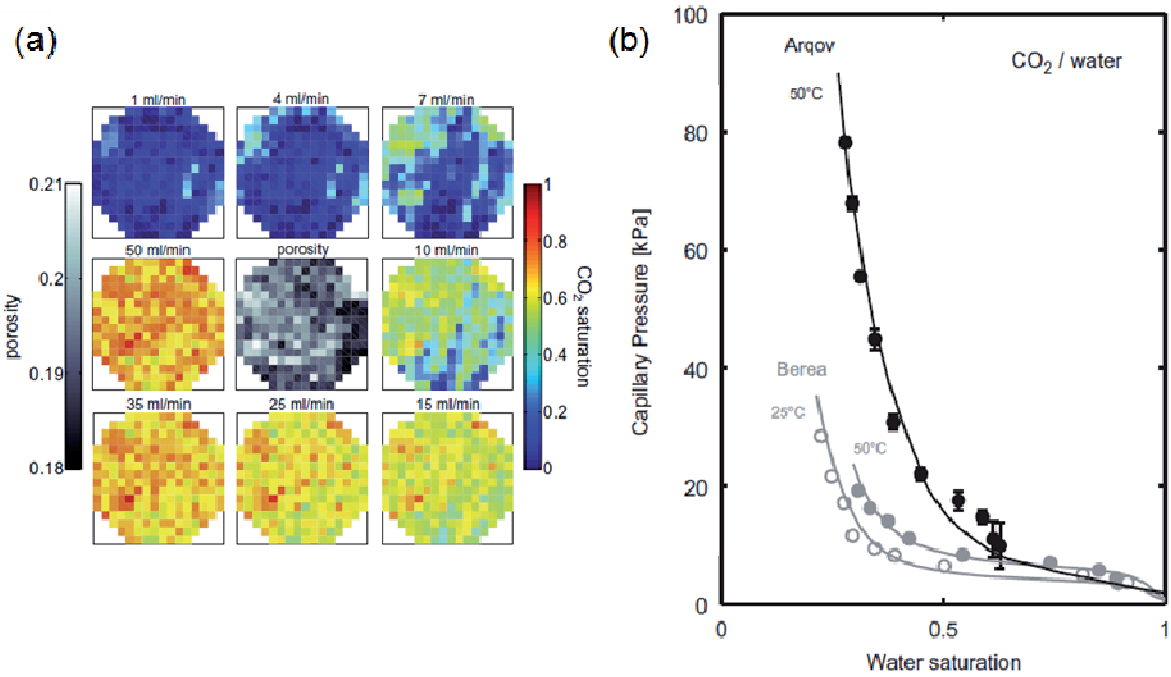

Fig. 1-21 *(a) CO_2 saturation and porosity maps; (b) Capillary pressure curves as a function of water saturation.*

Core scale method has addressed a certain degree of advantages for studying the displacement of CO_2 in brine at reservoir conditions. First, it can well replicate the real rock properties and reservoir conditions (p, T, wettability, etc.). Second, this technology can directly obtain the core saturation and CO_2 spatial distribution by X-ray Computed Tomography images analysis during the drainage process. However, core scale experiments need several days or even months to reach the steady state. Moreover, it is difficult to control the drainage process in the core. These disadvantages limit this research scale for in-depth studies of CO_2 trapping mechanisms. This shortcoming has leaded to the rise of micromodels pore-scale experiments.

6.3.2 Micro scale experiments

Microfluidic systems have addressed excellent heat and mass transfer, vast improvements in energy efficiency, and a much finer degree of process control. Pore network micromodels have been widely used for laboratory studies of two phase flow in porous media. Usually, pore scale experiments are conducted to study the detailed displacement mechanisms of CO_2, and to qualitatively analyze the effects factors on the CO_2 drainage process, such as capillary heterogeneity, wettability, permeability, capillary forces, and viscous forces. The experimental setups consist of patterned homogeneous or heterogeneous network microchannels (Fig. 1-22) with an inverted microscope for viewing and a CCD camera to record the flow images.

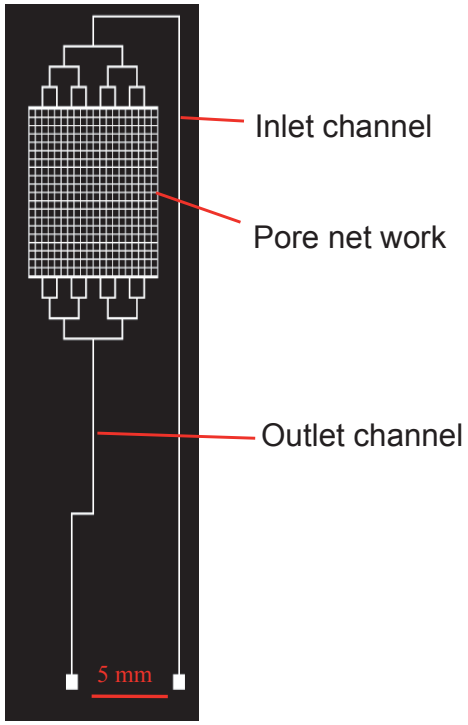

Fig. 1-22 *A typical network micromodel design (from ICMCB-CNRS).*

6.3.2.1 Micro scale study on relative permeability

The relative permeability measurements at micro scale are much faster and easier than core scale methods. *Gutiérrez et al*. [77] used a glass micromodel to measure the relative permeability of the wetting phase depending on the capillary number. Experimental tests were performed inside a 9 mm^2 flow area glass micromodel with a high-speed Kodak Ektapro camera, a monitor, and a workstation to record the captured images to estimate the relative permeability, saturation, pressure drop of each phase, and porous media data. The porosity of the glass micromodel was 53 % and its absolute permeability was 18 D. The non-wetting phase was air. Three diluted glycerin solutions were used as the wetting phase. Initially, the micromodel was perfectly wet by the wetting phase, and the nonwetting phase was injected by adjusting the pressure with a synchronized dual pump system. At the outlet, they were separated by gravity in a separator, then recycled back to each tank.

The experimental equipment was designed to determine the relative permeability at steady-state conditions. Steady state was assumed once pressure drop was stabilized.

After that, the high speed camera recorded glass micromodel flow images to calculate the saturation of all of the phases (Fig. 1-23).

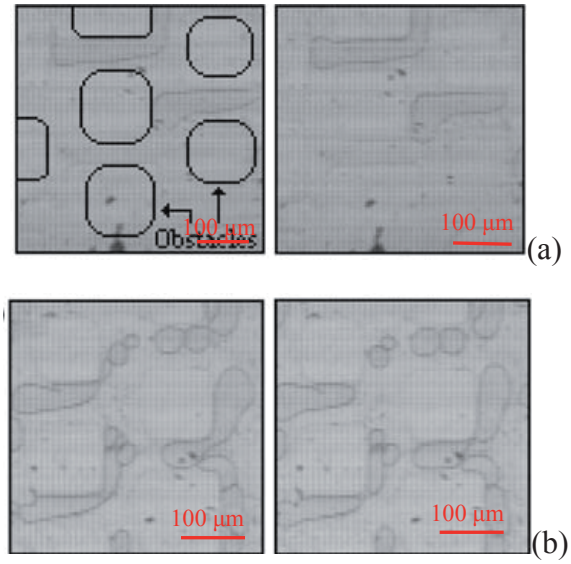

Fig. 1-23 *Air flow visualization in the glass micromodel: (a) slug flow and (b) dispersed flow with time.*

This study proved that visualization with high-speed video cameras can be used to determine saturation and this efficient and accurate *in situ* technique can be used to observe and study the flow mechanism inside the porous media. Capillary number and viscous coupling effects on the relative permeability and liquid flow mechanism were observed during the drainage process.

6.3.2.2 Wettability

The wettability of reservoir minerals and rocks is a critical factor to predict the capillary pressure in porous media. In the CO_2 drainage process, the aqueous brine is typically the wetting phase and the injected supercritical CO_2 ($scCO_2$) is usually assumed to behave as the non-wetting phase. However, CO_2 can exhibit weak wetting behavior under certain conditions [78-79]. The contact angle variation depends on the relative affinity of CO_2/brine/rocks. An increasing pressure, decreasing temperature

and salinity can cause an increasing solubility of CO_2 in water, a decreasing pH of the solution (from 6-7 to 3), which can further weaken the relative affinity.

Kim et al. [80] used high-pressure silica plates micromodels with homogeneous 20 mm × 10 mm pore network to measure micro-scale wettability and wettability alteration in $scCO_2$-silica-brine systems. The micromodel was fully saturated with degassed brine. Then $scCO_2$ was injected into the system at a constant flow rate for 20 min, at p = 8.5 MPa and T = 45 ºC. The digital camera recorded images of phase distributions in the micromodel to obtain the time-dependent saturation distributions. The ImageJ Software combined with a contact angle plug-in was used to analyze the acquired images. As shown in Fig. 1-24 (b), after the $scCO_2$ displaced the water, the residual water formed a thick film around the hydrophilic silica. Upon dissolution of $scCO_2$ in water, the adhesive force between water and silica surface became weaker, resulting in water film thinning and $scCO_2$ contact angle increasing. This work demonstrated the weak wetting behavior of CO_2 over the silica surface under deep reservoir conditions. The contact angle of CO_2 on silica increased from initially ～0° up to ～80°, with the increasing ionic strength.

This dewetting phenomenon has important consequences on reducing the capillary entry pressure, especially when the pressure and temperature are around the critical point, because the capillary pressure changes with the cosine of the wetting angle [81-82].

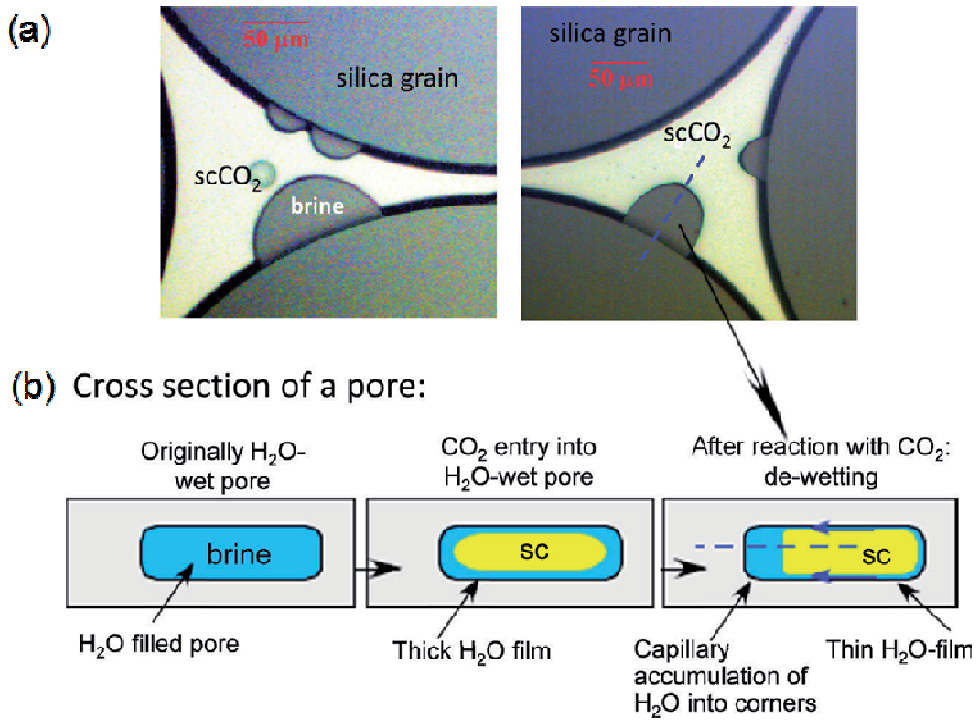

Fig. 1-24 *Dewetting process in a pore [80]: (a) experimental images and (b) process scheme.*

6.3.2.3 Displacement mechanism

Micromodels are ideal tools to investigate the displacement mechanisms due to their finer process control and visualization set up. Thus, a large body of microscale works has been published to investigate the displacement stability on the drainage process. The displacement stability will be discussed in detail in chapter 2. Unstable displacements play an important role in CO_2 capillary trapping within deep saline aquifers. Therefore, most of the opening literatures are focused on studying the effects of operation conditions (flow rate, temperature, pressure), fluids properties (viscosity and density ratio) and characteristics of the pore network (permeability, size distribution of pore throat and wettability) on unstable displacement transition from capillary fingering to viscous fingering. (please see Chapter 2, 3.3 for more details)

For example, *Løvoll et al*. [83] addressed drainage in a random two-dimensional glass beads to compare the gravity, capillary and viscous forces. They reported that

the decreasing gravity can lead to a transition from a capillary fingering behavior to a viscous fingering behavior.

Zhang et al. [84] performed a series of displacement experiments in a homogeneous water-wet pore network micromodel to investigate the impacts of viscous and capillary forces on displacement stability and fluid saturation distributions. According to their experiment results, CO_2 saturation increases with an increasing capillary number. At low flow rates and capillary numbers, capillary fingering occurs, while many viscous fingers form by increasing the injection rate. They pointed out that at constant same capillary number, capillary fingering lead to higher non-wetting fluid saturations compared to viscous fingering.

They also designed a pore network micromodel with two distinct permeability zones to investigate the permeability effect on the displacement stabilities, CO_2 flow pathways, and saturation levels [85]. They showed that CO_2 displaced water preferentially in the high permeability zone with the mechanism shifting from capillary fingering to viscous fingering with an increasing capillary number. The distribution patterns of CO_2 in the capillary fingering showed obvious lateral and backward flow, while flows are straighter in the viscous fingering mechanism (Fig. 1-25).

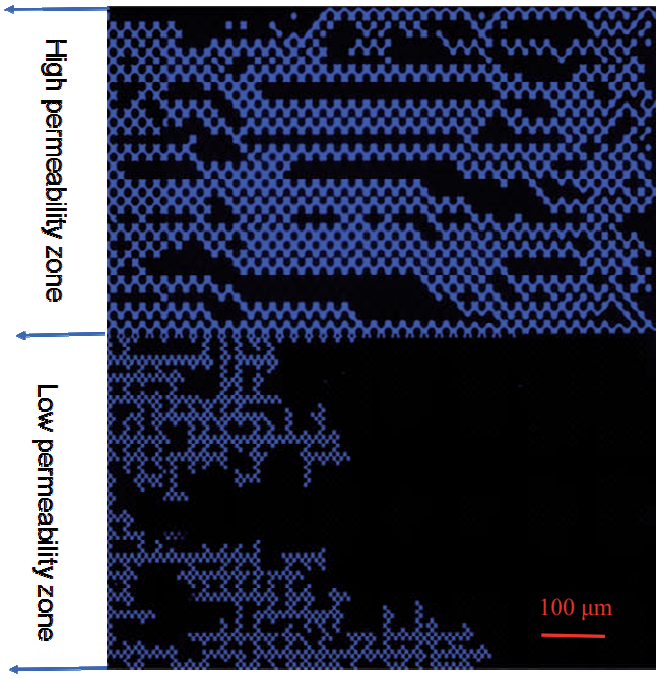

Fig. 1-25 *Viscous fingering in the higher permeability zone and capillary fingering in the lower permeability zone [85].*

6.4 Conclusion

In a word, core scale approaches can replicate the real rock properties to measure the the relative permeability, capillary pressure during CO_2 drainage process at representative reservoir pressure and temperatures. However, they also have limited control over the injection process, local temperature and concentration gradients and are time-consuming.

Micromodels have limitations to replicate the real reservoir rock characteristics (minerals, geochemistry) and conditions (p, T), but address excellent heat and mass transfer, vast improvements in energy efficiency, and a much finer degree of process control. Therefore, there is an increasing interest in developing new types of micromodels especially high pressure microsystems, to improve investigations of the CO_2 storage trapping studies including microscopic observation of fluid distribution and fluid/rock interaction.

Additionally, microfluidic techniques have now quickly evolved to allow the fabrication micromodels with well-defined surface and geometrical features, which can simulate the really storage conditions and rocks characteristics. We will detail deeply microfluidics and high pressure micromodels fabrication in chapter 2.

7. Solubility Trapping

Dissolution of CO_2 in brine is one of the most important long term storage mechanisms (Fig. 1-10). It is active over the full regarded period. The dissolved fraction may be eventually converted to solid carbonate minerals, thereby increasing storage capacity and effectiveness. Under reservoir conditions, the CO_2-rich fluid will flood on top of the brine-rich fluid, due to a density difference. At the interface between the two fluids, both CO_2 dissolution in brine and water in CO_2, can take place. Thus, in the reservoir p-T range, two phases coexist in this system: CO_2-rich phase and brine-rich phase.

Brine in deep saline aquifers dissolves large concentrations of salts. Na is the dominant cation in the saline groundwaters and water formations (90 $g \cdot L^{-1}$ in the Ketzin CO2SINK reservoir formation). The mutual solubilities of H_2O-CO_2 and H_2O-CO_2-NaCl systems have been discussed to be the key physical process for analyzing fluid inclusion data, for studying the carbonate precipitation and for enhancing the accuracy of the quantities of residual CO_2 trapping and storage calculations [86-87].

7.1 CO_2 solubilization in brine

The dissolution of CO_2 in brine not only depends on the reservoir conditions and the geologic properties, but also on plume migration. The migration of the CO_2 front and the convective mixing can greatly enhance the dissolution rate. Capillary pressure

in the porous media generates menisci contact area of brine-CO_2 that increases solubility trapping. In addition, the dissolved CO_2 can lead to pH decreasing and increasing brine density. Subsequently, the reverse density gradients result in a density-driven downward migration and dissolution of more CO_2 [88]. Once dissolved, CO_2 can precipitate onto the aquifer rock as carbonate mineral and drive reaction continuously to the right. Over time, an escalation in CO_2 dispersion and diffusion into the brine increases the storage safety through this mechanism [89].

7.2 Mutual solubilities of H_2O and CO_2 at reservoir conditions

CO_2 solubility in H_2O-rich phase is reported to increase approximately linearly with *in situ* pressure until the supercritical pressure is reached, and decreases with increasing temperature and salinity (see the right list of Fig. 1-26). The high solubility of CO_2 in brine (approximately 40 $kg \cdot m^{-3}$) in deep saline aquifers is favorable for long-term sequestration since the dissolved CO_2 is no longer subjected to upward buoyancy forces.

The H_2O solubility in CO_2 increases with increasing pressure and temperature above the critical point. In the lower temperature range, the solubility first decreases and then increases with a pressure increase (Fig. 1-26). This sharp discontinuity is due to a phase change at critical point. Above the critical temperature, the H_2O solubility trend with pressure becomes progressively smoother. The amount of H_2O dissolved in the CO_2 is quite small, an order of a magnitude less than the solubility of CO_2 into water. However, this explains the formation dry-out and salt precipitation occurring in the solution close to the injection points.

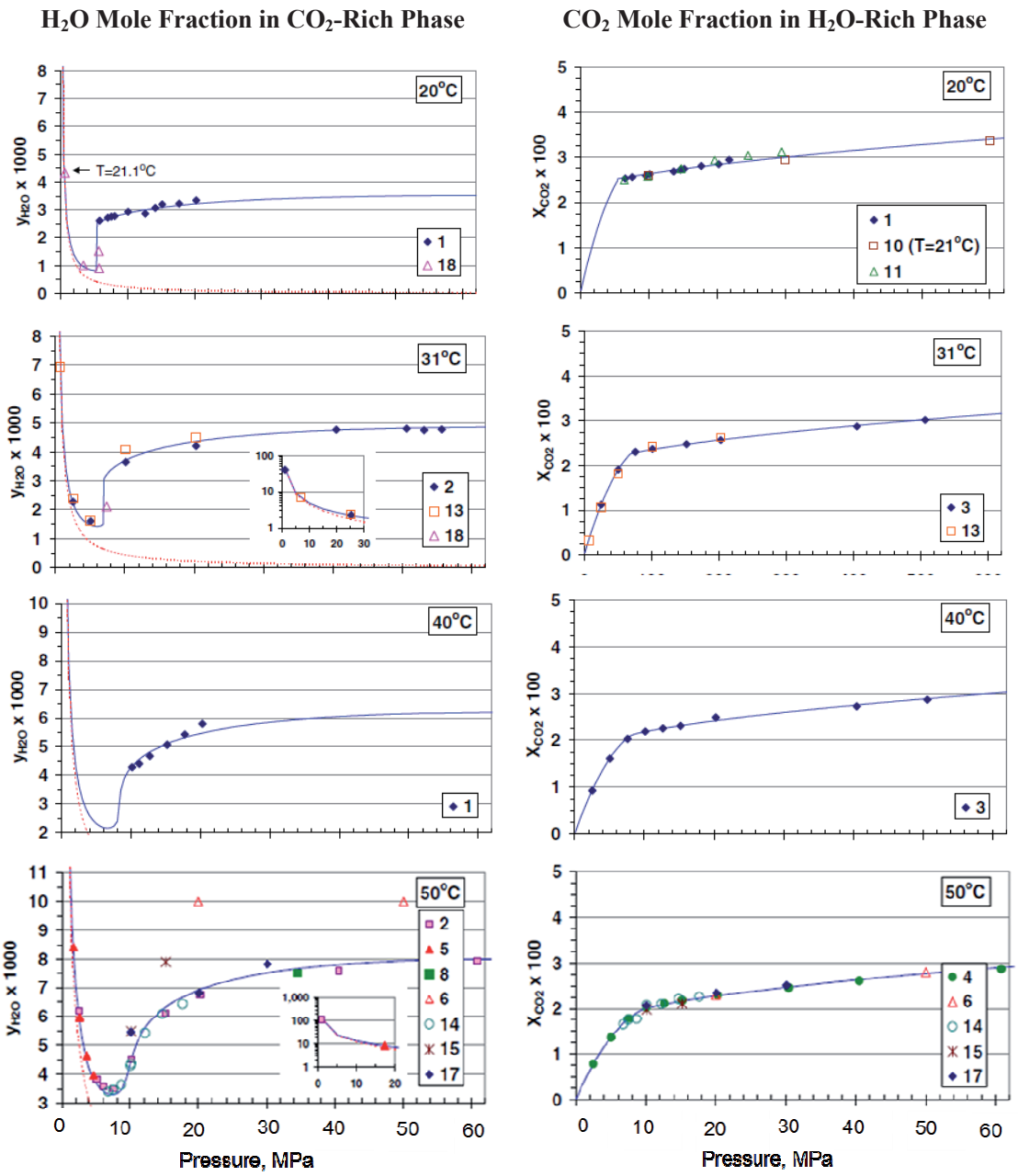

Fig. 1-26 *Mutual solubilities of H_2O and CO_2 at 20, 31, 40, 50 and 75 ºC and pressures to 600 bar from Spycher et al. [90]. Reference numbers are as follows: (1) King et al. [91], (2) Wiebe and Gaddy [92], (3) Wiebe and Gaddy [93], (4) Wiebe and Gaddy [94], (5) Coan and King [95], (6) Todheide and Frank [96], (7) Takenouchi and Kennedy [97], (8) Jackson et al. [98], (9) Greenwood and Barnes [99], (10) Rosenbauer et al. [100], (11) Teng et al. [101], (12) Müller et al. [102], (13) Gillepsie and Wilson [103], (14) Briones et al. [104], (15) D'Souza et al. [105], (16) Sako et al. [106], (17) Dohrn et al. [107], and (18) Song and Kobayashi [108].*

7.3 Review of experimental solubility measurements methods

The early experimental work mainly focused on high temperatures and pressures applicable to the crucial conditions of metamorphic processes. The ternary system H_2O-CO_2-NaCl has been investigated at pressures up to 800 °C and 900 MPa [109]. In the last few decades, a number of experimental studies corresponding to reservoir conditions have been conducted in the two-phase region. Various methods have been used to measure the mutual solubilities of CO_2-H_2O and CO_2-Chloride aqueous solutions.

7.3.1 Fluid inclusion techniques

Fluid inclusion refers to the mineral trapping of a fluid in harsh conditions, which remains in the fluid state during cooling the inclusion to ambient temperatures (Fig. 1-27) [110]. Thus, fluid inclusion techniques have been widely used to measure thermodynamic properties of fluids at high pressure and temperature. After fracturing the crystals (for instance quartz) by thermal shock, the crystals and desired fluid are sealed in noble-metal capsules for subsequent hydrothermal annealing. The fractures heal for 7-10 days and trap fluids samples as inclusions. The chemical analysis of fluid inclusions can be realized by microthermometry, scanning electron microscopy (SEM), energy dispersive analysis (EDA), and Raman spectroscopy [111-112].

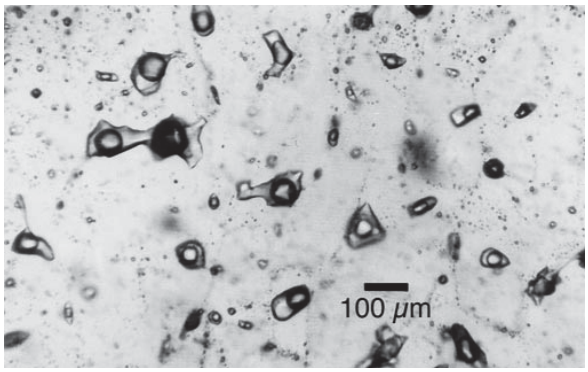

Fig. 1-27 *Photomicrographs of fluid inclusions in quartz [109].*

Shmulovich and Graham applied the synthetic fluid inclusions technique in quartz at 500 and 800 °C, 0.5 M NaCl or $CaCl_2$ and 900 MPa to determine the phase equilibrium in the ternary systems H_2O-CO_2-NaCl and H_2O-CO_2-$CaCl_2$. A large, inclusion-free synthetic quartz crystal was diced by a diamond saw. After washing, quartz crystals, SiO_2 gel, oxalic acid dihydrate ($H_2C_2O_4.2H_2O$) (as the CO_2 source), NaCl powder and water, were loaded into Pt capsules for the heating-freezing stage. The phase transformations in inclusions were measured on a Linkam Scientific Instruments TMS-92 heating-freezing stage. Micro-Raman spectroscopy was used to characterize the products in the fluid inclusions.

Fluid inclusion techniques are flexible tools applicable in studying thermodynamic properties of fluids at high pressure and temperature. However, the range of temperatures and pressures of fluid inclusion is too high for the conditions in DSA. Additionally, the fluid inclusion composition cannot be changed once sealed in the quartz. Therefore, the experimental studies corresponding to reservoir conditions have also been performed in macroscale reactors or micromodels.

7.3.2 Macroscale reactor

The macroscale methods usually consist of a high pressure experimental vessel containing a known volume of water and brine, an oil bath or heating elements to control the temperature, and a pump to introduce CO_2 into the tank at the appropriate pressure. After equilibrate for several hours or days, a sample would be drawn out of the system for analyzing the solubility data. The common analysis methods include depressurization, titration, weighing and Ostwald method, which will be discussed in detail in chapter 3.

In order to increase CO_2 diffusion into water, nearly all the studies used some forms of stirring in the vessels to reduce the equilibrium time (Table 1-2). Even after stirring, the report equilibration times still range from 30 min (*King et al*. [91]) to 48h (*Wiebe et al* [92-94]).

Table 1-2 *Experimental details relevant to CO_2–H_2O equilibration extracted from [113].*

Reference	Approach to equilibrium	Agitation	Equilibration time
Hähnel et al. [114]	From high P_{CO2}; CO_2 dissolution into under-saturated water	Shaking	6 h
Wiebe et al. [92-94]	Reversed from high and low P_{CO2}	Bubbling CO2 gas	Several hours to days
Müller et al. [102]	Fixed V and T; CO_2 dissolution into under-saturated water	Stirring	12 h
King et al. [91]	Constant P_{CO2} maintained by pumping against dissolution of CO_2 into under-saturated water	Stirring then bubbling CO_2 gas	20‑30 min

7.3.3 Micromodels observations

As mentioned earlier, micromodels are the ideal tools for observing two phase flow behaviors in the microchannels. *Tumarkin et al*. [115] used a polymer microfluidic flow-focusing bubbles generator with two different temperature zones for studying temperature-dependent dissolution of CO_2 bubbles. The solubility of CO_2 in water decreases with increasing temperature. Fig. 1-28 shows CO_2 bubbles in liquid shrinkage and expansion with temperature variation. When the temperature decreases, the solubility of CO_2 in water increases, which leads to a reduction of the bubble size. The solubility of CO_2 decreases with an increase in temperature, leading to bubble expansion.

However, these experimental measurements were performed at p = 0.1 MPa. The low CO_2 density at this pressure allows to follow the bubbles size variation, which is not the case for higher CO_2 density at high pressure in real reservoir conditions.

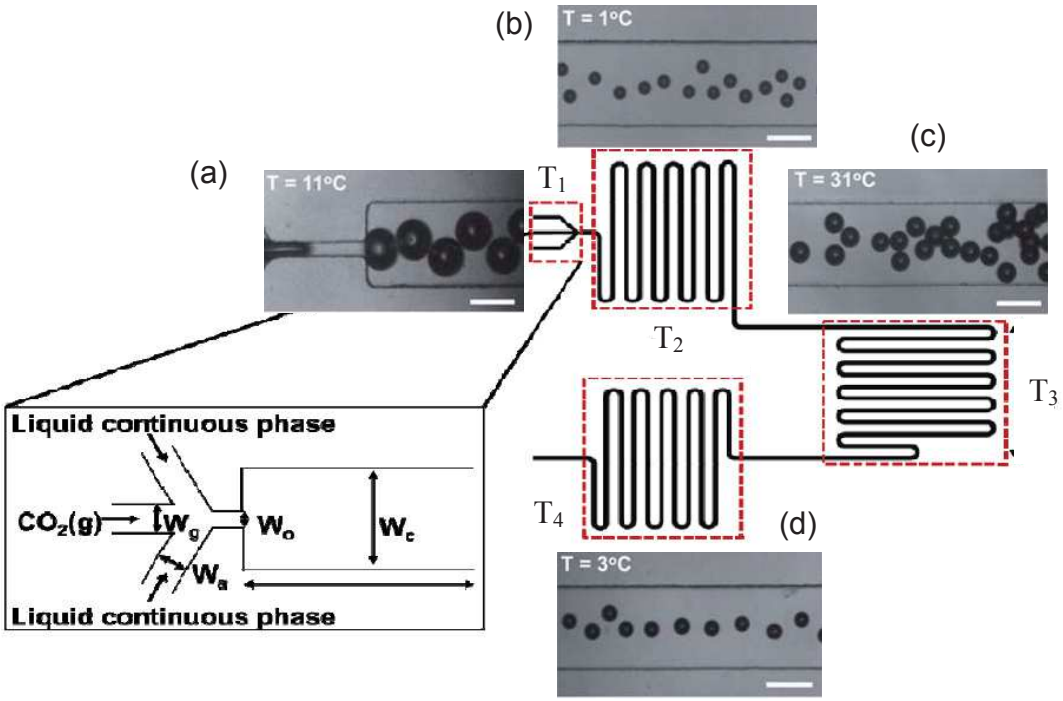

Fig. 1-28 *Optical microscopy images of CO_2 bubbles breathing with temperatures from [115]. (a) CO_2 bubbles generated at T_1 = 11 °C in the inlet zone; (b) rapidly shrank in the cooling zone, T_2 = 1 °C; (c) expanded in the heated region T_3 = 31 °C; (d) subsequently, shrank in the cooled region, T_4 = 3 °C.*

Nevertheless, from this study, the micromodels present the advantage of fast mass and energy transfer, finer process control and *in situ* observation. Therefore, their combination with an *in situ* analysis method (such as Raman spectrometry) should lead to a perfect tool for CO_2 solubility studies. In chapter 3, we introduce a novel and fast method by using pressurized micromodels and Raman spectroscopy for determining the CO_2 solubility in water or saltwater in CO_2 storage conditions. The equilibration time in this study is reached in less than 1 min due to the fast heat and mass transfers provided by the microscale experiments.

7.4 Conclusion

In conclusion, accurate description of the mutual solubilities of CO_2-H_2O/brine system is needed to assess projects concerning CO_2 disposal in deep saline aquifers.

CO_2 solubility in water increases with pressure and decreases with increasing temperature and salinity. While the H_2O solubility in CO_2 has a discontinuity before the CO_2 critical point, it increases with the pressure and temperature above the critical point. The experimental methods in the opening literatures need complicated procedures and long equilibrium times. Therefore, there is an increasing need for fast and reproducible methods, which can be provided by pressurized microfluidic approaches.

8. Mineral trapping

Mineral trapping is the most secure stage of CO_2 geological storage but only occurs at long time scales (see Fig. 1-10). The time line for the carbonate precipitation varies at different rates from days to years to thousands of years, which depends on the partial pressure of CO_2, the mineral and brine composition, and the temperature and pressure conditions [116-117]. The reaction pathways and kinetics are the most important parameters for characterizing the precipitation. As an example, however not the exactly appropriate for the saline aquifers, table 1-3 gives the CO_2 sequestration potential of some major rock forming minerals from [118].

Table 1-3 *CO_2 sequestration potential of some major rock forming minerals.*

Mineral name	**Mineral formula**	**Potential CO_2 fixed ($kg \cdot m^{-3}$ of mineral)**
Plagioclase (anorthite)	$Ca(Al_2Si_2O_8)$	436.4
Olivine (forsterite-fayalite)	Mg_2SiO_4–Fe_2SiO_4	2014.7–1896.3
Pyroxene group-enstatite	$(Mg,Fe)_2Si_2O_6$	1404.2
Augite	$(Ca,Mg,Fe(II),Al)_2(Si,Al)_2O_6$	1306.3
Common hornblende	$Ca_2Na_{0-1}(Mg,Fe(II))_{3-5}(Al,Fe(III))_{2-0}[Si_{6-8}Al_{2-0}O_{22}](O,OH)_2$	1000.4
Calcium amphiboles-tremolite	$Ca_2Na_{0-1}(Mg,Fe(II))_{3-5}(Al,Fe(III))_{2-0}[Si_{6-8}Al_{2-0}O_{22}](O,OH)_2$	1119.3

Mica group-phlogopite	$K_2(Mg,Fe(II))_6[Si_6Al_2O_{20}](OH)_4$	881.8
Serpentine	$Mg_6Si_4O_{10}(OH)_8$	1232.7
Chlorite group	$(Mg,Al,Fe(II))_{12}[(Si,Al)_8O_{20}](OH)_{16}$	923.4
Clay minerals-illite	$K_{1-1.5}(Fe(III),Al,Fe(II),Mg)_{4.0}[Si_{7-6.5}Al;_{1-1.5}O_{20}](OH)_4$	78.42

8.1 Carbonates formation / dissolution

The dissolved CO_2 can react with the minerals of the surrounding rocks to form and precipitate solid carbonates, such as calcite, magnesite, dolomite, and siderite. First, the aqueous CO_2 dissociates in water, producing carbonic acid, as follow:

$$CO_2 + H_2O \Rightarrow H_2CO_3 \overset{pKa=6.3}{\leftrightarrow} H^+ + HCO_3^- \overset{pKa=10.33}{\leftrightarrow} 2H^+ + CO_3^{2-} \quad \text{Eq. 1-11}$$

The acid attacks many of the primary host rock minerals like anorthite (see Table 1-3 and Eq. 1-12), which in turn causes complexation of dissolved cations with bicarbonate ions.

$$CaAl_2Si_2O_8 + H^+ \leftrightarrow Ca^{2+} + Al_2Si_2O_5(OH)_4 \quad \text{Eq. 1-12}$$

The dissolved bicarbonate species react with divalent cations to form metallic carbonates, such as siderite ($FeCO_3$), magnesite ($MgCO_3$), and calcite ($CaCO_3$ - see Eq. 1-13). Carbonates dissolution occurs in the reverse process.

$$Ca^{2+} + HCO_3^- \leftrightarrow CaCO_3 + H^+ \quad \text{Eq. 1-13}$$

8.2 Experimental methods for studying carbonate precipitation

The mineral trapping studies from the literature involve two reactions: (i) mineral dissolution and (ii) carbonate precipitation. Their effects are investigated over the dissolution and failure of the caprock, the reducing permeability and the reservoir

capacity. Calcium carbonate dissolution and precipitation reactions are influenced not only by the existing minerals and solutes, pH, temperature, and pressure, but also by the flow conditions and the advective and diffusive mixing processes.

Although this mechanism favors the permanent CO_2 sequestration, minerals dissolution and carbonate minerals precipitation in the reservoir scale occurs over large time scales, from decades to millions of years, due to the slow kinetics. Numerical simulation is relatively convenient to model the reactions of CO_2 in the brine over thousands of years. Lab experimental studies usually occurred in the smaller core holder or micromodels with some agitations.

8.2.1 Carbonate precipitation at core scale

Core scale studies usually occur in a small core holder where CO_2 and brine are contacted with the rock samples for weeks or months. Carbonate formation is characterized by transmission electron microscopy (TEM) and scanning electron microscopy (SEM) [119] (*ex situ* analysis).

Carteret et al. [120] showed that in a batch system, different types of carbonates precipitated from the solution, depending on temperature: first, vaterite at low temperature, and then aragonite at temperatures above 50 ºC; *Kaszuba et al*. [119] injected CO_2 into a Au-Ti reaction cell loaded with arkose and Maplewood Shale chips for 80 days to determine the extent of fluid-rock reactions. They concluded that the desiccation of the brine by water solubility in the injected supercritical CO_2 resulted in the local high ionic strength, which introduced additional complications for reactions. *Pokrovsky et al*. [121] characterized the dissolution kinetics of carbonate minerals in the salted solution at temperature ranging from 25 to 150 °C and P_{CO2} ranging from 0.1 to 5.5 MPa. High temperature experiments showed very weak effect of P_{CO2} on dissolution rates of all carbonate minerals. *Hernandez et al*. [122] carried the experiments in a stirred reactor filled with $Ca(OH)_2$ solution. They found that high CO_2 pressure increased the initial precipitation rate, carbonation efficiency and purity.

8.2.2 Microscale on carbonate precipitation

A novel technology has been developed to dramatically reduce the experimental time to minutes and hours by using two dimension micromodels with *in situ* chemical reactions. In micro scale experiments, $CaCl_2$ and Na_2CO_3 aqueous solutions were covertly injected into a homogeneous pore network micromodel at p = 0.1 MPa, T = 25 ºC, in order to determine the impact of diffusive mixing on precipitation rates, porosity and permeability. They observed that precipitates formed along the center mixing lines of micromodels, mainly composed of calcite crystals at lower concentrations. As the concentration increased, more vaterite is formed along the precipitate line. The main limitations of this study are: (i) CO_2 was not directly used the carbonates precursor; (ii) the operating conditions were not those of real reservoirs.

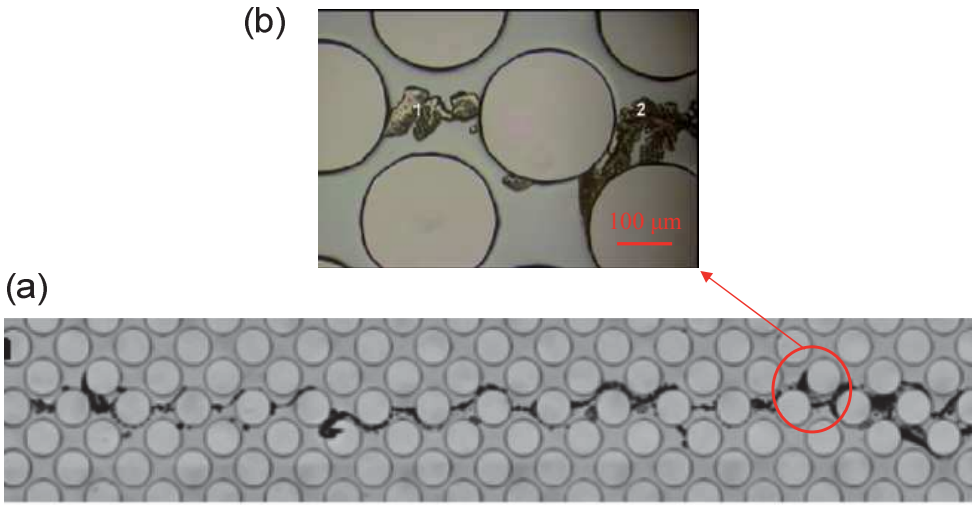

Fig. 1-29 *Images of $CaCO_3$ precipitates formed along the mixing zone in micromodels by mixing two aqueous solutions of $CaCl_2$ and Na_2CO_3 at p = 0.1 MPa, T = 25 ºC [123].*

8.3 Carbonate dissolution

Carbonate dissolution can affect storage capacity by altering the permeability of the aquifer near the injection site [118]. To understand this process, lab scale experiments usually are performed by injecting HCl through calcium carbonate (i.e., limestone)

cores. During the acid flowing through the carbonate pore, the carbonate dissolves into the acid current. Thus the permeability for the injected acid increases, which results in more acid flowing into the pore. Because of the uneven distribution of pore sizes in the carbonate porous media, a "wormhole" will be formed (see Fig. 1-30) [124,125,126].

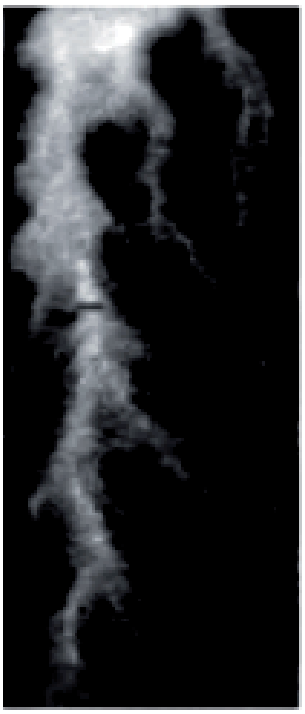

Fig. 1-30 *Example of a typical "wormhole" (white part) in the network from [127].*

8.4 Conclusion

Given the slow dissolution kinetics of silicate minerals and carbonate minerals precipitation, large scale experiments are not suitable. Some experiments ran month-long reactions, while no dissolution or new reaction products were observed. Therefore, there is an increasing need for tools with much faster mass transfer to accelerate the dissolution and precipitation process, which can be provided by micromodels.

9. Conclusions

In this chapter we overviewed the emergence of CO_2 storage in deep saline aquifers and the current investigations concerning the parameters influencing its trapping mechanisms (relative permeability, capillary conditions, solubility and precipitation). These involve the various processes characteristics among which are the injection rate, the fluid properties (viscosity, pressure, temperature, and interfacial tension) and the rock properties (wettability, porosity, permeability, chemical composition). The recent laboratory-scale experimental measurements of interactions occurring in CO_2-brine-rock systems at core- and micro- scale have been reviewed (Table 1-4).

Core-scale approaches present a certain degree of advantages in the studies of CO_2 storage in deep saline aquifers. First, the core holder can easily reach the reservoir conditions, and the loading rock sample can directly be extracted from the real reservoir. Next, the analysis methods allow obtaining the 3D core saturation and CO_2 spatial distribution maps using X-ray Computed Tomography scan. Therefore, core-scale approaches can provide the relative reliable results to predict the storage capacity and safety. However, core scale experiments show major disadvantages in exhibiting limiting control over the injection process, the local temperature and the concentration gradients. Additionally, they require much longer experimental times. The experiments usually need a few days or even months (a few months for the precipitation studies) to reach the steady state. Moreover, it is difficult to control the drainage process in the core. These disadvantages limit this research scale for in-depth studies of CO_2 trapping mechanisms.

Microfluidic systems have addressed excellent heat and mass transfer, vast improvements in energy efficiency, and a much finer degree of process control. For the detailed and time-consuming studies, micromodels exhibit undeniable advantages. However, only few studies were performed so far under reservoir conditions due to the limited operating temperature and pressure range in the glass and PDMS micromodels. Therefore, there is a need for the emergence of microfabrication technology that allows for stronger, more powerful and durable devices able to mimic

the reservoir conditions and rocks properties, which can be provided by the high pressure microreactors, especially silicon/Pyrex microreactors. We will detail microfabrication of high pressure porous micromodels in the following chapter.

Table 1-4 *Experimental scales in different trapping mechanisms.*

Trapping mechanism	**Structural trapping**	**Residual trapping**	**Solubility trapping**	**Mineral trapping**
Graphic symbol		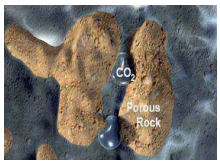		
Main characteristics parameters	- Porosity; - Fracture	-Displacement mechanisms; -Viscous and capillary forces	-The mutual solubilities of CO_2 and H_2O	-Carbonate precipitation; -Mineral dissolution
Numeral simulation	Reservoir scale	Reservoir, Core, Pore scales	Yes (?)	Yes (?)
Reservoir scale	Most	-	-	-
Core scale	Few	Yes	-	Yes
Micro scale at reservoir conditions	Few	Few	Few	Few

References

1 IPCC, Cambridge University Press (2001).

2 R.J. Francey, C.E. Allison, D.M. Etheridge, C.M. Trudinger, I.G. Enting, M. Leuenberger, R.L. Langenfelds, E. Michel, L.P. Steele, Tellus B 51 (1999) 170-193.

3 IPCC, Cambridge University Press (2002).

4 Committee on the Science of Climate Change, National Research Council (2001).

5 CDIAC, Cdiac.ornl.gov. (2010).

6 IPCC, Cambridge Univ. Press (2007).

7 J. Lu, A.G. Vechhi, T. Reichler, Geophysical Research Let. 34 (2007) L06805.

8 Energy Information Administration, Tech. Rep. (2006).

9 S. Pacala, R. Socolow, Science 305 (2004) 968-972, .

10 World Resources Institute. Guidelines for Carbon Dioxide Capture, Transport, and Storage (2008).

11 S. Bachu, Prog. Energy Combust Sci. 34 (2008) 254-273.

12 IPCC, Cambridge University Press (2005).

13 S. Pacala, R. Socolow, Sci. 305 (2004) 968-972.

14 E.J. Manrique, V.E. Muci, M.E. Gurfinkel, SPE Reserv. Eval. Eng. 10 (2007) 667-686

15 S. Holloway, Annual Review of Energy and the Environ. 26 (2001) 145-166.

16 S. Angus, B. Armstrong, K.M. De Reuck, Pergamon Press (1976).

17 United States Department of Energy, Washington (2011).

18 IEA, CO2 Emissions from Fuel Combustion (2006).

19 Oil and Gas Journal, Special Report 108 (2010).

20 W.D. Gunter, T. Gentzis, B.A. Rottenfusser, R.J.H. Richardson, Energy Convers Mgmt. 38 (1997) S217-S222.

21 C.M. White, D.H. Smith, K.L. Jones, Energy and Fuels 19 (2005) 659724 .

22 S. Reeves, Advanced Resources International (2002).

23 S. Martens, T. Kempka, A. Liebscher, S. Lüth, F. Möller, A. Myrttinen, B. Norden, C. Schmidt-Hattenberger, M. Zimmer, M. Kühn, Environ Earth Sci. Special Issue 67 (2012) 323-334.

24 J. Ennis-King, L. Paterson, Proceedings of the fifth international conference on greenhouse gas control technologies 290 (2000).

25 H. Koide, Y. Tazaki, Y. Noguchi, S. Nakayama, M. Iijima, K. Ito, Y. Shindo, Energy Convers. Manage. 33 (1992) 619.

26 S. Bachu, W. D. Gunter, E. H. Perkins, Energy Convers. Manage. 35 (1994) 269.

27 R.T. Okwen, M.T. Stewart, J.A. Cunningham, Int. J. of Greenhouse Gas Control 4 (2010) 102-107

28 H.T. Zhang, D.G. Wen, Y.L. Li, J.Q. Zhang, J.C. Lu, Geological Bulletin of China, 24 (2005) 1107-1110.

29 S. Bachu, Energy Convers. Manage. 43 (2002) 87-102.

30 S. Holloway, Annual Reviews in Energy and the Environment 26 (2001) 145-166.

31 S. Sun, Sci. News 14 (2006) 2.

32 S. Martens, T. Kempka, A. Liebscher, S. Lüth, F. Möller, A. Myrttinen, B.Norden, C. Schmidt-Hattenberger, M. Zimmer, M. Kühn, Environ Earth Sci. Special Issue (2012).

33 A. Forster, B. Norden, K. Zinck-Jørgensen, P. Frykman, J. Kulenkampff, E. Spangenberg, J. Erzinger, M. Zimmer, J. Kopp, G. Borm, C. Juhlin, C.G. Cosma, S. Hurter, Environmental Geosci. 13 (2006) 145-161.

34 S. Martens, A. Liebscher, F. Möller, H. Würdemann, F. Schilling, M. Kühn, Energy Procedia 4 (2011) 3246-3253.

35 W. D. Gunter, B. Wiwchar, E. H. Perkins, Mineralogy and Petrology 59 (1997) 121-140.

36 J. Bradshaw, S. Bachu, D. Bonijoly, R. Burruss, S. Holloway, N. P. Christensen, O. M. Mathiassen, Int. J. Greenhouse Gas Control 1 (2007) 62.

37 G. Aydin, I. Karakurt and K. Aydiner, Energy Policy 38(2010) 5072.

38 M. Hesse, F.M.J. Orr, H. Tchelepi, J. Fluid Mech. 611 (2008) 35-60.

39 K. Pruess, T. Xu, J. Apps, J. Garcia, SPE J. 8(2003) 49 - 60.

40 T. Sato, S. P. White, Z, Xue, Proceedings, TOUGH Symposium (2006).

41 S. Salvi, F. Quattrocchi, M. Angelone, C.A. Brunori, A. Billi, F. Buongiorno, F. Doumaz, R. Funiciello, M. Guerra, S. Lombardi, G. Mele, L. Pizzino and F. Salvini, Natural Hazard 20 (2000) 255-278.

42 Y. Zhao, Y. Song, T. Wang, Y. Liu, L. Jiang, N. Zhu, W. Yang, Energy Procedia 37 (2013) 6942-6949.

43 V. Er, T. Babadagli, Z. Xu, Energy Fuels 24 (2010) 1421-1430.

44 A. Kumar, R. Ozah, M. Noh, G. A. Pope, S. Bryant, K. Sepehrnoori, L. W. Lake, SPE J. 10 (2005) 336-348.

45 M.A. Hesse, F.M. Orr Jr., H.A. Tchelepi, Energy Proc. 1 (2009) 3275-3281.

46 P. Audigane, I. Gaus, I. Czernichowski-Lauriol, K. Pruess, T. F. Xu, American J. of Sci. 307 (2007) 974-1008.

47 S.M. Benson, J.C. Perrin, L. Miljkovic, C.W. Kuo, M. Krause, E. Chabora, Stanford University (2008).

48 S.M. Benson, Process report, Stanford University (2011).

49 M. Burton, N. Kumar, S. Bryant, 9th International Conference on Greenhouse Gas Control Technologies (2008).

50 K. Pruess, N. Müller, Water Res. 45 (2009a) W03402.

51 K. Pruess, N. Müller, Water Res. 45 (2009b) W03403.

52 A. Kopp, H. Class, R. Helmig, Int. J. Greenh. Gas Control 3 (2009a) 263-276.

53 A. Kopp, H. Class, R. Helmig, Int. J. Greenh. Gas Control 3 (2009b) 277-287.

54 V. A. Kuuskraa, G. J. Koperna, D. Riestenberg, R. Esposito, Energy Procedia 1 (2009) 3063-3070.

55 L. Marini, Elsevier 11 (2007) 453.

56 A. Busch, S. Alles, Y. Gensterblum, D. Prinz, D.N. Dewhurst, M.D. Raven, H. Stanjek, B.M. Krooss, Int. J. Greenh. Gas Control 2 (2008) 297-308.

57 E.M. Chapman, J. Yang, J.P. Crawshaw, E.S. Boek, Energy Procedia 00 (2013) 000-000.

58 J.C. Perrin, M. Krause, C.W. Kuo, L. Miljkovic, E. Charoba, S. M. Benson, Energy Procedia 1 (2009) 3515-3522.

59 H. Alkan, Y. Cinar, E. B. Ülker, Transp. Porous Med. 84 (2010) 799-819.

60 J. BEAR, Dover Publications (1972).

61 M.J. Golding, J.A. Neufeld, M.A. Hesse, H.E. Huppert, J. Fluid Mech. 678 (2011) 248-270.

62 R.H. Brooks and A.T. Corey, Colorado State University (1964) 3.

63 M.Th. van Genuchten, Soil Sci. Soc. Am. J. 44 (1980) 892-898.

64 R. Lenormand, C. Zarcone, A. Sarr, J. Fluid Mech. 135 (1983) 337-353.

65 M.J. Blunt, Current Opinion in Colloid & Interface Sci. 6 (2001) 197-207.

66 U.C. Bandara, A.M. Tartakovsky, B.J. Palmer, Int. J. Greenh. Gas Control 5 (2011) 1566-1577.

67 C. Chalbaud, M. Robin, J.M. Lombard, F. Martin, P. Egermann, H. Bertin, Adv. Water Res. 32 (2009) 98-109.

68 S. Abaci, J.S. Edwards, B.N. Whittaker, Mine Water Environ. 11(1992) 11-16.

69 N. Müller, Transp. Porous Med. 87 (2011) 367-383.

70 M. Flett, R. Gurton, I. Taggart, Proceedings of the SPE Asia Pacific Oil and Gas Conference and Exhibition (2004) SPE 88485.

71 J.C. Perrin, S.M. Benson, Transp. Porous Med. 82 (2010) 93-109.

72 L. Zuo, S. Krevor, R. W. Falta, S.M. Benson, Transp. Porous Med. 91 (2012) 459-478.

73 C.H. Pentland, S. Iglauer, R. El-Maghraby, Y. Tsuchiya, H. Okabe, M.J. Blunt, Geophys. Research Let. 38 (2011) L06401.

74 A. Busch, N. Müller, Energy Procedia 4 (2011) 6053-6060.

75 R. Pini, S. Krevor, M. Krause, S.M. Benson, Energy Procedia 00 (2013) 000-000.

76 R. Pini, S. Krevor, M. Krause, S.M. Benson, Adv. Water Res. 38 (2012) 48-59.

77 B. Gutiérrez, F. Juarez, L. Ornelas, S. Zeppieri, A. López, Int. J. Thermophys. 29 (2008) 2126-2135.

78 C. Chalbaud, M. Robin, S. Bekri, P. Egermann, The International Symposium of the Society of Core Analysts (2007).

79 C. Chalbaud, J.M. Lombard, F. Martin, M. Robin, H. Bertin, P. Egermann, Reservoir Characterization and Simulation Conference (2007) SPE 111420.

80 Y. Kim, J. Wan, T. J. Kneafsey, T. K. Tokunaga, Environ. Sci. Technol. 46 (2012) 4228-4235.

81 E. Saadatpoor, S.L. Bryant, K. Sepehrnoori, Transp. Porous Med. 82 (2010) 3-17.

82 Z.W. Li, M. Z. Dong, S. L. Li, S. Huang, Energy Convers. Manage. 47 (2006) 1372-1382.

83 G. Løvoll, Y. Méheust, K.J. Måløy, E. Aker, J. Schmittbuhl, Energy Fuels 30 (2005) 861-872.

84 C. Zhang, M. Oostrom, T.W. Wietsma, J.W. Grate, M.G. Warner, Energy Fuels 25 (2011) 3493-3505.

85 C. Zhang, M. Oostrom, J. W. Grate, T. W. Wietsma, M. G. Warner, Environ. Sci. Technol. 45 (2011), 7581-7588.

86 S. Portier, C. Rochelle, Chemical Geology 217 (2005) 187-199.

87 S.S. Butcher, R.J. Charlson, G.H. Orians, G.V. Wolfe, Academic Press (1992).

88 E. Lindeberg, D. Wessel-Berg, Energy Convers. Managem. 38 (1997) 5229-5234.

89 A. Bielinski, Dissertation, Institut fur Wasserbau (2006).

90 N. Spycher, K. Pruess, J. Ennis-King, Geochimica et Cosmochimica Acta 67 (2003) 3015-3031.

91 M.B. King, A. Mubarak, J.D. Kim, T.R. Bott, J. Supercrit. Fluids 5 (1992) 296-302.

92 R. Wiebe, V.L. Gaddy, J. Am. Chem. Soc. 63 (1941) 475-477.

93 R. Wiebe, V.L. Gaddy, J. Am. Chem. Soc. 62 (1940) 815-817.

94 R. Wiebe, V.L. Gaddy, J. Am. Chem. Soc. 61 (1939) 315-318.

95 C.R. Coan, Jr. A.D. King, J. Am. Chem. Soc. 93 (1971) 1857-1862.

96 K. Tödheide, E.U. Frank, Phys. Chem. 37 (1963) 387-401.

97 S. Takenouchi, G.C. Kennedy, Am. J. Sci. 262 (1964) 1055-1074.

98 K. Jackson, L.E. Bowman, J.L. Fulton, Anal. Chem. 67 (1995) 2368-2372.

99 H.J. Greenwood, H.L. Barnes, Handbook of Physical Constants (1966).

100 R.J. Rosenbauer, J.L. Bischoff, A.S. Radke, Econ. Geol. 78 (1983) 1701-1710.

101 H. Teng, A. Yamasaki, M.-K. Chun, H. Lee, J. Chem. Thermodyn. 29 (1997) 1301-1310.

102 G. Müller, E. Bender, G. Maurer, Berichte der Bunsen-Gesellshaft für Physikalische Chemie 92 (1988) 148-160.

103 P.C. Gillepsie, G.M. Wilson, Research report RR-48 (1982).

104 J.A. Briones, J.C. Mullins, M.C. Thies, Fuild Phase Equilib. 36 (1987) 235-246.

105 R. D'Souza, J.R. Patrick, A.S. Teja, Can. J. Chem. Eng. 66 (1988) 319-323.

106 T. Sako, T. Sugeta, N. Nakazawa, T. Obuko, M. Sato, T. Taguchi, T. Hiaki, J. Chem. Eng. Japan 24 (1991) 449-454.

107 R. Dohrn, Bünz, F. Devlieghere, D. Thelen, Fluid Phase Equilib. 83 (1993) 149-158.

108 K.Y. Song, R. Kobayashi, SPE Formation Evaluation, 2 (1987) 500-508.

109 K.. Shmulovich, C. M. Graham, Contrib. Mineral. Petrol. 136 (1999) 247-257

110 E. Roedder (1984) Fluid inclusions. Miner Soc Am, Rev Mineral 12

111 F.M. Haynes, S.M. Sterne, R.J. Bodnar, Geochemica et Cosmockimica Acia 52 (1987) 969-977.

112 M.L. Frezzotti, F. Tecce, A. Casagli, J. Geochem. Exploration 112 (2012) 1-20.

113 L.W. Diamond, N.N. Akinfiev / Fluid Phase Equilibria 208 (2003) 265–290

114 O. Hähnel, Centr. Min. Geol. 25 (1920) 25-32.

115 E. Tumarkin, Z. Nie, J. Il Park, M. Abolhasani, J. Greener, Lab on a Chip 11 (2011) 35-45.

116 B.N. Sass, J. Gupta, J. Ickes, M. Eagelhard, P.D. Bergman, C. Byaer, 1st National Conference on Carbon Sequestration (2001).

117 I. Lebro'n, D. L. Suarez, Geochim. Cosmochim. Acta 62 (1998) 405-416.

118 B. Zerai, Doctoral thesis, Case Western Reserve University (2006).

119 J.P. Kaszuba, D.R. Janecky, M.G. Snow, Appl. Geochem. 18 (2003) 1065-1080.

120 C. Carteret, A. Dandeu, S. Moussaoui, H. Muhr, B. Humbert, E. Plasari, Cryst. Growth J. 9 (2009) 807-812.

121 O.S. Pokrovsky, S.V. Golubev, J. Schott, A. Castillo, Chem. Geology 265 (2009) 20-32.

122 G. Montes-Hernandez, F. Renard, N. Geoffroy, L. Charlet, J. Pironon, Crystal. Growth J. 308 (2007) 228-236.

123 M. F. Fanizza, H. Yoon,C. Zhang, M. Oostrom,T. W. Wietsma, N. J. Hess, M. E. Bowden, T. J. Strathmann, K. T. Finneran, C. J. Werth, Water Resources Research 49 (2013) 874–890.

124 H. S. Fogler and J. Jasti, AIChE J. 36 (1990) 827.

125 C. Fredd and H. S. Fogler, Soc. Petr. Engrg.J. 13 (1998) 33.

126 C. Fredd and H. S. Fogler, AIChE J. 44(1998) 1933.

127 F. GolfierI, B. Bazin, R. Lenormand, M. Quintard, Comput. Appl. Math. 23 (2004) 2-3.

Chapter 2

High Pressure on Chip Porous Media: Fundamentals and Microfabrication

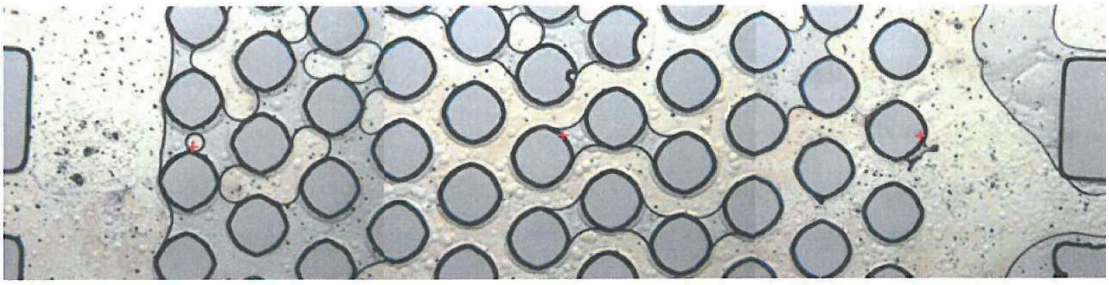

I. Introduction

Over the last decades, micromodels have been commonly used to investigate and visualize physical, chemical, and biological processes in porous media. The micromodels extract some geometrical information from real porous structures and include some essential schematization of reality. Although they are idealized structures, they have helped revealing many processes and applications such as multiphase transport in porous media and reservoir engineering. *Chatenever and Calhoun* conducted one of the first micro-model for investigating microscale mechanisms of fluid behavior in porous media in 1952 [1]. One of the earliest 2D micromodels was developed by *Lenormand* in the eighties of the last century, which consists of a random square network between two layers of Plexiglass for investigating microscale mechanisms of water displacing oil in porous media. Since then, micromodels have long been used to understand multi phase flow in porous media at pore scale involving oil recovery mechanisms, displacements in porous media, effects of various displacement process factors, and so on.

The behavior of fluids at the microscale breaks mechanisms of “macrofluidic” due to surface tension and viscous forces that dominate the system. These micromodels investigations can now take advantage of the wide development of Microfluidics over the past 15 years.

Microfluidics refers to controlling and manipulating fluid flows at micrometer length scale, which already have many applications in nature, such as, a tree bringing water and nutrients to the leaves *via* a complex network of capillaries, the red blood cells delivering oxygen in the lungs or gills through the body’s capillaries (Fig. 2-1). This miniaturization has three main physical characteristics: (i) flows are essentiality laminar (no turbulent mixing), (ii) surface to volume ratio increases and (iii) viscosity and capillary effects have an increasing importance. Since the first micro silicon gas chromatographic analyzer fabricated by *Terry* in 1975 and the initial concept of

lab-on-a-chip dominated by *Manz et al* in the 90's, the advantages of microfluidic systems were thrust into the spotlight, and then all sorts of micro devices began to be fabricated. Man-made microfluidics systems provide new advantages with low reagent consumption but with high resolution and sensitivity, excellent heat and mass transfer and unparalleled capability for the process controlling. Thus, these merits have received priority for applications in chemical engineering, biological sensing, drug delivery, cell biology, etc. Since polymers, especially PDMS, are mainly used for fabricating the microfluidics systems, there has been a rapid expansion of new types of micromodels.

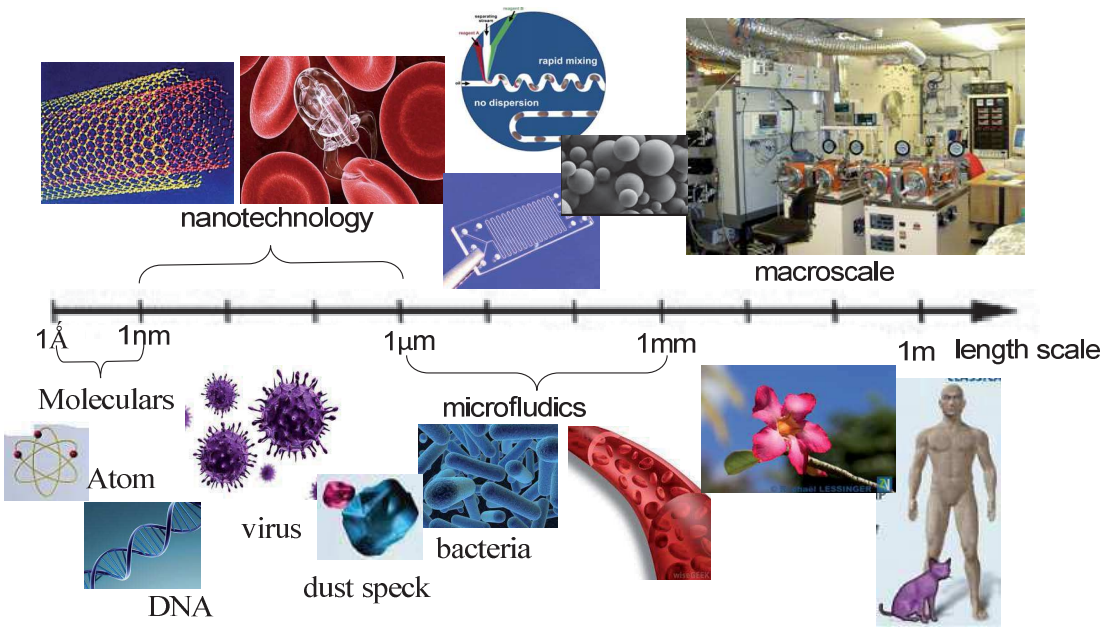

Fig. 2-1 *Size characteristics of fluidic systems [images from google images].*

As we mentioned before, micromodels have long been fabricated to investigate the fluids flow in porous media for certain conditions.

Polymers, such as PMMA (Poly-methyl-meth-acrylate), and PDMS (Poly-di-methyl-siloxane), are cheap, flexible and easy to be depicted features of porous media, which have been widespread used in pore scale studies of immiscible fluids displacement. Although they can replicate the structures of rocks in aquifers by extracting the 2D pore network features from the 3D images of rock sample, they

cannot be employed for the high temperature and pressure conditions concerning deep saline aquifers due to their poor temperature and pressure resistance.

Therefore, most micromodels in recent studies concerning geological fluid flows have been fabricated by etching regular pore networks on glass. Glass/glass microreactors can reach high pressures, and are widely used for higher temperature (< 100 ºC) or pressure (< 10 MPa) studies [2-3]. These microreactors have stable wettability properties and mechanical and chemical stability, and can easily construct to 3D glass-bead micro-models. However, the low thermal conductivity of glass is not ideal when considering operating temperatures above 100 ºC for apparent thermal gradient.

Therefore, new high pressure and high temperature porous media microsystems are needed to cater the harsh conditions of deep saline aquifers and replicate the real rocks characterizations.

In this chapter, we will first present high pressure Microfluidics (applications and microfabrication strategies) and later give a short overview of two-phase flows in porous media.

II. High pressure microfluidics

Since 2005, high pressure/high temperature microreactors have been widely developed to withstand the supercritical conditions. “Supercritical microfluidics” - carried out at ICMCB - combines the advantages of microsystems and the unique properties of supercritical fluids, which have opened avenues towards new fields of investigation in the last few years.

1. HP microsystems

Capillary tubings (steel or silicon) are the most simple and cheap high pressure microfluidic devices for continuous high pressure flow experiments with easy manipulation of operating parameters [4]. Silica capillaries-based microfluidic systems have been used for the investigations of two-phase microfluidics flows [5], and chemical or materials synthesis [6-8]. However, this type of microsystem exhibits limitations in terms of design flexibility, visualization and *in situ* analysis.

“On chip” microsystems provide a wide range of designs from two to three dimensional structures. Glass and polymer micromodels have limitations in replicating the reservoir conditions and rock characteristics (Fig. 2-2). Reactors microfabricated in silicon and Pyrex inherit the good thermal, chemical and pressure characteristics from the silicon substract, while maintaining optical access through the Pyrex side. These microsystems exhibit a good temperature and pressure resistance (400 ºC and 20 MPa) and well defined wettability properties of microchannels, making them suitable tools for CO_2 sequestration investigations.

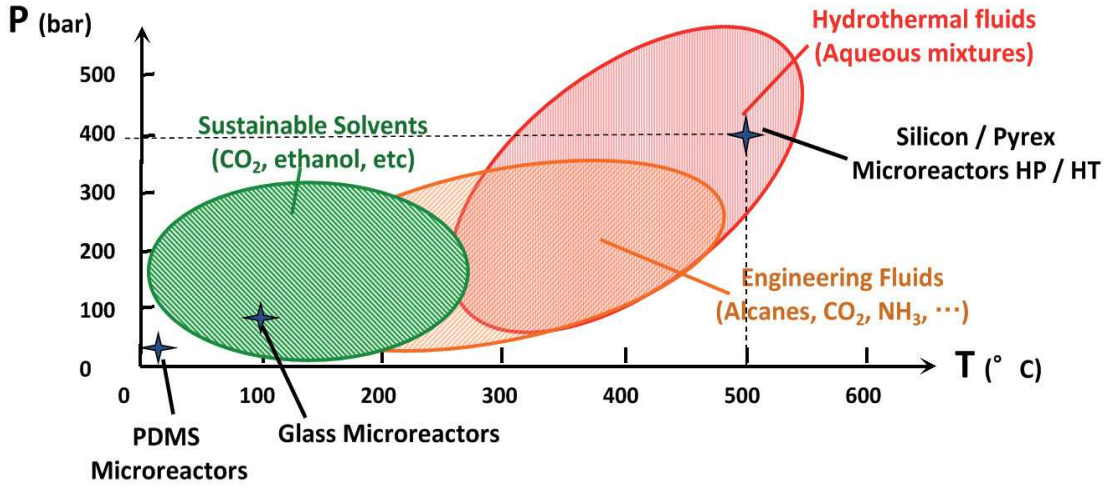

Fig. 2-2 *Typical operating conditions for different materials microsystems [9].*

2. Applications of high pressure microdevices

High pressure microfluidics (including supercritical microfluidics) opened a new chapter for chemical reaction and nanostructures synthesis in an advanced controlled environment. Supercritical CO_2 can be operated in most microsystems due to its accessible critical point (T_c = 31 ºC; P_c = 7.4 MPa), which makes it popular in supercritical microfluidics.

First, the advantages of supercritical microfluidics like hydrodynamics control, enhancement of mass and heat transfers, reproducibility, rapid screening of parameters, and low reagent consumption, motivate microreactors to develop the synthesis of advanced nanocrystals on chips within microsystems. *Gendrineau et al*. [10] have used this approach to perform synthesize palladium NCs in a toluene / CO_2 mixture at 100 ºC and 25 MPa within coflowing capillary tubes (Fig. 2-3). $ScCO_2$ allows increasing the H_2 solubility in the solvent system, therefore overcoming the mass-transfer limited reduction of Palladium (II) precursor by H_2. This study reported the contribution of supercritical microfluidics to access a library of tunable surface properties of NCs.

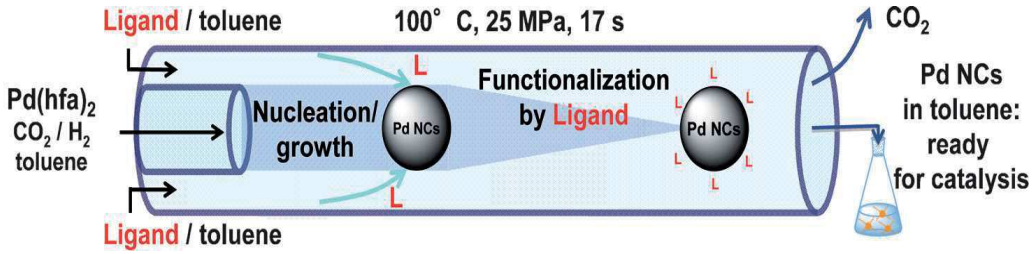

Fig. 2-3 *The synthesis of palladium NCs wih tailored surface properties in microfluidic co-flow process [10].*

In addition, for organic synthesis processes, $scCO_2$ is a promising solvent due to its potential useful characteristics. *Kobayashi et al.* [11] developed a palladium surface-decorated glass-glass microreactor for hydrogenation reactions in $scCO_2$ (Fig. 2-4 (a)). Thanks to the best use of $scCO_2$ and the large interfacial area of microchannels, the reactions proceeded within 1 second.

Trachsel et al. firstly used Raman spectroscopy to *in situ* monitor the hydrogenation of cyclohexene in supercritical CO_2 within a Pd/Al_2O_3 catalyst packed bed in Si/glass microreactor [12-13] (Fig. 2-4 (b)). This study shows the novel opportunities in spectroscopic high pressure reaction profiling, which can be performed directly *in situ*.

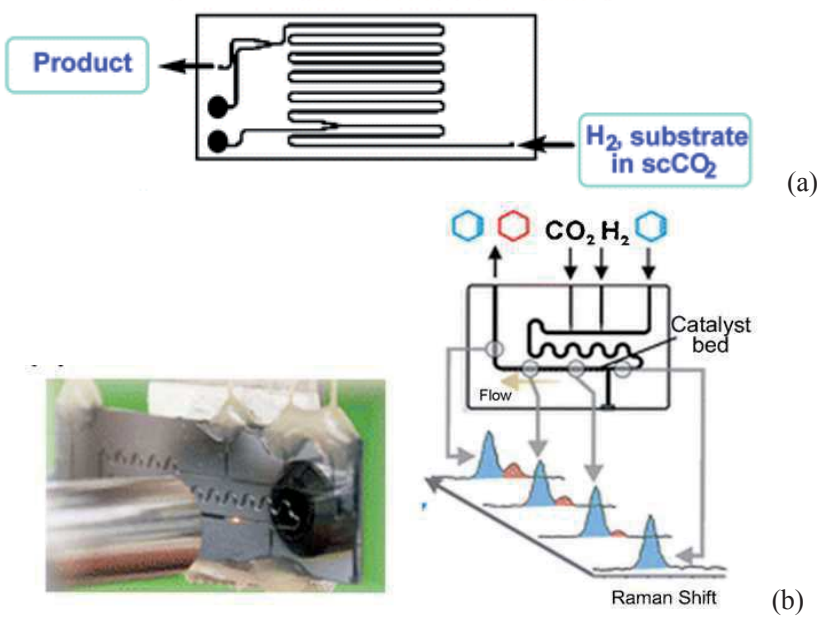

Fig. 2-4 *(a) Glass-glass microreactor developed for hydrogenation reactions by Kobayashi et al. [11]; (b) microreactor with Raman probe by Trachsel et al. [12].*

Therefore, we can conclude that supercritical microfluidics have been widely used in the chemical reactivity and material synthesis. Conventional glass or polymer micromodels are useful tools to investigate and visualize pore scale multi-phase flow in porous media. But only Si/Pyrex microsystems can reach the rigid supercritical conditions of high pressure and high temperature and allow for *in situ* observations and characterizations. Therefore, they can also be used to investigate and visualize two-phase flow in porous microsystems in real storage conditions, such as the injection of supercritical CO_2 into deep saline aquifers.

We detail hereafter our strategy to design and microfabricate such "Geological lab on chip" experimental setups.

III. Microfabrication of high pressure porous micromodels

1. Introduction

A porous medium is characterized by a skeleton material with a number of pore spaces. Porosity is most often used to represent the porous media. Natural porous media consist of random pores structures and complex surface properties. Understanding the multiphase flows in such media has a variety of both petroleum and environmental applications. Micromodels were developed to schematize real porous media into a regular graph network etches in different substrates, named as "Reservoir-on-a-chip" [14]. For modeling the complex porous structures, the micromodels can only represent a small fraction of the real porous structure and extract some geometrical information from the 3D rock sample. The real porous space is schematized into a 2D or 3D regular graph network (Fig. 2-5).

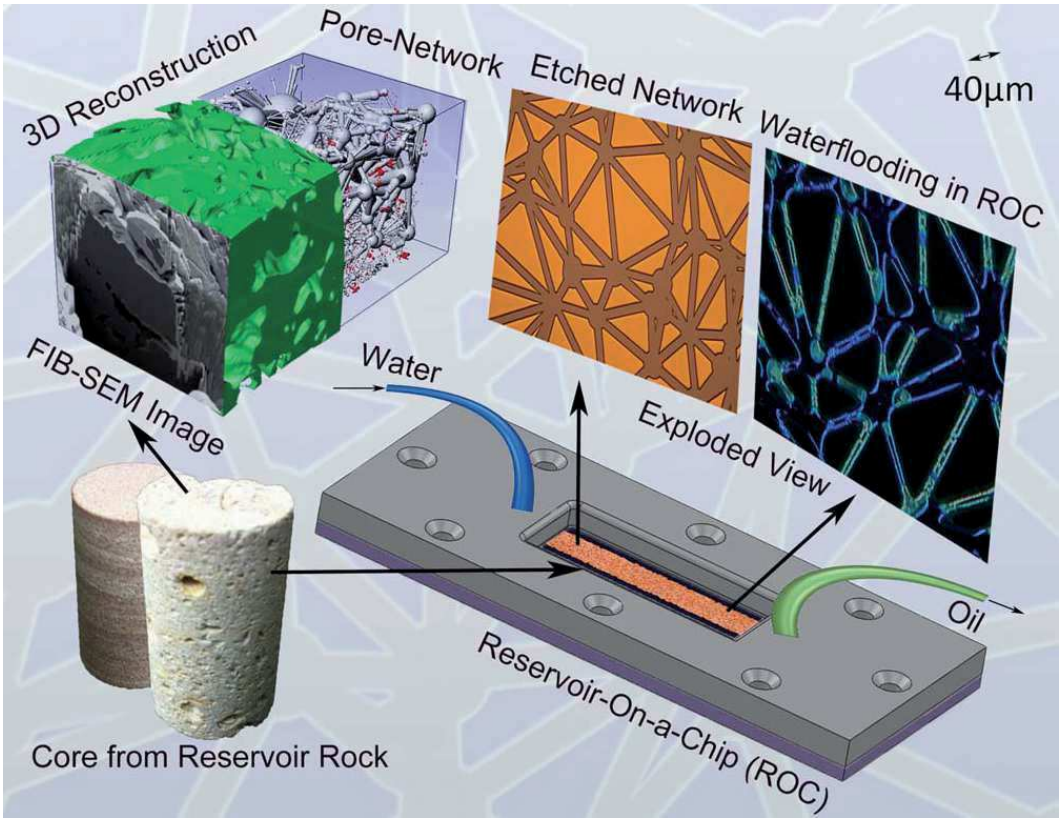

Fig. 2-5 *The conceptual flow-map for "Reservoir-on-a-Chip": a 2D pore network of silicon micromodel by extraction from 3D FIB-SEM images of sandstone from reservoir using Delaunay triangulation routine in Matlab and AutoCAD developed by Siva et al. [14].*

2. Types of porous microsystems

In order to study the flow mechanisms in porous media, the structures of real porous media have been designed to pore networks etched on substracts. Here, we overview micromodels used for studying two-phase flow and transport in porous media, according to the dimensions and substrates materials involving glass, polymer and silicon.

2.1 2D micromodels

Two-dimension pore network micromodels are the most common tools to quantify basic transport phenomena. In the 80s, Schlumberger Corporation developed a random square network to study water displacement of oil. The 2D patterns have been proved as a very convenient tool to visualize the ongoing two-phase flow processes in the porous media. To date, a large number of works has been published involving the pore-scale displacement mechanisms for both imbibition and drainage, residual saturation of fluids, relative permeabilities, capillary pressure curves, etc. The pore network at this dimension has been designed to simplify some resemblance elements of real porous media structures that are easier to fabricate and characterize, like homogeneous, circular bodies and hydrophilic surfaces. These simplified elements play a important role in the qualitative analysis. Dual-permeability pore network micromodels were then designed to characterize the permeability effects on the CO_2 displacement of water [15]. *Kim et al*. [16] observed changes of the contact angle when flowing CO_2 through a water-wetting silicon micromodel with circular bodies (Fig. 2-6 (a)).

Artificial heterogeneous micromodels are also created by manipulating the sizes of channels. One easy method is to randomly change the structures and diameters of pore spaces. *Cottin et al*. [17] used a quadrilateral-network with differing channels widths varying around an average value to study water invasion mechanism depending on capillary numbers (Fig. 2-6 (b)). *Riazi et al*. [18] used a semi-geometrical micromodel with random maze-like structure to visualize CO_2 drainage process (Fig. 2-6 (c)).

Another more realistic microstructural information is extracted from the 3D images of real core samples. The 3D images can be reconstructed from the real reservoir samples using micro-computed tomography (micro-CT) [19 - 22], focused ion beam-scanning electron microscope (FIB-SEM) [23], nuclear magnetic resonance (NMR) imaging [24] or ultrasonic scanning [25]. A 2D pore-network can be extracted from the 3D images by using stochastic random network generators [26] or Delaunay triangulation [27]. *George et al*. [28] created a silicon micromodel based on a

representative sandstone sample to study the effect of viscosity on gas driving oil production. *Siva et al*. [14] developed a silicon micromodel pore network using Delaunay triangulation routine in Matlab and AutoCAD to define the sizes of pore bodies and throats (Fig. 2-6 (d)). *Karadimitriou et al.* [29] developed the Siva's works to generate a uniform wettability glass micromodel with cylindrical pore bodies connected by parallelepiped pore throats.

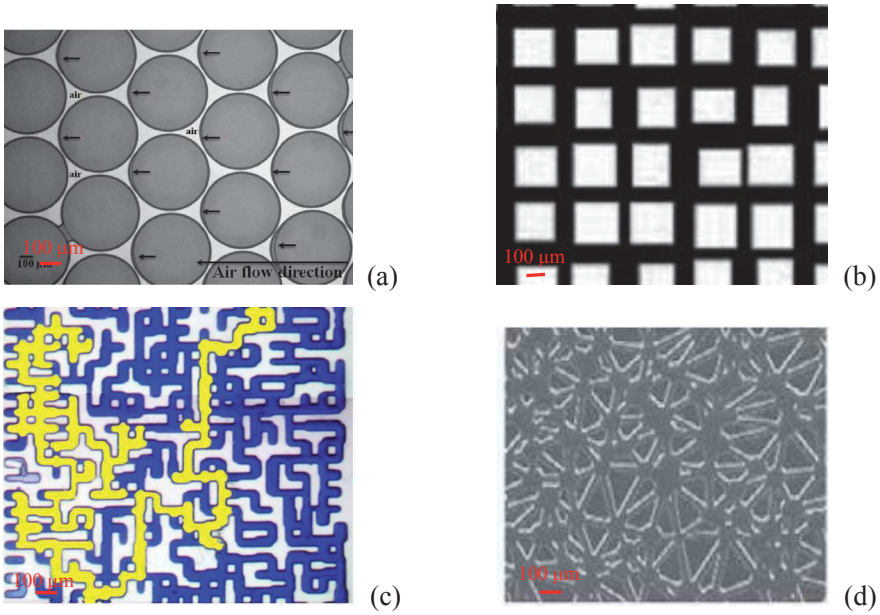

Fig. 2-6 *Several types of network design: (a) homogeneous circular pore network patterns [16]; (b) Heterogeneous square lattice [17]; (c) Maze-type random [18]; (d) Rock-based pore-throat network [14].*

The devices surface characteristics can also be patterned or altered by organic films coating with bifunctional molecules. Silanes are widely used to form self-assembled monolayers (SAM), which can change the surfaces strongly and uniformly in silicon and PDMS micromodels [30-32], making them hydrophilic or hydrophobic (Fig. 2-7). The SAM coating can be easily removed using strong alkaline solutions, like NaOH or KOH.

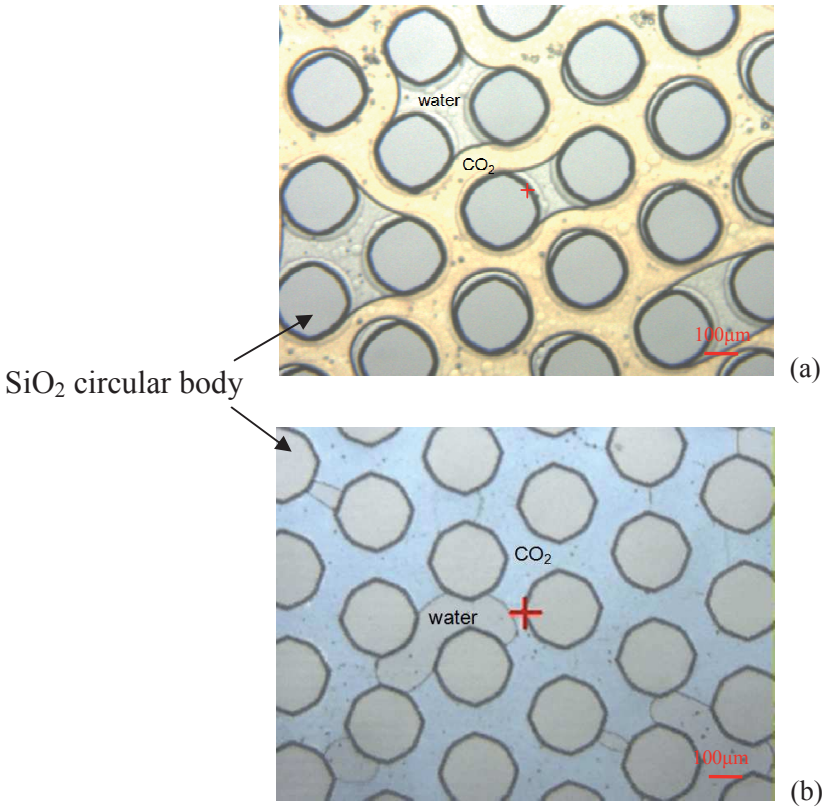

Fig. 2-7 *Images of CO_2 flow path in hydrophilic (a) and hydrophobic (b) micromodels.*

However, 2D pore networks cannot be fully representative of the complex properties of real porous media like heterogeneity or rock properties. Homogeneous pore depth in 2D pattern leads to increasing resistance forces, reduces the pore-level variations and restricts the length scale studies such as out-of-plane velocity distributions and gravity effects.

2.2 2.5D and 3D micromodels

The 2.5D micromodels consist of a two-dimensional pore networks with varying depths. *Crandall* [33] introduced a novel stereolithography flowcell to generate a micromodel with uniform distributed throat widths and a varying throat height in seven distinct layers. The pores have quasi-three-dimensional nature due to the depth, called "2.5 dimension model" (Fig. 2-8 (a)). This 2.5D pattern allows overcoming the limitations of constant matrix height in the two-dimension micromodels, meanwhile

retaining its merits such as transparency, surface paintability, which will play an important role in the investigations of multiphase flow in the porous media.

2D and 2.5D micromodels can be used to visualize the complex flow behavior in the porous media; however, it is necessary to design three-dimensional porous media for a complete understanding of the physics mechanism [34-35].

3D structures consist of active infinite clusters and inactive bones [36]. One easy way to make 3D micromodels with stratified structure is to pack several 2D micromodel slides with vertical openings, referring to multi-sandwiches (Fig. 2-8 (b)). The multi-sandwich micromodels offer opportunities for a wide range of pore structures by modifying the characterizations of every 2D micromodel slide. *Hornof and Morrow* [37] used thin layers of sintered glass beads micromodel to investigate the effects of interfacial tension on displacement behavior. *Krummel et al*. [38] used this type of densely packed hydrophilic glass beads to visualize the drainage and imbibition process of oil and water. *Cinar et al*. [39] performed a series of experiments in glass bead packs to investigate flow regimes of CO_2 injection.

Another method consists in filling deep 2D microchannels with smaller particles with given size distributions (Fig. 2-8 (c)). The difficulty of the three-dimensional micromodels is the visualization setup due to its random and multilayer structure. Indeed, optical characterization techniques can be used only if fluid and skeleton are index matched. Therefore, confocal microscopy and X-ray Computed Tomography scan will be the dominate tools for image the ongoing process in this kind of micromodels.

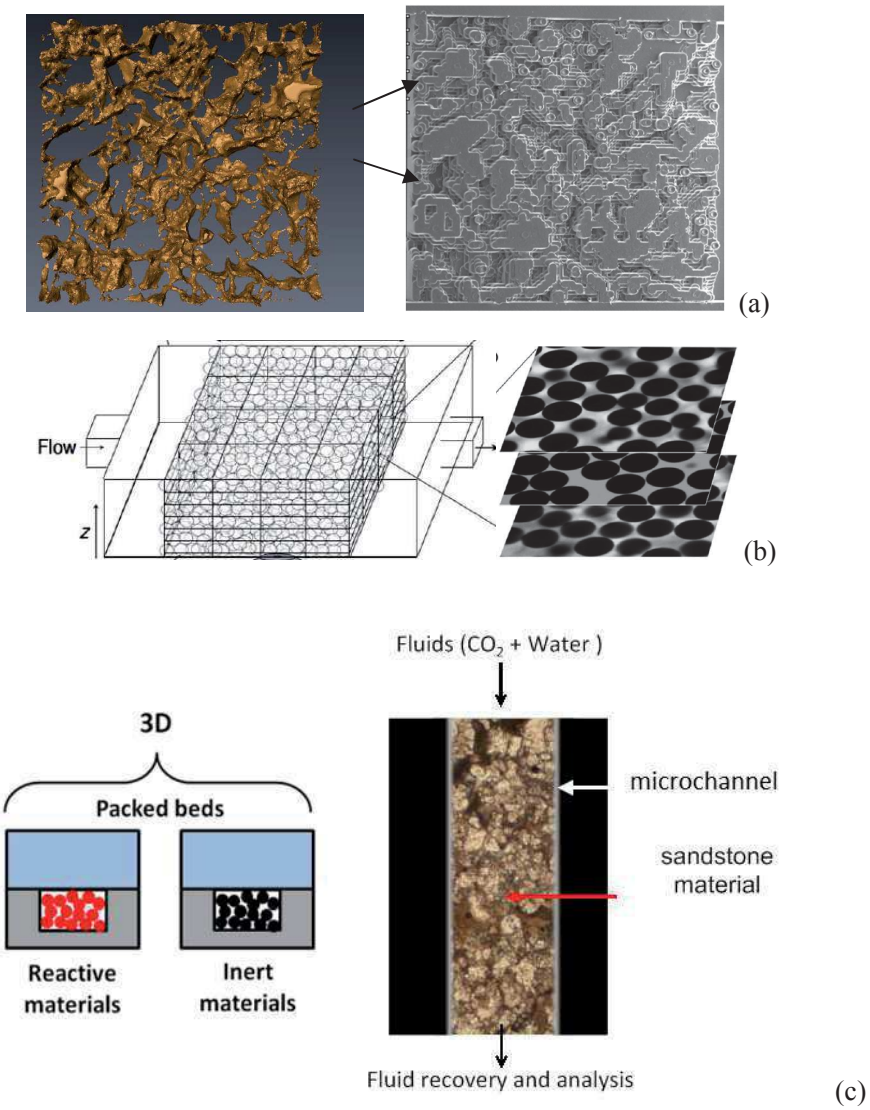

Fig. 2-8 *(a) 2.5-D PMMA chip SEM image [33]; (b) Multi-sandwich construction micromodel glass beads [37]; (c) Scheme of filling core type of 3D pattern.*

3. Available construction materials and packaging

3.1 Construction materials

Meterials used for micromodel fabrication usually depends on objectives and studies' operating conditions, where each displaces its merits and limitations. Advantages and limitations of PDMS, glass and silicon-Pyrex micromodels are listed in Table 2-1.

Table 2-1 *Comparison of different micromodels' construction materials.*

Materials	Fabrication	Suitable for	Limitations
PDMS-Glass	-cheap -easy to make -non need for clean room environment	-complex pore structures -mixed wettability	-poor temperature and pressure resistance -react or absorb fluids and chemicals -change of properties with time
Glass-Glass	-relatively cheap -stiff and rigid -generally require clean room environment	-well-defined wetting properties -withstand moderate pressures -hardly react with fluids	- poor heat transfer at high temperature.
Silicon-Pyrex	-slightly expensive, rigid, -generally require clean room environment	-HP/HT -well-defined wetting properties -hardly react with fluids	

Glass micromodels are widely used for medium temperature (< 150 ºC) or pressure (< 10 MPa) studies [40]. They provide high qualities fabrication, can be reused, have well-defined wetting properties, and can handle reactive and less neutral fluids.

Polymers like PMMA (Poly-methyl-meth-acrylate), or PDMS (Poly-di-methyl-siloxane), are more flexible and easier to be depicted than glass,

which is widespread in pore network micromodels as we discussed before. However, they can only operate in a very small range of conditions, as they react or absorb some fluids and are very sensitive to the temperature or pressure.

Silicon/Pyrex micromodels have the same fabrication way than glass ones, while they present much better heat transfer and high pressure resistance (up to 20 MPa and 400 ºC) [41-43]. Because silicon wafers are not transparent to visible light, they are usually bonded with borosilicate plates for visualization.

The fabrication condition for glass and silicon micromodels is tough, especially the bonding step. Clean room facilities are necessary to increase the quality of micromodels, while the polymer ones can be bonded at normal laboratory conditions and are very cheap to make.

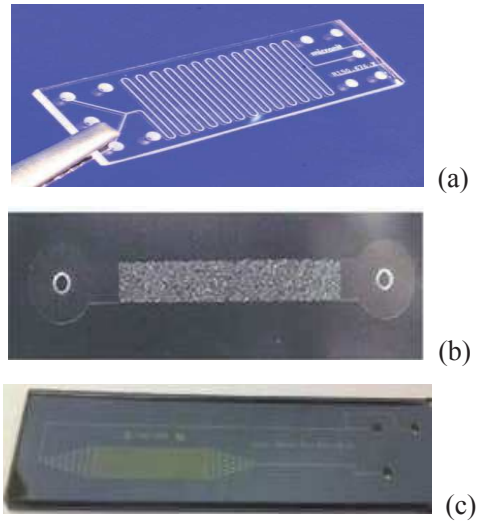

Fig. 2-9 *Micromodels with different materials: (a) Glass [44], (b) PDMS [14] and (c) silicon/Pyrex used in this study.*

3.2 Microchannel designs

Multiple types of inlet designs have been developed to create different flow patterns for two-phase flow studies. Among them, the T-junction and flow focusing are most used for studying the droplet size (Fig. 2-10). For example, in the T-junction microchannel, the dispersed phase entering through a perpendicular channel is

sheared off by the continuous phase from a horizontal channel to form slug or droplet flow by the interplay of the shear stresses and interfacial forces [45]. At low capillary numbers, the dominant interfacial tension force lead to the rate-of-flow-controlled breakup across the emerging slugs or droplets. The droplet size decreases with the flowrate ratio of the continuous phase to the dispersed phase.

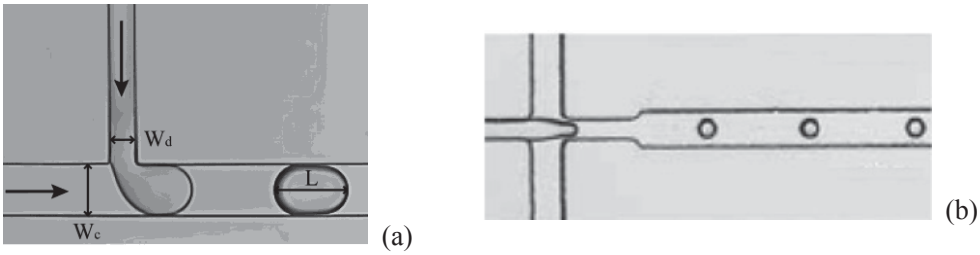

Fig. 2-10 *Droplet formation in a T-junction (a) [46] or in a flow focusing regime (b) [47].*

3.3 Packaging

The connection of microreactors to macroscopic fluid has historically been a challenge due to size and cost. Currently, two major methods exist for making microfluidic connections on microreactor chips: permanent integrated connections including epoxy gluing, metal soldering, anodic bonding of Kovar tubes to glass, and non-permanent modular connections such as commercial microfluidic interfaces assembly or compression sealing with rubber O-rings (Fig. 2-11). Each method displaces advantages and limitations in designs (see Table 2-2). Epoxy gluing is the simplest method to attach capillary to glass, silicon or polymer microchips. The microchannel has to reach a certain depth to fit the insert capillary. However, epoxy glues have limited compatibility with organic solvents and frequently clog the channels. Compression sealing uses flexible O-ring to pressurize the fluid ports on the microchip and the external flow channels. This method is reversible, and can withstand high pressure. However, the compression chucks must be carefully built to avoid leaks. For high temperature processes, an insolation zone has to be created on

the microchip between the heated part and the fluid ports to reduce heat transfer to the O-rings.

Table 2-2 *Maximum P,T operating conditions of different types of connections.*

	epoxy gluing	**metal soldering**	**anodic bonding**	**compression sealing**
Temperature (ºC)	150 [48]	150 [49]	1300 [50]	400 [9]
Pressure (MPa)	30 [51]	20 [49]	20 [52]	40 [9]

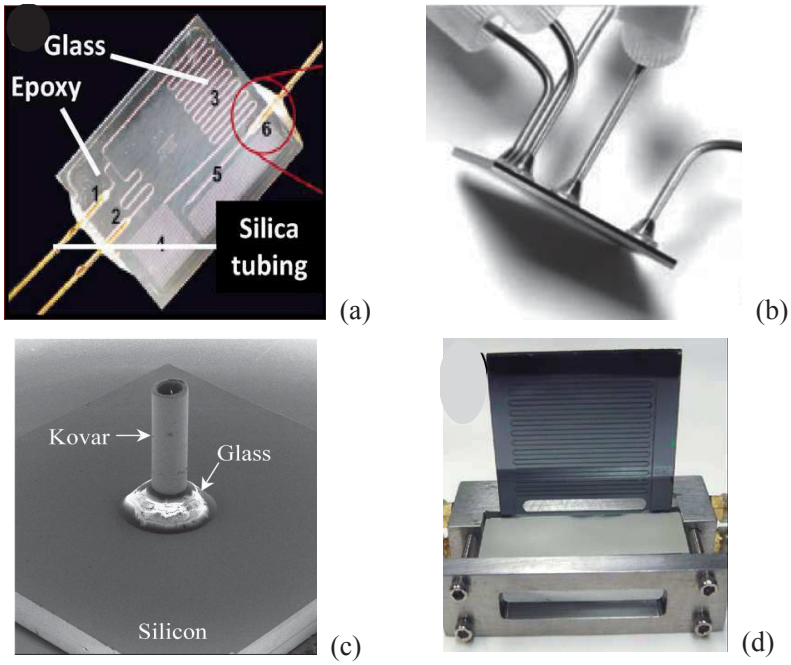

Fig. 2-11 *Examples of packaging techniques: (a) epoxy gluing [48], (b) metal soldering [49], (c) anodic bonding of Kovar tubes [50]; and (d) compression sealing [9].*

In brief, micromodels based on microfluidics fabrication strategies could provide valuable insight into pore-scale studies, which can be applied to our study: CO_2/water or brine flow in the deep saline aquifer. As shown in Table 2-3, only silicon/Pyrex and glass micromodels can conform to the high pressure conditions encountered in

reservoirs. In this study, we chose the two dimension pore network silicon/Pyrex microreactors with circular bodies for the CO_2 displacement of water in the high temperature and pressure (up to 50 ºC and 10 MPa).

Table 2-3 *Comparison of different dimensions of micromodels in the pore scale studies of two-phase flow in porous media.*

Dimension	Materials	Maximum p, T operating conditions	Observation methods	Research fields
2D	- Polymer - Glass - Si/Pyrex	- Polymer: $p \leq 0.2$ MPa, $T \leq 100$ ºC - Glass: $p \leq 10$ MPa, $T \leq 150$ ºC - Si/Pyrex: $p \leq 20$ MPa, $T \leq 400$ ºC	CCD camera	- basic theory research, - displacement mechanisms - all the effect factors.
2.5D	- PMMA	$p \leq 0.2$ MPa $T \leq 100$ ºC	CCD camera	- 2D - velocity distributions - heterogeneity effects
3D	- Glass - Si/Pyrex	- Glass: $p \leq 10$ MPa, $T \leq 150$ ºC - Si/Pyrex: $p \leq 20$ MPa, $T \leq 400$ ºC	X-ray CT	- comprehensive studies - all the factors - precipitation processes.

4. Silicon-Pyrex microfabrication procedure

Fabrication of silicon/Pyrex microreactors includes three steps: lithography, alkaline etching and anodic bonding (Fig. 2-12). The details are shown below extracted from Yann ROIG's thesis [53].

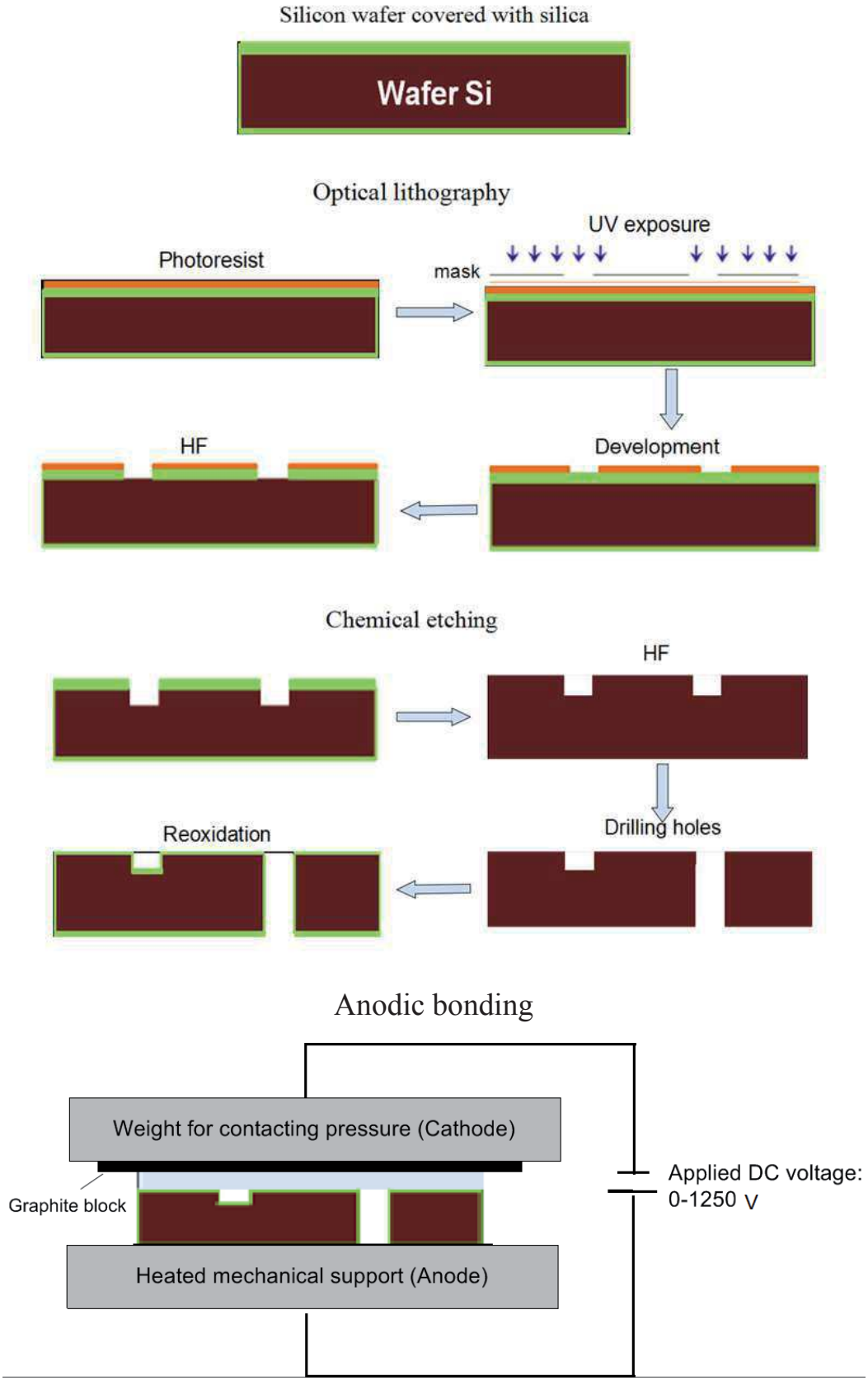

Fig. 2-12 *Silicon/Pyrex microreactor fabrication procedures.*

4.1 Photolithography

Photoresist

The silicon wafer with silica cover has been well cleaned by ethanol and acetone, then coated with a thin layer of photoresist by spin coating. The thickness of the photoresist layer depends on the duration and rotating speed of spinning (around 4 μm in this study). After that, the substrate is soft baked in 115 ºC for 4 min to harden the photoresist.

Exposure

The mask is positive projected on the photoresist layer using ultraviolet light (λ = 365 nm). The exposure time and intensity is determined by the detail of the mask. Indeed, the pore bodies and inlet structures with small size can be cleared by over exposure.

Development

After exposure, the photoresist is further developed by MF 319 developer solution. After secondary soft bake, the unprotected silica cover is removed with a HF solution. Then, the wafer is rinsed with acetone to wash away the photoresist, which left flow channels of silicon and solid part with silica cover.

4.2 Chemical etching

The etching method is based on chemical reactions between silicon and TMAH (tetramethylammonium hydroxide), which leads to trapezoidal channels. The open area of wafer will be etched at around 20-30 μm/h in a 25 % TMAH alkaline bath at 90 ºC. This method has a big shortcoming that the walls are sloped rather than vertical.

After reaching the desired depth, a sandblasting equipment is used to thirl the inlet and outlet holes. Then, the wafer is successively rinsed by acetone, water, and HF to

remove the silica cover. In next step, a thermal SiO_2 layer is grown on the perfectly cleaned wafer at 1000 ºC in a water vapour environment.

4.3 Anodic Bonding

As shown in Fig. 2-13, anodic bonding consists in sealing silicon and Pyrex through a sufficiently powerful electrostatic field. The cleaning requirements for the silicon wafer and Pyrex surfaces are very high. The substrate and glass wafer are simultaneously put in a piranha solution (3 volumes sulfuric acid (H_2SO_4): 1 volume hydrogen peroxide (H_2O_2)) to create hydroxyl groups on the surface. After 10 min, both are cleaned by DI water and ethanol. Then, a drop of DI water is set between the silicon/Pyrex assembly, and pressed to well spread (pre-bonding).

Heating up the pre-bonded substrates to 400 °C, an electrostatic field is applied through the assembly. As the bonding goes, the resistance will increase. The current has been controlled in a smaller range by increasing the voltage slightly until reaching the maximum voltage. This is the key effect factor for a successful bonding, because too high current through can entrap air bubbles between the assembly. The procedure can be repeated once or twice to enhance the connection. After cooling down, the bonded microreactor is cut with a diamond saw to a certain size fitting to the compression part.

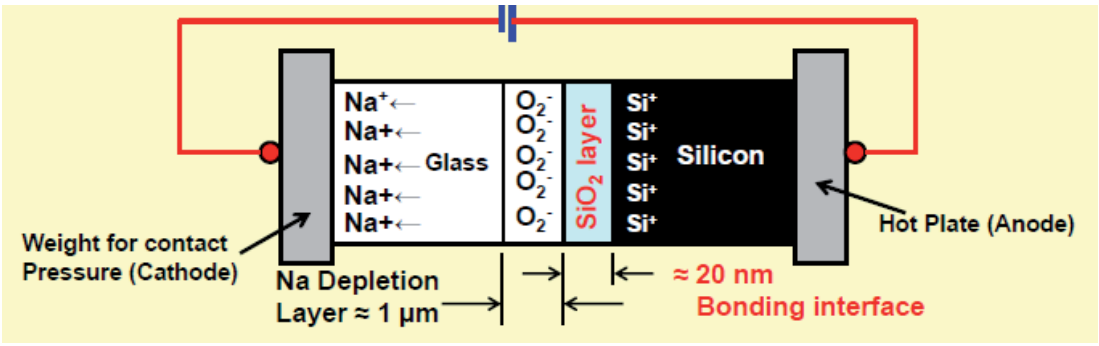

Fig. 2-13 *Working principle of Glass-to-silicon wafer bonding (image from Lecture on Microsystems Design and Manufacture chapter 11).*

4.4 Surface treatments

The microreacor fabricated with this procedure can reach a uniform well water-wetting surface feature due to the piranha treatment during the procedure. For the hydrophilic observations, to ensure the same wetting properties for each experiment, the micromodel was thoroughly cleaned using a rigorous cleaning procedure in the following order before each experiment: isopropanol, deionized (DI) water, H_2O_2 solution, and DI water.

The following procedure has been used to alternate the wettability of silica surface from hydrophilic to hydrophobic by injecting the octadecyltri-chlorosilane (CH_3-$(CH_2)_{17}SiCl_3$, OTS). First, the silica surface of the micromodel was thoroughly oxidated by H_2O_2 at lab condition, then in turn, rinsed by isopropanol and toluene to prepare for wearing a Self-Assembly Monolayer (SAM). The self-assembly solution consists of 1mM octadecyltrichlorosilane (OTS) solution in toluene and was injected at 50 $\mu l \cdot min^{-1}$ into the micromodel for 45 min within a glove box under dry ambient conditions. After rinsed by toluene and isopropanol, the hydrophobic micromodel was completed.

Before flowing fluid inside, the microreactor need a packaging and then to be tested to check the quality of fabrication, such as the compression capacity, and the bugs in the flow network, clogging or leakage.

5. Packaging, Testing and Monitoring

The connection between the microreactor and its external environment is made through the use of a stainless steel compression chuck (Fig. 2-14). One piece with several holes is dedicated to connect the inlet and outlet of microreactor to the macro tubes. Another piece coupled to O-rings aims at sealing the microreactor and holding

the pressure. The insulation zone through etched inside the silicon part of the microreactor between the heating part and the injection part of micromodel is needed to protect the O-rings from heat transfer from the heating zone. Before use, the microsystem assembly is first put into oven at 400 °C for 24 h and cooled down in 24 h for reducing mechanical stress in the material through an annealing process. The pressure resistance test was performed by injecting N_2 at high pressure for 15 min.

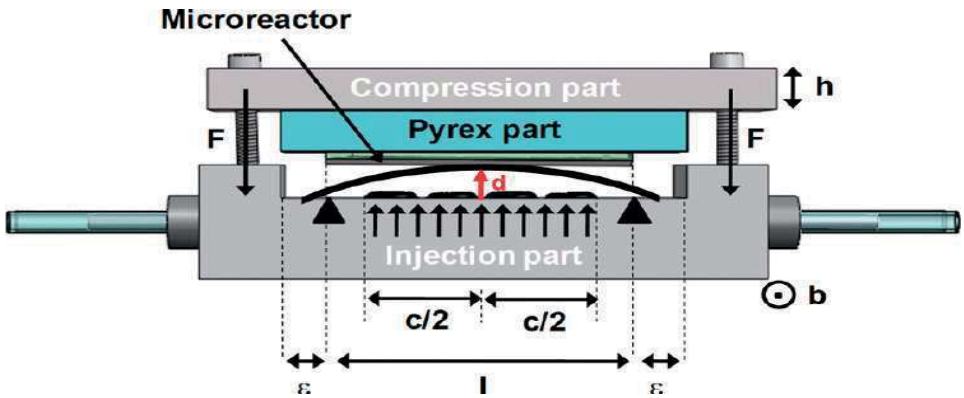

Fig. 2-14 *Scheme of the compression part [41].*

5.1 Temperature and Pressure control

The microreactors were heated with heating cartridges inserted into an aluminum block in contact with the microreactors. The temperature was monitored using a thermocouple pasted to the Si backside of the microreactor, which is connected to a Eurotherm ® temperature controller. The probe was placed between the flat microreactor and the heating block. Given the good thermal conductivity of silicon, we can assume that the temperature measured at this location is almost equal to that of fluids within the microchannels. This heating assembly allows working with microreactors in a wide range of temperatures (RT - 400 ºC) (RT = Room Temperature).

The fluids were injected with high-pressure syringe pumps “HARVARD PHD 2000” or “Teledyne Isco” (Fig. 2-15). “HARVARD PHD 2000” can only pump the

liquid at room temperature with a maximum pressure of 12 MPa at low flowrate (down to 10^{-3} µl·min^{-1}). The "Teledyne Isco 100 DM" pumps are capable of injecting at very high pressures up to 70 MPa and wide range of flow rates (10^{-2} to 10^{5} µl·min^{-1}), in either a constant pressure or a constant flow mode. The fluid temperature within the pump can be controlled by a thermostatted jacket surrounding the injection cylinder in a temperature range from -20 ºC to 100 ºC. The pressure within microreactor is controlled by a pressure regulator connected with N_2 tank, which is put downstream of the outlet. The final microsystem assembly is shown in Fig. 2-16.

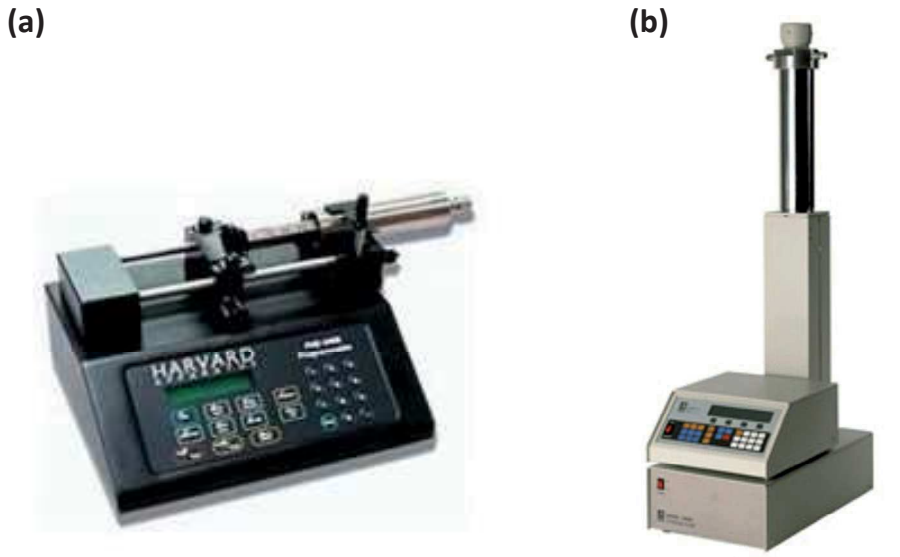

Fig. 2-15 *High pressure syringe pumps: (a) HARVARD PHD 2000; (b) Teledyne Isco 100 DM.*

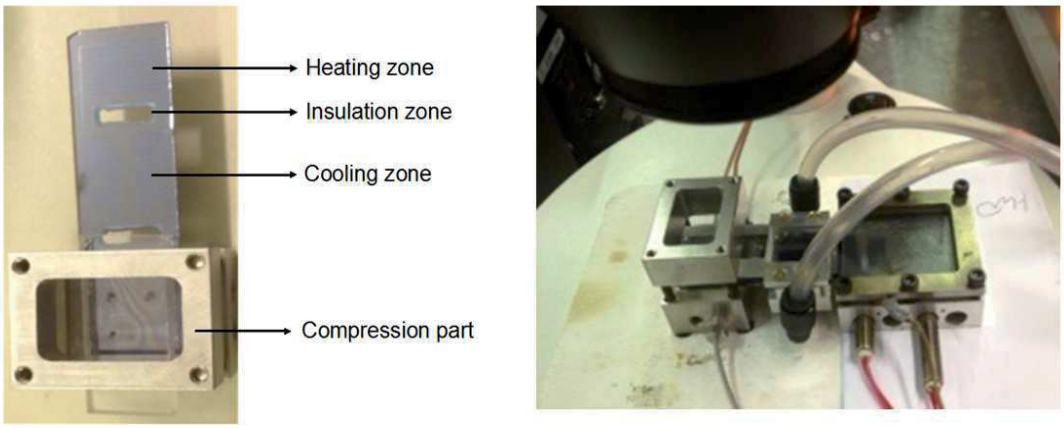

Fig. 2-16 *Images of the microsystem final assembly.*

5.2 Monitoring and on-line characterization

A significant advantage of using micromodels is the ability to monitor fluids configuration, fluid flow, and various features inside the micromodel. In a two-phase flow experiment, the measurements of phase saturation and specific interfacial area are based on the study of obtained pictures or movies. Moreover, for dynamic analysis, fluids distributions need to be recorded as a function of time by a high speed camera. Visualization methods used to capture the images of two-phase flow, statically or dynamically, can be realized by a microscope-camera, digital camera with sophisticated CCD sensors, confocal microscopy and so on. In this study, we used the confocal microscope from the Raman spectrometer. The CamStudio software was used to record movies. Raman spectroscopy was used to *in situ* characterize the dissolution and reactions between CO_2 and brine.

Through these steps, we fabricated both the paralleled multi-channels microreactors to analyze the solubility of CO_2 in water, which can work up to 15 MPa and 400 ºC, and the homogeneous pore network micromodels (hydrophilic or hydrophobic) for the studies of CO_2 displacement and carbonate precipitation (10 MPa - 100 ºC).

IV. Two-phase Flow in Porous Microsystems

1. Introduction

Two-phase flow in porous media plays a central role in many natural and industrial systems, among which CO_2 geological storage is a typical example. The investigations of phase distributions and interactions of CO_2/brine/rocks at macro scale are time-consuming and difficult to be controlled in a precise way, while micromodels could address these shortcomings. Moreover, the micromodels can provide visual observation of the fluids flow and colloids movement. The majority of micromodels applications in studies of flow and transport in porous media are related to the displacement of two fluids phases [54]. A large part of literature investigate drainage and imbibition processes, as well as dominated mechanisms, like viscous or capillary fingering at pore scale, which have been published, as discussed in chapter 1.

2. From pore scale to Darcy scale

Transient two-phase flow within micromodels involves dynamic terms at Darcy scale, such as relative permeability for two-phase flows, and pore space characteristics, such as the effects of surface tension. The topic of this manuscript part is the prediction of model parameters and processes for flow and transport processes at the Darcy scale and pore scale.

2.1 Darcy scale

Darcy's law is an empirical relationship for flow in porous media, established by Henry Darcy in 1856. It shows that the flow velocity is linearly proportional to the pressure drop and gravitational force (Eq. 2-1).

$$u_i = -K \frac{k_{ri}}{\mu_i} (\nabla P_i - \rho g), i = n, w \qquad \text{Eq. 2-1}$$

where, u_i is Darcy's velocity ($m \cdot s^{-1}$) for either the non-wetting (n) or the wetting (w) fluid, K is the absolute permeability (m^2), which is the permeability of a porous medium saturated with a single fluid; Effective permeability (K_i) is the permeability of a porous medium for one fluid phase when the medium is saturated with more than one fluid. k_{ri} is the relative permeability (dimensionless), which is the ratio of the effective permeability to the absolute permeability (K_i/K); ρ is density ($kg \cdot m^{-3}$), μ is dynamic viscosity (Pa·s), ∇p is the pressure gradient vector ($Pa \cdot m^{-1}$), g is the gravitational acceleration vector ($m \cdot s^{-2}$). The acting forces in the displacement include gravity forces caused by fluid density gradients, viscous forces driven by adverse viscosity ratios and capillary forces coming from interfacial tension.

From Eq 2-1, it is known that the relative permeability for the wetting and the non-wetting phase is the most effective factor to determine the flow and transport processes in the porous media at Darcy scale.

2.2 Pore scale

The fluid transport processes in porous media occurring at pore scale mainly depends on the microscopic structure and the interfacial tension. The capillary pressure caused by the surface tension at the interface between two phases can be expressed by the Young−Laplace equation [16]:

$$p_{cap} = \frac{2\gamma \cos\theta}{r} \qquad \text{Eq. 2-2}$$

where γ is the interfacial tension (IFT) (Pa·m), θ is the contact angle of the aqueous phase on the mineral surface, and r is the characteristic radius of the pores (m).

One can noticed from Eq 2-2 that interfacial interactions (interfacial tension and wettability) and sizes of micro structures play important roles on fluid distribution and behaviour in porous media. Therefore, the studies of surface tension, wettability and heterogeneity are key parameters on the effectiveness of pore scale fluid flow processes in porous media.

In this study, we use the average scale to study the two-phase flow within micromodels, using permeability and porosity from Darcy scale and pore space characteristics.

3. Displacement process

3.1 Dimensionless numbers

Since the Reynolds number in microfluidic systems is low (far smaller than 1), the underlying flow regimes at macroscale methods are usually not sensible to microscale data. The most significant change is the stronger internal forces (viscous and capillary forces), while the external forces (*e.g.* gravity) effects are weaken. In the internal environment, viscous force from the wetting phase, viscous force from the non wetting phase and capillary forces from the interfacial tension dominate the behavior of two-phase flow in the microfluidic elements.

Among the increasing internal effects at microscale, the capillary number (Ca), which describes the relative importance of viscous forces to capillary forces, is one of the most important parameters in microfluidic. Ca is given by:

$$Ca = \frac{\mu u}{\gamma \cos\theta} \qquad \text{Eq. 2-3}$$

where, μ is dynamic viscosity (Pa·s), u is the fluid velocity ($m \cdot s^{-1}$), γ is the interfacial tension (Pa·m), θ is the contact angle. The value of capillary number displays the dominate force in the two phase microfluidics flow. For low capillary numbers, capillary forces dominate the flow in porous media, whereas for high capillary number the capillary forces are negligible compared to the viscous force.

In addition, viscous effects play a small role in most of the flow field at macroscale. However, at microscale, viscosity ratio determined the stability of displacement. Viscosity ratio (M), is usually defined to specify the displacements of wetting phase and non-wetting phase in the operating conditions.

$$M = \frac{\mu_n}{\mu_w} \qquad \text{Eq. 2-4}$$

where, the subscript *w* represents water, wetting phase, and *n* the non-wetting phase. For M>1, the injected non-wetting phase can travel faster than the wetting phase and form the favorable displacement, like oil driving water. While for M<1, an unstable displacement can be caused by viscous forces at high injecting rate, like CO_2 displacement of water.

Almost all the studies on displacement process at pore scale focus on the effects of capillary number and viscosity ratio on the displacement mechanisms. Here, we detail the average scale (Darcy scale and pore scale) model occurring in a drainage process.

3.2 Drainage at micro scale

During displacement process, drainage occurs when the non-wetting phase displaces the wetting phase within the pore space. Imbibition is the opposite process. Here, we consider a drainage process where a non-wetting fluid (n) invades a porous medium that is initially saturated with a wetting fluid (w).

The fraction of the fluid in the pore space is named saturation (S_i):

$$S_i = \frac{\phi_i}{\phi}, i = n, w \qquad \text{Eq. 2-5}$$

where, ϕ is porosity (dimensionless), ϕ_i is the representative volume of phase i in a porous medium. For two immiscible fluids, the non-wetting phase and the wetting phase generally coexist in the pores. Therefore:

$$S_n + S_w = 1 \qquad \text{Eq. 2-6}$$

The residual wetting phase coats the rocks surfaces as continuous films, while the non-wetting phase is immobilized by the capillary forces. When considering two miscible fluids, the residual wetting phase could be thoroughly removed by dissolution (S_n=1).

The saturation of the displacing phase reflects the displacement efficiency, which can be obtained by local mass conservation in each phase:

$$\phi \frac{\partial}{\partial t}(S_i) + \nabla \cdot u_i = 0 \qquad \text{Eq. 2-7}$$

where, u is Darcy's velocity ($m \cdot s^{-1}$), which is assumed to be the extension of Darcy's law. Upon shrinking to the micro scale, the dominant forces of physical phenomena change. The most significant change is the stronger capillary and viscous forces, while the gravity effect is weakened and ignored in most pore scale cases. Thus, the expression of Darcy's velocity is simplified as:

$$u_i = -K \frac{k_{ri}}{\mu_i} \nabla p, i = n, w \qquad \text{Eq. 2-8}$$

The absolute permeability (K) can be calculated from the steady-state flow equation (1D, linear Flow):

$$K = \frac{\mu q L}{A \Delta p} \qquad \text{Eq. 2-9}$$

where, q is the injection flowrate ($m^3 \cdot s^{-1}$), L is the length of porous structures (m), A is the flow area in the porous medium (m^2), Δp is the pressure drop across the porous media (Pa).

The relative permeability of a phase (k_{ri}) is represented as a function of wetting phase saturation (S_w). Thus, the relative permeability curve as a function of saturation under a wide range of experimental conditions is an important parameter for a primary pore scale drainage process, which can be obtained using the following binary equation:

$$\phi \frac{\partial}{\partial t}(S_i) + \nabla \cdot (-K \frac{k_{ri}}{\mu_i} \nabla p) = 0 \qquad \text{Eq. 2-10}$$

Within micromodels, the relative permeability is not only a function of saturation but also strongly depends on the capillary number. In a pore scale drainage process, a higher capillary number can result in a higher displacing fluid saturation and also a higher relative permeabilities (Fig. 2-17) [55-56].

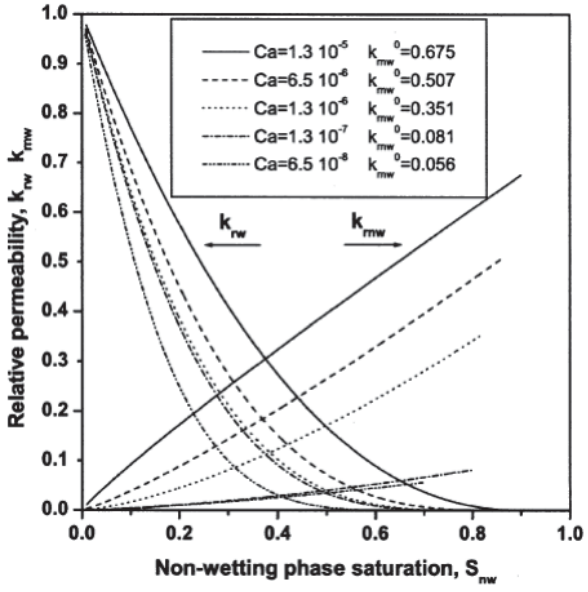

Fig. 2-17 *Estimated relative permeability—saturation curves for different capillary numbers of paraffin oil displacing distilled water within a glass-etched micromodel developed by Tsakiroglou et al. [56].*

During the drainage process, the Δp between the two phases refers to capillary pressure, which can corrected by the Brooks-Corey equation [57]:

$$p_n - p_w = p_c = p_e S_{We}^{-\lambda} \quad \text{Eq. 2-11}$$

where 1/λ is the pore-size distribution index from a small value corresponding to a wide distribution of pore sizes to the infinite homogeneous pores (λ=0 in our homogeneous micro porous media); S_{we} is effective non-wetting phase saturation:

$$S_{we} = \frac{S_w - S_{wi}}{1 - S_{wi}} \quad \text{Eq. 2-12}$$

where S_w is the wetting phase saturation, S_{wi} is the irreducible wetting phase saturation, which represents the saturation of the wetting phase remaining within the pores after the steady state of drainage and is assumed to be constant. Therefore, at macro scale, the capillary pressure is assumed to be a function of saturation only [58]. Nevertheless, the increasing capillary pressure at pore scale is also affected by the pore conditions (temperatures and pressures), fluids properties and front flows. *Dong and Chatzis* [59] found that capillary pressure dominates the imbibition of wetting film ahead of the main displacement front using a consolidated glass-beads micromodel. *Kim et al* [16] demonstrated that CO_2 dissolution in water results in increasing contact angles, and therefore decreasing capillary pressure.

In brief, capillary pressures and relative permeabilities are two most important parameters for the determination of two-phase flows in a porous medium. As the dimensions shrink down to microscale, viscous and capillary forces dominate the fluids flows in the pore, but gravitational effects are usually excluded. Capillary pressures and relative permeabilities are not only functions of saturation, but also influenced by the dissolution of fluids and capillary numbers when the non-wetting phase is invading the porous medium for the first time.

3.3 Displacement patterns

Lenormand et al. [60] observed three main types of displacements during imbibition based on water-wet 2D pore–throat micromodel experiments with square pores (Fig. 2-18): piston-like displacement, snap-off and pore-body filling. The piston like displacement is an extreme simplification of real displacement, which assumed that behind the front there is no movement of the irreducible phase. Among the displacement process, a stable, piston-like displacement attains maximum sweep efficiency.

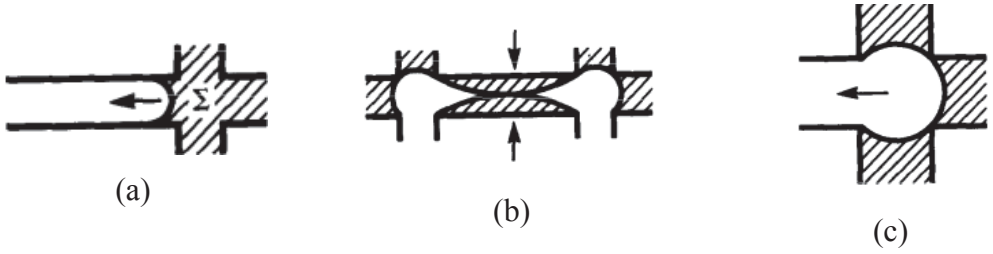

Fig. 2-18 *Different types of displacement: (a) piston-like; (b) snap-off; (c) pore-body filling [61].*

During the imbibition process, the wetting phase enters the pore throat though a continuous corner wetting film. As capillary pressure decreases, the wetting film starts swelling. Until capillary pressure reaches the critical capillary pressure, the wetting phase totally fills the pore throat by means of snap-off and pushes the non wetting phase into the pores. Therefore, the critical capillary pressure is the key to the snap-off displacement mechanism in a pore-throat network, which is estimated by [61]:

$$P_{snap} = \frac{2\gamma(\cos\theta - \sin\theta)}{d} \qquad \text{Eq. 2-13}$$

with θ is the contact angle, γ is surface tension (Pa·m), and d is the width of the throat (m).

Pore body filling consists in having the residual fluid collected in the center of a pore body by connecting pore throats filled with the displacing fluid. The capillary

entry pressure for the pore body depends on the size of the pore body and the number of non-wetting pore throats connected to it [62].

During the displacement process, a moving interface is created between the displacing and the displaced fluid. However, different fluid properties and capillary forces can lead to two main unstable displacement fronts: viscous fingering and capillary fingering.

Viscous fingering occurs when the viscous forces are dominating the displacement. From the images (Fig. 2-19 (a)), the flow paths of viscous fingering primarily progressed forward across the pore network with limited or no lateral flow [15]. It is reported that viscous fingering only occurs at unfavorable displacement ($M<1$) and dominates at higher capillary numbers. When a fluid pushes a more viscous fluid, the interface between the fluids develops an instability leading to the formation of viscous fingering [63]. Keeping increasing the viscosity difference between two fluids, viscous fingering can occur at average or even lower capillary numbers.

Capillary fingers are caused by the capillary forces. From the images (Fig. 2-19 (c)), capillary fingering shows obvious lateral and backward flow. It is reported that for $M>1$, capillary fingering occurred for the displacements at low capillary numbers, while for larger capillary numbers, the displacements gradually became stable. However, for $M<1$, the unstable fingering changed from capillary to viscous with an increasing capillary number. For moderate capillary numbers, both capillary and viscous fingering coexist (Fig. 2-19 (b)) [64-66].

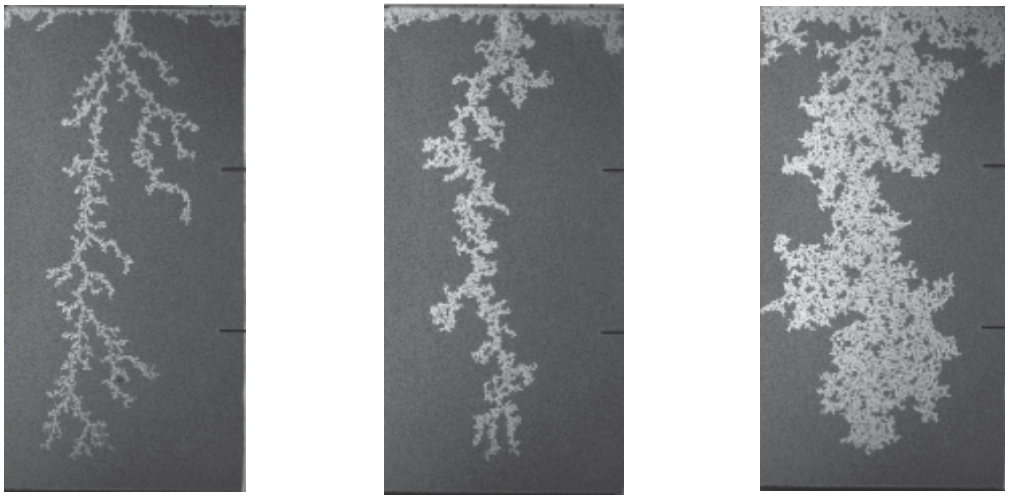

(a) (b) (c)

Ca= 0.20 Ca= 0.060 Ca= 0.015

Fig. 2-19 *A continuous transition from viscous fingering to capillary fingering as function of Ca in air displacing water within a Hele-Shaw cell [67].*

Zhang et al. [68] completed a large number of displacement experiments for several wetting/non-wetting fluid pairs with different viscosity ratios in a well water-wetting silicon micromodel (Fig. 2-20 (a)). In a micromodel, initially saturated with the wetting fluid, a non-wetting fluid was injected at different flow rates. The non-wetting fluid saturations and interfacial area were visualized and measured by fluorescent microscopy during the displacement process. Finally, a displacement stability diagram was developed depending on capillary numbers and viscosity ratios (Fig. 2-20 (b)).

In addition, permeability also play an important role on the displacement stability. *Zhang et al*. [15] also designed a pore network micromodel with two distinct permeability zones to investigate the permeability effect on the displacement stabilities. The fluids pair in this study consists in liquid CO_2 displacing pure water within a high pressure micromodel. They showed that CO_2 displaced water preferentially in the high permeability zone with the mechanism shifting from capillary fingering to viscous fingering with an increasing capillary number.

Unstable displacement processes have significant effects on two-phase flows in the porous media. Viscous and capillary fingering demonstrate different characteristics in the primary displacement for different applications. For example, for the oil recovery industry, if instability occurs, viscous fingering with dendritic branching can considerably lower the sweep efficiency. Capillary trapping could be a problem because the large entrapped water is hard to be removed. However, the case of CO_2 / water system is totally different.

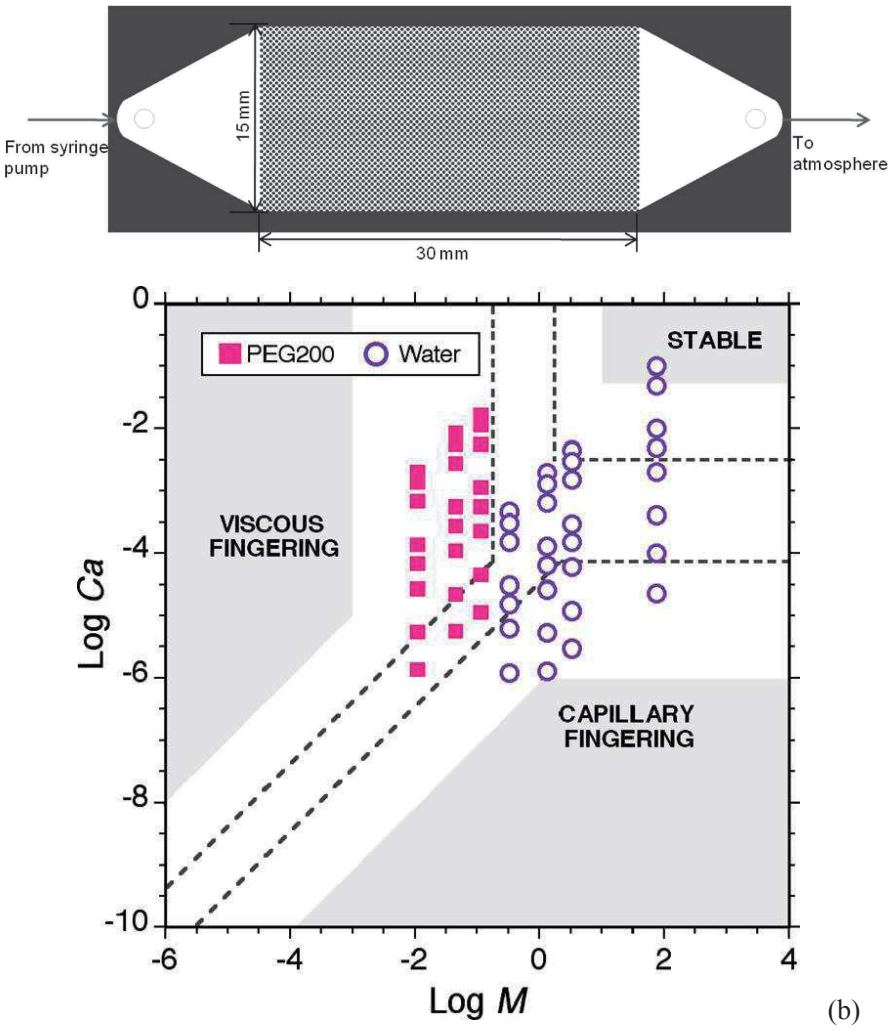

Fig. 2-20 *(a) Scheme of the micromodel developed Zhang et al. [66]; (b) Stability diagram resulting from the displacement experiments [68].*

3.4 CO_2 displacement of water

In the particular case of CO_2/water drainage, unstable displacements occurred at all injection rates due to the low viscosity ratio between CO_2 and water. CO_2 saturation increased with increasing capillary number. At low flow rates and capillary numbers, capillary fingering occurs, while many viscous fingers form by increasing the injection rate.

Viscous fingering can lead to an early breakthrough, while capillary fingering has a better sweep efficiency for the displacement process. In addition, capillary trapping is one of main trapping mechanisms for the long-term geological CO_2 storage, which can increase the contacted area of CO_2/brine/rocks and therefore be beneficial for dissolution and mineral trapping. The residual water will finally be removed from the porous media due to the mutual solubilities of water and CO_2.

4. Conclusion

In this chapter, we mainly discussed the microscale models for the displacement process studies in porous media. The relative permeability and capillary pressure are two key parameters to characterize the drainage process of two-phase flows in the porous media. During the drainage process, viscous forces and capillary forces dominate the displacement mechanisms and flow patterns. Two dimensionless numbers, the capillary number (Ca) and the viscosity ratio (M), are used to study the effects of these dominating forces. When a fluid invades a porous media saturated with a more viscous fluid (CO_2 displacing water), the front of displacement develops unstable flow patterns, *e.g.* viscous fingers or capillary fingers. Unstable displacement processes have significant effects on CO_2 displacement. Viscous fingering allows fast breakthrough of the capillary barrier in the pore space, while capillary fingering can increase the interfacial areas of CO_2 and water. Therefore, unstable displacements

during CO_2 injection into deep saline aquifers could cause CO_2 early breakthrough and increase storage capacity and safety.

In the next two chapters, we will present experimental results obtained for both solubility investigations of CO_2 in water or saltwater using microfluidic systems and CO_2 invasion processes characterization in porous micromodels.

References

1 A. Chatenever, Jr., J.C. Calhoun, Petroleum Transactions AIME. 195 (1952) 149-156.

2 S. Sayegh, D. Fisher, Canadian International Petroleum Conference/SPE Gas Technology Symposium 2008 Joint Conference (2008) 1-16.

3 M. Sohrabi, A. Danesh, M. Jamiolahmady, Transportation in Porous Media 74 (2007) 239-257.

4 H. Nakamura, Y. Yamaguchi, M. Miyazaki, H. Maeda, M. Uehara, P. Mulvaney, Chemical Communications (2002) 2844-2845.

5 S. Marre, C. Aymonier, P. Subra, E. Mignard, Applied Physics Letters 95 (2009) 134105.

6 N. Lorber, F. Sarrazin, P. Guillot, P. Panizza, A. Colin, B. Pavageau, C. Hany, P. Maestro, S. Marre, T. Delclos, C. Aymonier, P. Subra, L. Prat, C. Gourdon, E. Mignard, Lab on a Chip 11 (2011) 779-787.

7 N. Lorber, B. Pavageau, E. Mignard, Macromolecules 43 (2010) 5524-5529.

8 A. Perro, C. Nicolet, J. Angy, S. Lecommandoux, J.F. Le Meins, A. Colin, Langmuir 27 (2011) 9034-9042.

9 S. Marre, Y. Roig, C. Aymonier, J. of Supercritical Fluids 66 (2012) 251-264.

10 T. Gendrineau, S. Marre, M. Vaultier, M. Pucheault, C. Aymonier, Angew. Chem. Int. Ed. 51 (2012) 1-5.

11 J. Kobayashi, Y. Mori, S. Kobayashi, Chemical Communications (2005) 2567-2568.

12 F. Trachsel, B. Tidona, S. Desportes, P.R. von Rohr, J. of Supercritical Fluids 48 (2009) 146-153.

13 A. Urakawa, F. Trachsel, P.R. von Rohr, A. Baiker, Analyst 133 (2008) 1352-1354.

14 G. N. Siva, B. Bera, N. K. Karadimitriou, S. K. Mitra, S. M. Hassanizadeh, Lab on a Chip, 11 (2011) 3785-3792.

15 C. Zhang, M. Oostrom, J. W. Grate, T. W. Wietsma, M. G. Warner, Environ. Sci. Technol. 45 (2011), 7581-7588.

16 Y. Kim, J. Wan, T. J. Kneafsey, T. K. Tokunaga, Environ. Sci. Technol. 46 (2012) 4228-4235.

17 C. Cottin, H. Bodiguel, A. Colin, Phys. Rev. 82 (2010) 046315.

18 M. Riazi, M. Sohrabi, C. Bernstone, M. Jamiolahmady, S. Ireland, Chemical Engineering Research and Design 89 (2011) 1827-1840.

19 M. J. Blunt, M. D. Jackson, M. Piri, P. H. Valvatne, Adv. Water Resour. 25 (2002) 1069-1089.

20 P. Valvatne, M. Blunt, Water Resour. Res. 40 (2004) W074061-W0740621.

21 M. Blunt, C. Opin, Colloid Interface Sci. 6 (2001) 197-207.

22 C. S. Willson, R. W. Stacey, K. Ham, K. E. Thompson, Proceedings of SPIE - The International Society for Optical Engineering (2004) 101-111.

23 B. Bera, S. K. Mitra, D. Vick, Micron 42 (2011) 412-418.

24 J. D. Seymour, P. T. Callaghan, AIChE J. 43 (1997) 2096-2111.

25 J. T. Geller, L. R. Myer, J. Contam, Hydrol. 19 (1995) 85-104.

26 N. A. Idowu, M. J. Blunt, Transp, Porous Media 83 (2010) 151-169.

27 N. K. Karadimitriou, S. M. Hassanizadeh, P. J. Kleingeld, First nternational Conference on Frontiers in Shallow Subsurface Technology (2010).

28 D. George, O. Hayat, A. Kovscek, J. of Petroleum Science and Engineering 46 (2005) 101-119.

29 N. K. Karadimitriou, V. Joekar-Niasar, S. M. Hassanizadeh, P. J. Kleingeld, L. J. Pyrak-Nolte, Lab on a Chip 12 (2012) 3413-3418.

30 C. B. Mao, H. D. Li, F. Z. Cui, Q. G. Feng, H. Wang, C. L. Ma, J. of Materials Chemistry 8 (1998) 2795-2801.

31 F. Saharil, C. F. Carlborg, T. Haraldsson, W. van der Wijngaart, Lab on a Chip 12 (2012) 3032-3035.

32 C. S. Chen, E. Ostuni, G. M. Whitesides, D. E. Ingber, Methods Mol Biol. 522 (2009) 183-194.

33 E. Crandall, Rev. of Scientific instruments 79 (2008) 044501.

34 G. R. Jerauld, S. J. Salter, Transp Porous Media 5 (1990) 103.

35 I. Chatzis, F. Dullien, International Chemical Engineering 25 (1985) 47-66.

36 J. Pražák, Colloquium Fluid Dynamics (2012) 24-26.

37 V. Hornof, N. Morrow, SPE Reservoir Engineering 11 (1998) 251-256.

38 A. T. Krummel, S. S. Datta, S. Muunster, D. A. Weitz, AIChE J. 00 (2013) 00.

39 Y. Cinar, A. Riaz, H.A. Tchelepi, SPE J. (2009) 588-594.

40 M. Sohrabi, A. Danesh, M. Jamiolahmady, Transportation in Porous Media 74 (2007) 239-257.

41 S. Marre, A. Adamo, S. Basak, C. Aymonier, K. F. Jensen, Ind. Eng. Chem. Res. 49 (2010) 11310-11320.

42 R. M. Tiggelaar, F. Benito-Lopez, D. C. Hermes, H. Rathgen,R. J. M. Egberink, F. G. Mugele, D. N. Reinhoudt, A. van den Berg, W. Verboom, H. Gardeniers, Chem. Eng. J. 131 (2007) 163-170.

43 E. R. Murphy, T. Inoue, H. R. Sahoo, N. Zaborenko, K. F. Jensen, Lab on a Chip 7 (2007) 1309-1314.

44 C. Iliescu, B. Chen, J. Miao, Sensors and Actuators A 143 (2008) 154-161.

45 T. Cubaud, U. Ulmanella, Chih-Ming Ho, 5th International Conference on Multiphase Flow (2004) PL5.

46 H. Gu, M. H. G. Duits, F. Mugele, Int. J. Mol. Sci. 12 (2011) 2572-2597.

47 M. Lounaci, P. Rigolet, C. Abraham, M. L. Berre, Y. Chen, Microelectronic Engineering 84 (2007) 1758-1761.

48 S. Mukherjee, M. K. Hatalis, M. V. Kothare, Catalysis Today 120 (2007) 107-120.

49 E.R. Murphy, T. Inoue, H.R. Sahoo, N. Zaborenko, K.F. Jensen, Lab on a Chip 7 (2007) 1309-1314.

50 Y. Peles, J. Microelectromech. Syst. 13 (2004) 31-40.

51 R. M. Tiggelaar, F. Benito-Lopez, D. C. Hermes, H. Rathgen, R. J. M. Egberink, F. G. Mugele, D. N. Reinhoudt, A. van den Berg, W. Verboom and H. Gardeniers, Chem. Eng. J. 131 (2007) 163-170.

52 M. T. Blom, J. Micromech, Microeng 11 (2001) 382-385.

53 Y. Roig, Doctoral thesis, University of Bordeaux (2011).

54 D. G. Avraam, A. C. Payatakes, Ind. Eng. Chem. Res. 38 (1999) 778-786.

55 L. C. Chang, H. Chen, H. Y. Shan, Environ Geol. 56 (2009) 1437-1447.

56 C. D. Tsakiroglou, M. A. Theodopoulou, V. Karoutsos, AICHE J. 49 (2003) 2472-2486.

57 C. Zhao, A.P.J. Middelberg, Chemical Engineering Science 66 (2011) 1394-1411.

58 J. Bear, D. Zaslavsky, S. Imray, J. of Hydrology 12 (1970) 63.

59 M. Dong, I. Chatzis, Petroleum Science and Technology 28 (2010) 955-968.

60 R. Lenormand, C. Zarcone, A. Sarr, J. of Fluid Mechanics 135 (1983) 337-353.

61 R. Lenormand, C. Zarcone, Soc of Petroleum Engineers of AIME (1984) 13264.

62 D.S. Park, S.B. Mikael, S. King, K.E. Thompson, C.S. Willson, D.E. Nikitopoulos, 16th International Conference on Miniaturized Systems for Chemistry and Life Sciences (2012).

63 C. Chevalier, M. B. Amar, D. Bonn, A. Lindner, J. Fluid Mech. 552 (2006) 83-97.

64 R. Lenormand, E. Touboul, C. Zarcone, J. Fluid Mech. 189 (1988) 165-187.

65 M. Ferer, C. Ji, G. S. Bromhal, J. Cook, G. Ahmadi, D. H. Smith, Phys. Rev. E 70 (2004) 016303.

66 C. Y. Zhang, C. J. Werth, A. G. Webb, Environ. Sci. Technol. 41 (2007) 3672-3678.

67 R. Toussaint, J. Schmittbuhl, K. J. M°aløy, G. Løvoll, Y. M'eheust, Phys. Rev. E 70 (2004) 026301.

68 C. Zhang, M. Oostrom, T. W. Wietsma, J. W. Grate, M. G. Warner. Energy Fuels 25 (2011) 3493-3505.

Chapter 3

Microfluidic approach for studying CO_2 solubility in Water and Saltwater Using Raman Spectroscopy

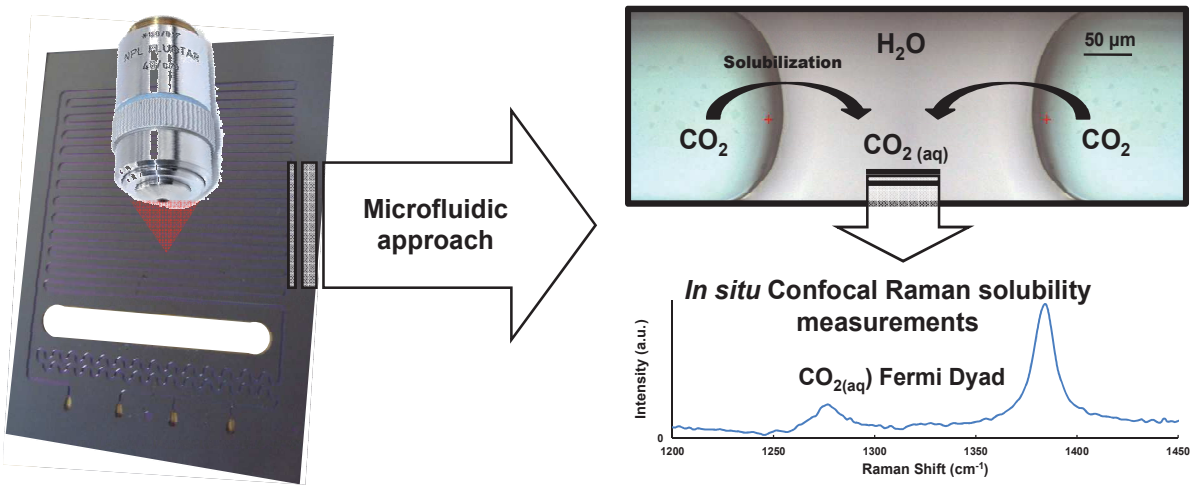

Note to readers:

This work has already been published in Chem. Phys. Lett. (Please see page 157). This chapter gives a larger vision of this work including experimental details.

1. Introduction

The solubility data of CO_2 in H_2O and saltwater in deep saline aquifers (DSA) conditions is necessary to enhance the reliability of numerical simulations for CO_2 storage capacity and sustainable geological storage. The solubility varies as a function of salinity, pressure, and temperature. A number of CO_2 solubility models (CSM) and experimental investigations has been published to describe this relationship in various ranges [1-5]. Experimental methods conducted on CO_2 solubility in pure water have a history of more than one hundred years, since the oldest work was conducted by *Wroblewski* in 1883 [6]. Most of the data are included in the 1996 IUPAC Solubility Series Volume [7]. Since then, many studies have been performed to enlarge the p-T range and improve the accuracy of data (see details in chapter 1).

The CO_2-H_2O mixture with respect to phase equilibrium under Deep Saline Aquifers conditions (the red square on Fig. 3-1) includes four patterns involving CO_2-bearing aqueous solution (Laq), CO_2-rich vapour (V), liquid (LCO_2) and $scCO_2$. At equilibrium point (LCEP), these four patterns coexist. The lower critical end-point (LCEP) of the CO_2-H_2O binary is reported to be slightly higher than the critical point of pure CO_2 from 7.3773 MPa - 30.98 ºC to 7.390 MPa - 31.05 ºC [8], or 7.411 MPa - 31.48 ºC [9]. This phase equilibrium diagram plays an important role on the correction of experimental data and defines the state equations for the solubility models. The p, T conditions of our studies correspond to the black square on Fig. 3-1, which cover most part of DSA area.

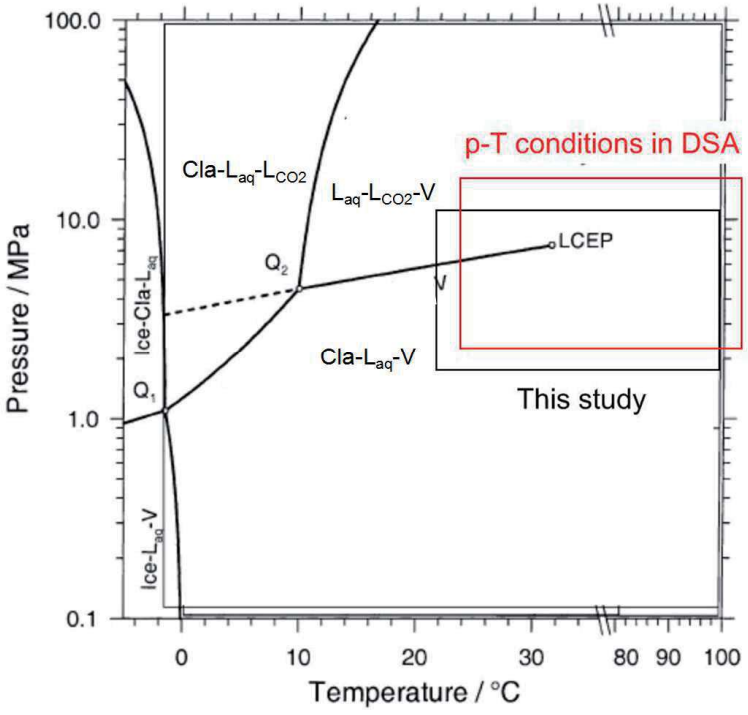

(a)

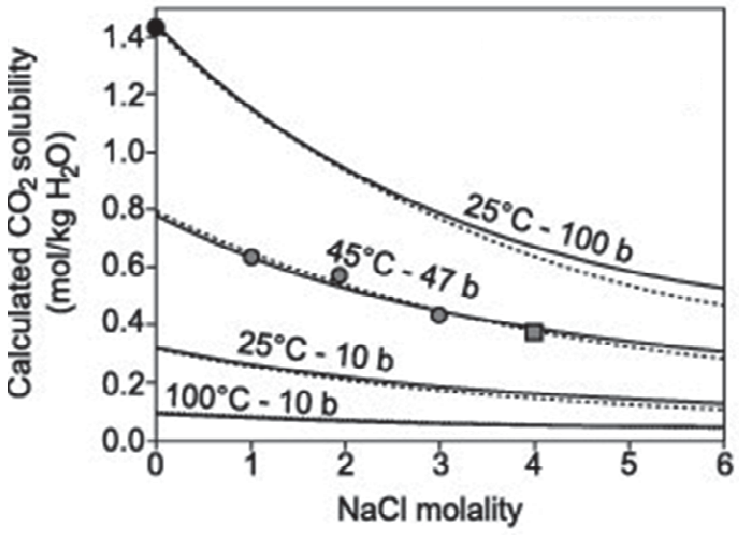

(b)

Fig. 3-1 (a) *Phase diagram of the CO_2-H_2O system in the pressure-temperature region with water stable developed by Diamond and Akinfiev [2]; (b) Solubility of CO_2 as a function of concentration of NaCl [10].*

Various experimental methods have been conducted to measure the CO_2 solubility encountered in DSA. However, these macro scale methods need several hours or days to reach phase equilibria and have limitations in increasing the accuracy of the solubility data. Therefore, it is necessary to introduce a fast and facile approach to reduce the equilibration time and improve the accuracy.

2. Conventional experimental measurements

The conventional methods used to measure the solubility of carbon dioxide in pure water and aqueous solutions usually involved a well-sealed tank containing a known volume of solution and a pump to introduce CO_2 at the appropriate temperature and pressure. After equilibrate for several hours or days, an aliquot is withdrawn from the system. The amount of carbon dioxide dissolved in solution can be analyzed by (i) depressurization [11-15], (ii) titration [16-17], (iii) weighting [18-21] and (iv) Ostwald method [22-23].

(i) Depressurization refers to release the sample to atmospheric pressure and room temperature and use Bunsen absorption coefficient to measure the evolved volume of carbon dioxide.

$$C(aq) = \alpha P \qquad \text{Eq. 3-1}$$

where, C is the solubility of gas, P is the partial pressure of gas. The Bunsen absorption coefficient (α) of a gas in a solution is defined as the volume of gas, reduced to 273.15 K and 101.3 KPa pressure, that dissolves in 1 litre of liquid under the partial pressure of the gas of 1 atm [24].

(ii) In case of titration, a known amount of alkaline fluid is used to neutralize the dissolved carbon dioxide. Then the completely reacted solution is titrated to determine the amount of remaining OH^-.

(iii) Weighting method consists in weight the aliquot and subsequently inject it into the weighted tubes containing CO_2-absorbing components and Carbosorb. The tubes and the aliquot are eventually re-weighted. The weight loss of the aliquot gives the mass of carbon dioxide dissolved in a certain mass of water.

(iv) Ostwald method is a well know fast and accurate approach for measuring the gas solubility in liquid. The principle of the Ostwald method consists in contacting a gas with a known quantity of liquid. Upon equilibrium, the gas volume variation is measured, allowing back calculating the amount dissolved in the liquid.

3. *In situ* analysis by Raman spectroscopy

White [25] introduced an *in situ* analysis method based on laser Raman spectroscopy to determine carbon dioxide and methane concentrations in water and seawater. An optical cell equipped with a sapphire window is first pressurized with liquid and gas using a high pressure pump and valves system at a certain temperature and pressure condition (see Fig. 3-2 (a)). The Raman spectra of the solution with dissolved gas supported the quantitative and qualitative information of gas concentrations. A ratio between the gas bands to the O-H stretching band of water was proved to be linear to the gas concentration (see Fig. 3-2 (b)). The qualitative analysis from Raman spectra provides a reliable measurement.

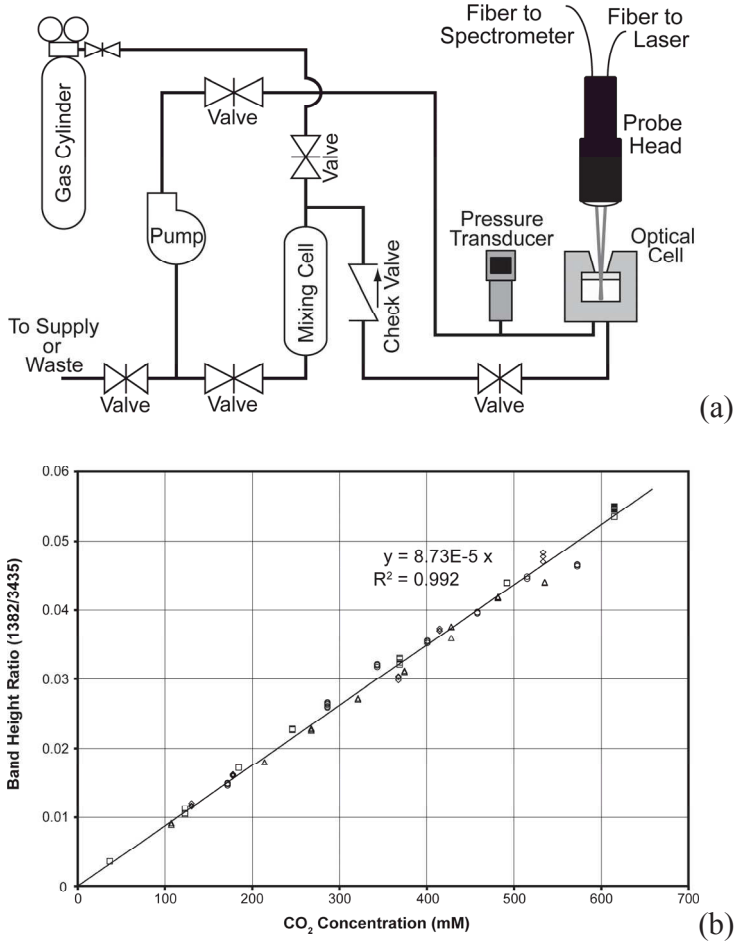

Fig.3-2 *(a) Schematic of optical cell coupled Raman probe for creating and analyzing dissolved gases; (b) Plot of dissolved CO_2 concentration vs. band height ratio at lower pressure and temperature range (from [25]).*

In this study, we first used a stirred stainless steel tank (containing a known volume of water), coupled to a high pressure syringe pump for pressuring the tank with CO_2 to measure the solubility data at high temperature and pressure. The stainless steel tank was immersed in an oil bath to control the temperature, while pressure in the system was determined using the pump's pressure sensor. After injecting CO_2 into the tank at a constant pressure, the system was left 24 h to reach the phase equilibrium. Stirring was used to accelerate the dissolution process. We then

used potentiometric titration to determine CO_2 concentrations. After reaching the phase equilibrium, the valve at the inlet side was closed, while the outlet was opened to let the saturated solution rush into an analysis tank containing a known volume and concentration of an alkaline solution (NaOH). An aliquot was therefore titrated by an HCl solution until neutral. As shown in Fig. 3-3, the results from this method were not in good agreement with the predicted data from the Duan and Sun CO_2 Solubility Model. Although the general trend is correct, a large experimental error is introduced. At this point, we have attributed these to the gradients of temperatures and pressures in the agitation tank, the uncontrolled-depressurization when opening the outlet valve, and the titration.

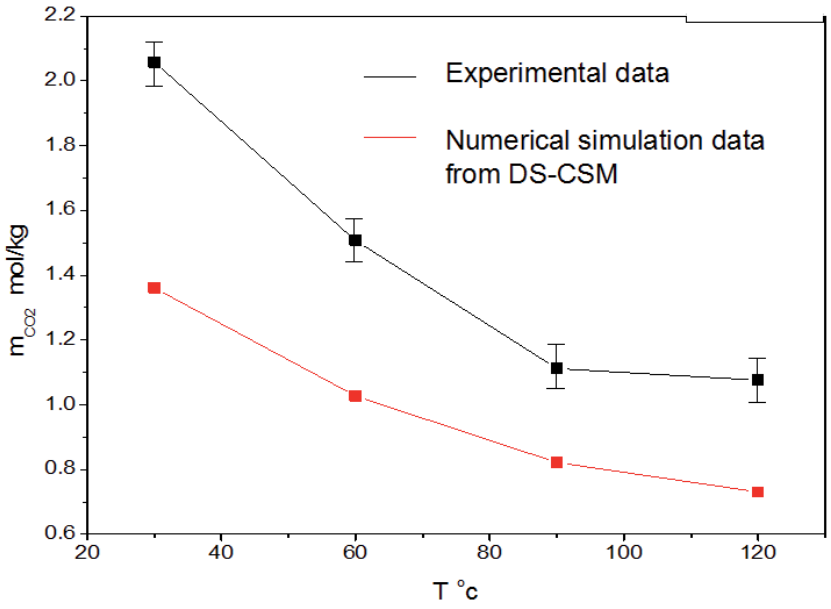

Fig. 3-3 *Comparison between experimental results and CO_2 solubility model from Duan and Sun [29].*

In a word, these macroscale experimental methods generally require fastidious and time-consuming experiments, with large relaxation time (at least 24 h) to reach the phase equilibrium. Additionally there exists difficulties to analyze the alkaline-preserved samples by

potentiometric titration after reacting with base solution, which can introduce non negligible secondary errors. Finally, it is difficult to ensure perfectly homogeneous T and p conditions in the tank. Therefore, there is an increasing need for fast and reproducible methods for determining solubility data related to CO_2 storage in deep saline aquifers, which can be provided by pressurized microfluidic approaches, as discussed in chapter 2 (Fig. 3-4).

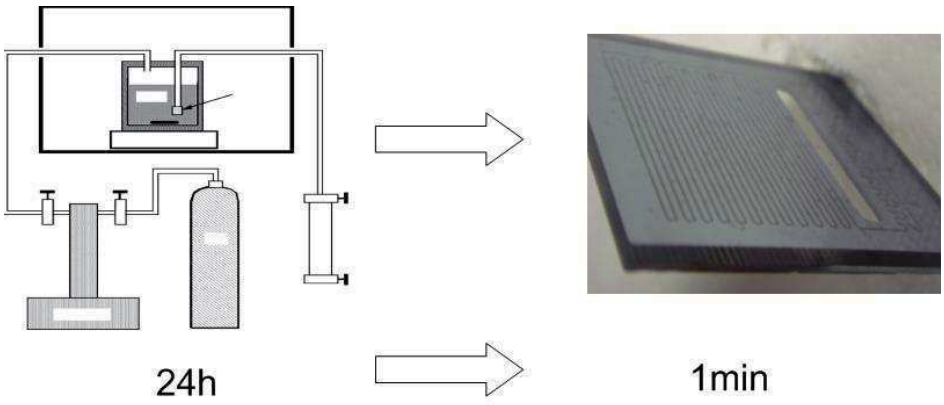

Fig. 3-4 *Strategy envisioned in this work: Replacing the macro scale batch cell by microreactor for faster and more accurate measurement.*

Here, we introduce a novel method for determining the CO_2 solubility in water or saltwater related to CO_2 storage conditions, coupling pressurized microreactors and Raman spectroscopy. Since many published data already exist from modelling, we choose this step as a starting point to test the suitability of microfluidics tools for the CO_2 storage studies.

4. CO_2 solubility models

In the last few decades, several CO_2 solubility models (CSM) have been developed to properly access the solubility of CO_2 in brine solution over a wide range of salinity, temperature and pressure conditions typically encountered in deep saline aquifers (see Table 3-1). Most of CSM are based on equations of state (EOS) by applying correction factors to a modified Henry's law [26-28]:

$$\varphi P = k_H X_{CO2} \qquad \text{Eq. 3-2}$$

where φ is the CO_2 fugacity coefficient, P is the partial pressure of gas above the solution, k_H is the modified Henry's law constant, X is the concentration of CO_2. The modified Henry's coefficient and fugacity coefficient correct the non-ideal behaviors of real solutions with increasing temperature and salinity.

Table 3-1 *CO_2 solubility models and their range of temperature, pressure and salinity.*

Name	Temperature (K)	Pressure (MPa)	Salinity (mol/l)	Salt composition	Ref
PG-CSM	298-623	0-50	0-5	NaCl	[26]
SP-CSM	285-373	0-60	0	Pure water	[27]
McPC-CSM	288-523	0-100	0	Pure water	[28]
DS-CSM	273-533	0-200	0-4.3	Na^+,K^+, Ca^{2+}, Mg^{2+}, Cl^-, and SO_4^{2-}	[1,29]

The four main CSM re detailed hereafter.

PG-CSM:

Pruess and Garcia CSM [26] uses an extended Henry's coefficient dependent on temperature and salinity for calculating solubility of CO_2 in brine. The fugacity coefficient Φ used a correlation expression developed by Spycher and Reed [30]. The equation is given by:

$$X_{CO2} = e^{F(P,T)} p / K_H \qquad \text{Eq. 3-3}$$

$$K_H = B\left(T^5\right) \times 10^{mC\left(T^4\right)} \qquad \text{Eq. 3-4}$$

where X_{CO2} is mole fraction of CO_2, F(p, T) is modified fugacity coefficient, K_H (Pa) is the Henry's coefficient, m is the molal concentration of salts, $B(T^5)$ and $C(T^4)$ are polynomial fit coefficients of temperature.

SP-CSM:

Spycher and Pruess CSM [27] provides the mutual solubility of CO_2 and H_2O in two coexisting phases given by:

$$X_{CO2} = e^{\left(\frac{-(p-p^0)V}{RT}\right)} \frac{\varphi p}{55.51K} \qquad \text{Eq. 3-5}$$

where p_0 is a reference pressure only determined by temperature, K is the equilibrium constant as a polynomial function of temperature. The fugacity coefficient φ is expressed to be a function of T, p, V according to Redlich-Kwong equation of state.

McPC-CSM:

McPherson and Cole CSM [28] is only applicable for the solubility of CO_2 in pure water. At equilibrium, the CO_2 solubility is calculated according to Henry's law:

$$X_{CO2} = \exp(\ln\varphi + \ln p - \ln H - \frac{V^{\infty}}{RT}(p - p_v)) \quad \text{Eq. 3-6}$$

where V^{∞} is the average partial molar volume of the gaseous solute at infinite dilution in the volatile liquid solvent ($m^3 \cdot mol^{-1}$) and P_v is vapor pressure of pure water (Pa).

DS-CSM:

Duan and Sun CSM [1] is based on the balance of between the CO_2 chemical potential in the liquid phase and in the gas phase. At equilibrium:

$$\mu_{CO2}^{aq} = \mu_{CO2}^{g} \quad \text{Eq. 3-7}$$

The EOS developed by *Duan et al* [31,32] is used to represent the chemical potential of CO_2 in the vapour phase. This EOS can be applied in a wide range of temperature and pressure from 0 to 1000 °C and 0 to 800 MPa with remarkable accuracy. The specific interaction model of Pitzer [33] describes the chemical potential in the liquid phase. The final form of the solubility model is:

$$\begin{aligned}\ln m_{co_2} = {} & \ln\varphi_{co_2} y_{co_2} p - \frac{\mu_{co_2}^{l0}(T,p)}{RT} - 2\lambda_{co_2\_Na}(m_{Na} + m_K + 2m_{Ca} + 2m_{Mg}) \\ & - \zeta_{co_2\_Na-Cl}\, m_{Cl}(m_{Na} + m_K + m_{Ca} + m_{Mg}) + 0.07 m_{SO_4}\end{aligned} \quad \text{Eq. 3-8}$$

where m is molality of CO_2 or salts in the liquid phase, T (K) is absolute temperature, p (bar) represents the total pressure of the system, R is universal gas constant = 8.314 $Pa \cdot m^3 \cdot k^{-1} \cdot mol^{-1}$, y_{CO2} is the mole fraction of CO_2 in vapor phase, which can be approximately calculated from the

pure water pressure, p_{H2O}:

$$y_{co_2} = \frac{p - p_{H2O}}{p} \qquad \text{Eq. 3-9}$$

$$p_{H2O} = \frac{p_c T}{T_c}\left[\, 1 + a_1(-t)^{1.9} + a_2 t + a_3 t^2 + a_4 t^3 + a_5 t^4 \right] \qquad \text{Eq. 3-10}$$

where $t = (T-T_c)/T_c$, T_c and p_c are the critical temperature and critical pressure of water (T_c = 647.29 K, p_c = 22.085 MPa), respectively and the a_i are the dimensionless coefficient parameters determined by an empirical model. These are listed in Table 3-2.

Table 3-2 *Dimensionless coefficient parameters from [1].*

a_1	a_2	a_3	a_4	a_5
-38.640844	5.8948420	59.876516	26.654627	10.637097

φ_{CO2} is the fugacity coefficient, which depends on temperature and pressure given by *Duan et al.* [31]:

$$\begin{aligned} \ln\varphi(T,p) = Z - 1 - \ln Z &+ \frac{b_1 + b_2/T_r^2 + b_3/T_r^3}{V_r} + \frac{b_4 + b_5/T_r^2 + b_6/T_r^3}{2V_r^2} \\ &+ \frac{b_7 + b_8/T_r^2 + b_9/T_r^3}{4V_r^4} + \frac{b_{10} + b_{11}/T_r^2 + b_{12}/T_r^3}{5V_r^5} \\ &+ \frac{b_{13}}{2T_r^3 b_{15}}\left[b_{14} + 1 - \left(b_{14} + 1 + \frac{b_{15}}{V_r^2} \right) \exp\left(-\frac{b_{15}}{V_r^2} \right) \right] \end{aligned} \qquad \text{Eq. 3-11}$$

where,

$$Z = \frac{p_r V_r}{T_r} = 1 + \frac{b_1 + b_2 / T_r^2 + b_3 / T_r^3}{V_r} + \frac{b_4 + b_5 / T_r^2 + b_6 / T_r^3}{V_r^2} + \frac{b_7 + b_8 / T_r^2 + b_9 / T_r^3}{V_r^4} + \frac{b_{10} + b_{11} / T_r^2 + b_{12} / T_r^3}{V_r^5} + \frac{b_{13}}{T_r^3 V_r^2}\left(b_{14} + \frac{b_{15}}{V_r^2}\right)\exp\left(-\frac{b_{15}}{V_r^2}\right) \quad \text{Eq. 3-12}$$

where, $p_r = p / p_c$, $T_r = T / T_c$, $V_r = VP_c / RT_c$. At a given pressure and temperature, p_r and T_r are obtained. V_r is computed iteratively using equation of Z. The "bi" series parameters are listed in Table 3-3.

Table 3-3 *Parameter coefficients for the above equations from [32].*

b1	8.99288497e-2	b9	-1.77265112e-3
b2	-4.94783127e-1	b10	-2.51101973e-5
b3	4.77922245e-2	b11	8.93353441e-5
b4	1.03808883e-2	b12	7.88998563e-5
b5	-2.82516861e-2	b13	-1.66727022e-2
b6	9.49887563e-2	b14	1.39800000
b7	5.20600880e-4	b15	2.96000000e-2
b8	-2.93540971e-4		

μ^0, λ and ξ are the interaction parameters, which can obtained by empirical equations only depending on temperature and total pressure [33]:

$$\mu_{CO2}^{l0} / RT = 28.9447706 - 0.0354581768\mathrm{T} - 4770.67077/\mathrm{T} + 1.02782768 \cdot 10^{-5}\mathrm{T}^2 + 33.8126098/(630 - \mathrm{T}) + 9.04037140 \cdot 10^{-3}\mathrm{p} - 1.14934031 \cdot 10^{-3}\mathrm{p}\ln\mathrm{T} - 0.307405726\mathrm{p}/\mathrm{T} - 0.0907301486\,\mathrm{p}/(630 - \mathrm{T}) + 9.32713393 \cdot 10^{-4}\mathrm{p}^2/(630 - \mathrm{T})^2 \quad \text{Eq. 3-13}$$

$$\lambda_{CO2-Na} = -0.411370585 + 6.07632013 \cdot 10^{-4}\,\mathrm{T} + 97.5347708\,/\mathrm{T} + 1.02782768 \cdot 10^{-5}\,\mathrm{T}^2 - 0.0237622469\,\mathrm{p/T} + 0.0170656236\,\mathrm{p}/(630 - \mathrm{T}) + 1.41335834 \cdot 10^{-5}\,T \ln p \qquad \text{Eq. 3-14}$$

$$\xi_{CO2-Na-Cl} = 3.36389723 \cdot 10^{-4} - 1.98298980 \cdot 10^{-5}\,\mathrm{T} + 2.12220830 \cdot 10^{-3}\,\mathrm{p/T} - 5.24873303 \cdot 10^{-3}\,\mathrm{p}/(630 - \mathrm{T}) \qquad \text{Eq. 3-15}$$

Here, the solubility of CO_2 using the DS-CSM can be calculated for a given [p, T, salts molality] system in the liquid phase. A very high accuracy could be obtained from this model in comparison with experimental data from the literature in the temperature range [273-533 K], pressures [0-200 MPa], and ionic strength [0-4.3 M].

Fig 3-5 compares the accuracy of these four CSMs with experimental data. After comparison, the Duan and Sun CSM (DS-CSM) was chosen as the model for calculating the solubility of CO_2 in brine, being by far the most accurate CO_2 solubility model in a wide range of temperature, pressure and salinity, which are typically encountered in real deep saline aquifers. Additionally, it takes into account not only NaCl rich solutions but also divalent cations salts such as $MgCl_2$ and $CaCl_2$.

Once being able to model with precision the CO_2 solubility in water or brine in our experimental conditions, we managed to find a non-invasive and *in situ* measurement method to experimentally determine the CO_2 solubility. Raman spectroscopy turns out to be an outstanding characterization technique for such measurement. We detailed this in the next section.

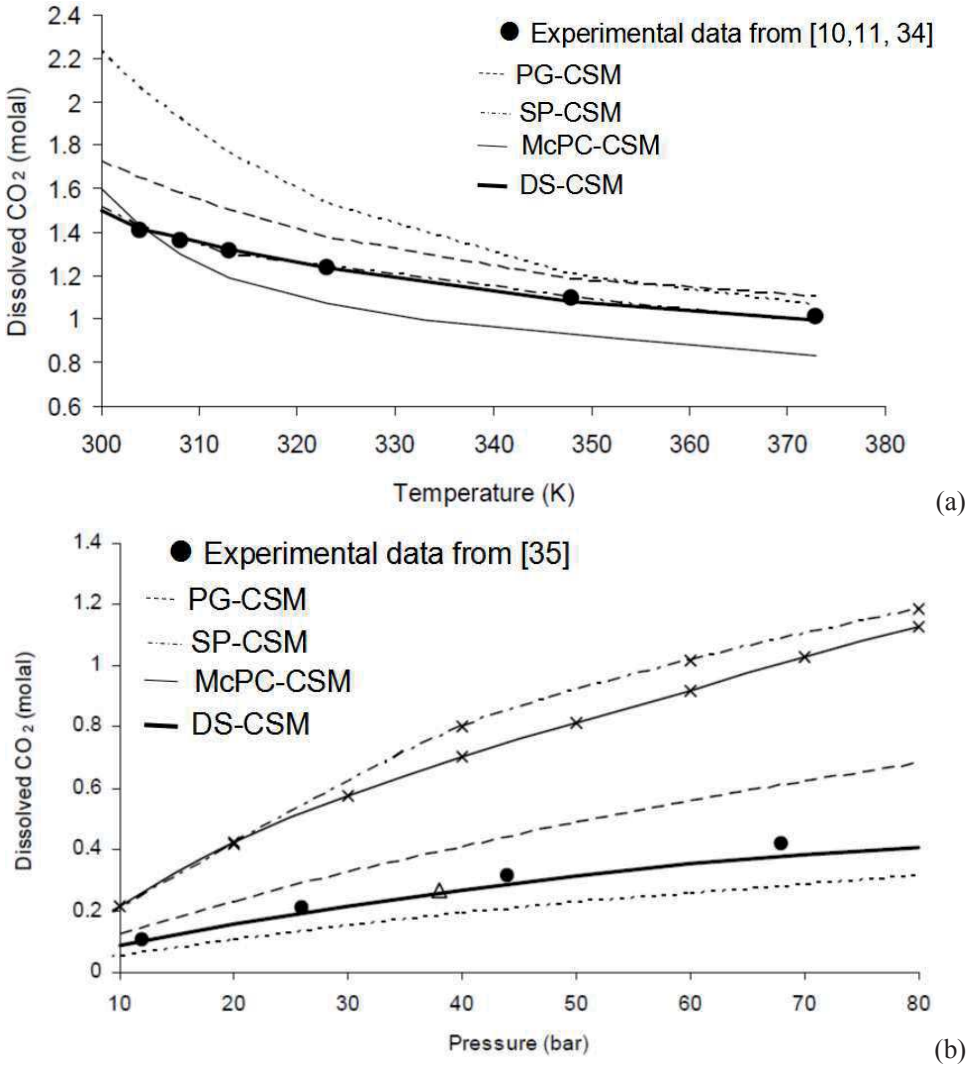

Fig. 3-5 *Comparison of CSMs with experimental data extracted from Zerai [34]: (a) as a function of temperature (P = 7.6 MPa) in pure water from Wiebe and Gaddy [11-121] and King et al. [35], and (b) as a function of pressure (at T = 313 K) in 4 mol of NaCl solution from Rumpf et al [36].*

5. Raman spectroscopy

Raman spectroscopy is a well-known non-destructive and non-invasive technique, which characterizes the vibrational, rotational, and low-frequency modes for identifying unknowns, solving materials/chemical problems and characterizing structural changes. This *in situ* spectroscopic analysis technique has recently gained increasing interest for studies in extreme environments, such as deep-sea hydrothermal vent environments or CO_2 geological storage. *Brewer et al*. have applied it for *in situ* measurements of gases, solids, clathrate hydrates, and biomolecules in the deep ocean [37]. In the last few years, Raman spectroscopy has also been widely used in CO_2 geological experiments to measure the CO_2 dissolution rate [25] and to identify the aragonite and calcite phases of $CaCO_3$ in mineral precipitations [38]. Lastly, some works have shown that confocal Raman spectroscopy offers a powerful alternative method for quantitatively monitoring the solubility of gases such as CO_2 or CH_4 in aqueous solution in a wide range of pressures and temperatures, as demonstrated in large scale high pressure cells [24].

Although Raman signals depend on several experimental factors, peaks ratio can be used to determine relative concentrations, which technique was previously reported [39-40]. The intensity of Raman scattering can be written in simple form as:

$$I_R = (I_L \eta \sigma) PC \qquad \text{Eq. 3-16}$$

where I_R is the measured Raman intensity, I_L is the laser intensity, η includes instrument parameters such as optical transmission and collection efficiency, σ is the Raman cross–section or scattering efficiency, P is the sample path length, and C is the concentration. For a mixture [A+B], we therefore have:

$$\frac{C_A}{C_B} = \frac{I_A \sigma_B \eta_B}{I_B \sigma_A \eta_A} = \frac{I_A}{I_B} \frac{F_B}{F_A} \qquad \text{Eq. 3-17}$$

where F_i (i = A, B) is defined as the "Raman quantification factor", which only depends on the Raman instrument. From this equation, it is obvious that the concentration ratio in the solution corresponds to the ratio of peaks intensities, which offers the theoretical basis of quantitative *in situ* analysis by Raman spectra. In our case, we will consider CO_2 and water as A and B.

5.1 Instrumentation

The laboratory instrumentation used for this work is a Thermo Scientific DXR Raman Microscope, which consist of dispersive Raman spectrometer and a confocal microscope with three lasers: 532 nm solid state laser, 633 nm He-Ne gas laser, and 780 nm solid state laser (Fig. 3-6). Confocal microscopy has a much smaller background and higher resolution than conventional ones. Thus, the confocal Raman spectroscopy could provide both the complete Raman spectrum at every image pixel and high resolution images for displaying the spectra with exceptional sensitivity and spatial resolution for working applications. The DXR Raman microscope allows taking data quickly and extracting the relevant information (peak intensity, width, position etc.) from the OMNIC software.

Here, Full–Range Grating with 532 nm wavelength excitation laser at 10 mW output power are chosen as the operating parameters. The Effective Focal Length is 18.2 mm and spectral resolution is 0.3 cm^{-1}. In order to obtain a less noise spectrum each time, we set the exposure time as 60 s and collect twice for one point. The Raman peaks intensities are directly obtained from OMNIC and Origin software to calculate the relation between the Raman bands intensity ratio (I_{CO2} / I_{H2O}) as a function of the solubility of CO_2 in water or brine.

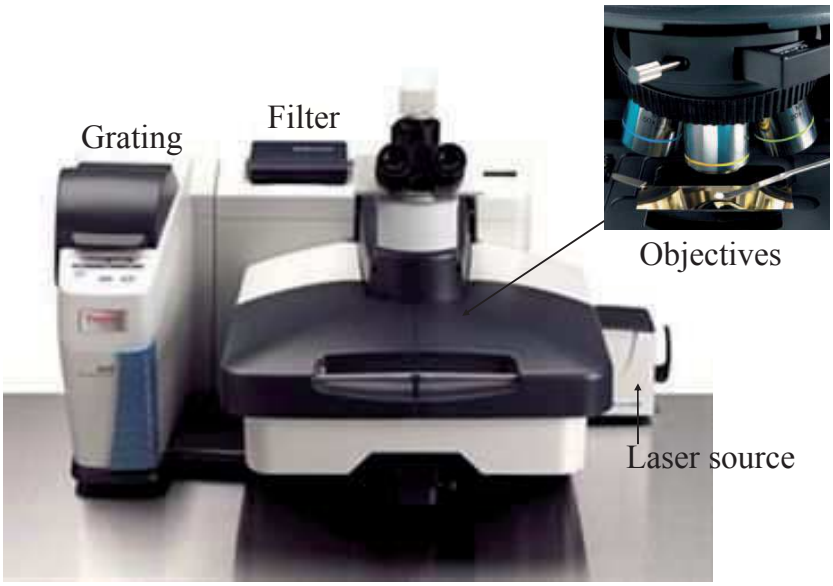

Fig. 3-6 *Image of Thermo Scientific DXR Raman microscope.*

5.2 Raman spectra of aqueous phase

The spectrum of pure water consist of the H-O-H bending band at ～1600 cm^{-1} and the O-H stretching bands in the 3300-3500 cm^{-1} region. Fig. 3-7 is a spectra of pure water obtained from the DXR Spectrometer coupled to a Si/Pyrex microreactor containing water at 35 ºC and 3 MPa. It can be seen that the peak intensity of O-H stretching bands is more pronounced than the H-O-H bending band (due to the limitation of the instrument, only part of the O-H stretching bands can be obtained in this work). Thus, for the purpose of this work, we only considered the O-H stretching band to characterize the aqueous phase. However, temperature and pressure can slightly affect both the O-H stretching band position and intensity.

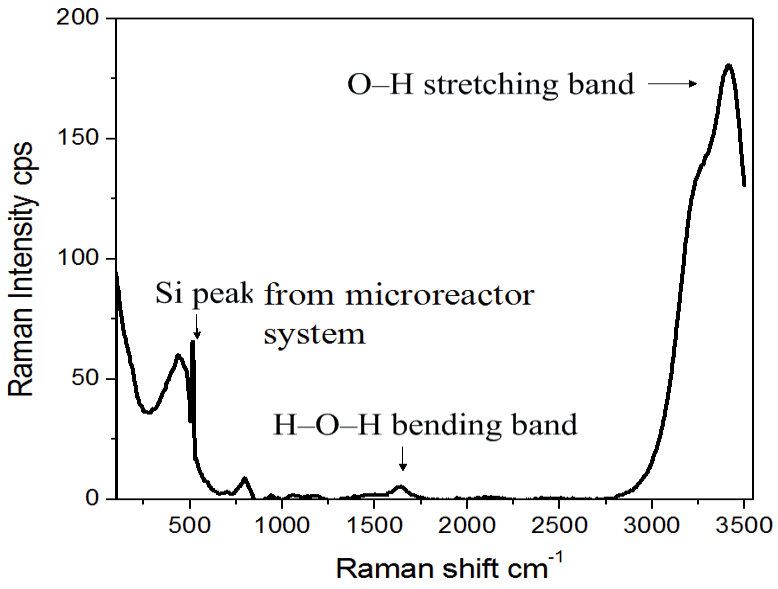

Fig. 3-7 *Raman spectra of pure water in a Silicon/Pyrex microreactor at 35°C and 3 MPa.*

First, pressure has little effect on the Raman spectrum of water. Raman spectra were collected from DI water at pressures of 3 to 10 MPa, while temperature was maintained at 35 °C. The laser power setting and exposure time were constant. There were little changes to be found in this range of band positions and band heights (Fig. 3-8 (a)). The typical intensity variation was less than 1%.

Then, temperature exhibits a small effect on the Raman spectrum of water. Pressure was held constant at 6.6 MPa and temperature ranges from 30 to 100 °C. As seen in Fig. 3-8 (b), the bands in the O–H stretching region show somewhat greater variation with temperature than with pressure. The O–H bands positions shift to the higher Raman shift and decrease slightly in intensity (2.4 %) with increasing temperature.

Finally, spectra were collected for salted water with a salinity of 1 M and 2 M (NaCl in the DI water) and compared with the DI water spectrum. The O-H stretching band of higher salinity

water is much sharper than for lower salinity water (Fig. 3-8 (c)). There is a small effect on band positions, which were found to be slightly shifted. However, the effect on band height and area could not be definitively determined; it does not appear to be significant. In addition to the slight band position changes, the relative intensity of the O-H stretching band decreases a little with increasing salinity.

As the measurement errors for the Raman spectra (≤ 1%), there is barely change of the relative intensity of the O-H stretching band in the operating conditions, both pure water and in salted water cases, which well corresponds to the previous works [25,41]. Thus, the maximum height of the OH–stretching band can apparently serve as a reference for quantitative Raman analysis in the range [22 ºC < T < 100 °C] and [1 < P < 10 MPa].

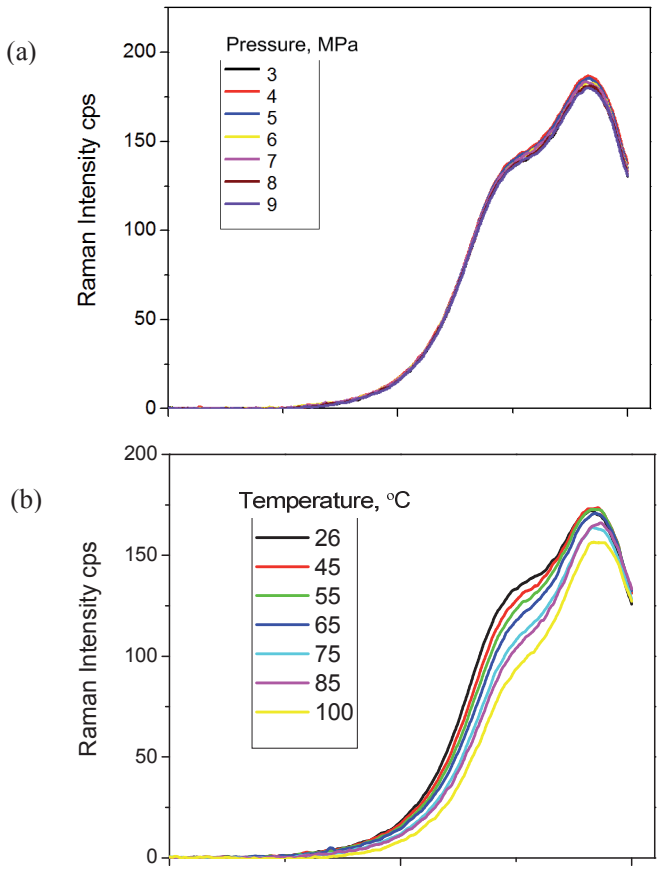

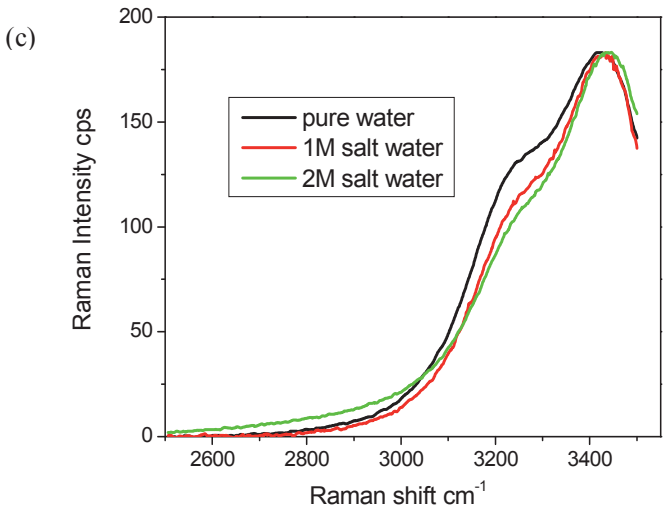

Fig. 3-8 *(a) Raman spectra of water in the O–H stretching region at 35 °C for different pressures; (b) Raman spectra of DI water at 6.6 MPa and different temperatures from 26 to 100 °C; (c) Raman spectra of DI water, 1 M and 2 M salted water at 3 MPa and 40 °C.*

5.3 Raman spectra of pure CO_2

Raman spectra of carbon dioxide (CO_2) is mainly characterized by two main narrow peaks at ~1280 cm^{-1} from the bending mode (ν_l) and ~1385 cm^{-1} (ν_u) from the symmetric stretching mode which are split by the Fermi resonance (Fig 3-9).

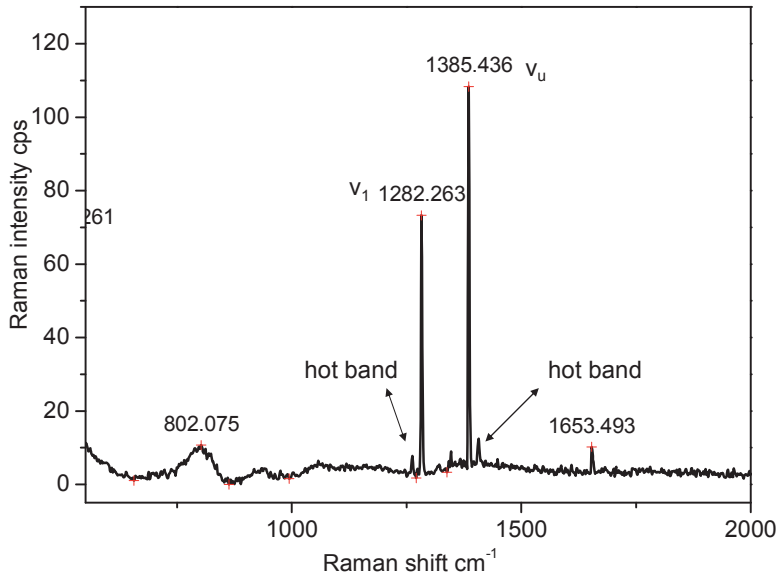

Fig. 3-9 *Raman spectra of pure CO_2 at 8MPa and 30 ºC.*

Raman spectra of CO_2 contain useful information for characterizing its density (see Fig. 3-10). Raman spectra of pure CO_2 was measured at 35 °C in the pressure range from 3 to 10 MPa and at 6.6 MPa in the temperature range from 26 to 100 °C, to examine the dependence of ν_l and ν_u bands on density. The intensities of both the two Fermi bands increase with an increasing pressure and decreasing temperature (Fig. 3-10 (a) and (b)).

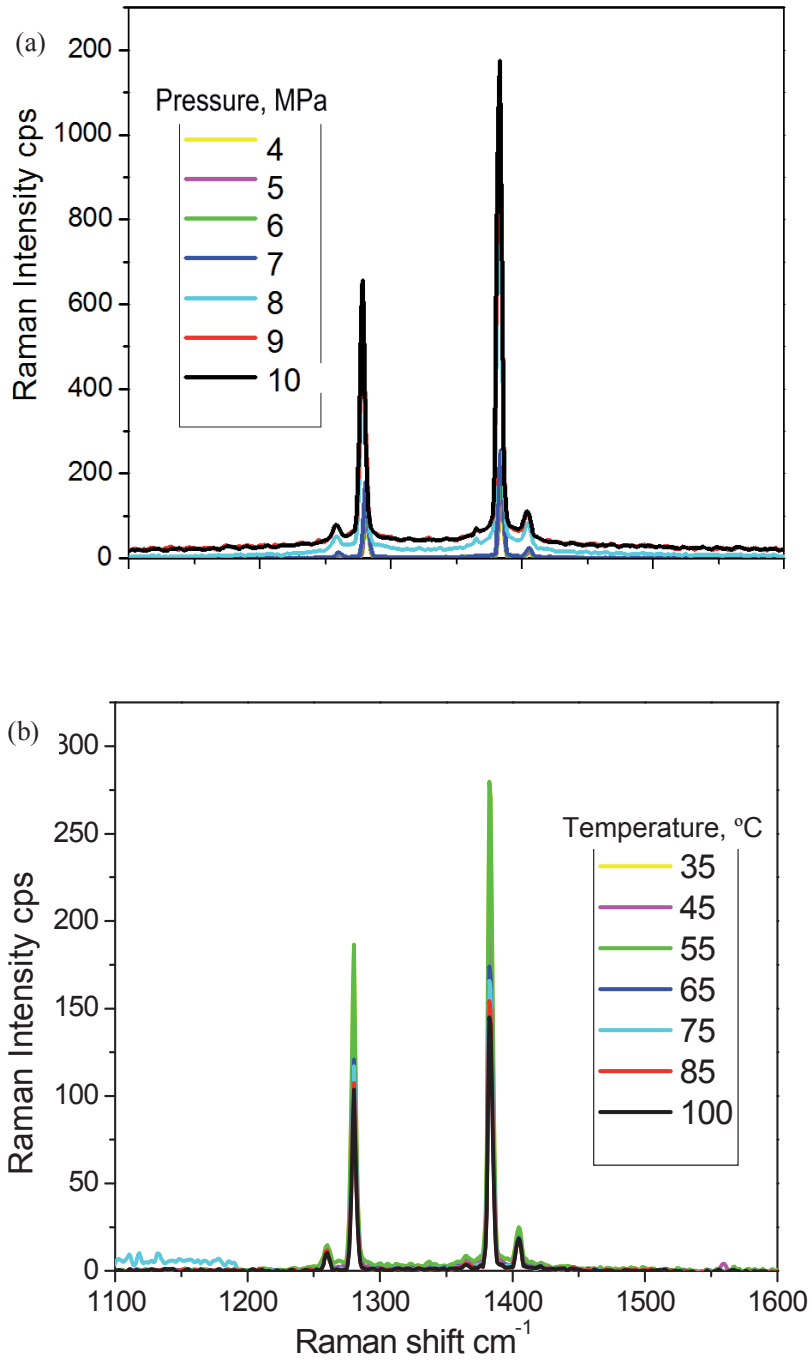

Fig. 3-10 *(a) Raman spectra of CO_2 measured at 35 °C from 4 to 10 MPa and (b) Raman spectra of CO_2 measured at 6.6 MPa from 35 to 100 °C.*

In addition to intensity, the positions of two Fermi bands (v_1 and v_u) and the distance between two Fermi bands (Delta) are also pressure dependent. In particular, the link between the Delta value and density (pressure) of CO_2 has been demonstrated to fit to a 3rd degree expression in the lower density [42]:

$$\rho = -0.01917\ (\Delta - 100)^3 + 0.1984\ (\Delta - 100)^2 - 0.2410\ (\Delta - 100) - 0.341 \qquad \text{Eq. 3-18}$$

$\Delta = f(\rho)$ is plot in Fig. 3-11. The Delta value increases concomitantly with pressure, which well corresponds to the extended expression between the density and Delta value at low CO_2 density from the literature.

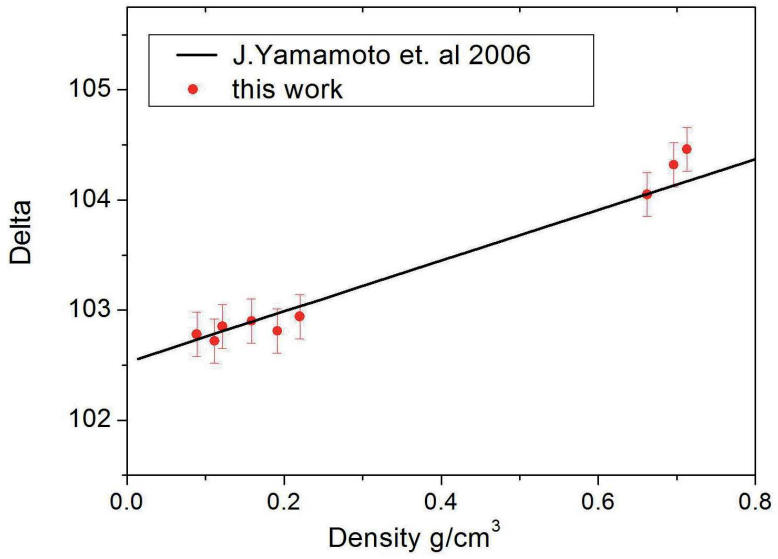

Fig. 3-11 *Plots of Delta vs. CO_2 density.*

Additionally, the v_1 and v_u bands of CO_2 shift linearly to the lower wavenumbers with

increasing density (Fig. 3-12). Our results are consistent with those reported previously and indicate that our experimental method is effective [43-44].

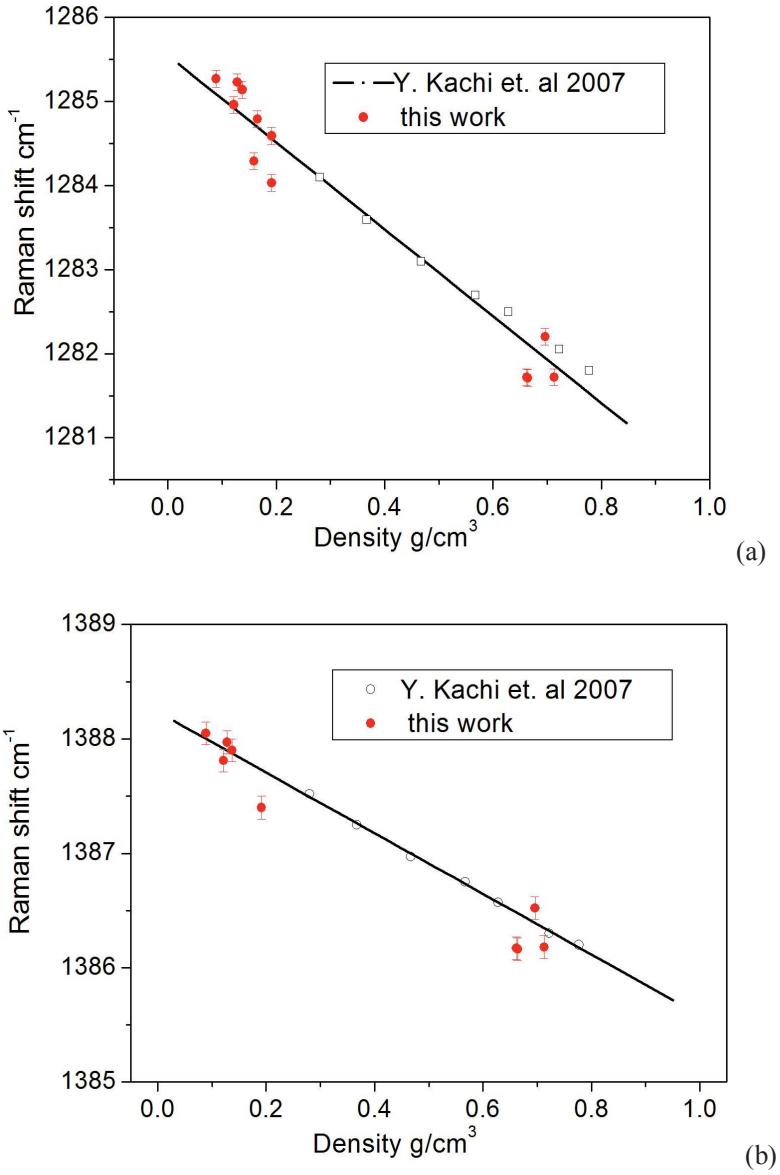

Fig. 3-12 *(a) CO_2 v_1 band Raman shift and (b) CO_2 v_u band Raman shift as a function of density.*

We used the density effect on the Raman spectra of the CO_2 Fermi dyad to confirm the

calibration of our experimental set-up. The calibration was also verified using the ~ 520 cm^{-1} silicon band from the microreactor itself as a reference in the Raman spectrum position.

5.4 Raman spectra of CO_2 in water

When CO_2 dissolved in water, the spectral features of CO_2 (aq) are somewhat different from the pure CO_2 bands (Fig. 3-13). First, both Fermi dyad bands shift to lower wavenumbers positions, like ν_u from ~ 1384 cm^{-1} of pure CO_2 to ~ 1378 cm^{-1} of CO_2 (aq). While the distance of two Fermi dyad bands are broadened ($\Delta \geq 106$ cm^{-1}). Next, the band intensity ratio (I_{vu} / I_{v1}) increases. Hot bands asides both Fermi dyad bands (see Fig. 3-9) are flattened in the aqueous phase.

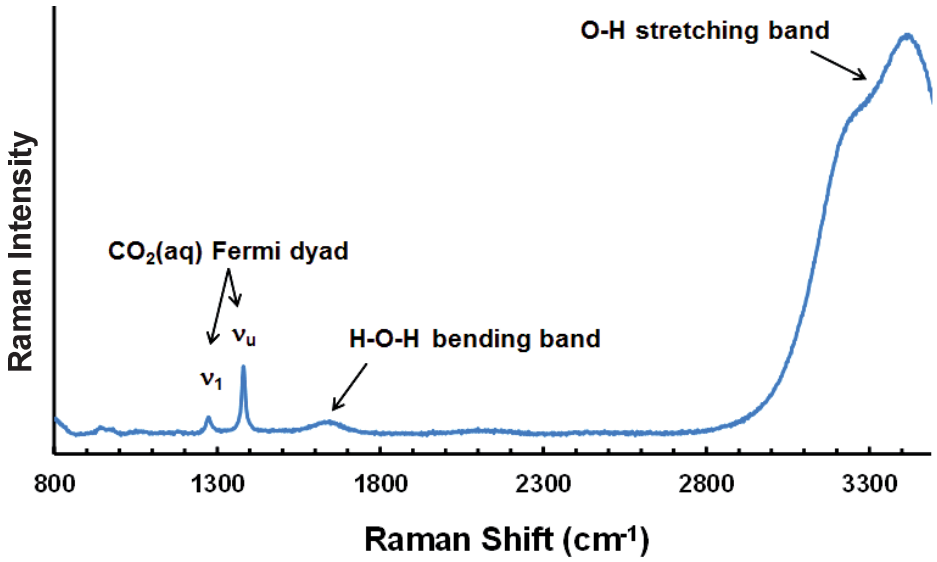

Fig. 3-13 *Raman spectroscopy of CO_2 dissolved in water.*

The general strategy employed in this study consists in taking Raman spectra of the aqueous

phase containing dissolved CO_2 and to use the intensity ratio of the CO_2 (aq) upper band height at ~ 1385 cm^{-1} over the water band height at ~ 3430 cm^{-1} for extracting quantitative information, independently from the equipment (the water band serving as reference). In this study, H_2O band intensity height was chosen for determining calibration curves as it is barely affected by salinity, temperature and pressure (see § 5.2).

6. Experimental Procedure

This section aims at describing the experimental procedure developed for the study of CO_2 solubility in water and saltwater within supercritical microreactors. We used silicon/Pyrex microreactors for injecting fluid under high pressure (up to 20 MPa), which were presented in Chapter 2. The silicon/Pyrex microreactors consist in a 1 m long microchannel (200 µm wide, 100 µm deep) and were fabricated using standard lithography/wet etching techniques. The general set-up for this study is shown in Fig. 3-14.

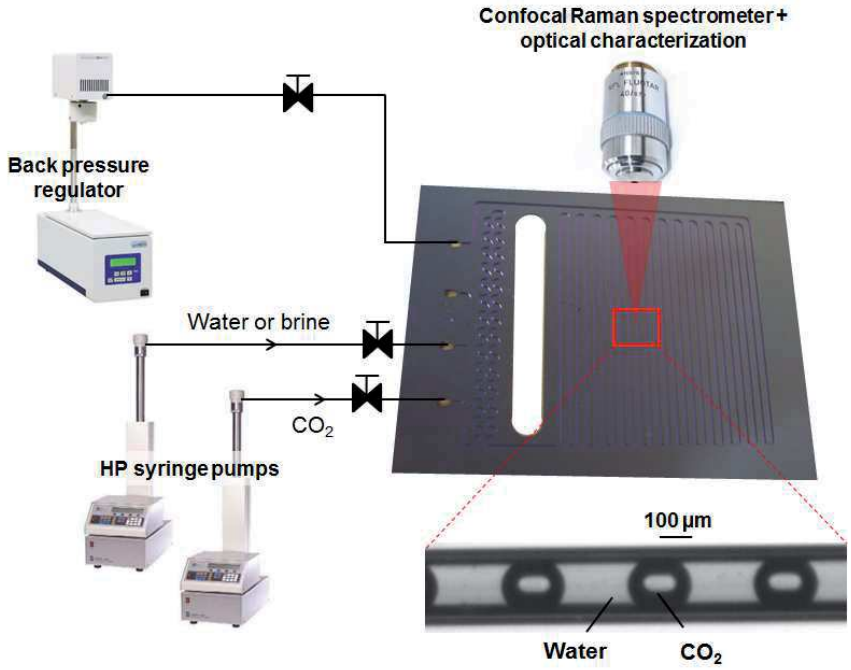

Fig. 3-14 *Scheme of the experimental set-up including silicon microreactor, heater, high pressure pumps, back pressure regulator and confocal Raman spectrometer.*

6.1 CO_2/water segmented flow in microchannels

Two high pressure syringe pumps (ISCO 100DM) continuously inject aqueous solution and CO_2 within the microreactor. CO_2 and brine meet at a T-junction generating a CO_2-water segmented flow, as previously reported (see chapter 2). The pressure is controlled by a back pressure regulator (Jasco BP2080) placed downstream the microsystem, while a heating element contacting the microreactor achieves the proper temperature conditions within the microchannel. Additional HP valves allow for working either in continuous or stop-flow mode.

After the formation of the CO_2/water segmented flow in the chosen conditions, the valves are closed; immobilizing the segmented flow and the system is left in conditions during 10 min to

reach the phase equilibrium before any spectrum is taken from the continuous aqueous phase or the CO_2 slugs (Fig. 3-15).

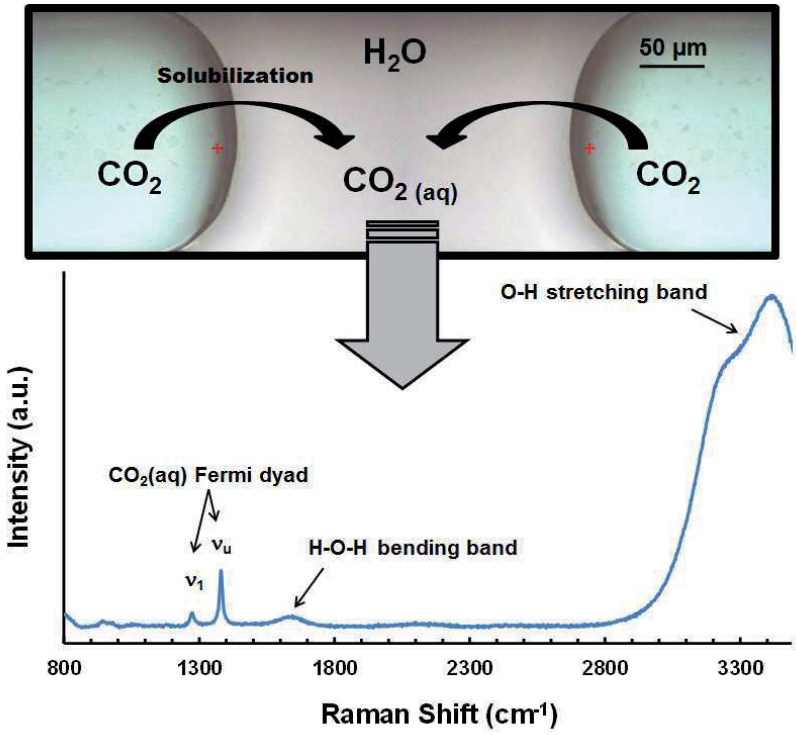

Fig. 3-15 *Optical image of a CO_2/water segmented flow inside a microchannel and corresponding confocal Raman spectra within a water slug containing dissolved CO_2.*

6.2 Carbon species

When CO_2 dissolved in water, three species can coexist in the solution, CO_2(aq), HCO_3^-, and CO_3^{2-}:

$$CO_2 + H_2O \Rightarrow H_2CO_3 \overset{pKa=6.3}{\leftrightarrow} H^+ + HCO_3^- \overset{pKa=10.33}{\leftrightarrow} 2H^+ + CO_3^{2-}$$

However, given our pH conditions both upstream (pH = 5) and downstream the microreactor (pH = 3) and the pKa of both CO_2 / HCO_3^- (pKa = 6.3) and HCO_3^- / CO_3^{2-} (pKa = 10.33) equilibria, we can reasonably assume that CO_2(aq) is the main carbonate specie in the aqueous phase (see Fig 3-16). Therefore, only CO_2(aq) is considered in this study since the concentrations of the other carbonate species (HCO_3^- and CO_3^{2-}) are in too low concentrations to be detected with the Raman spectrometer in either water or in brine.

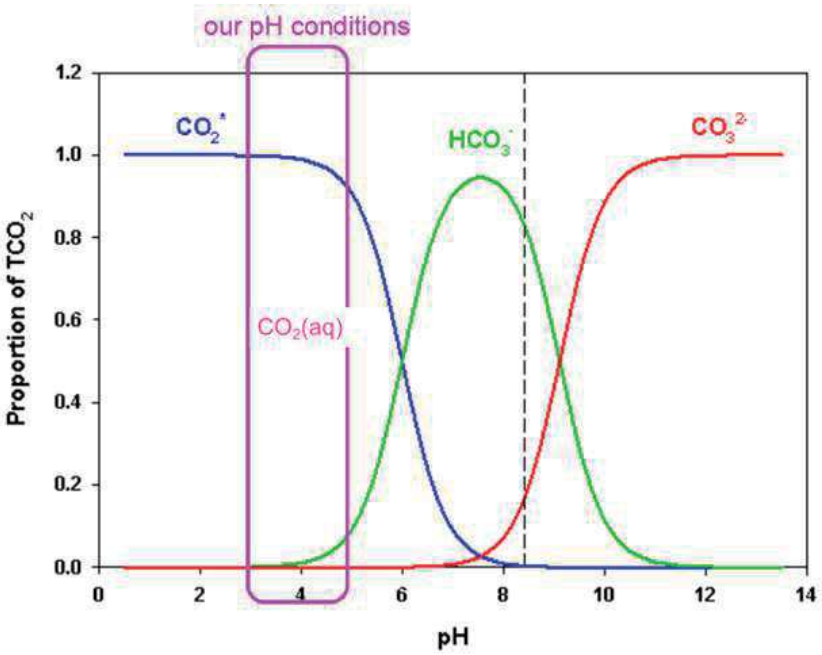

Fig. 3-16 *pH diagram of CO_2-H_2O system.*

6.3 Equilibrium time

The fast heat and mass transfers provided by microreactors allows for easily reaching the phase equilibrium in the microchannel within a short period of time. Indeed, the mass diffusion time in the microreactor can be estimated as:

$$t_D \sim x^2/2D \qquad \text{Eq. 3-19}$$

with $D = \frac{k_B T}{6\pi\eta a}$ from the Stokes-Einstein equation, x the characteristic length (typically the average half-distance between two CO_2 slugs) and D the diffusion coefficient of CO_2 in the considered aqueous phase. Considering x = 200 µm and approximating D to the Stokes-Einstein diffusion coefficient of the CO_2 Brownian motion in pure water (with $k_B = 1.38\times10^{-23}$ $J\cdot K^{-1}$, the Boltzman constant, T = 323 K (50 °C) the temperature, η = 1 mPa·s the water viscosity and a = 3 Å the typical size of a CO_2 molecule), we obtain $D = 0.8.10^{-9}$ $m^2\cdot s^{-1}$, giving $t_D \sim 25$ s, which is much less than the experimental lag time of 10 min. To confirm these theoretical considerations, additional experiments over the DI water / CO_2 system were run to get insights in the time required to reach equilibrium in our conditions inside a microchannel.

Raman spectra of the aqueous phase were taken at various time from t = 1 min to t = 45 min after CO_2 and water were contacted (assimilated to t = 0 min). As shown in Fig. 3-17, the variation of the CO_2 ν_u band intensity at $\sim$ 1385 cm^{-1} in the time range investigated (from 1 min to 45 min) is negligible (less than 2.5 %, which can be attributed to experimental error). This observation therefore demonstrates that equilibrium is reached in less than 1 min using the microfluidic approach.

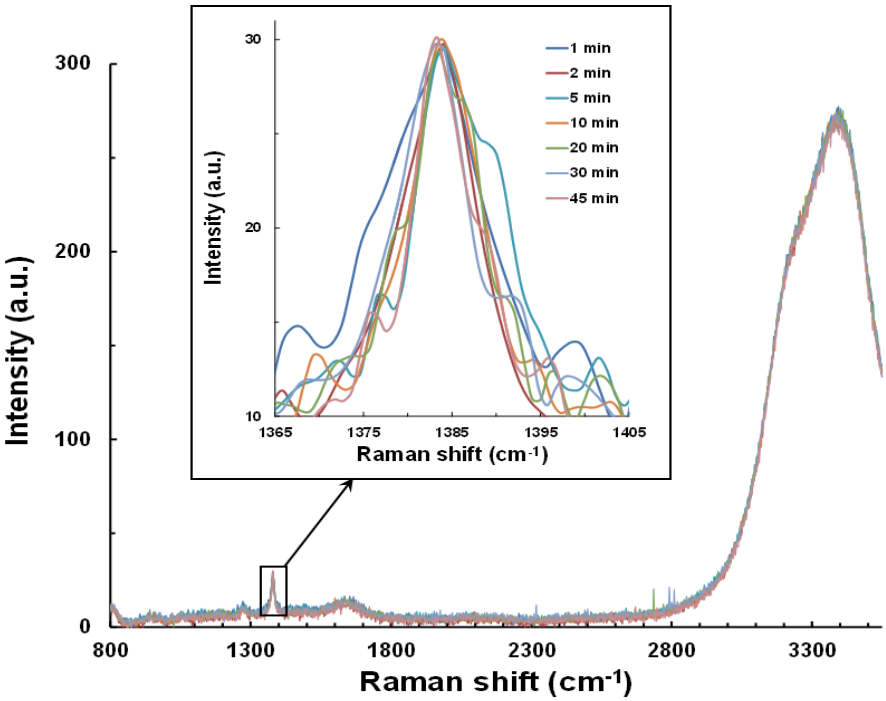

Fig. 3-17 *Raman spectra of CO_2(aq) in DI water from 1 min to 1 hour.*

This is one of the undeniable advantage of this method compared to macro scale measurement tools, for which equilibrium time of several hours is required. After 10 min waiting time, the spectra of both liquid phase and CO_2 droplets were taken for the calculation of the relationship of intensity ratio and CO_2 solubility.

7. Relationship between intensity ratio (I_{CO2} / I_{H2O}) and solubility

In order to link the measurements from Raman spectra and the CO_2 solubility, we first modeled the solubility data relating to experimental conditions using the DS-CSM. Then, the intensities of the CO_2 fermi dyad band ν_u and the O-H stretching band were extracted from the experiments spectra. The relationship between intensity ratio I_r and CO_2 solubility are presented hereafter.

7.1 Results

Four sets of experiments were run with CO_2 dissolved in: (i) DI water (temperature from 22 to 100 °C, pressure from 1.1 to 7 MPa), (ii) 1 M (NaCl) salted water (temperature from 30 to 100 °C, pressure from 3 to 10 MPa), (iii) 2 M (NaCl) salted water (temperature from 30 to 100 °C, pressure 4 to 6 MPa) and (iv) 3 M (NaCl) salted water (temperature from 35 to 55 °C, pressure 7 to 9.5 MPa).

The band heights ratio (named I_r) of the CO_2 ν_u band (～ 1385 cm^{-1}) to the O-H stretching band (～ 3430 cm^{-1}) versus the calculated CO_2 solubility (S) in aqueous media was plotted in Fig. 3-18 for both CO_2/DI water and CO_2/1 M, 2 M and 3 M NaCl saltwater systems. This curve is critical in the determination of the solubility of CO_2 in aqueous media by Raman spectroscopy, since it gives the relation between the actual experimental data and the real solubility values. It can be noticed that the data – both in DI or salted water – can be reasonably linearly fitted in the low CO_2 solubility area (for $S < 0.007$ mol/mol of water, $R = 0.99$), in accordance with previous

reported works [25].

However, for higher CO_2 solubility, generally encountered at higher CO_2 densities (not investigated in previous studies), we found out that it is necessary to correct the linear fit with a quadratic and third-order term varying depending on the salinity. For instance, for the CO_2 / DI water system, the best fit is: $I_r = 9.05\times S-17\times S^2-0.65.10^3\times S^3$, while for CO_2 / 1M, 2M and 3M NaCl water, it turns out to be: $I_r = 9.05\times S-29\times S^2-2.3.10^3\times S^3$, $I_r = 9.05\times S-36\times S^2-7.3.10^3\times S^3$ and $I_r = 9.05\times S-45\times S^2-10.5.10^3\times S^3$, respectively. Note that in the two latter (2M and 3M salted water), it is difficult to access high solubility values for CO_2 (see Fig. 3-18).

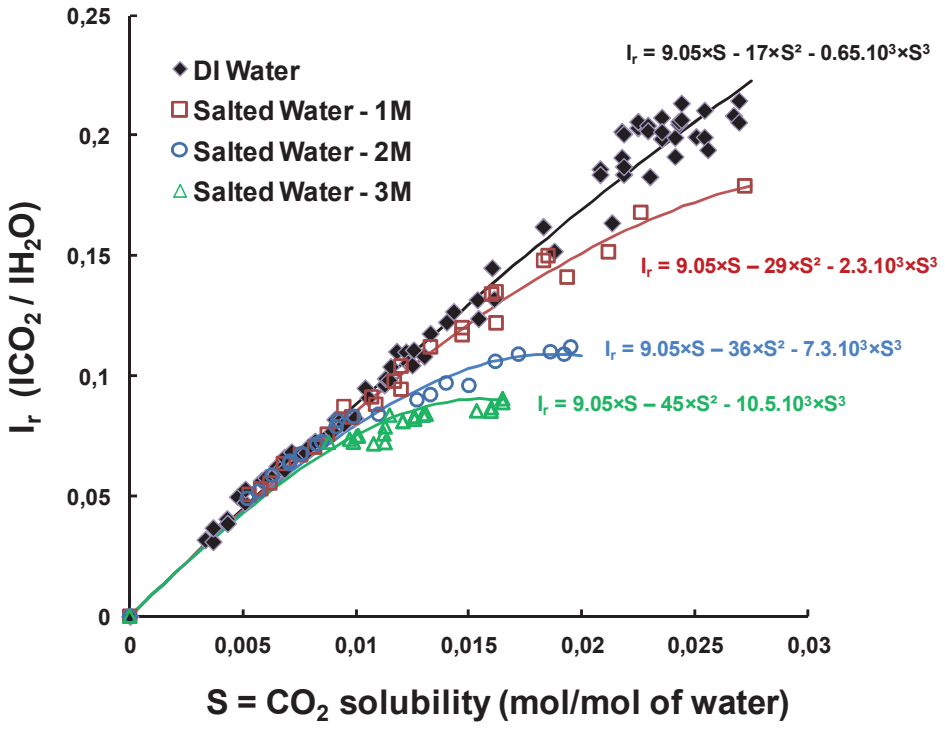

Fig. 3-18 *Plots of CO_2 and water Raman bands intensity ratio ($I_r = I_{CO2}$ (~1385 cm^{-1}) / I_{H2O} (~3430 cm^{-1})) for CO_2(aq) in DI water and salted water (NaCl, 1M, 2M and 3M) vs. CO_2 solubility (S) obtained through the DS-CSM model.*

7.2 Effects on non-linearity at high CO_2 density

In all cases, the non-linearity between the Raman intensity ratio and the CO_2 solubility at high CO_2 densities can find physical explanation in the steric hindrance created by the increasing concentration of CO_2 or salts in the aqueous media.

First, we can mention that the significant changes of the gas-to-liquid Fermi dyad of a space-constrained CO_2 molecule directly reflects the molecular changes in its neighboring environment due to the local density increases (see Fig. 3-19). It is worth noticing also that the negligible change of the water molecule environment – in pure water and in salted water cases – due to the increasing dissolution of CO_2 molecules, results in little influence on the water band in the Raman spectrum. The I_r ratio is thus mainly sensitive to the evolution of the CO_2 molecule within its molecular neighboring environment, especially accounting that an increasing number of salt molecules probably reduces concomitantly the number of CO_2 molecules. Therefore, the observed non linearity of the I_r ratio as a function of S primarily reflects the intensity changes of the ν_u band of CO_2, which are thus representatives of severe modifications of the Fermi resonance due to the changes in the neighboring environment of the CO_2 molecules, mainly due to the presence of the salt molecules.

As seen in the case of DI water, an increase of CO_2 density has little effect on the linear behavior of the $I_r = f(S)$ curve, since the quadratic and the third order terms are very small (-17 and $-0.65 \cdot 10^3$, respectively). However, the salt concentration has a much more pronounced effect, the linear behavior being lost for S values as small as 0.007 mol CO_2/mol of water for 3 M NaCl experiments. The space-constrained CO_2 molecule that dissolved in the pure water phase therefore faces more defavourable neighboring environment in a salted water phase to create its needed similar space-contraint in the aqueous media. This is probably due to an increasing

contribution of highly anisotropic shielding effect due to an increasing number of neighboring salt molecules, which increases the ionic force contribution, and which, in turn, reduces the CO_2 dissolution in aqueous salted mixtures.

The general influence of the three main parameters (CO_2 density, water salinity and temperature) over I_r or S is presented hereafter

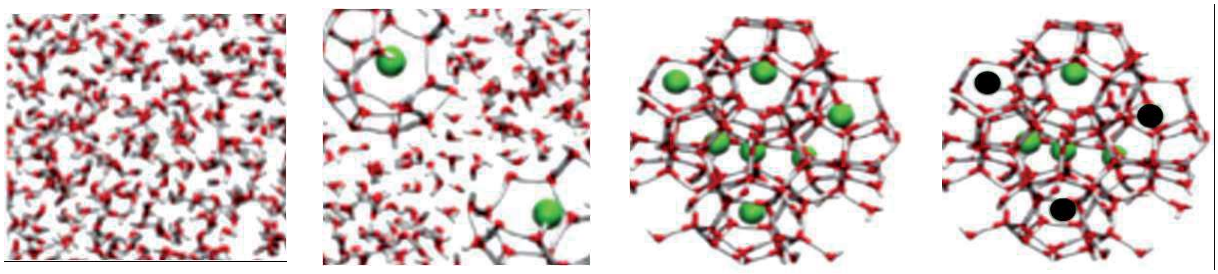

(a) (b) (c) (d)

Fig. 3-19 *Scheme of CO_2 molecules (green balls) dissolved into a water neighboring environment (red skeleton). (a) pure water; (b) unsaturated state which can dissolve more CO_2 into water with increasing CO_2 density. (c) saturated state means no more CO_2 inserting inside; (d) salt effect, the increasing salt molecules (black balls) reduces the possibility for CO_2 molecules. (Adapted from [45])*

8. Effects of the operating parameters on CO_2 solubility

8.1 Pressure effect on I_r

As seen in Fig. 3-20, an increasing CO_2 density (corresponding to a higher pressure) leads to a higher solubility in water and therefore a higher Raman intensity ratio. This effect can be easily understood through the Henry's law with the concentration of a solute being dependent on its gas partial pressure above the solution.

Note, however, that for CO_2 density values above the critical density (ρ_c = 0.4678 g·cm^{-3}), the I_r ratio seems to saturate, which can be probably results from a limited neighboring number of CO_2 molecules inserted through the anisotropic distribution of the water molecules highly linked by hydrogen bounding. However, this particular behavior of the Fermi resonance of constrained CO_2 molecules in quasi-similar neighboring environments was not further investigated.

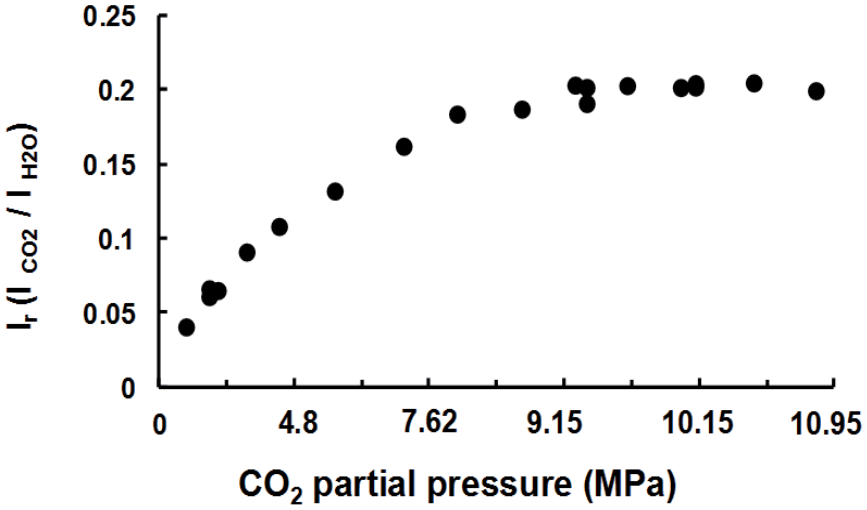

Fig. 3-20 *CO_2 partial pressure effect over the intensity ratio (I_r) in DI water for T = 50 °C.*

8.2 Salinity and Temperature effects on S

The salt concentration – or more exactly, the ionic force, as suggested above – has also a great influence over the CO_2 solubility in brine. As mentioned earlier, it not only influences the I_r ratio (with a loss of the linear behavior as a function of S), but also reduces the possibility for a similar constrained CO_2 molecule to dissolve in aqueous salted mixture compared to pure water, resulting in a lower CO_2 solubility for a higher salt concentration (Fig. 3-21).

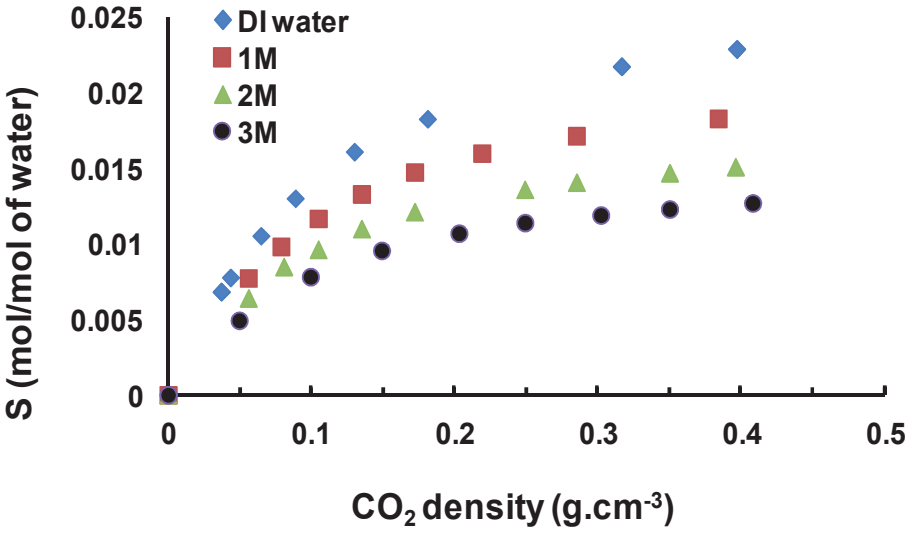

Fig. 3-21 *Temperature and low density effect over the CO_2 solubility in DI water obtained through the DS-CSM model.*

The temperature effect accounts for the molecular agitation of CO_2 molecules. When a molecule undergoes high molecular agitation, its partial volume increases. Therefore, in the case of CO_2 in water, the constrained CO_2 molecule will require more "space" in the water phase to dissolve at high temperature than at low temperature, meaning the higher the temperature, the lower the CO_2 solubility (Fig. 3-22).

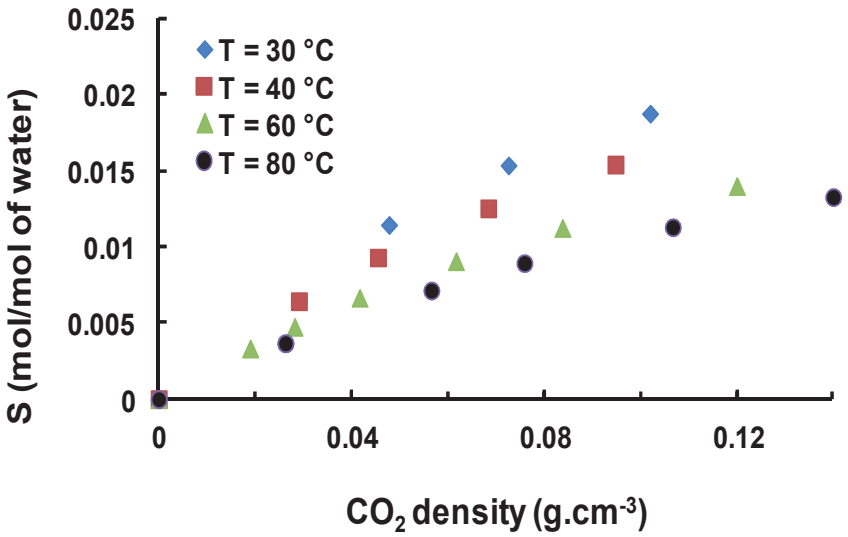

Fig. 3-22 *Influence of the salt concentration in brine over the solubility of CO_2 obtained through the DS-CSM model.*

Once having determined the relationship between the intensity ratio (I_r) and the solubility of CO_2 in the aqueous phase (S), the confocal Raman spectroscopy / microfluidics approach is largely flexible and allows for fast screening of the operating conditions for getting insights in CO_2 solubility in aqueous media, which can be measured in the range $2 \cdot 10^{-3}$ - $2.7 \cdot 10^{-2}$ mol CO_2/mol of water, covering most of the conditions encountered in real deep aquifers geological storage configurations.

9. Conclusion

As a conclusion, the focus of this work was to quantify the solubility of carbon dioxide in water and salted water using microreactors probed by confocal Raman spectroscopy. Similarly to previous studies, the calibration curves for CO_2 to relate band height ratios (the dissolved CO_2 bands are referenced to the O–H stretching band of water) to solubility can be linearly fitted when considering low solubility (typical from low CO_2 densities). However, we have shown that in the high solubility range ($S > 7 \cdot 10^{-5}$ mol/mol of water), the calibration curve requires a correction with a quadratic term, which characterizes the considered salinity.

This study proved that Raman measurement method can be extended to high CO_2 concentration range. More importantly, this method drastically reduces the experiment time. The pressurized microfluidic systems combining Raman measurement technique is viable in the laboratory and confirms the interest of geological lab on chip for studying processes related to CO_2 underground storage. Besides, such an approach can be widely used in various other fields of research.

References

1 Z. Duan, R. Sun, Chemical Geology 193 (2003) 257-271.

2 L. W. Diamond, N. N. Akinfiev, Fluid Phase Equilibria 208 (2003) 265.

3 G. K. Anderson, J. Chem. Eng. Data 47 (2002) 219.

4 S. Someya, S. Bando, B. Chen et al, Int. J. Heat and Mass Transfer 48 (2005) 2503.

5 S. Portier, C. Rochelle, Chemical Geology 217 (2005) 187.

6 S.V. Wroblewski, Ann. Phys. Chem. 18 (1883) 290-308.

7 P. Scharlin, Oxford University Press. 62 (1996) 383.

8 K.Y. Song, R. Kobayashi, SPE Form. Eval. 2 (1987) 500-508.

9 M. Wendland, H. Hasse, G. Maurer, J. Chem. Eng. Data 44 (1999) 901-906.

10 B. Dubacq, M. J. Bickle, K. A. Evans, Geochimica et Cosmochimica Acta 110 (2013) 229–252.

11 R.Wiebe, V. L. Gaddy, J. Am. Chem. Soc. 61 (1939) 315-318.

12 R.Wiebe, V. L. Gaddy, J. Am. Chem. Soc. 62 (1940) 815-817.

13 C. F. Prutton, R. L. Savage, J. Am. Chem. Soc. 67 (1945) 1550-1554.

14 K. Tödheide, E. U. Franck, Z. Phys. Chemie Neue Folge 37 (1963) 387-401.

15 J. A. Nighswander, N. Kalogerakis, A. K. Mehrotra, J. Chem. Eng. Data 34 (1989) 355-360.

16 S. Takenouchi, G. C. Kennedy, Am. J. Sci. 262 (1964) 1055-1074.

17 P. B. Stewart, P. Munjal, J. Chem. Eng. Data 15 (1970) 67-71.

18 S. D. Malinin, N. I. Savalyeva, Geochem. Int. 9 (1972) 410-418.

19 S. D. Malinin, Geochem. Int. 3 (1959) 292-306.

20 A. J. Ellis, R. M. Golding, Am. J. Sci. 261 (1963) 47-60.

21 S. D. Malinin, N. A. Kurovskaya, Geochem. Int. 12 (1975) 199-201.

22 A. E. Markham, K. A. Kobe, J. Am. Chem. Soc., 63 (1941) 449-454.

23 J. Kiepe, S. Horstmann, K. Fischer, J. Gmehling, Ind. Eng. Chem. Res. 41 (2002) 4393-4398.

24 P.G.T. Fogg, W. Gerrard, John Wiley & Sons (1991) ISBN 0 471 9225 5.

25 S.N. White, Applied Spectroscopy 64 (2010) 819.

26 K. Pruess, J. Garcia, Environmental Geology 42 (2002) 282-295.

27 N. Spycher, K. Pruess, J. Ennis-King, Geochimica et Cosmochimica Acta 16 (2003) 3015-3031.

28 J. O. L. B. McPherson, S.B. Cole, Journal of Geochemical Exploration 69 (2000) 65-69.

29 Z. Duan, R. Sun, C. Zhu, I-M. Chou, Marine Chemistry 98 (2006) 131-139.

30 N.F. Spycher, M.H. Reed, Geochim. Cosmochim. Acta 52 (1988) 739-749.

31 Z. Duan, N. Møller, J. H. Weare, Geochim. Cosmochim. Acta 56 (1992a) 2605-2617.

32 Z. Duan, N. Møller, J. H. Weare, Geochim. Cosmochim. Acta 56 (1992b) 2619-2631.

33 K.S. Pitzer, J. Phys. Chem. 77 (1973) 268.

34 B. Zerai, Doctoral thesis, Case Western Reserve University (2006).

35 M.B. King, A. Mubarak, J.D. Kim, T.R. Bott, J. Supercrit. Fluids 5 (1992) 296-302.

36 B. Rumpf, H. Nicolaisen, C. Ocal, G. Maurer, J. Solution Chem. 23 (1994) 431-448.

37 P. G. Brewer, G. E. Malby, J. D. Pasteris, S. N. White, E. T. Peltzer, B. Wopenka, J. Freeman, M. O. Brown, Deep-Sea Res. 51 (2004) 739-753.

38 C. Zhang, K. Dehoff, N. Hess, M. Oostrom, T. W. Wietsma, A. J. Valocchi, B. W. Fouke, J. C. Werth, Environ. Sci. Technol. 44 (2010) 7833-7838

39 B. Wopenka, J. D. Pasteris, Anal. Chem. 59 (1987) 2165.

40 A. K. Sun, R. C. Burruss, E. D. Sloan, J. Phys. Chem. B 101 (1997) 7371.

41 W. Lua, et al. Geochimica et Cosmochimica Acta 72 (2008) 412 – 422.

42 J. Yamamoto, H. Kagi, Chemistry Letters 35 (2006) 6.

43 Y. Kachi, T. Tsukahara, Y. Kayaki, T. Ikariya, J. Sato, Y. Ikeda, J. of Supercritical Fluids 40 (2007) 20-26 .

44 Y. Garrabos, R. Tufeu, B.L. Neindre, G. Zalczer, D. Beysens, J. Chem. Phys.72 (1980) 4637 .

45 L.C. Nielsen, I.C. Bourg, G. Sposito, Geochim. Cosmochim. Acta 81 (2012) 28-38.

Chemical Physics Letters 551 (2012) 139–143

Contents lists available at SciVerse ScienceDirect

Chemical Physics Letters

journal homepage: www.elsevier.com/locate/cplett

Microfluidic approach for studying CO_2 solubility in water and brine using confocal Raman spectroscopy

N. Liu, C. Aymonier, C. Lecoutre, Y. Garrabos, S. Marre *

CNRS, ICMCB, UPR9048, F-33600 Pessac, France
Univ. Bordeaux, ICMCB, UPR9048, F-33600 Pessac, France

ARTICLE INFO

Article history:
Received 20 July 2012
In final form 4 September 2012
Available online 19 September 2012

ABSTRACT

This Letter reports a fast and accurate method to quantify dissolved carbon dioxide in water and salted water (NaCl) using microfluidic systems probed by confocal Raman spectroscopy. The relationship of CO_2 solubility and Raman band intensity ratios (the v_u of the CO_2 Fermi dyad over the water stretching band) can be fit from third order polynomial forms, depending on NaCl concentration. This approach allows for a much faster determination of CO_2 solubility measurements in pressurized aqueous media. More generally, by easily managing lithospheric fluids in microdevices, this strategy opens avenues towards true 'Geological Lab on chip'.

Injection of captured CO_2 from major stationary sources into deep geological formations (geological CO_2 storage) is a promising way to reduce emitting CO_2 into the atmosphere. Selected geological reservoirs include unmineable coal seams, depleted oil and gas reservoirs and deep saline aquifers, the most promising in terms of storage capacity. Saline aquifers are made up of deep sedimentary rocks saturated with formation waters or brines containing high concentrations of dissolved salts. To enhance the reliability of numerical simulations for CO_2 storage capacity and sustainable geological storage, it is thus necessary to access accurate solubility data in CO_2–H_2O–salts systems. The solubility of CO_2 in brine varies as a function of salinity, pressure, and temperature. Numerous models and experimental works for CO_2 solubility in aqueous solutions have been published to describe this relationship [1–5]. However, these macroscale methods generally require fastidious and time-consuming experiments, with large relaxation time (at least 24 h) to reach the phase equilibrium and difficulties to analyze the alkaline-preserved samples by potentiometric titration after reacting with base solution, (which can introduce non negligible secondary errors). Therefore, there is an increasing need for fast and reproducible methods for determining key physicochemical data related to CO_2 storage applications, which can be provided by pressurized microfluidic approaches, through the use of 'Geological Lab on chip'.

Microfluidic systems have been increasingly adapted to many chemical [6,7] and geochemical applications thanks to their low reagent consumption, efficient heat and mass transfer and a much finer degree of process control. Recently, several papers describe the use of such systems either called 'microreactors' or 'micromodels', which design can be easily adapted to the targeted application. However, most of the conducted studies to date – including fluid flows characterization and solubility measurements – are performed close to ambient conditions of temperature and pressure [8–11], far from the true CO_2 storage conditions in deep saline aquifers (typically: $30 < T(°C) < 80$ and $6 < p\,(MPa) < 15$). Only a very recent work reports on high pressure micromodels for studying CO_2/brine systems [12].

Most microfluidics studies dealing with CO_2 solubility in brine or other solvents are based on CO_2 slugs' size variations measurements along with the operating conditions [8–10], which are very convenient approaches when considering low density gaseous CO_2. However, at higher pressures, the CO_2 density largely increases when turning liquid or 'supercritical' therefore the slug size variations are too small to be measured accurately anymore. Confocal Raman spectroscopy offers a powerful alternative method for quantitatively monitoring the solubility of gases such as CO_2 or CH_4 in aqueous solution in a wide range of pressures and temperatures, as demonstrated in large scale high pressure cells [13,14]. Although Raman signals are dependent upon several experimental factors, peaks ratio can be used to determine relative concentrations, which technique was previously reported [13,15,16].

We present in this Letter a fast and facile route towards CO_2 solubility measurements in water and brine using silicon–Pyrex microreactors coupled to confocal Raman spectroscopy. In particular, we have investigated the relation between the Raman bands intensity ratio (I_{CO2}/I_{H2O}) as a function of the solubility of CO_2 in water or brine in a wide range of CO_2 density and temperature.

* Corresponding author at: ICMCB-CNRS, 87 avenue du Dr Albert Schweitzer, 33608 Pessac cedex, France.
E-mail address: marre@icmcb-bordeaux.cnrs.fr (S. Marre).

0009-2614/$ - see front matter © 2012 Elsevier B.V. All rights reserved.
http://dx.doi.org/10.1016/j.cplett.2012.09.007

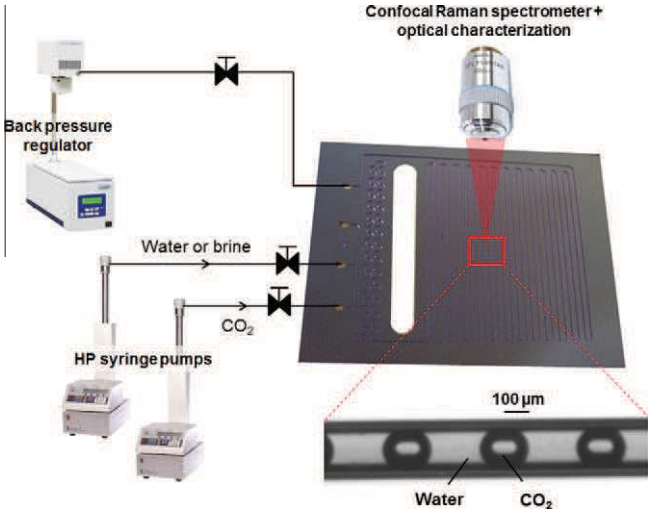

Figure 1. Scheme of the experimental set-up including silicon microreactor, high pressure pumps, back pressure regulator and confocal Raman spectrometer.

Silicon–Pyrex microreactors have already demonstrated outstanding pressure and temperature capabilities [17,18] in addition to improved heat transfer compared to glass–glass microsystems. The general set-up for this Letter is shown in Figure 1 and was previously described elsewhere [17].

Briefly, two high-pressure syringe pumps (ISCO 100DM) continuously inject aqueous solution and CO_2 within the microreactor. CO_2 and brine meet at a T-junction generating a CO_2–water segmented flow, as previously reported [19,20]. The pressure is controlled by a back pressure regulator (Jasco BP2080) placed downstream the microsystem, while a heating element contacting the microreactor achieves the proper temperature conditions within the microchannel. Additional HP valves allow for working either in continuous or stop-flow mode. The microreactor itself consists in a 1 m long microchannel (200 µm wide, 100 µm deep) and was fabricated using standard lithography/wet etching techniques. Spectra were acquired from a Thermo Scientific DXR Raman microscope with a 532 nm wavelength excitation laser operating at 10 mW output power (see Figure 2).

After the formation of the CO_2/water segmented flow in the chosen conditions, the valves are closed; immobilizing the segmented flow and the system is left in conditions during 10 min to reach the phase equilibrium before any spectrum is taken from the continuous aqueous phase or the CO_2 slugs. Note that only $CO_{2(aq)}$ is considered since the concentrations of the other carbonate species (HCO_3^- and CO_3^{2-}) are in too low concentrations to be detected with this instrument in either water or brine. However, given our pH conditions both upstream (pH = 5) and downstream the microreactor (pH = 3) and the pKa of both $H_2CO_3 \Longleftrightarrow HCO_3^- + H^+$ ($pKa = 6.3$) and $HCO_3^- \Longleftrightarrow CO_3^{2-} + H^+$ ($pKa = 10.33$) equilibria, we can reasonably assume that $CO_{2(aq)}$ is the main carbonate specie in the aqueous phase.

The fast heat and mass transfers provided by microreactors allow for easily reaching the phase equilibrium in the microchannel within a brief period. Indeed, the mass diffusion time in the microreactor can be estimated as $t_D \sim x^2/2D$, typically, with x the characteristic length (typically the average half-distance between two CO_2 slugs) and D the diffusion coefficient of CO_2 in the considered aqueous phase. Considering $x = 200$ µm and approximating D to the Stokes–Einstein diffusion coefficient $D = k_B T/6\pi\eta a$ of the CO_2 Brownian motion in pure water (with $k_B = 1.38 \times 10^{-23}$ the Boltzman constant, $T = 323$ K (50 °C) the temperature, $\eta = 1$ mPa s the water viscosity and $a = 3$ Å the typical size of a CO_2 molecule), we obtain $D = 0.8.10^{-9}$ m^2 s^{-1}, giving $t_D \sim 25$ s, which is much less than the experimental lag time of 10 min. To confirm these theoretical considerations, additional experiments over the DI water/CO_2 system were run to get insights in the time required to reach equilibrium in our conditions inside a microchannel. Raman spectra of the aqueous phase were taken at various time from $t = 1$ min to $t = 45$ min after CO_2 and water were contacted

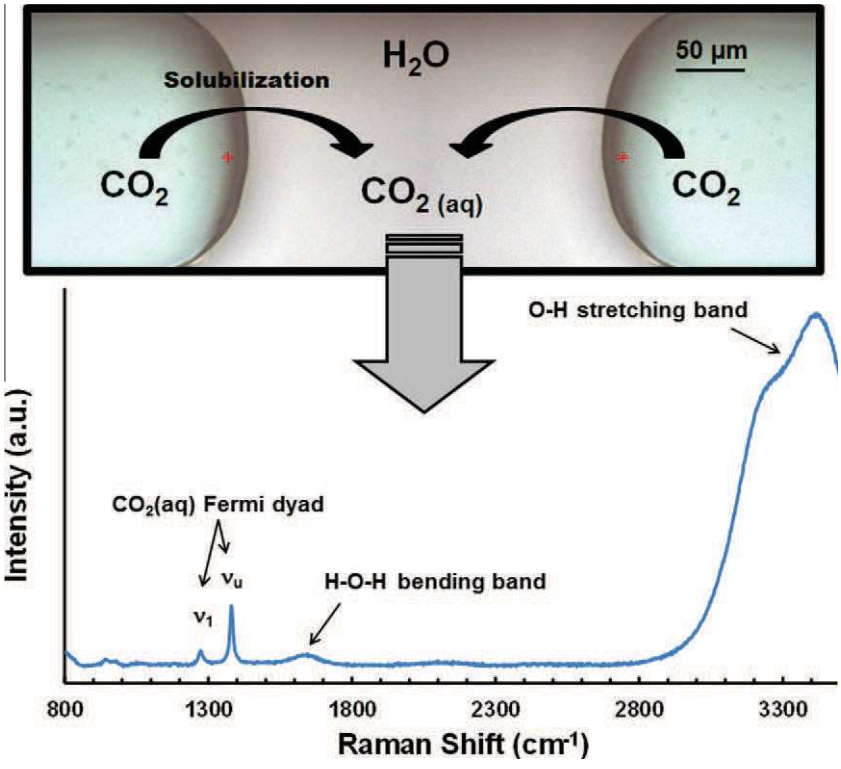

Figure 2. Optical image of a CO_2/water segmented flow inside a microchannel and corresponding confocal Raman spectra within a water slug containing dissolved CO_2.

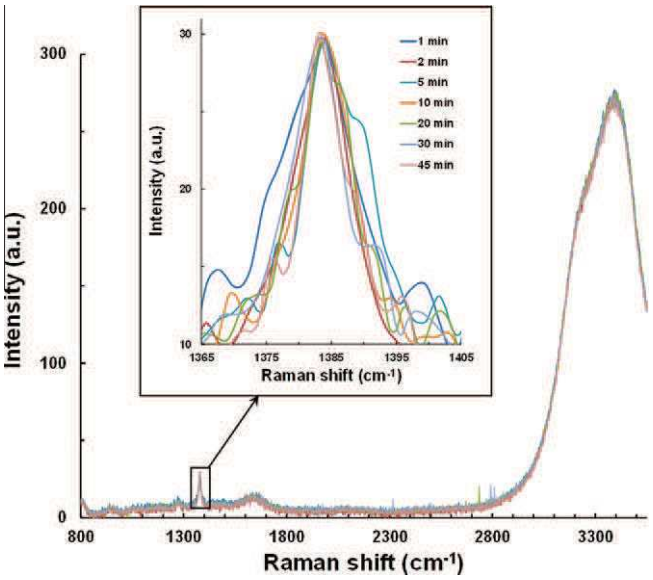

Figure 3. Raman spectra of $CO_{2(aq)}$ in DI water from 1 min to 45 min.

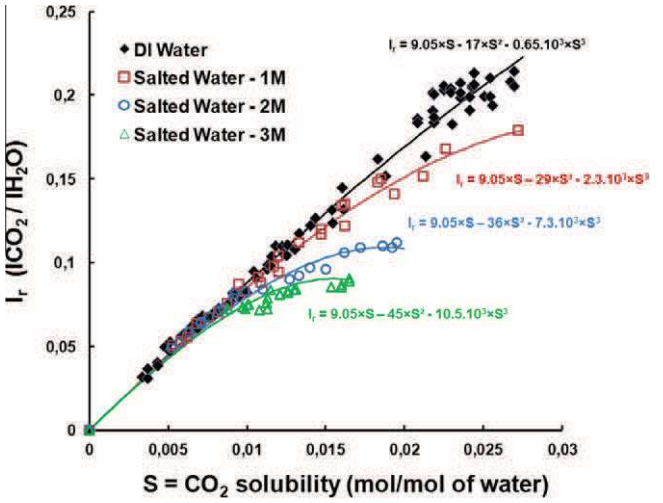

Figure 4. Plots of CO_2 and water Raman bands intensity ratio (I_r = ICO_2 (~1385 cm^{-1})/IH_2O (~3430 cm^{-1})) for $CO_{2(aq)}$ in DI water and salted water (NaCl, 1, 2 and 3 M) vs. CO_2 solubility (S) obtained through the DS–CSM model.

(assimilated to $t = 0$). As shown in Figure 3, the variation of the CO_2 v_u band intensity at ~1385 cm^{-1} in the time range investigated (from 1 to 45 min) is negligible (less than 2.5%). This observation therefore demonstrates that equilibrium is reached in less than 1 min using the microfluidic approach.

The CO_2 solubility model of Duan and Sun (DS–CSM) [1] was chosen for modeling the CO_2 solubility. Several models were developed over the past 10 years for predicting CO_2 solubility in pure water (McPherson and Cole [21], Spycher et al. [22] and Diamond and Akinfiev [2]) and/or brine (Pruess and Garcia [23], Xu et al. [24]); however, the DS–CSM is by far the most accurate CO_2 solubility model [25]. This model is based on chemical potential energy; CO_2 solubility in aqueous solutions being determined from the balance between its chemical potential in the liquid phase and the gas phase using the specific interaction model of Pitzer [26]. The latter being used to calculate the activity coefficient of CO_2, while the CO_2 fugacity coefficient is determined using an equation of state developed by Duan et al. [27]. The DS–CSM accurately describes CO_2 solubility in pure water and aqueous solutions in a wide range of temperature (25–260 °C), pressure (0.1–200 MPa) and salinity (0–4.3 M), which are typically encountered in real deep saline aquifer reservoirs. This model is also extended to predict CO_2 solubility in more complex brines (salts included NaCl, $MgCl_2$, $CaCl_2$ or sulfates) such as seawater with remarkable accuracy.

Four sets of experiments were run with CO_2 dissolved in: (i) DI water (temperature from 22 to 100 °C, pressure from 1.1 to 10 MPa), (ii) 1 M (NaCl) salted water (temperature from 30 to 100 °C, pressure from 3 to 10 MPa), (iii) 2 M (NaCl) salted water (temperature from 30 to 100 °C, pressure 4 to 10 MPa) and (iv) 3 M (NaCl) salted water (temperature from 35 to 55 °C, pressure 7 to 9.5 MPa). The results are presented hereafter.

The band heights ratio (named I_r) of the CO_2 v_u band ~1385 cm^{-1} to the O–H stretching band ~3430 cm^{-1} versus the expected CO_2 solubility (S) in aqueous media was plotted in Figure 4 for both CO_2/DI water and CO_2/1 M, 2 M and 3 M NaCl salted water systems. This curve is critical in the determination of the solubility of CO_2 in aqueous media by Raman spectroscopy, since it gives the relation between the actual experimental data and the real solubility values. It can be noticed that the data – both in DI or salted water – can be reasonably linearly fitted in the low CO_2 solubility area (for $S < 0.009$ mol/mol of water), in accordance with previous reported works [13]. Note, however, that a different slope value is obtained in our case (see the Supporting information-iii). For higher CO_2 solubility, generally encountered at higher CO_2 densities (not investigated in previous studies), we found out that it is necessary to correct the linear fit with a quadratic and third-order term varying depending on the salinity. For instance, for the CO_2/DI water system, the best fit is: $I_r = 9.05 \times S - 17 \times S^2 - 0.65.10^3 \times S^3$, while for CO_2/1, 2 and 3 M NaCl water, it turns out to be: $I_r = 9.05 \times S - 29 \times S^2 - 2.3.10^3 \times S^3$, $I_r = 9.05 \times S - 36 \times S^2 - 7.3.10^3 \times S^3$ and $I_r = 9.05 \times S - 45 \times S^2 - 10.5.10^3 \times S^3$, respectively. Note that in the two latters (2 and 3 M salted water), it is difficult to access high solubility values for CO_2 (see Figure 4).

In all cases, the non-linearity between the Raman intensity ratio and the CO_2 solubility at high CO_2 densities can find physical explanation in steric hindrance created by the increasing concentration of CO_2 or salts in the aqueous media. First, note that the significant changes of the gas-to-liquid Fermi dyad of a space-constrained CO_2 molecule directly reflects the molecular changes in its neighboring environment due to the local density increases, as exemplified for instance in [28]. It is worth noticing also that the barely change of water molecule environment – in pure water and in salted water cases – due to the increasing dissolution of CO_2 molecules, results in little influence on the ν_1 water band in the Raman spectrum. The I_r ratio is thus mainly sensitive to the evolution of the CO_2 molecule within its molecular neighboring environment, especially accounting for an increasing number of CO_2 and salt molecules and probably reducing concomitantly the number of water molecules. Therefore, the observed non linearity of the I_r ratio as a function of S primarily reflects the intensity changes of the v_u band of CO_2, which are thus representative of severe modifications of the Fermi resonance induced by changes in the neighboring environment of the CO_2 molecules, mainly due to the presence of the salt molecules. As seen in the case of DI water, an increase of CO_2 density has little effect on the linear behavior of the $I_r = f(S)$ curve, since the quadratic and the third order terms are very small (-17 and -0.65×10^3, respectively). However, the salt concentration has a much pronounced effect, the linear behavior being lost for S values as small as 0.009 mol/mol of water for 3 M NaCl experiments.

The space-constrained CO_2 molecule that dissolved in the pure water phase therefore faces more unfavorable neighboring environment in a salted water phase to create its needed similar space-constraint in the aqueous media. This is probably due to a

growing contribution of highly anisotropic shielding effect generated from an increasing number of neighboring salt molecules, which increases the ionic force contribution, and which, in turn, reduces the CO_2 dissolution in aqueous salted mixtures (see below).

Once having determined the relationship between the intensity ratio (I_r) and the solubility of CO_2 in the aqueous phase (S), the confocal Raman spectroscopy/microfluidics approach is largely flexible and allows for fast screening of the operating conditions for getting insights in CO_2 solubility in aqueous media, which can be measured in the range 2×10^{-3}–2.7×10^{-2} mol/mol of water, covering most of the conditions encountered in real deep aquifers geological storage configurations.

The general influence of the three main parameters (CO_2 density, water salinity and temperature) over I_r or S is presented hereafter (Figure 5).

As seen in Figure 5A, an increasing CO_2 density (corresponding to a higher pressure) leads to a higher solubility in water and therefore a higher Raman intensity ratio. This effect can be easily understood since the concentration of a solute is dependent on its gas partial pressure above the solution (from the Henry's law which, although simple, gives good general tendencies). Note, however, that for CO_2 density values above the critical density ($\rho_c = 0.4678$ g cm^{-3}), the I_r ratio seems to saturate, which can probably be attributed to a similar arrangement of neighboring (water + CO_2) molecules. Such an arrangement could results from a limited neighboring number of CO_2 molecules inserted through the anisotropic distribution of the water molecules highly linked by hydrogen bounding. However, this particular behavior of the Fermi resonance of constrained CO_2 molecules in quasi-similar neighboring environments was not investigated in here.

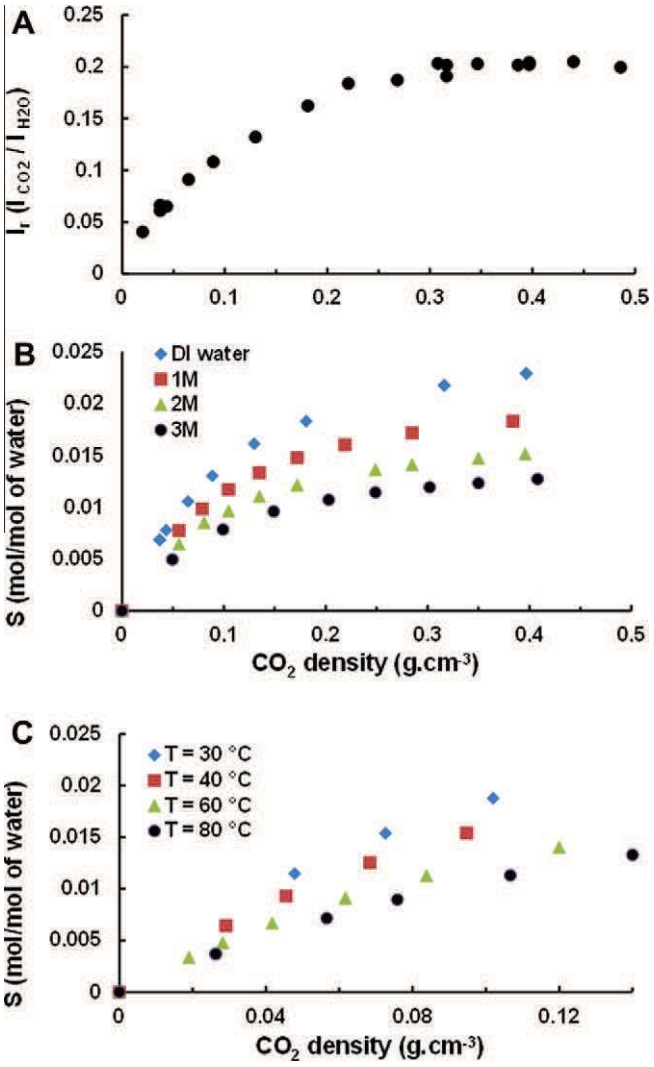

Figure 5. (A) CO_2 density effect over the intensity ratio (I_r) in DI water for $T = 50$ °C, (B) influence of the salt concentration in brine over the solubility of CO_2 and (C) temperature and low density effect over the CO_2 solubility in DI water obtained through the DS–CSM model.

The salt concentration – or more exactly, the ionic force, as suggested above – has also a great influence over the CO_2 solubility in brine. As mentioned earlier, it not only influences the I_r ratio (with a loss of the linear behavior as a function of S), but also reduces the possibility for a similar constrained CO_2 molecule to dissolve in aqueous salted mixture compared to pure water, resulting in a lower CO_2 solubility for a higher salt concentration (see Figure 5B).

Finally, the temperature effect (Figure 5C) accounts for the molecular agitation of CO_2 molecules. When a molecule undergoes high molecular agitation, its partial volume increases. Therefore, in the case of CO_2 in water, the constrained CO_2 molecule will require more 'space' in the water phase to dissolve at high temperature than at low temperature, meaning the higher the temperature, the lower the CO_2 solubility (see Figure 5C).

As a conclusion, the focus of this Letter is quantifying the solubility of carbon dioxide in water and salted water by using microreactors probed by confocal Raman spectroscopy. Similarly to previous studies, the calibration curves for CO_2 to relate band height ratios (the dissolved CO_2 bands are referenced to the O–H stretching band of water) to solubility can be linearly fitted when considering low solubility (typical from low CO_2 densities). However, we have shown that in the high solubility range ($S > 0.009$ mol/mol of water), the calibration curve requires a correction with a quadratic and a third order term, which characterizes the considered salinity. This Raman measurement method can be extended to high CO_2 concentration range, and drastically reduces the experiment time. This technique is proved viable in the laboratory and opens avenues towards the extended use of pressurized microfluidic systems as true geological lab on chips to perform studies related to CO_2 underground storage in wider chemical fields resulting from different geological formations of concern.

Acknowledgments

The authors gratefully acknowledge the support of the Région Aquitaine through the GIS Advanced Materials in Aquitaine, the French spatial agency CNES for 'aide à la recherche' and the French Agence Nationale pour la Recherche (ANR) under Grant SCμF No. ANR-09-BLAN-0105-01 ('Supercritical Microfluidics'). Na Liu thanks the University of Bordeaux for PhD grant.

Appendix A. Supplementary data

Supplementary data associated with this Letter can be found, in the online version, at http://dx.doi.org/10.1016/j.cplett.2012.09.007.

References

[1] Z. Duan, R. Sun, Chem. Geol. 193 (2003) 257.
[2] L.W. Diamond, N.N. Akinfiev, Fluid Phase Equilib. 208 (2003) 265.
[3] G.K. Anderson, J. Chem. Eng. Data 47 (2002) 219.
[4] S. Someya, S. Bando, Y. Song, B. Chen, M. Nishio, J. Heat Mass Transfer 48 (2005) 2503.
[5] S. Portier, C. Rochelle, Chem. Geol. 217 (2005) 187.
[6] R.L. Hartman, K.F. Jensen, Lab Chip 9 (2009) 2495.
[7] S. Marre, K.F. Jensen, Chem. Soc. Rev. 39 (2010) 1183.
[8] M. Abolhasani, M. Singh, E. Kumacheva, A. Günther, Lab Chip 12 (2012) 1611.
[9] E. Tumarkin et al., Lab Chip 11 (2011) 3545.
[10] T. Cubaud, M. Sauzade, R. Sun, Biomicrofluidics 6 (2012) 022002.

[11] N.S.K. Gunda, B. Bera, N.K. Karadimitriou, S.K. Mitra, S.M. Hassanizadeh, Lab Chip 11 (2011) 3785.
[12] Y. Kim, J.M. Wan, T.J. Kneafsey, T.K. Tokunaga, Environ. Sci. Technol. 46 (2012) 4228.
[13] S.N. White, Appl. Spectrosc. 64 (2010) 819.
[14] J.P. Savy, N. Bigalke, G. Aloisi, M. Pansegrau, E. Kossel, M. Haeckel, Geochim. Cosmochim. Acta 74 (2010) A915.
[15] B. Wopenka, J.D. Pasteris, Anal. Chem. 59 (1987) 2165.
[16] A.K. Sun, R.C. Burruss, E.D. Sloan, J. Phys. Chem. B 101 (1997) 7371.
[17] S. Marre, A. Adamo, S. Basak, C. Aymonier, K.F. Jensen, Ind. Eng. Chem. Res. 49 (2010) 11310.
[18] S. Marre, J. Baek, J. Park, M.G. Bawendi, K.F. Jensen, Jala 14 (2009) 367.
[19] N. Lorber et al., Lab Chip 11 (2011) 779.
[20] S. Marre, C. Aymonier, P. Subra, E. Mignard, Appl. Phys. Lett. 95 (2009) 134105.
[21] B.J.O.L. McPherson, B.S. Cole, J. Geochem. Explor. 69 (2000) 65.
[22] N. Spycher, K. Pruess, J. Ennis-King, Geochim. Cosmochim. Acta 67 (2003) 3015.
[23] K. Pruess, J. Garcia, Environ. Geol. 42 (2002) 282.
[24] T. Xu, E. Sonnenthal, N. Spycher, K. Pruess, Comput. Geosci. 32 (2006) 145.
[25] B. Zerai, Ph.D. Thesis, Case Western Reserve University, Cleveland, OH, 2006.
[26] K.S. Pitzer, J. Phys. Chem. 77 (1973) 268.
[27] Z. Duan, N. Moller, J.H. Weare, Geochim. Cosmochim. Acta 56 (1992) 2619.
[28] Y. Garrabos, R. Tufeu, B. LeNeindre, G. Zalczer, D. Beysens, J. Chem. Phys. 72 (1980) 4637.

Chapter 4

CO_2 invasion and drainage at pore-scale in 2-D micromodels

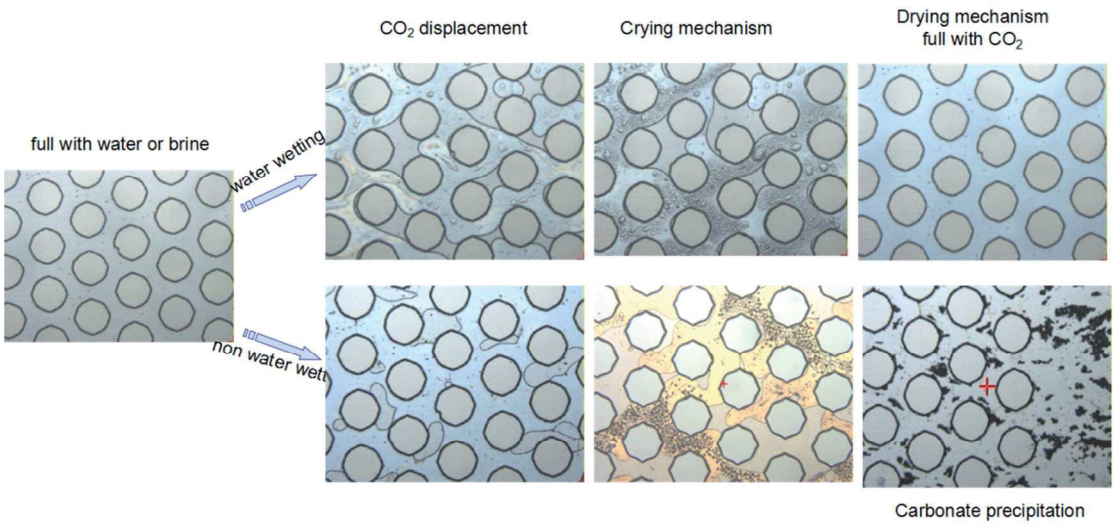

1. Introduction

When CO_2 is injected into a deep saline aquifer, the reservoir properties (for instance: porosity and permeability) and the sweep efficiency of the CO_2 dynamic drainage within the reservoir are among the most important parameters affecting the CO_2 storage capacity. In particular, the evolution of the CO_2/water phase distribution of the injected CO_2 within the reservoir is a key parameter to be determined to estimate the true storage capacity of the aquifer. Therefore the phase distribution is of paramount importance to study and understand the CO_2 displacement mechanisms, which can have a significant contribution to the long-term storage safety.

High-pressure micromodels are very useful tools to directly visualize the pore-scale fluid distribution and displacement, by injecting CO_2 into a water-saturated micro porous media at geological reservoir conditions. This chapter is thus based on key series of two-phase fluid flow experiments performed within a well-designed two-dimensional pore network inside high-pressure silicon/Pyrex micromodels. Obviously, such micromodels have a low pertinence with respect to the local complexity encountered in the 3D porous media of the geological formations and the measurements of the local velocity field always remain a non-resolved challenging problem, especially at high pressure and high temperature. However, we can nevertheless take advantage of their 2D characteristics to observe, for the first time in real p,T conditions, the behavior of the two-phase distribution at different operating conditions. The combination between flow rate and pressure measurements, wettability change of the solid walls, and the video recording of the pore network, can be then used to capture some of the key mechanisms of the CO_2 invasion at a typical pore scale of few tens of micrometers.

To mimic the CO_2 injection and the CO_2 invasion in the geological reservoir, we have conceived a simple experiment schematized in Fig. 4-1, where the micromodel at the temperature T is connected upstream and downstream to two high-pressure pumps.

Here, ***the first main novelty is readily provided by the high-pressure, high-temperature characteristics of the experiment.*** Indeed, the micromodel heated at the temperature T operates in the true p,T conditions of a selected geological fluid formation, since each pump gives access to the fluid flow rate and to the operating pressure gradient.

CO_2 injection uses the inlet (left) high-pressure pump "A" working in constant flow rate mode (q_i) and at constant temperature $T_i = 0$ °C (to insure flow monitoring of the pump with the liquid CO_2 at constant density, assumed non-compressible). At the initial time, the experimental set-up is fully saturated with flowing brine at an average pressure p and average temperature T of the geological formation (see below for preparing the initial state). The p,T ***geological-like situation*** is obtained from: 1) a heating part in contact with the micro device and, 2) the outlet (right) high-pressure pump "B", now working in a constant pressure mode ($p_o \sim p$) and constant (ambient) temperature ($T_o = 25$ °C). Each pressure sensor integrated inside the pump records the time (t) evolution of the pressure [$p_i(t)$, p_o] at each pump level, while each flow rate [q_i, $q_o(t)$] is given by each pump controller.

The time responses of the inlet pressure drop change $p_i(t) > p_o$ and the output flow rate change $q_o(t) > 0$ are then due to the CO_2 injection and the CO_2 flowing process through the experimental set-up. The latter is schematized from a design made of one external part connected to the micromodel itself, which is in contact with a heating device operating at a constant temperature T. The external part of the micromodels consists of two similar - inlet (left) and outlet (right) - cylindrical high-pressure tubes made of stainless steel. The complete micromodel consists of both adaptive parts boarding the internal central pore network. Each adaptive part of the micromodel is made of two sections, which consist in a single feeding microchannel to be further divided successively into an adaptive partition area (see below the schematic representation of Fig. 4-1) The main objective is to provide the homogeneous partition of the flows from a (inlet/outlet) single channel (first part) to the 2, 3,…., 8 channels (second part) in front of the (input/output) 2D pore network. In such a

design, it is important to note that the trapezoidal cross section of all the channels is conserved. Therefore, the external tubing/micromodel connecting device assumes continuity for the spatial change of i) the fluid flow regimes and ii) the fluid temperature profile.

The pressure change is expected to have similar characteristic behavior (discussed below) in the inlet channel part, the partition/adaptive channel part, and in the pore network of the micromodel, while the main temperature gradient is assumed to exist only along the feeding tubing and the inlet/outlet channel far from the pore network. Moreover, as the lowest dimension of the microchannel shape is 15 µm (see below), it is easy to verify using Eq. 2.2 and a typical value of 40 mN/m for the $scCO_2$/water interfacial tension (see Table 5 below and Ref. [1]), that the capillary entry pressure is certainly lower than 5 kPa (*i.e.*, 0.05 bar) and at least two order of magnitude lower than the initial pressure resistance due to the viscous forces induced by the water saturating the micromodel. Therefore, this schematized design is governed by two hypothetic flowing conditions, which can easily be controlled assuming the monitored values of the CO_2 injected volumetric flow, the water viscosity, and the geometrical characteristics of the complete experimental set-up. These two assumptions are:

i) a laminar viscous flow satisfying the Hagen-Poiseuille equation in the external cylindrical tube, leading to a pressure drop scaled by the inverse fourth power of the tubing diameter;

ii) a micromodel viscous flow separated in 1) a laminar viscous flow satisfying the Hagen-Poiseuille equation in the inlet/outlet channels and the input/output partition channels, leading to a pressure drop scaled by the inverse fourth power of the equivalent hydraulic diameter of the channel and 2) a porous viscous flow satisfying the Darcy equation in the pore network, leading to a pressure drop mainly scaled by the inverse permeability and the interstice (superficial) velocity of the flow (both properties being unknown, unfortunately).

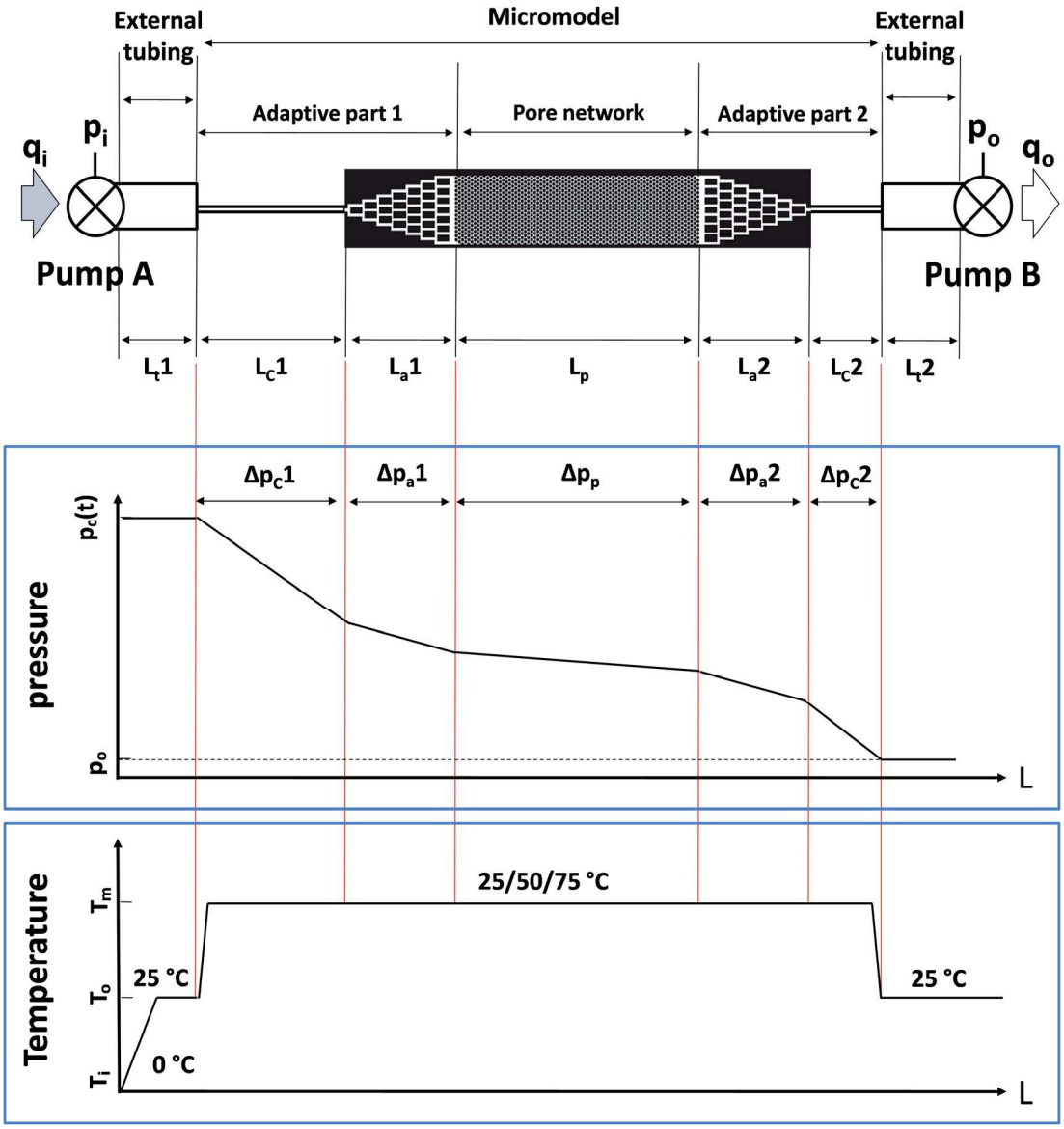

Fig. 4-1 *Schematic view of temperature and pressure distribution within the experimental set-up during the water imbibition of the micromodel (see § 2.2.1 for detail).*

The exact nature of the two-phase flow in the single channel and in the partition channels is expected to be complex in this non-trivial 3D/2D geometry. Moreover, we are deeply concerned about the lack of pressure gradient measurements between the different constitutive elements (while assuming that the temperature gradient can be neglected). Consequently, in a first approximation, we will treat the flow regime as a laminar flow in all the wetted channels present in the micromodel parts. Therefore,

the pressure drop in the channel is proportional to the length of the wetted channel and proportional to the mean velocity in this channel. That leads to the expected instantaneous spatial profiles of the pressure (and the temperature) given in Fig. 4.1, which remain to be discussed and validated.

Indeed, the time evolution of the measured quantities q_i, q_o, p_i, and p_o, such as the ones observed in Figs. 4.2, can provide the supporting results to make the distinction between the characteristic time-periods related to the CO_2 and/or brine displacements in the inlet and outlet adaptive parts, boarding the time period of the CO_2 invasion in the pore network part, which volumes are initially filled with brine.

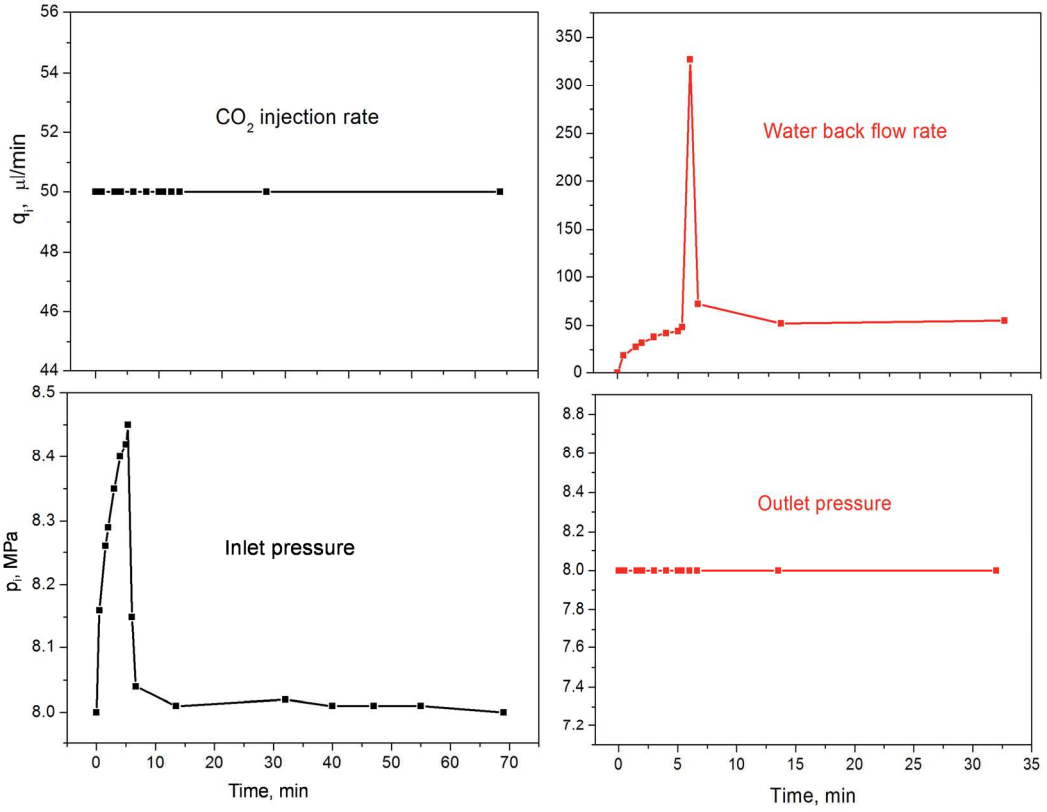

Fig. 4-2 *Time plots of the inlet flow rate ($q_i = f(t)$), inlet pressure ($p_i = f(t)$), outlet flow rate ($q_o = f(t)$) and outlet pressure ($p_o = f(t)$).*

From the above hypothetic situation, the input/output pressure drop across the micromodel thus characterizes the sweep force during the pore network invasion by CO_2, while the modification of the effective pore network porosity accounts for the

residual stationary brine. Similarly, the sudden change in the inlet pump pressure, concomitant with the sudden change of the outlet pump flow rate gives access to the CO_2 breakthrough time, which occurs during the primary drainage process of the micromodel (neglecting thus dissolution effects, as discussed below). Obviously, the expected final situation with full water removal from the micromodel (through dissolution and drying processes) can be reached when the stationary flow of CO_2 alone is observed, *i.e.* $p_i(t) = p_o$. Indeed, the low $scCO_2$ viscosity reduces drastically the pressure drop to only few hundredths of MPa in this final CO_2 stationary flowing regime. In such a situation, the pressure drop across the micromodel is too small to be measured by a pressure difference from the two pumps.

The second main novelty of our micromodels investigations concerns the coupling of the external p, T measurements with in situ visualization provided by a camera mounted on a microscope, which captured the fluid phases (CO_2 and brine) migration and distribution in the 2D pore network. Movies and pictures analyses can then be used to investigate the flowing and storage mechanisms at pore scale. Different characteristic parameters of the pore scale network can thus be checked for various conditions representative of the different geological formations selected for the CO_2 storage.

Therefore, our following interest will be focused on reporting the primary ***geological-like observations*** of the porosity, capillary and wettability effects on the CO_2 invasion of brine saturated micromodels, with or without solubility effects, complemented by the first attempts to capture the reactions among CO_2, brines and silica minerals when the microscope observation uses the Raman spectroscopy technique presented in Chapter 3. The main objective of the results and the analyses given in this last chapter is thus to provide the first validation of the ***Geological Laboratory on Chip (GLoC)*** concept.

2. Materials and methods

2.1. High pressure micromodels

Two types of micromodels (noted L and H in the following) were used in this study. They were fabricated from silicon wafers by the previously reported microfabrication processes, involving lithography, wet etching and bonding (see Chapter 2). L and H type micromodels share the same original 2D mask design, the only difference being their etching depth (15 µm for L and 17 µm for H). The main characteristics of these two types have been selected to validate the design of an experiment in which the main objective is to provide the needed data for the specification definition of the future evolutions of the porous part used to mimic the *geological* formation. Therefore, in this first experimental approach, the micromodels are based on one of the most simple pore network concept, which consists on a staggered plot disposal following a triangular pavement, one side in the transverse direction to the mean flow direction, starting with an ideal 1286 plots mask, 78 plots (transverse) lines, 16.5 plots (longitudinal) staggered lines. The staggered characteristic wavelength of the mask is λ= 300 µm. The circular plot diameter of the mask is d_M = 250 µm (see Fig. 4.3 (a)). The mask porosity is therefore given by:

$$\phi_m = 1 - \frac{\pi d_M^{\,2}}{2\sqrt{3\lambda^2}} = 0.3702 \qquad \text{Eq. 4-1}$$

After microfabrication, each micromodel consists of a one-port inlet channel, 231×15 (or 251×17) μm^2 rectangular section, 22 mm length, and a two-port outlet channel 231×15 (or 251×17) μm^2 rectangular section, 66.5 mm length, connected to the homogeneous pore network (Fig. 4-3 (a)), with a depth of 15 (or 17) µm, as above mentioned. The L and H micromodels types are distinguished by the size dimensions given between brackets, their difference being driven by the etching depth that characterizes each type, leading to a low porosity (L: Φ = 0.5155), and high porosity

(H: $\Phi = 0.6$), see below). Note that the difference between Φ and Φ_m in Eq. 4-1 is due to the etching process, as explained above.

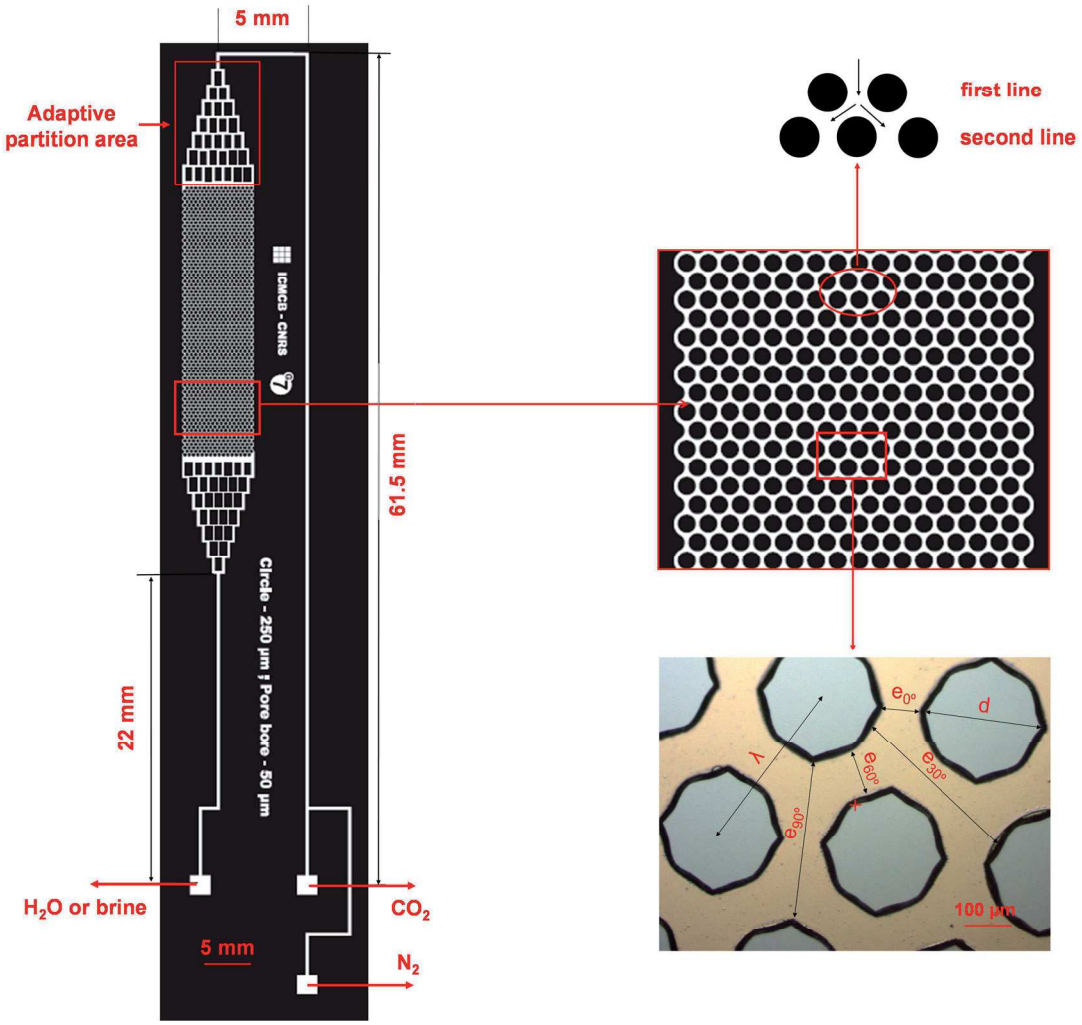

Fig. 4-3 *(a) Full view of the micromodel design with a typical 2D pore pattern connected to a single port of the output channel and two ports of the input channel. The external dimensions are 78×20 mm^2, while the pore network area is 20.2×5 mm^2. (b) Enlargement of the red rectangular area (4.4×5 mm^2) of part (a). (c) Real picture of the enlarged (red part) fabricated micromodel (real size: 0.8×0.6 mm^2).*

The width (transverse to the mean flow direction) and the length (parallel to the mean flow direction) of the staggered pore network are w = 5 mm and l = 20.2 mm, respectively (the L versus H difference being negligible). The staggered pore network

contains a patterned area of 20.2×5 mm^2, composed of 1286 discoid silica grains (circular-like of mean diameter d_m = 219 (199) μm - always lower than d_M, due to the etching process), disposed following a triangular pavement of characteristic length λ= 300 μm (along the transverse direction from the flow).

The transverse (0°) pore throat width is then e_0 =81 (101) μm (equal to the 60° pore throat width e_{60}), while the 30° pore throat width is e_{30} = 300.6 (320.6) μm, equal to the longitudinal (90°) pore throat width e_{90} (see Fig. 4-3 (c)). All the above dimensions (summarized in Table 1) are with a typical uncertainty of (±0.1) μm. Figs. 4-3 (b) and (c) are the enlargements of the schematic design and the final microscope picture (slightly tilted) corresponding to a 0.8×0.6 mm^2 pore network of the H type micromodels after microfabrication. The top of the discoid silica grains appears in blue color, while the black contour is due to the 54.8°-inclination of the etched wall.

An important remark anticipating the following discussion of Section 2.2.1, concerns the connecting free zone (500 μm longitudinal width, 5 mm transverse length) from the 8-adaptive input microchannels to the first two plots lines of the pore network (with a similar output adaptive design). Using the L type micromodels as an example, the injection of the fluid is supplied by 8 trapezoidal channels corresponding to a total input area of ~ 28000 μm^2 (see Tables 1 and 2 for details). The free transverse cross section from the 16-plots first line is ~ 19440 μm^2, while the 60° inclination cross section from the first plot line to the second one is twice larger. The corresponding mean input area $\frac{3}{2}\times 19440 = 29160$ μm^2 of the two-first staggered plot lines is then comparable to the injecting area (5.4 % difference). In addition, using the mean length unit ($\frac{3}{2}\times\lambda$) related to the above mean area, the associated linear-like porosity is given by $\phi_l = 1-\frac{d_m}{\lambda}\times\frac{2}{3} = 0.487$ (using the mean diameter d_m of the plot). However, despite an apparent well agreement with the bulk porosity (surface-like) $\phi = 1-\frac{\pi d_m^{\,2}}{2\sqrt{3}\lambda} = 1-\frac{S_p}{S_T} = 0.5155$ (where S_p is the total area covered by the

plots and S_T is the total area of the pore network), it should be noticed that the transverse open cross section area estimated from the surface porosity ($\phi \times w \times h =$ 38276 µm^2) is 1.38 time greater than the opened transverse cross section of the first plots line. Nevertheless, the design of the connecting zone appears well-optimized in regards to the continuity (on a ratio of order 1.4 to 1.5) of the channel mean velocity and the superficial mean velocity from the injecting channels to the pore network.

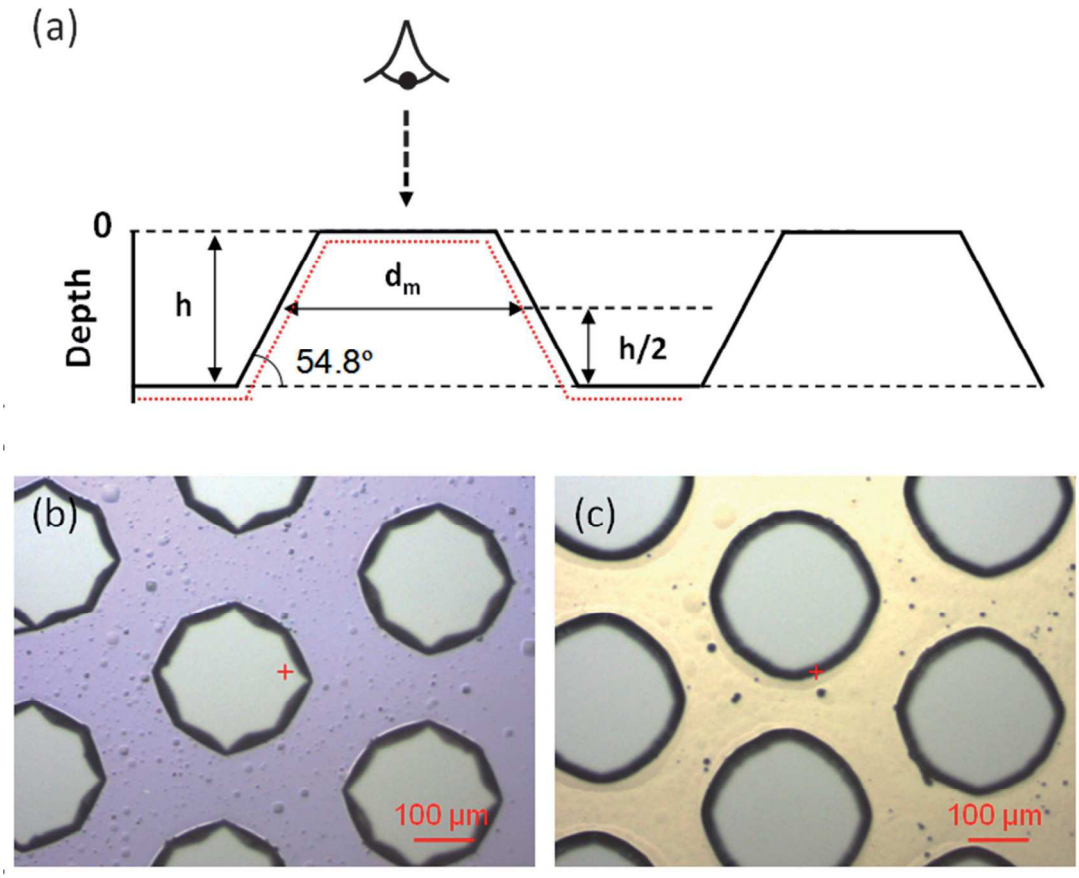

Fig. 4-4 *(a) Cross section scheme of a single silicon plot. The effects of two different (short and long) etching times are schematized by the black and red profiles, respectively (b) H type micromodel (long etching time, high porosity and depth 17 µm); (c) L type micromodel (short etching time, low porosity and depth 15 µm).*

Table 1 *Summary of the experimental conditions and geometrical dimensions of the micromodels used in the present work.*

Experimental conditions		
Pressure (MPa)	6/8/10	
Flowrate (µL·min^{-1})	25/50/100	
Temperature (ºC)	25/50	

Pore network properties		
Micromodel type	**L**	**H**
Length (mm)	20.2	
Width (mm)	5	
Wavelength (µm)	300	
Longitudinal length	259.81	
Transverse grain number	16.5	
Longitudinal grain number	78	
Total number of grains	1286	
Depth (µm)	15	17
Top grain size (µm)	208.47	187
Bottom grain size (µm)	229.53	211
Grain mean diameter – d_m (µm)	219	199
e_0 pore width (µm)	81	101
e_{30} pore width (µm)	300.62	320.62
e_{60} pore width (µm)	81	101
e_{90} pore width (µm)	300.62	320.62
Bulk (surfacic like) porosity	0.5155	0.600

Channel / pore network connecting zone		
Input area (8 channels) (µm^2)	27660	34136
1st transverse line free area (16 pores) (µm^2)	19440	27472
2nd staggered line free area (32 pores) (µm^2)	38880	54944
Poral interstice area unit - A_p (µm^2)	1215	1717
Entry linear porosity (see text)	0.5133	0.558

The homogeneous pore network types considered on this chapter were etched on a silicon wafer using a wet chemical etching technique (under a thermal alkaline solution) at various etching times (45 min and 50 min). Therefore, two different

etching depths (15 and 17 μm) and the two different relative positions of the (54.8° inclination) etching walls can be obtained. Although both were generated from the same mask, the final results for the cross sections (channel and plots) exhibit relative differences in the trapezoidal shaped channels and the trapezoidal shaped silica plots of polygonal form (approximated in the following by a cylindrical shape). The related details for better understanding of the etching effects are given in Fig. 4-4.

Table 1 summarizes the values of the dimensional sizes of the pore networks for the two families of micromodels used in this study. Finally, a cover wafer of Pyrex glass was anodically bonded to the etched silicon wafer to form the 2D porous micromodel.

The high-pressure micromodel can operate at pressures up to 15 MPa and temperature of 400 ºC. The high thermal conductivity of silicon (see Chapter 2) favors the temperature homogeneity in the main part of the micromodel, especially at the pore network level. Note that the design of the inlet/outlet feeding microchannels was made to ensure isothermal fluid flows in the pore network, making our initial hypothetic temperature profile realistic. This is supported by results from numerical simulations of the Graetz - Nusselt configuration previously obtained for a flowing fluid in a cylindrical tube (internal diameter 250 μm) maintained at constant temperature [2]. It was indeed demonstrated that the length extension to reach homogeneous temperature is of order of a few centimeters.

The micromodels are supposed to have an uniform well water-wetting surface feature, due to the piranha treatment before bonding; however, extra care was given to ensure the hydrophilic nature of the surface by thoroughly cleaning the micromodels before each experiment by injecting (each time for 10 min at 50 $\mu L.min^{-1}$) in the following order: isopropanol, deionized (DI) water, H_2O_2 solution, DI water. The micromodel were finally flushed by N_2 at a few bar for 15 min, and dried at 150 °C for several hours in an oven.

2.2 Experimental Procedures

After assembling and cleaning the microsystem, all the external components directly connected with the micromodel leads to the illustrative view of the experimental setup shown in Fig. 4-5.

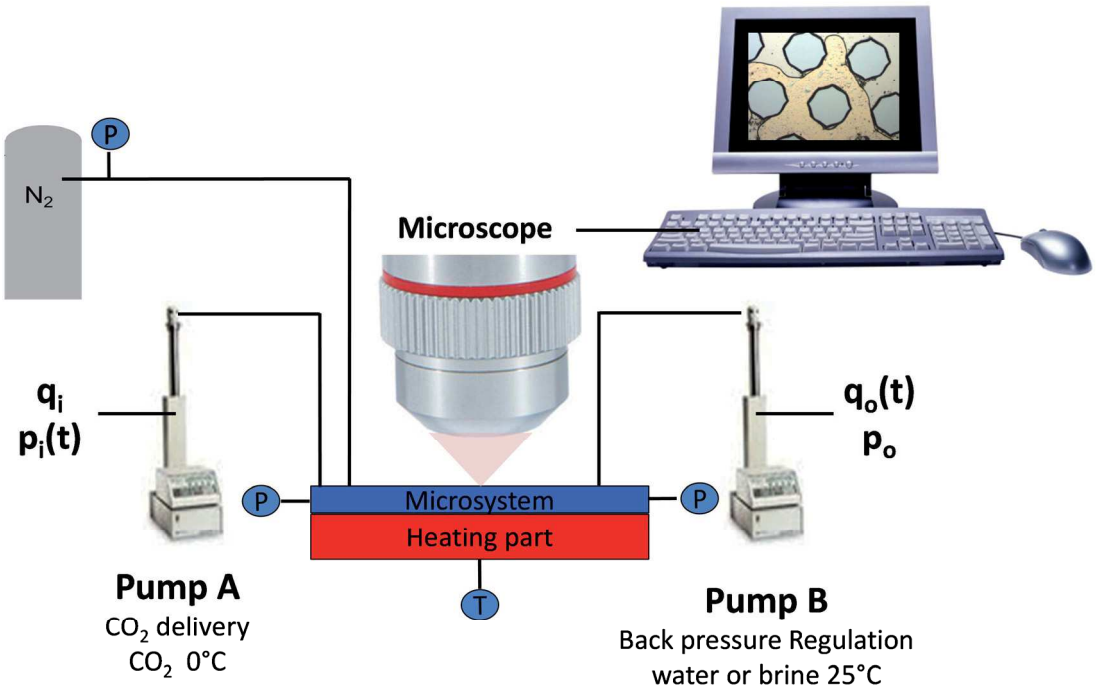

Fig. 4-5 *Illustrative view of the experimental setup corresponding to schematic view of Fig. 4-1. Pictures show the syringe pumps with q(t), p(t) fine controller leading to the monitoring of the supplied flow rate or the working pressure. The two additional pressure sensors inserted at the inlet/outlet of the micro device are only used when considering pure water flow (see Section 2.2.1). Temperature in the micromodel is maintained constant thanks to a heating part contacting the microdevice and controlled by a temperature controller (Eurotherm®).*

The high-pressure pumps A and B are Teledyne ISCO 100DM model syringe pump with fine pressure and flow rate control. From comparison with the schematic setup of Fig. 4-1, the only noticeable difference is the cleaning line, which connects the high pressure nitrogen bottle (N_2 quality) to the second port of the micromodel inlet

channel (see Fig. 4-3(a)). The use of the cleaning line is thus restricted to the required operations (mainly water, brine, and/or CO_2 drying of the internal wall surfaces of the various setup fluid volumes) that separate successive experiments using different fluid systems.

2.2.1 Preliminary experiments with pure water imbibition

We first ran experiments with pure water imbibition of the micromodel with two main objectives:

i) Validate the hypothetic flowing regimes in the tubing part, the channel part, and the pore network part;
ii) Estimate the pressure drop of the two micromodel types and their related permeabilities.

In order to replace the initial gas inside the micromodel (N_2 or Air) by pure water, the latter was first injected into the micromodel through pump B (outlet) monitored at constant flow rate until the full set-up is completely saturated (water flow from right to left in the illustrative views of Figs. 4-1 and 4-5). Then, both pumps (A and B) are loaded with pure water in order to compare the effect of injection from one side of the experimental set-up or the other.

In this first step, the inlet (or outlet) port of the micromodel (depending on whether pump A or pump B in used for water injection) is opened ($p_i = p_{atm}$ = atmospheric pressure). The increasing upstream pressure $p_o(t)$ is recorded as a function of time until the stationary flowing regime is reached, *e.g.*, when the constant maximum value $p_{o,max}$ is reached. The corresponding behavior of the normalized pressure drop $p_o(t)/p_{o,max}$ is illustrated in Fig. 4-6.

Depending on whether the water is injected from pump A or pump B, one can notice a hysteresis behavior in the $p_i = f(t)$ curve at constant $q_i = 50\ \mu L \cdot min^{-1}$. This is in complete agreement with the non-symmetry of the micromodel design, since the lengths of the feeding microchannel in the adaptive part of the micromodel are different (see Fig. 4-1), while the typical time duration of the experiment (~ 20 min) is

mainly due to the resistance of the moving triple contact line water/gas/silica. Nevertheless, the same final pressure drop is obtained, whatever the flow direction, as expected.

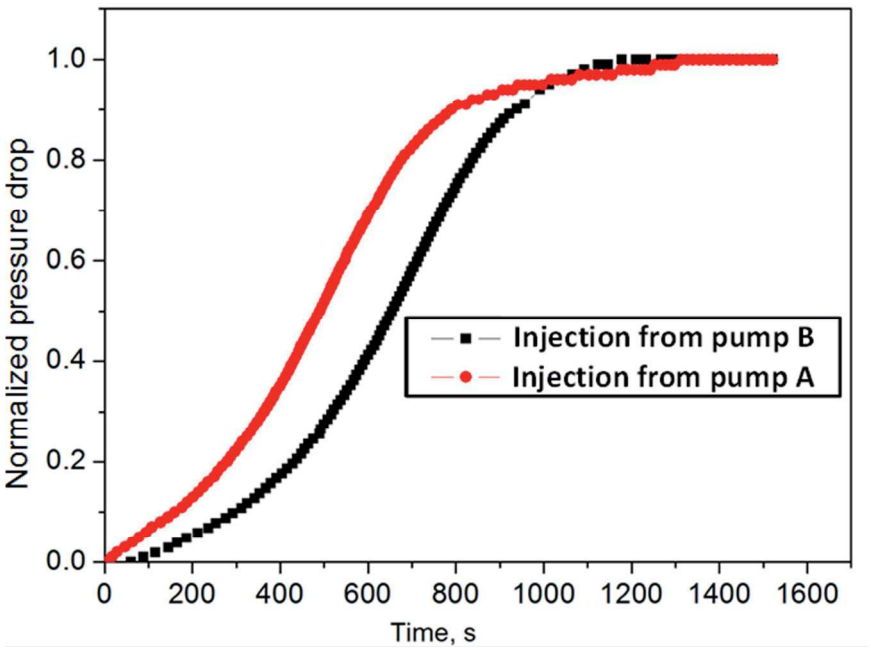

Fig. 4-6 *Normalized pressure drop measured in water imbibition experiments from both side of the experimental set-up (the downstream pressure being maintained at 0.1 MPa). The experimental setup was initially filled with a gas (air or N_2).*

An additional pressure sensor was also inserted close to the connecting block, at the entry port of the microdevice. While flowing pure water at 50 µl·min^{-1} through the experimental setup, no difference was observed between the pressures measured in the pump and at the inlet of the microdevice (except an intrinsic pressure offset (~ 0.01 MPa) due to their respective calibration). This result demonstrates that the feeding tubings connecting the pumps to the microdevice (internal diameter: 500 µm) do not generate any pressure drop, as expected. It also confirms the expected laminar Stokes flow of water inside the tubing part (typically, at 25 °C, using a water flow rate of 50 µl·min^{-1} with a 1 m length, 500 µm diameter tube, the expected pressure drop calculated using the Hagen-Poiseuille law is of few ten of Pa).

In the second step, both pumps were then connected to the micromodel. The inlet pump (A or B) was working in constant flow mode, while the oulet pump (A or B) was working in a constant pressure mode. After water filling, the setup was gradually pressurized up to one typical value of the experimental pressure range (5 MPa). Then, similar procedures than the one of the first step are repeated for the two opposite directions and different volumetric flow rate values (50, 75 and 100 µL·min^{-1}) of water (reversing the constant flow rate/ constant pressure mode of pumps A and B, successively). Finally, the procedures were also performed at 8 MPa.

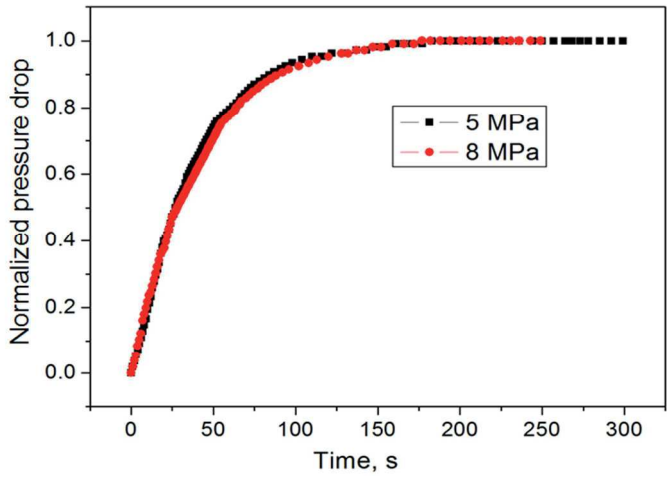

Fig. 4-7 *Normalized pressure drop measured in the micromodel by flowing water at q_i = 50 µL·min^{-1}, while applying a back pressure of 5 MPa and 8 MPa, respectively.*

As representative examples of the second step, we have reported in Fig. 4-7, the time response of the normalized pressure drop from reference to the maximum value of the pressure drop for the final stationary flow regime of water. The figure shows the similarity of the time responses at constant volumetric flow rate q_i = 50 µl·min^{-1} and at two different output pressures, 5 MPa and 8 MPa, due to viscous displacement of the initial water filling and wetting the free volume of the micromodel. Here, the typical experimental time (~ 4 min) is driven by the time required to exchange water in the volume (~200 µL) of the 1 m length of the external tubings, significantly larger than the total volume (~1.45 µL) of the micromodel (here is considered the H type

micromodel, where the typical volumes of the single channel, the adaptive area, and the pore network parts of the micromodel are 0.31, 0.36, and 0.78 μL, respectively). In all cases, the maximum value of the pressure drop corresponds to the final stationary flow regime of water only driven by the viscous effects and the volumetric flow rate. In addition, we have also reported in Table 5 the maximum values of the pressure drops for the stationary flow regime of water at 5 Mpa, for the flow rates 50, 75 and 100 $\mu l \cdot min^{-1}$, for both types of micromodels.

The pressure drop Δp across the micromodel can be modeled as the sum of three main contribution terms due to the viscous water flows across:

1) the inlet/outlet channels,
2) the input/output adaptive channels and,
3) the pore network itself.

The exact formulation of each pressure drop term remains a challenging situation in the absence of measurements of the flow velocity local field in all the different parts of the micro device. Nevertheless, it remains possible to use a phenomenological approach based on the water flow sensitivity to the hydraulic resistance. Indeed, the flow distinction is related to the geometrical key parameters of the expected flow regimes, namely, the inverse fourth power of the hydraulic diameter D for a laminar viscous flow in a channel and the unknown inverse permeability K^{-1} for the Darcy viscous flow in the pore network. Thus, to overcome the existing deficiencies in the K estimation, we assume, in a first step, that the permeability of the micromodel can be expressed in unit of a reference area (noted A_p below), characteristic of each pore network. Simultaneously, the small difference in the channel lengths and the pore network total area due to the etching process of each micromodel type is neglected.

Now, using the Hagen-Poiseuille equation, we obtain $\Delta p_{HP} \propto \frac{\mu}{D_c^4} \times L_c \times q_i$ for a given water volumetric flow rate q_i delivered to a channel of length L_c (labeled by the subscript "c") and typical hydraulic radius D_c (μ is the water viscosity and the subscript HP recall for the use of the Hagen-Poiseuille equation). Δp_{HP} is the pressure

drop across the inlet/outlet trapezoidal feeding microchannels of total length $L_c \approx 86.5$ mm and equivalent rectangular cross section $w \times h \approx 230.5 \times 15 \mu m^2$, or equivalent hydraulic diameter $D_c \sim 30$ μm. The pressure drop across these microchannels is much larger than across the external tube (labeled by the subscript "t") of length $L_t \sim 1$ m and diameter $D_t = 500$ μm, and must be accounted for as a first contribution term. However, comparing the micromodel type (labelled L and H, respectively), we expect that the pressure drop ratio $\left(\frac{\Delta p_L}{\Delta p_H}\right)_{c,HP}$ for the inlet/outlet channel part is only proportional to the fourth power $\left(\frac{D_{i,H}}{D_{i,L}}\right)^4$ of the hydraulic radius ratio. The similar reasoning applied for the similar partition channels involved in the input/output adaptive partition parts leads again to $\left(\frac{\Delta p_L}{\Delta p_H}\right)_{a,HP} \propto \left(\frac{D_{i,H}}{D_{i,L}}\right)^4$, where the subscript "a" now recalls for the adaptive partition part. However, for each type, it is essential not to forget that a supplementary geometrical factor accounts for the contributions of each unit of the patterned channel providing the successive partition of the input constant volumetric flow rate q_i. Introducing this geometrical factor leads to the following equivalent "single channel" length (labelled with the subscript (eq)):

$$L_{a(eq)} = \left(\frac{1}{2} + \frac{1}{3} \cdots + \frac{1}{8}\right) \times L_a \times 2 = 3.456 \times L_{pattern} \qquad \text{Eq. 4-2}$$

where $L_{pattern} = 1.7$ mm is the length of a channel unit pattern (similar for both micromodel types) and the factor 2 accounting for the input/output adaptive partition parts of the micromodel.

At the inlet of the connecting free zone discussed above, the input mean velocities at constant volumetric flow rate q_i are only driven by the related area $N_{ac} \times A_c$ of the injection channels (where $N_{ac} = 8$ is the number of injecting channels and A_c the trapezoidal cross section area of a single channel). At the outlet of the connecting free

zone, the effective entry flow cross-sectional area $A = \phi \times w \times h$ of the pore network is ~1.4-1.5 larger, and the resulting Darcy velocity always remains proportional to the single channel cross section A_c. On the other hand, the "pore network" equivalent length of the single channel of hydraulic diameter D_c with same flow rate q is then:

$$L_{p(eq)} = \frac{1}{N_{ac}} \times l \times \frac{N_{ac} \times A_c}{A} = 0.0893 \times l \qquad \text{Eq. 4-3}$$

where l = 20.2 mm is the true longitudinal length of the pore network. However, the equivalent length depends here on the selected micromodel type through the ratio A_c/A. In addition, the pore network permeability (expressed in m^2) can be assumed to be proportional to a characteristic pore area A_p (see above), as for instance the transverse pore area between two plots of the 16-plots first line, or equivalently, as the square of the equivalent hydraulic diameter $(D_c)^2$, when the main objective is the comparison of both micromodel types (L and H). Finally, for a given flow rate, the pore network contribution term of the pressure drop is then driven by the inverse products $\left(D_c^{\,2} \times A_p\right)^{-1}$, or $\left(D_c\right)^{-4}$ or $\left(A_c \times A_p\right)^{-1}$, equivalently. Now, using the Darcy equation, we obtain $\Delta p_D \propto \frac{\mu}{A_p} \times l \times \frac{q}{A_c}$ (the subscript "D" recalls for a description using the Darcy equation). Alternatively, using the Hagen-Poiseuille equation when the pore network is simulated by an equivalent single channel, we obtain $\Delta P_{p,HP} \propto \frac{\mu}{\left(D_c\right)^2} \times L_{p(eq)} \times \frac{q}{\left(D_c\right)^2}$ (the subscript "p,HP" recalls the pore network modeling using the Hagen-Poiseuille equation).

In both case, the expected pressure drop ratio $\left(\frac{\Delta p_L}{\Delta p_H}\right)_D$ for the two pore network families of true length l, or equivalent single channel length L_p, is given by the ratio of the inverse products $\left(\frac{D_{c,L}^{\,4}}{D_{c,H}^{\,4}}\right)_{HP}$ or $\left[\frac{\left(A_i \times A_p\right)_L}{\left(A_i \times A_p\right)_H}\right]_D$. As the condition

$K_{L,H} = \frac{(D_c^4)_L}{(D_c^4)_H} \approx \frac{(A_p \times A_c)_L}{(A_p \times A_c)_H}$ appears to be satisfied (see Table 2), we expect the following results:

$$\Delta P_H = K_{L,H} \times \Delta P_L \qquad \text{Eq. 4-4}$$

Where the pressure drop ΔP for the L or H family is the following three term summation of the channel $\Delta P_{c,HP}$, the adaptive $\Delta P_{a,HP}$ and the pore network $\Delta P_{p,D}$, pressure drop contributions:

$$\Delta P = \Delta P_c + \Delta P_a + \Delta P_p \qquad \text{Eq. 4-5}$$

Each contribution term writes as follows:

$$\begin{aligned} \Delta P_{c,H} &= K_{L,H} \times \Delta P_{c,L} \\ \Delta P_{a,H} &= K_{L,H} \times \Delta P_{a,L} \\ \Delta P_{p,H} &= K_{L,H} \times \Delta P_{p,L} \end{aligned} \qquad \text{Eq. 4-6}$$

Therefore, the pressure difference measurement $P_A - P_B$ from the two pumps A and B, equal to the total pressure drops ΔP_L or ΔP_H across the micromodel L or H, provides the entry data to validate the above geometrical characteristic behavior of each pressure drop term due to the laminar viscous flow and the equivalent porous viscous flow, respectively.

All the numerical values are reported in Tables 2 to 4, where the last column shows a satisfactory agreement for the expected geometrical characteristic ratios $K_{L,H}$ of the pressure drop across the various micro model parts and the experimental ratios $\frac{\Delta P_L}{\Delta P_H}$ at different volumetric flow rates. It is then possible to estimate separately, the

pressure drops due to the three parts of the micro model, as being proportional to their true or equivalent length L_c, $L_{a(eq)}$, and $L_{p(eq),HL}$, *i.e.*:

$$\left(\Delta P_{H,L}\right)_{HP} = \frac{L_c}{L_c + L_{a(eq)} + L_{p(eq),HL}} \times \Delta P_{HL}$$

$$\left(\Delta P_{H,L}\right)_{HP} = \frac{L_a}{L_c + L_{a(eq)} + L_{p(eq),HL}} \times \Delta P_{HL} \qquad \text{Eq. 4-7}$$

$$\left(\Delta P_{H,L}\right)_{D} = \frac{L_{p,HL}}{L_c + L_{a(eq)} + L_{p(eq),HL}} \times \Delta P_{H,L}$$

The equivalent total length is $L_c + L_{a(eq)} + L_{p(eq),HL} = 96.17$ (96.03) mm for H (L) family. In the following numerical estimations, we select a similar equivalent total length of 96.1 mm for the two families.

Finally, we have illustrated in Fig. 4.8 the above single channel modeling of the various pressure drops in the micro model taking into account the true lengths of the inlet/outlet feeding microchannels and the equivalent lengths of the entry/out adaptive partition parts and the pore network part. Therefore, a future check of this micro model modeling will be possible, performing a similar experiment where the "equivalent" capillary tube of true length $L_c + L_{a(eq)} + L_{p(eq),HL} = 96.17$ (96.03) mm and true diameter $D_c = 27.79$ (31.4) µm replaces the H (L) micro model. We also note that this experiment will be of interest to investigate the precise value of the numerical prefactor of the Hagen-Poiseuille equation and/or the precise definition of the analog hydraulic diameter for complex cross section shapes of the channels and pore networks. As illustrative examples from the present L type micromodel case, with diameter $D_c = 27.79$ µm, the *experimental* prefactor of the Hagen-Poiseuille

law is 11.5, compared to $\frac{128}{\pi} \approx 40.74$, while, with this theoretical prefactor, the *experimental* hydraulic diameter increases to 38.3 µm.

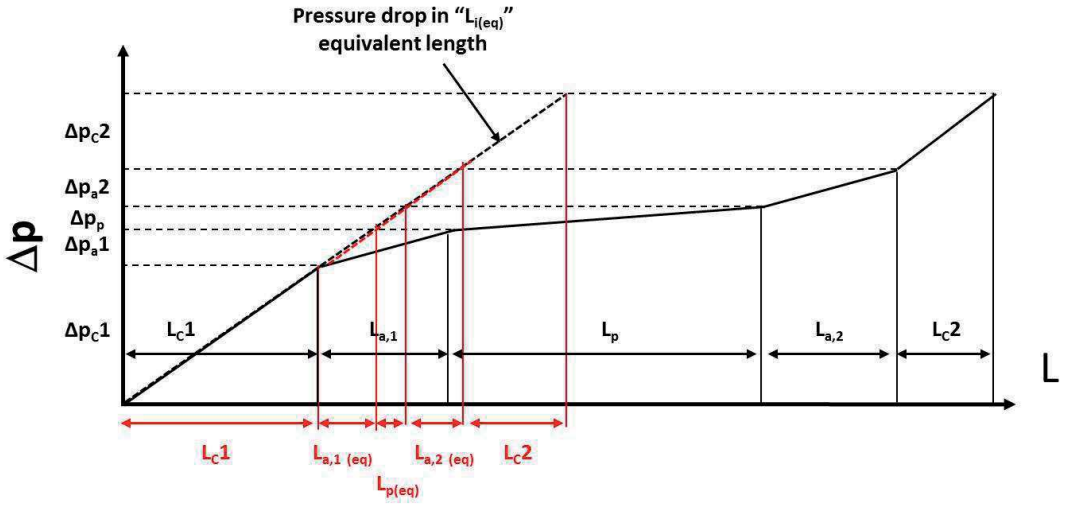

Fig. 4-8 *Illustration of the pressure drops in the different zones of the micromodel and their counter parts using the "$L_{i(eq)}$ equivalent" length of the single microchannel with hydraulic diameter D_c.*

These pressure drop values across the pore network are now used to calculate the permeability of each pore network type using Darcy's law as follows:

$$K_{H,L} = \frac{\mu \times Q \times L_p}{A \times (\Delta p_{H,L})_D} \qquad \text{Eq. 4-8}$$

The results are $K_L = (1.07\pm0.03)\times10^{-11}$ m^2 and $K_H = (1.14\pm0.04)\times10^{-11}$ m^2, respectively (see Table 4 for detail). The error bar is only indicative of the dispersion of the numerical estimations.

We note that the above results are similar to the ones recently published [3] from measurements of pressure drop and flow resistance in micromodels with integrated micro pillars. That reinforces the interest for experimentally checking the analogy mentioned above.

Table 2. *Geometrical characteristic data for the single channel modeling of the inlet/outlet channel part and the partition channels of the entry/out adaptive parts of the micromodel.*

Inlet/outlet/ adaptive channels				
Micromodel type		**L**	**H**	**Ratio**
Depth	**h (µm)**	15	17	
Inlet + outlet feeding µchannel length	**L_c (mm)**	88.5	88.5	
channel top width	**w_{ct} (µm)**	241.03	262	
channel bottom width	**w_{cb} (µm)**	219.97	240	
channel mean width	**w_c (µm)**	230.5	251	
Channel side	**s_{ch} (µm)**	18.36	20.80	
Channel cross section perimeter	**l_c (µm)**	497.713	543.608	
Channel cross section area	**A_c (µm^2)**	3457.5	4267	
Channel hydraulic diameter	**D_c (µm)**	27.79	31.46	
Laminar viscous flow parameter	**$(1/D_c)^4$ ($\times 10^{-6}$ µm^{-4})**	1.677	1.021	0.6135
(hydrau.) mean velocity (q_i=100 µL·min^{-1})	**(m.s^{-1})**	2.75	2.14	
Reynolds number (Q=100 µL·min^{-1})		85.9	75.9	
Adaptive partition channel length	**$L_{a(eq)}$ (mm)**	5.84		
Adaptive/ Pore network connecting area				
Input area (N_{ac} = 8 channels)	**(µm²)**	27660	34136	
1st Open area (16 holes, tranverse)	**(µm²)**	19440	27472	
2nd Open area (32 holes, 60° inclinaison)	**(µm²)**	38880	54944	
Poral interstice area unit	**A_p (µm^2)**	1215	1717	
Porous viscous flow parameter	**$1/A_pA_c$ ($\times 10^{-7}$ µm^{-4})**	2.380	1.365	0.5735

Table 3. *Geometrical characteristic data for the single channel modeling of the micromodels pore network area.*

Pore Network area				
Type of micromodel		**L**	**H**	**Ratio**
Depth	**h (μm)**	15	17	
Free transverse area	**A (μm²)**	38662	51000	
Pore network /Input channel area ratio	**$A/8A_c$**	1.398	1.494	
Pore interstice transverse area	**A_p (μm²)**	1215	1717	
Porous viscous flow parameter	**$1/A_pA_c$ ($\times 10^{-7}$ μm^{-4})**	2.380	1.365	0.5735
Equivalent length	**$L_{p(eq)}$ (mm)**	1.81	1.69	

Measured pressure drop in Micro model				
Flow rate 50 μL·min^{-1}	**ΔP (MPa)**	1.43±0.04	0.88±0.02	0.6154
Flow rate 75 μL·min^{-1}	**ΔP (MPa)**	2.08±0.05	1.26±0.02	0.6058
Flow rate 100 μL·min^{-1}	**ΔP (MPa)**	2.71±0.05	1.62±0.03	0.5978
Equivalent total length: $L_c+ L_{a(eq)}+ L_{p(eq)}$	**(mm)**	96.1±0.1		

Table 4. *Measured and calculated pressure drops across the micromodels and pore network permeability from the single channel modeling of each micromodel type at p = 5 MPa and 3 different volumetric flow rates. The viscosity value of pure water is 0.8884 mPa.s at p = 5 MPa and T = 25 °C (*). The error-bar is indicative of the uncertainty in the estimation of the equivalent length.*

Volumetric flow rate (µl/min)	**50**	**75**	**100**
L type micromodels			
Measured pressure drop (MPa)	1.43±0.04	2.08±0.05	2.71±0.05
Channel pressure drop (MPa)	1.08	1.57	2.05
Adaptive pressure drop (MPa)	0.31	0.455	0.59
Pore network pressure drop (MPa)	0.037±0.002	0.054±0.003	0.070±0.004
Pore network permeability (10^{-11} m^2) (*)	1.04	1.07	1.10
Darcy number $\left(\sqrt{\frac{K}{h^2}}\right)$	0.215	0.218	0.221
Mean velocity (mm.s^{-1})	21.55	32.33	43.11
Reynolds number (transverse pore width)	1.96	2.95	3.93
H type micromodels			
Measured pressure drop (MPa)	0.88±0.02	1.26±0.02	1.62±0.03
Channel pressure drop (MPa)	0.69	1.15	1.49
Adaptive pressure drop (MPa)	0.16	0.07	0.08
Pore network pressure drop (MPa)	0.027±0.001	0.038±0.002	0.050±0.003
Pore network permeability (10^{-11} m^2) (*)	1.09	1.16	1.17
Darcy number $\left(\sqrt{\frac{K}{h^2}}\right)$	0.220	0.227	0.228
Mean velocity (mm.s^{-1})	16.34	24.51	32.68
Reynolds number (transverse pore width)	1.86	2.78	3.71

2.2.2 CO_2 drainage experiments using the micromodels saturated with brines

After removing the two pressure sensors implemented at the micromodel (inlet/outlet) levels (see Fig. 4-5), brine was injected into the experimental setup to replace pure water using pump B until the flow lines and the micromodel were fully brine-saturated. The system was then gradually pressurized up to experimental pressures for 30 min. Then, the syringe pump on the brine side (B) withdrew brine at a constant pressure.

The syringe pump A was loaded with pure CO_2 at 10 MPa and 0 ºC for 1 h to ensure a constant CO_2 volume. The pressure of liquid CO_2 was first adjusted to the experimental mean pressure "$p>p_c$" representative of selected geological pressure (here we have selected the $scCO_2$ injection as a typical example). Then CO_2 was injected into the experimental setup at a constant volumetric flow rate (q_i), leading to the so-called CO_2 drainage process, *i.e.*, the CO_2 invasion of the fluid volume occupied by the brine. In the following discussion of the experimental results, the outer drainage process in both external feeding tubes (500 μm diameter, 0.5 m long each) connecting the pumps to the micromodel, which were also fully saturated with water at the initial time, is not considered, excepted the fact that the inlet external tube participates to the heating of the injected CO_2 in the micromodel (see Fig. 4-1 and the introductive section 1). At the outlet pump level, this external process produces two additional water flows, separated in time by the duration of the CO_2 invasion of the saturated micromodel, i.e., from the initial time where CO_2 reaches the inlet single channel of the micromodel to the so-called breakthrough time (see below) where the percolation of flowing CO_2 across the complete micromodel occurs. Therefore, the CO_2 drainage process of interest in our experiments starts when CO_2 reaches the inlet single channel of the micromodel. Moreover, as shown in Fig. 4-1, it is assumed that this flowing CO_2 also reaches quasi-simultaneously the experimental mean temperature "$T>T_c$" representative of the selected (here supercritical) temperature.

Obviously, the CO_2 drainage process part of main interest starts when the $scCO_2$ reaches the pore network. The pressure distribution across the micromodel was measured by the pumps A and B pressure transducers. Images of fluid phase distributions in the water/brine-CO_2 system were recorded throughout and after the drainage process using confocal microscopy described below.

2.3 Fluid systems used in the CO_2 drainage experiments

The typical fluids initially used in the experiments consisted of DI water, pure CO_2 and a chloride buffered solution. The brine was prepared by mixing deionized (DI) water and NaOH. Glycine and $CaCl_2$ (Sigma-Aldrich, ACS reagent grade) were additionally added to this solution when considering carbonates precipitation experiments. In that case, a NaOH-glycine buffered solution was first prepared, by adding 0.1 M $CaCl_2$ in the solution. Brines were degassed, stored at room temperature and used within 48h. The pH values of the brines were maintained at 10 before starting the CO_2 flowing experiment.

In most of the selected geological formations for the CO_2 storage at depths below about 800 m, CO_2 can reach the supercritical region (*e.g.* $p > p_c$ and $T > T_c$). Here we have investigated three distinct conditions of the CO_2 injection, which correspond to the p, T values where CO_2 is a pressurized liquid, a supercritical fluid or a dense gas, respectively. Therefore, the experiments were conducted at one temperature below ($T_{ambiant}$ = 25 °C) and two temperatures above (T = 50 °C and T = 75 °C) the CO_2 critical temperature (T_c = 31 °C), conjugated with two controlled pressure levels p = 6 MPa and p = 8 MPa, *e.g.,* below and above the CO_2 critical pressure (p_c = 7.39 MPa), respectively. For the selected (p, T) conditions investigated in this Chapter, Table 5 summarizes the physical properties of the fluid systems.

Table 5 *Summary of Fluid Properties in the operating conditions.*

P, T Conditions	8 MPa, 25 ºC	8 MPa, 50 ºC	8 MPa, 75 ºC	6 MPa, 50 ºC
Domain	Liquid	Supercritical		Gas
H_2O viscosity, μ_{H2O}, mPa·s	0.8884	0.5482	0.3798	0.5479
H_2O density, ρ_{H2O}, g·mL^{-1}	1.0006	0.9914	0.9783	0.9906
CO_2 viscosity, μ_{CO2}, mPa·s	0.067	0.0204	0.02	0.01793
CO_2 density, ρ_{CO2}, g·mL^{-1}	0.7647	0.2192	0.1681	0.1352
Viscosity ratio ($M=\mu_{CO2}/\mu_{H2O}$)	0.07542	0.03721	0.05266	0.03272
Interfacial tension[a], mN·m^{-1}	30.3	37.5	37.2	43.5

[a] from Chiquet *et al.* [4].

2.4 Optical system

The high resolution camera (10 x and 5 x) from the confocal Raman spectrometer microscope was used to acquire images of the CO_2 displacement process occurring in the micromodels. The CamStudio software was used to record live movies. The micromodel was placed horizontally on the isolation stage of the microscope, which can move at will. A homogeneous backlight was placed below the chip to improve the quality of images, whose contrast is reinforced by a spectral filter. On the images, the water phase thus slightly appears in gray, while the $scCO_2$ phase is brighter since its refractive index value is far from the one of SiO_2 (from the microreactor), oppositely to water* (Fig. 4-9). Raman spectroscopy was used to *in situ* characterize the local dissolution and reactions between CO_2 and brine.

* Refractive index in the considered conditions: Water: ~ 1.33, $scCO_2$: ~ 1.1, Silica: ~ 1.50.

The visualization setup can obtain enough qualitative information for studying the CO_2 invasion processes mechanisms. Anticipating the following discussions provided in the next parts of this chapter, we have already illustrated in Fig. 4-9 some remarkable configurations of the two-phase distributions between CO_2 and water during the CO_2 invasion process of water wetted pore network:

(i) In Fig. 4-9 (a), the so-called "***water bridge***" connects two hydrophilic neighboring plots through interfacial meniscus of similar concave curvature governed by the shortest distance between the plots, which means that the water bridges are like "compressed" by the flow of CO_2.

(ii) The so-called "***water pool***" connects three or more neighboring plots, which is also shown in Fig. 4-9 (a).

(iii) In Fig. 4-9 (b) a so-called "***water dome***" surrounds and isolates the hydrophilic plots, while its large curvature radius governed by the plot size diameter and opposite curvature, means that the water drop seems like "expanded" by the flow of CO_2. Note that the formation of the domes is not related to the flow direction.

(iv) In Fig. 4-9 (c), ***water droplets*** (so-called "***tears***") precipitate from the flowing CO_2 rich phase when heating the micromodel.

(v) In Fig. 4-9 (d) corresponding to the case of the non-water wetting micromodel, however, only isolated (or dewetted) water droplets and isolated (or dewetted) water pools can be observed (see Fig. 4-9 (d)).

For all the cases above illustrated in Fig. 4-9, the two-phase distributions correspond to a fraction of residual water entrapped in the pore network. Such a situation demonstrates the decrease of the effective porosity of the pore network, and consequently, the reduction of the stored CO_2 quantity. Investigating these mechanisms of CO_2 invasion in the real conditions of the geological formations is then of primary importance for the CO_2 geological storage.

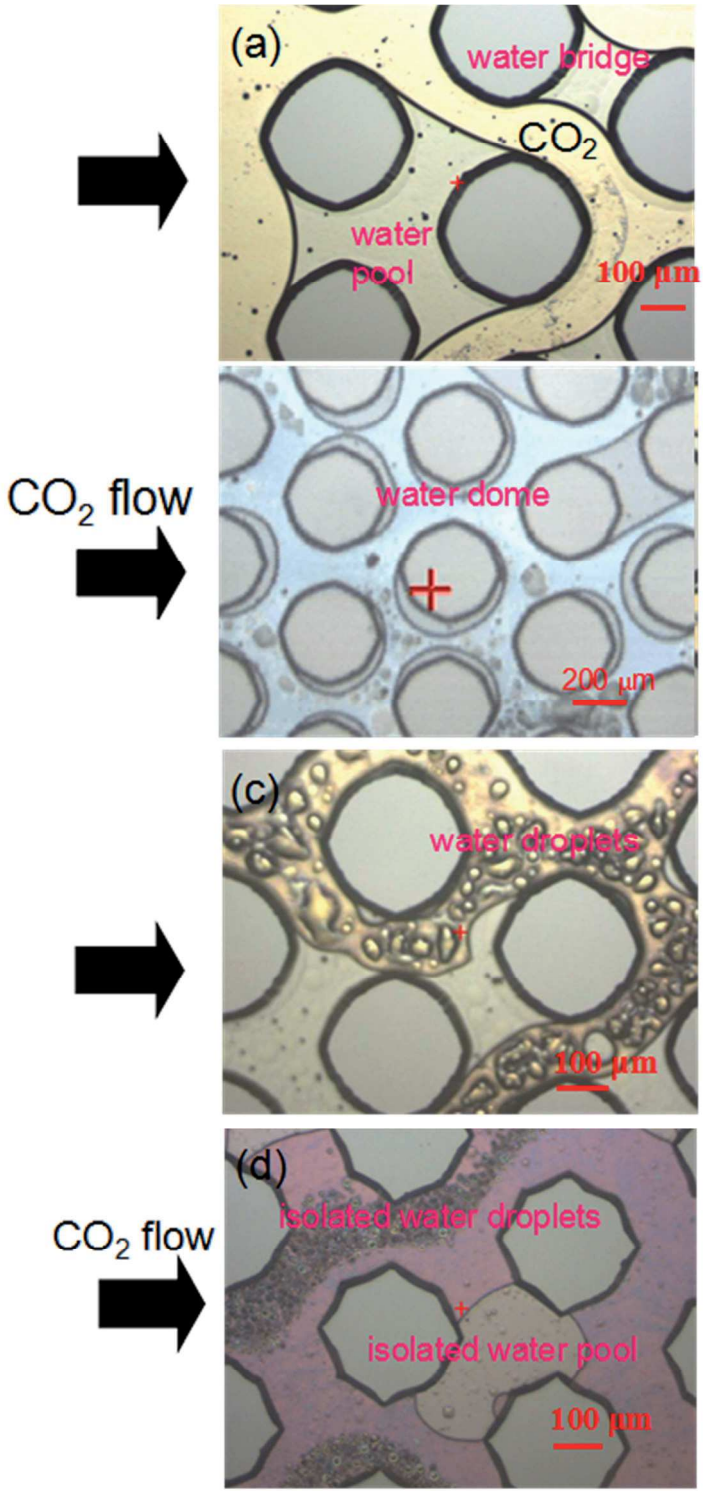

Fig. 4-9 *Examples of water phase and CO_2 phase apparent within the water wetting micromodel: (a) water bridge and water pool connecting silicon solids; (b) water dome around the solid; (c) water droplets in CO_2 phase; (d) the isolated water droplets and water pool within the non water wetting micromodel.*

To observe these remarkable configurations, three sets of experiments were run within three different micromodels:

(i) H-type micromodel (porosity = 0.6) with hydrophilic silica surface (6 MPa - 50 ºC - 50 μL·min^{-1}, 8 MPa - 25 ºC - 25/50/100 μL·min^{-1}, 8 MPa - 50 ºC - 25/50/100 μL·min^{-1}, 8 MPa - 75 ºC - 50 μL·min^{-1}),

(ii) L-type micromodel (porosity = 0.515) with hydrophilic silica surface (6 MPa - 50 ºC - 50 μL·min^{-1}, 8 MPa - 25 ºC - 25/50/100 μL·min^{-1}, 8 MPa - 50 ºC - 50/100 μL·min^{-1}),

(iii) L-type micromodel (porosity = 0.515) with hydrophobic silica surface (6 MPa - 50 ºC - 50 μL·min^{-1}, 8 MPa - 25 ºC - 25/50/100 μL·min^{-1}, 8 MPa - 50 ºC - 25/50/100 μL·min^{-1}).

The results are presented in the next Section, starting with the optical observations of the main phenomena of interest at the pore scale.

3. Results

3.1 General observations: pools, bridges, domes, tears…

During the drainage, viscous, wetting and capillary forces played significant roles by affecting local CO_2-water displacement and the subsequent CO_2 (or water) saturations in porous media. When the less viscous CO_2 phase drives the more viscous water phase out of the inlet channel of the micromodel, the viscous barrier from water phase caused a pressure distribution (Δp) across the microsystem, which can force CO_2 to push water into the inlet of micromodel.

The requirement for the fluid to enter the pore space is to break the capillary entry pressure (p_e), which occurs when $\Delta p > p_e$, the CO_2 phase therefore replacing water and remaining in the pore. As shown in Fig. 4-10, liquid CO_2 invades the porous medium, breaks the capillary barrier in the pore and displaces water to occupy the pore space.

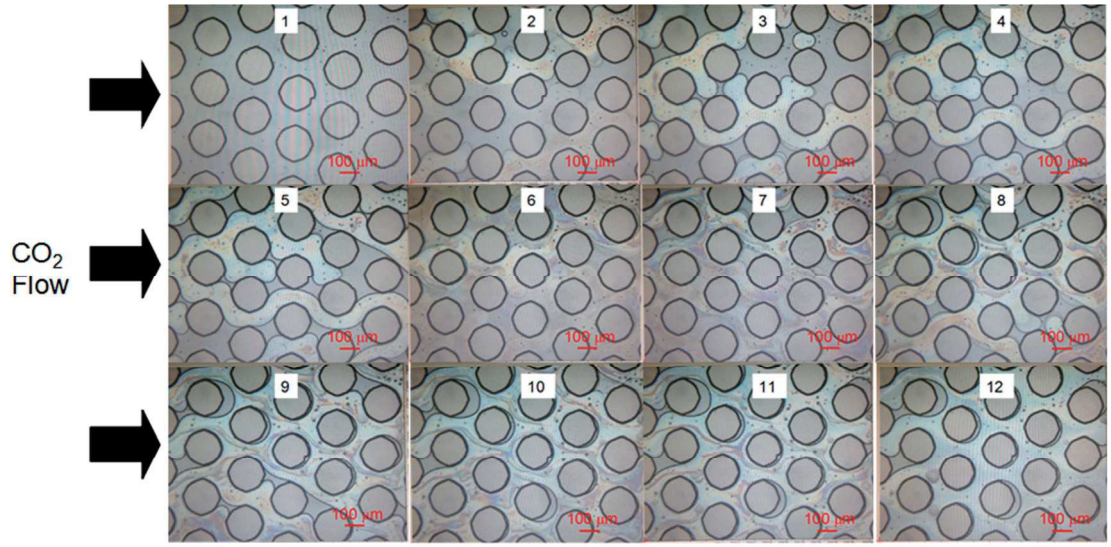

Fig. 4-10 *Images of CO_2 invasion into the water wetting micromodel saturated with water at 8 MPa - 25 ºC - 25 µL·min^{-1} captured by high speed camera (800 fr/s). The flow direction is from left to right (arrow).*

CO_2 occupied most pore spaces in the micromodel (close to the inlet), while the residual water is somewhat more present at the outlet of the micromodel (Fig. 4-11 (a)). The discontinuity of CO_2 stream on the micromodel sides occurred due to the low viscosity and flow pressure at the wall. This discontinuity in capillary pressure causes lower CO_2 saturation. Because of the hydrophilic surfaces of the porous medium silica skeleton, the residual water formed a thin wetting layer around the solid as wetted water pools (Fig. 4-11 (b)) or water bridges (Fig. 4-11 (c)).

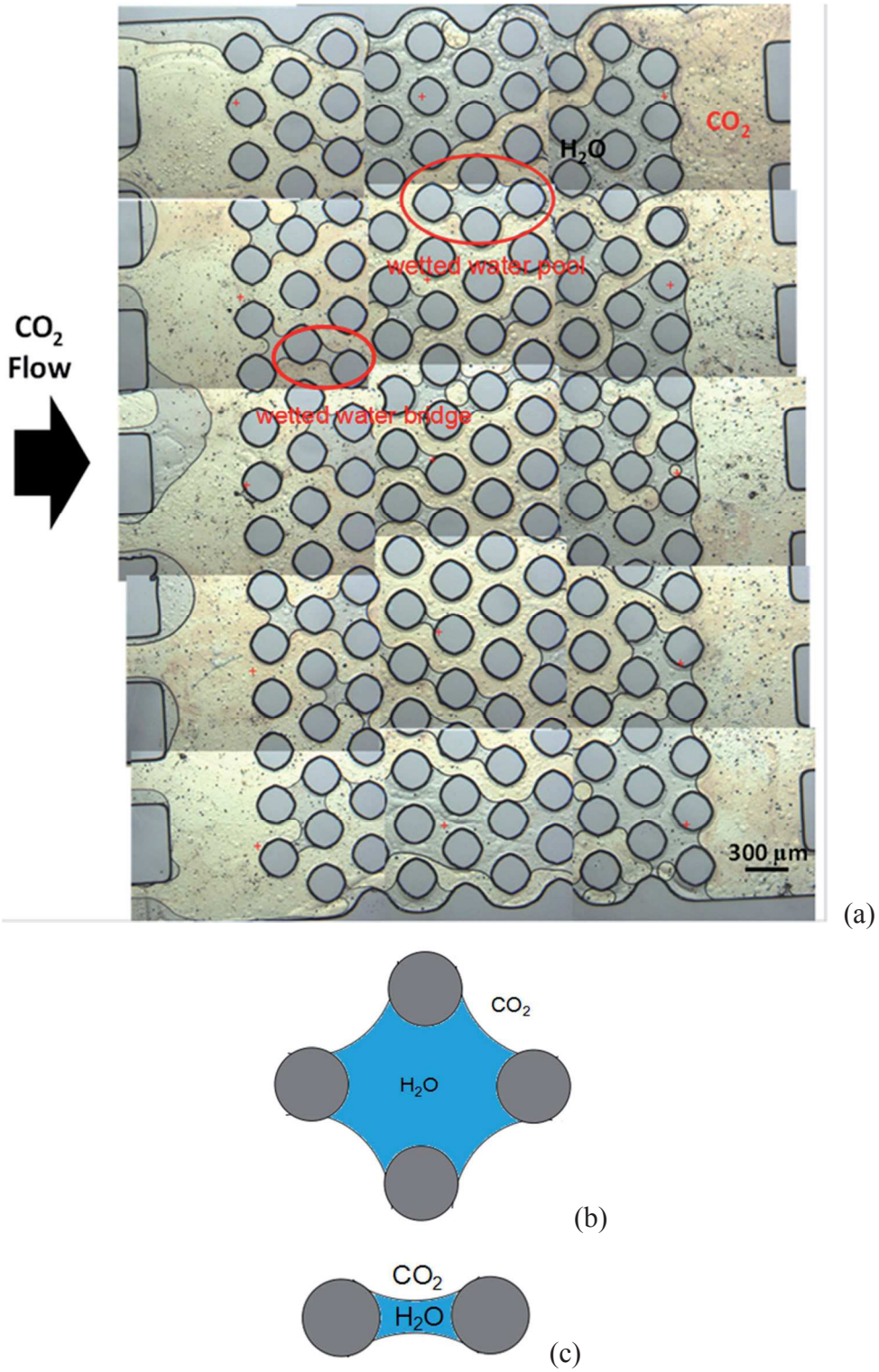

Fig. 4-11 *(a) Selected images of the CO_2 flow displacing water within the water wetting micromodel at 8 MPa - 25 ºC - 25 µL·min^{-1} (the flow direction of the displacing fluid is from left to right) . (b) Schematic drawing of the "wetted pool". (c) Schematic drawing of the "wetted bridge".*

The CO_2 distribution in a hydrophobic micromodel is shown in Fig. 4-12 (a). Since water cannot wet the surface of the surface-modified silica walls, only "dewetted pool" (or dewetted bridge) can be observed (see Fig. 4-12 (b)). Due to the high contact angle of CO_2 in such a micromodel, the capillary entry pressure is low. Thus, the injected CO_2 can easily occupy the small pores.

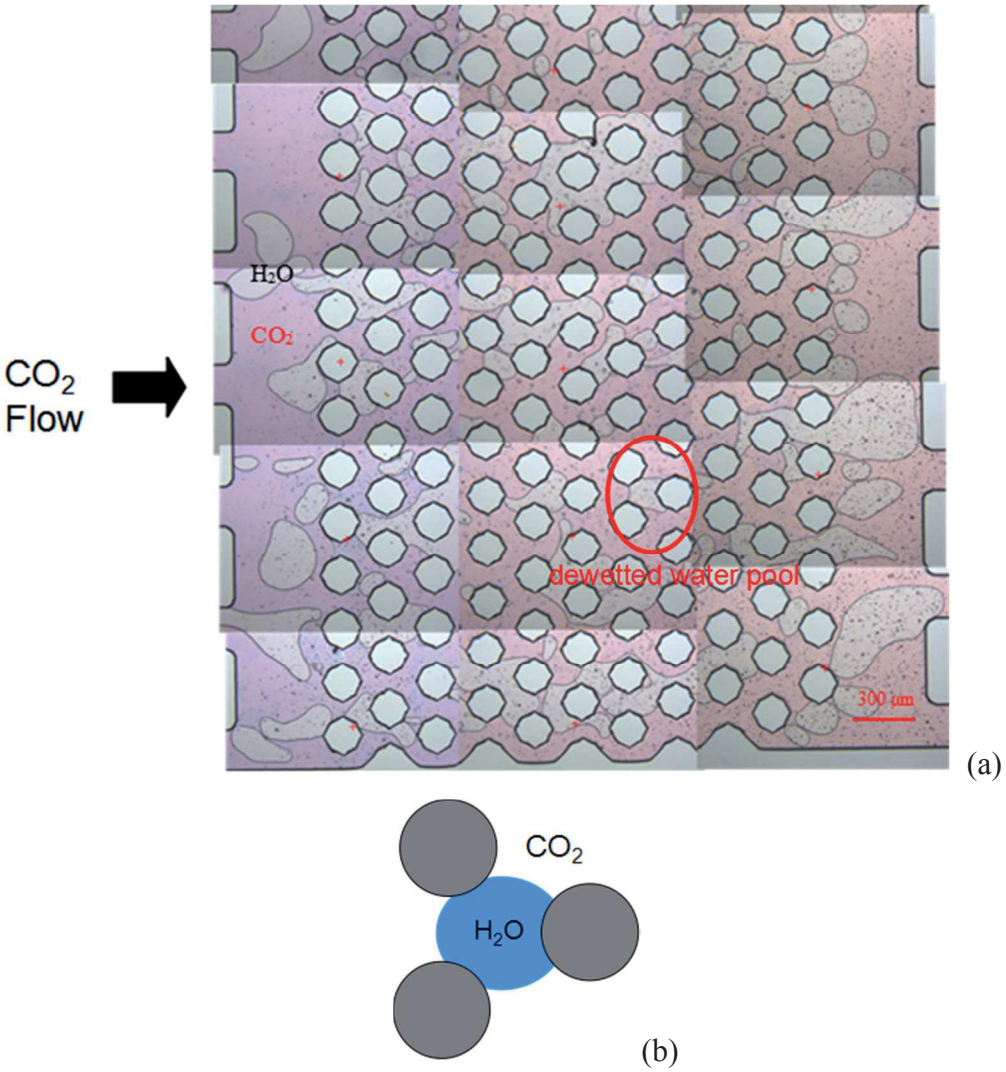

Fig. 4-12 *(a) Selected images of the CO_2 phase in a hydrophobic micromodel at 8 MPa - 25 °C - 50 µL·min^{-1}. CO_2 flow direction is given by the black arrow. (b) Schematic drawing of the "dewetted pool".*

The system reached the steady state in a short time (less than 5 minutes) due to the tiny pore size. In the meantime, the pressure drop (Δp) across the micromodel dramatically decreases to reach a plateau when CO_2 breaks through the porous system. When steady state is reached, the residual water slowly dissolved into the flowing CO_2 stream, eventually achieving CO_2 full saturation.

3.1.1 Displacement mechanisms

From this observation, two kinds of CO_2 storage mechanisms were observed, involving drainage caused by capillary trapping and drying mechanism by water dissolution in CO_2 flow. Capillary forces can create flow barriers preventing CO_2 flow from getting through the pore throat. As discussed in chapter 2, capillary entry pressure is proportional to the interfacial interactions (interfacial tension and wettability) and inversely proportional to the size of pore structure. Thus, CO_2 first entered the pore cross parts and is stopped before a pore throat unless the flow pressure achieved the capillary entry pressure of pore throat (Fig. 4-13). In addition, the CO_2 plume tail can be snapped off by the capillary force resulting in disconnected droplets, which reflects the impact of reservoir heterogeneity on CO_2 flow and distribution.

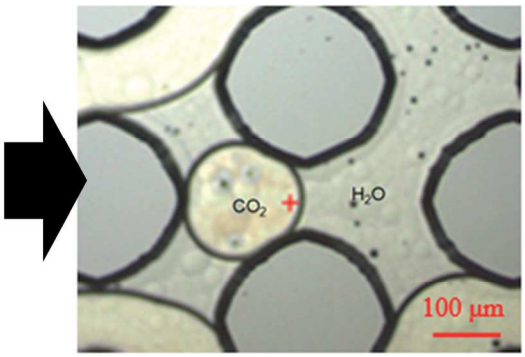

Fig. 4-13 *Typical residual trapping in a wetted pool at 8 MPa - 25 ºC - 25 µL·min^{-1} within the water wetting micromodel. CO_2 flow directions are given by the black arrows.*

The so-called “drying mechanism” refers to the water dissolved in CO_2 stream. The solubility of water in CO_2 is quite small in the considered experimental conditions (10^{-3} mole fraction), although this is compensated by fast mass transfer process at micro scale coupled to continuous feeding of the microsystem with fresh dry CO_2. Additionally, the two phase menisci generated by capillary pressure increased the contact area of water dissolution, therefore enhancing the drying process. Meanwhile, the dissolution of CO_2 into water reduces the stability of the water wetting dome. Therefore, the drying mechanism increases the saturation of CO_2 behind the displacement front.

3.1.2 Water domes and films

In water-wetted micromodels, some hydrophilic silica plots appear surrounded by an amazing water domes (Fig. 4-14 (a)), while, more probably, all the silica plots are always surrounded by a water film (Fig. 4-14 (b)). As the water dome contacts the majority of the silica solid surfaces, it increases the total volume of water still present in the porous medium, thus decreasing the saturation of CO_2. In addition, the dissolution of CO_2 in water decreases the water pH (from 6-7 to 3), therefore weakening the relative affinity of water to the silica surface (see Chapter 1, 6.3.2.2). These changes in affinity tend to increase the wetting contact angle of CO_2 and weaken the stability of the water dome. The formation of the water films is determined by the hydrogen bonds between the water molecules and the hydroxyl group of the silica surface. Note that the roughness of the silica porous medium (from microfabrication procedures) can affect the formation of these films.

Therefore, water domes around the solids surface trap a fraction of residual water in the pore at the primary of drainage process. Then the dissolution CO_2 into water due to mass transfer causes the reducing of water dome and the increase of contact angle. As the contact angle increases, the capillary entry pressure of the pore decreases until CO_2 enters into the pore and water dissolves into CO_2 stream. Eventually, the water domes dissolve into the CO_2 stream as CO_2 dries the porous medium and leaves a thin

water film which cannot be observed by the confocal microscopy used in this study (Fig. 4-14 (c)).

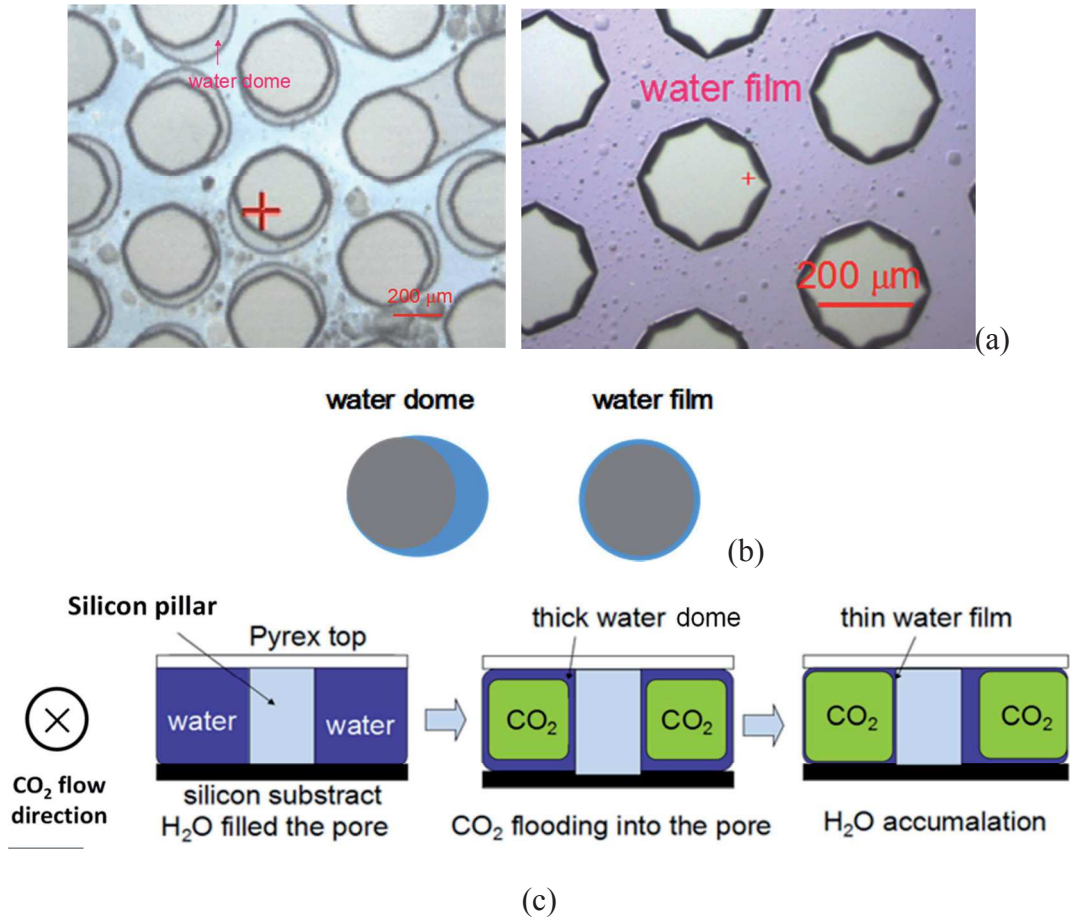

Fig. 4-14 *(a) Image of water domes and water films formed within the water wetted micromodels. (b) Schematic drawing of the "water dome"and "water film". (c) Scheme of water accumulation as a thin film after reaction with CO_2, ("thin" means that the thickness of the film is smaller than the pixel size of the image). CO_2 flow directions are given by the black arrows.*

3.1.3 Remark about CO_2 drainage in a squared pore network

As the previous observations are probably highly dependent on the pore network design and microfabrication process, we have also added a selected set of remarkable water-CO_2 configurations, which were captured using a squared pore network (not described in this thesis work). As shown by the pictures given in Fig. 4-15, due to the

etching effects, the squared pore network is made with circular-like (about 100µm diameter) pore volumes at the nodes of four channels with large length/size aspect ratio (the regular mask was made of 400 µm size separated by channels of 60 µm width – etching time leads to a 70 µm mean depth for the squared network with 70x70 µm mean cross-section for the channels). The pictures given in Fig. 4-15 can be then discussed comparing the remarkable configurations of Fig. 4-9.

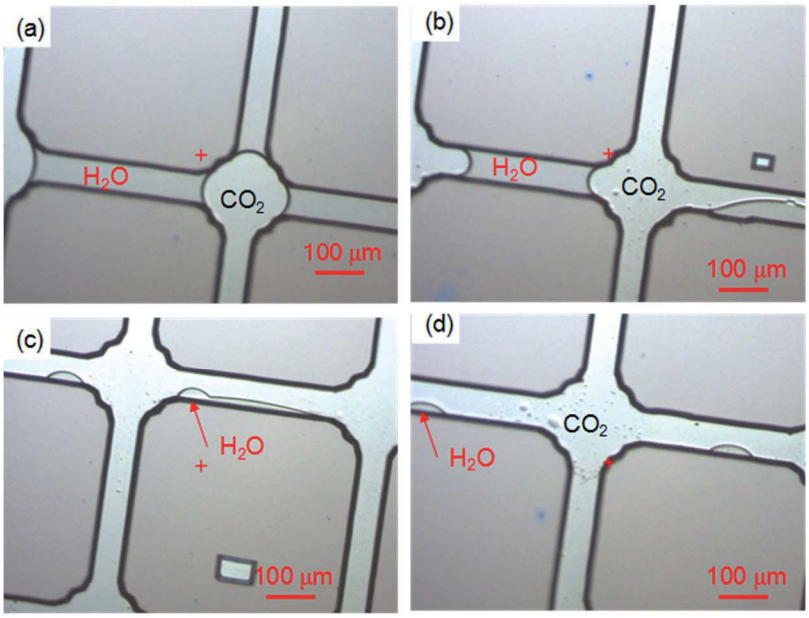

Fig. 4-15 *Images of CO_2 invasion into pore throats in the square pore network: (a) CO_2 is stopped by the capillary barrier in the pore throat; (b) CO_2 breaks into the pore throat; (c) the residual water capillary barrier in the pore throat in a square porous medium;*

When CO_2 invasion starts from one channel, it first entered the pore cross parts and can be stopped in a particular pore (see Fig. 4-15 (a)) unless the flow pressure achieved the capillary entry pressure of pore throat. As preferential flows occur, it is then possible to observe a water bridge between two CO_2 pores (Fig. 4-15 (a) and (b)). Increasing the flow rate leads to the formation of water domes (Fig. 4-15 (b) to (d)), whose volume decreases as the CO_2 flow rate increases.

Although remaining only qualitative, the above illustrations show the great interest of our micromodel experiments to mimic the two-phase distributions at pressure and temperature conditions of the geological formations.

3.1.4 Drying mechanism of a pool and a bridge

Behind the displacement front, the residual water can slowly dissolved into the flowing CO_2 stream. Lenormand's displacement patterns were observed during this drying process over time (Fig. 4-16): piston-like displacement, snap-off and pore-body filling (see details in chapter 2).

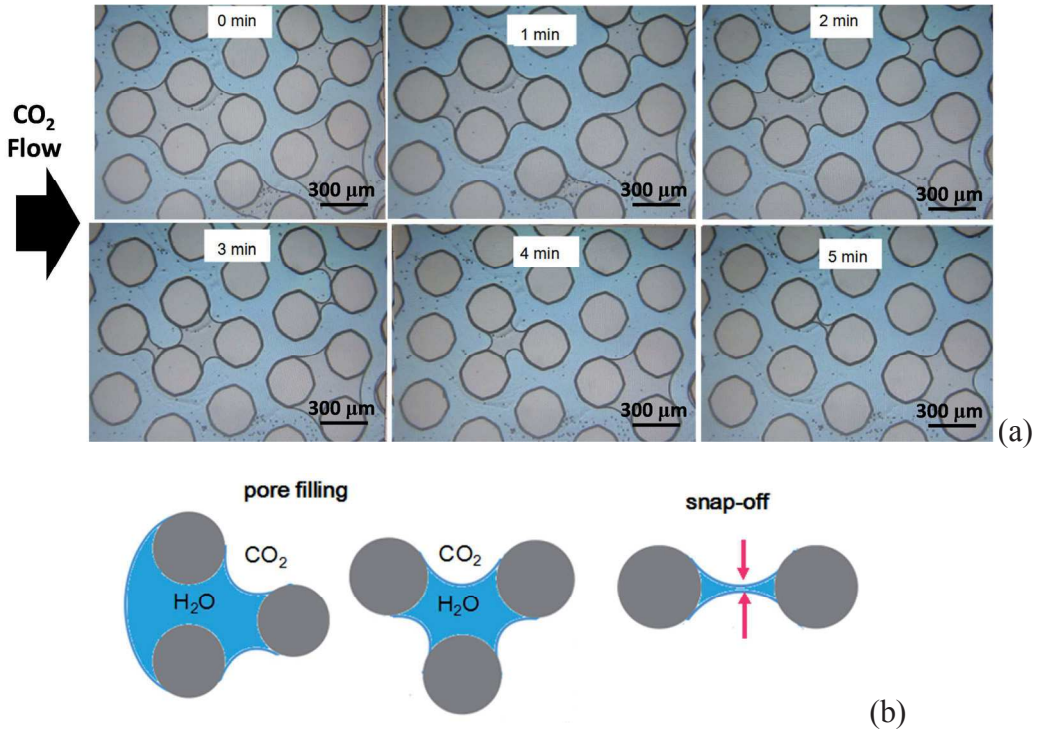

Fig. 4-16 *(a) Images of water displacement process over time within the water wetting micromodel (8 MPa - 25 ºC - 25 µL·min^{-1}). CO_2 flow direction is given by the black arrow. (b) Scheme of "pore filling" and "snap-off "displacement patterns: CO_2 drives the "water pool" (two types) out of the pore center to form the "water bridge"; CO_2 cuts off the "water bridge" between two solids.*

During the displacement process, CO_2 breaks the capillary pressure and displaces water in the pore space (piston-like displacement). The unconnected water is collected in the center of a pore body surrounding by CO_2 and the silica porous media skeleton. Due to the mutual solution and diffusion, water either dissolves into the CO_2 phase or is driven out of the pore center (pore-body filling).

Snap-off pattern refers to CO_2 cutting off the water bridges between two silicon pillars. During the drainage process, the wetting phase forms thin films around the solids connected though continuous wetting bridges. As the contact angle increases (due to CO_2 dissolution into water), the capillary pressure decreases until the critical capillary pressure is reached. CO_2 phase snaps off the wetting phase film, and subsequently dissolves it.

Therefore, through these three displacement patterns, the discontinuous water phase behind the displacement's front dissolves into the flowing CO_2 stream, which caused CO_2 full saturation over time.

3.1.5 Crying mechanisms after CO_2 percolation

The p,T conditions greatly influences the invasion process. Particular behaviors were experimentally observed in the higher temperature/low pressure range (*e.g.* lower CO_2 density). As shown in Fig. 4-17 (a), at T = 50 ºC and p = 8 MPa, tiny water droplets precipitate out from the CO_2 phase after CO_2 percolation. We called this phenomenon the "crying mechanism", which is primarily due to a phase separation of CO_2 and water. During our observations, we found that this crying mechanism occurs when increasing the temperature or decreasing the pressure, independently from the micromodel wetting characteristics (Fig. 4-17 (b)).

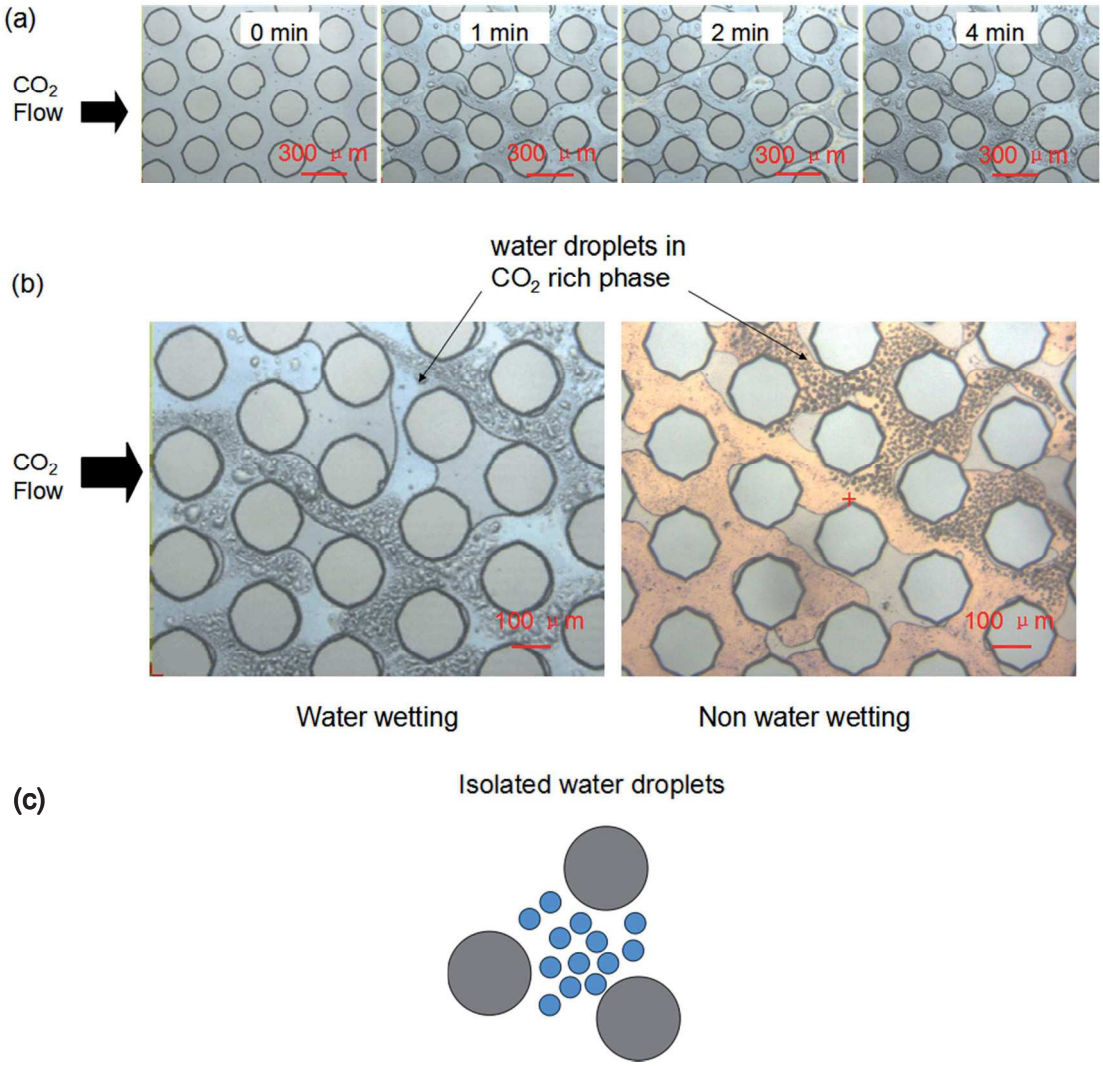

Fig. 4-17 *(a) Images of the crying mechanism over time in water wetting micromodels at 8 MPa - 50 °C - 50 µL·min^{-1}. (b) Images of water droplets within both water wetting and non-wetting micromodels. CO_2 flow directions are given by the black arrows. (c) Schematic drawing of "isolated water droplets".*

Experimentally, we never noticed any water droplets nucleation at room temperature, while working above CO_2 critical pressure (7.1 MPa) (Fig. 4-18 (a). However, the crying mechanism can be observed at lower CO_2 density (high temperature and/or low pressure, Fig. 4-18 (b)).

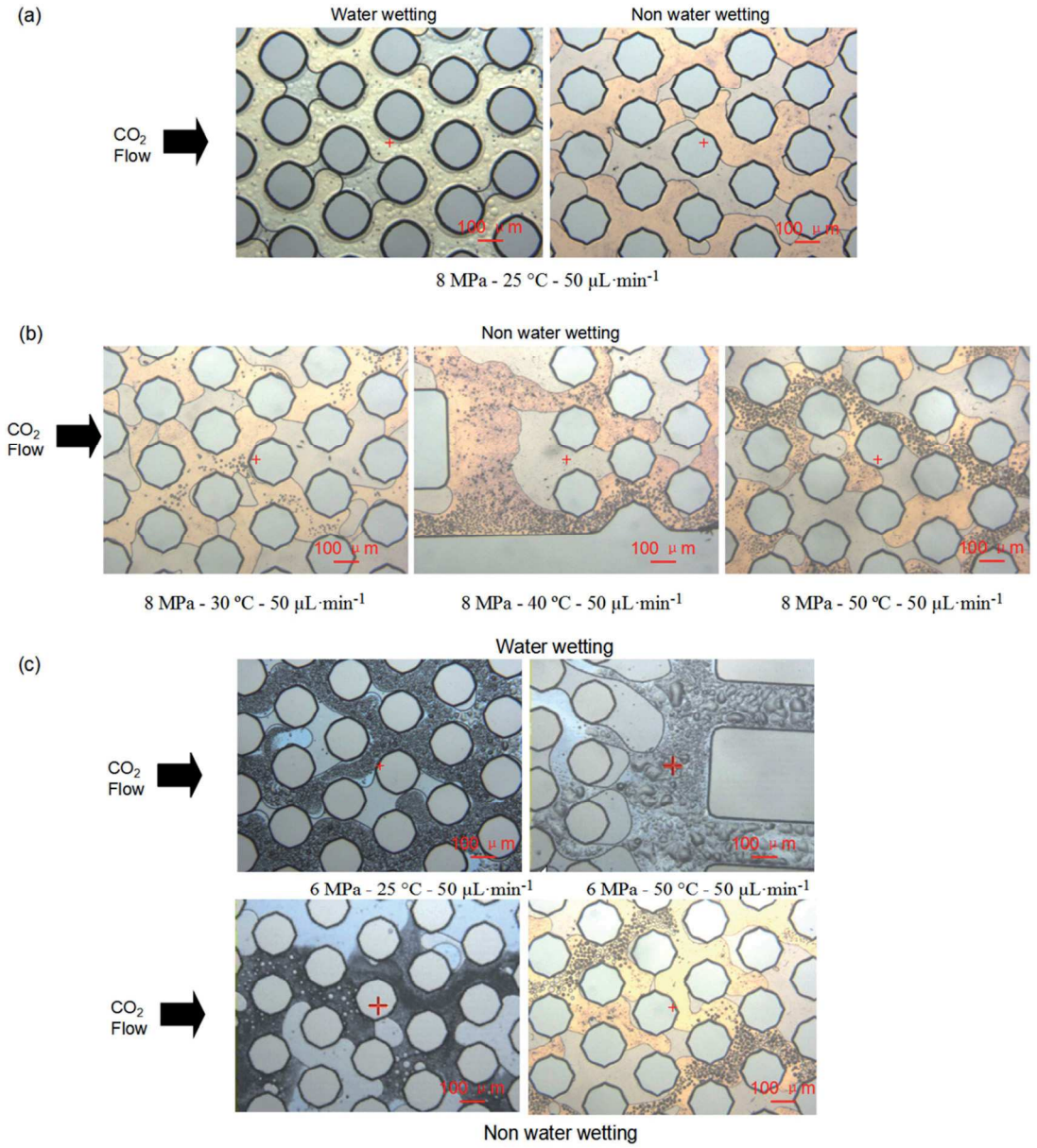

Fig. 4-18 *Images of water droplets at different conditions within both water wetting and non-wetting micromodels: (a) no droplets at room temperature and 8 MPa; (b) water droplets precipitated in different areas depending on temperature within non-wetting micromodels; (c) crying mechanism observed at 6MPa - 25/50 °C - 50 µL·min^{-1}. CO_2 flow directions are given by the black arrows.*

Considering experiments ran at constant pressure, the higher temperature, the higher the amount of water droplets (Fig. 4-18 (b)). However, the phenomenon does not occur always in the same micromodels' areas depending on temperature.

In the case of experiments ran at working pressures below the CO_2 critical pressure, the crying mechanism can be observed at room temperature, leading to water droplets nucleation everywhere in the micromodel at room temperature (Fig. 4-18 (c)).

Since the water droplets always nucleate from the CO_2 rich phase, they can re-dissolve into the CO_2 flow, or grow up and merge to bigger droplets trapped in the CO_2 phase (Fig. 4-19). The water droplets located near the micromodels' outlet can expand with time and connect together to form larger droplets. The concentration of water in the droplets increases as the over saturated CO_2 rich phase flows, which leads to the formation of large water droplets trapped in the CO_2 phase. This process is favored when the water droplets can wet the walls since they can merge to form a thick film on the porous medium surface. The droplets eventually grow up and coalesce with the neighboring residual water (Fig. 4-19 (a)). Note that this mechanism is somewhat different when considering non-water wetting micromodels. In such experiments, water droplets remain much smaller given that they cannot take benefit of the wall wetting properties to help them merging (Fig. 4-18 (c)).

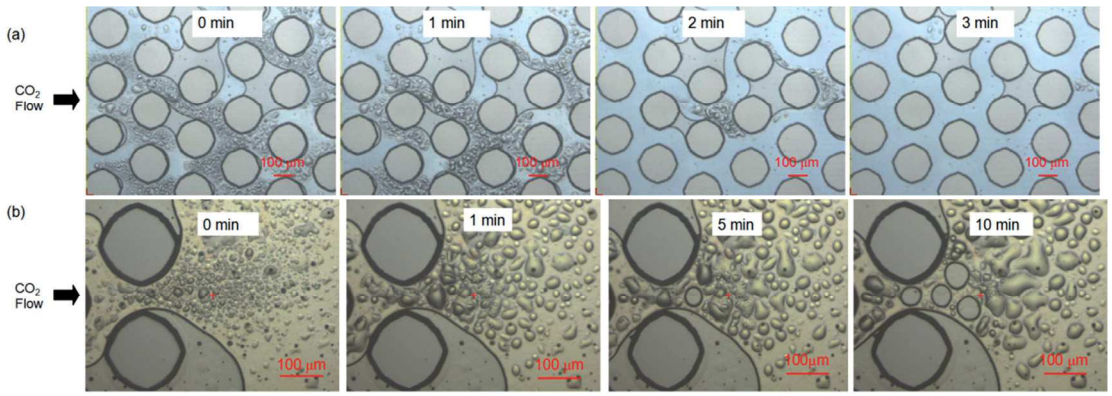

Fig. 4-19 *Images of water droplets in CO_2 phase: (a) dissolution at 8 MPa - 50 ºC - 50 µL·min^{-1}; (b) growing and merging process in the water wetting micromodel at 8 MPa - 50 ºC - 50 µL·min^{-1}. CO_2 flow directions are given by the arrows.*

The droplets growing and merging result in a water imbibition process, which reduces the CO_2 saturation. Meanwhile, it also increases the interface area between water and CO_2, which benefits the mutual dissolution of water and CO_2 and further the mineral trapping.

One explanation for this crying mechanism is the variations of the CO_2 density and the associated water solubility during the invasion. There is a sharp discontinuity of the water solubility in CO_2 near the latter's critical pressure (see Fig. 4-20). The discontinuity in the water solubility at subcritical temperatures coincides with the phase change from a gaseous to a liquid CO_2-rich phase. Before CO_2 entered the micromodel, CO_2 is a liquid ($0 < T\ (^{o}C) < 25$) and is in contact with water that fully saturates the inlet channel. Therefore, there already exists dissolution process of water in the CO_2 phase through this unique interface. When the saturated CO_2 entered the heated micromodel (mostly $T > 31\ ^{o}C$), the liquid CO_2 turns to gas or supercritical, leading to a dramatic decrease of the water solubility in CO_2. Oversaturated water could thus precipitates out from the CO_2 phase.

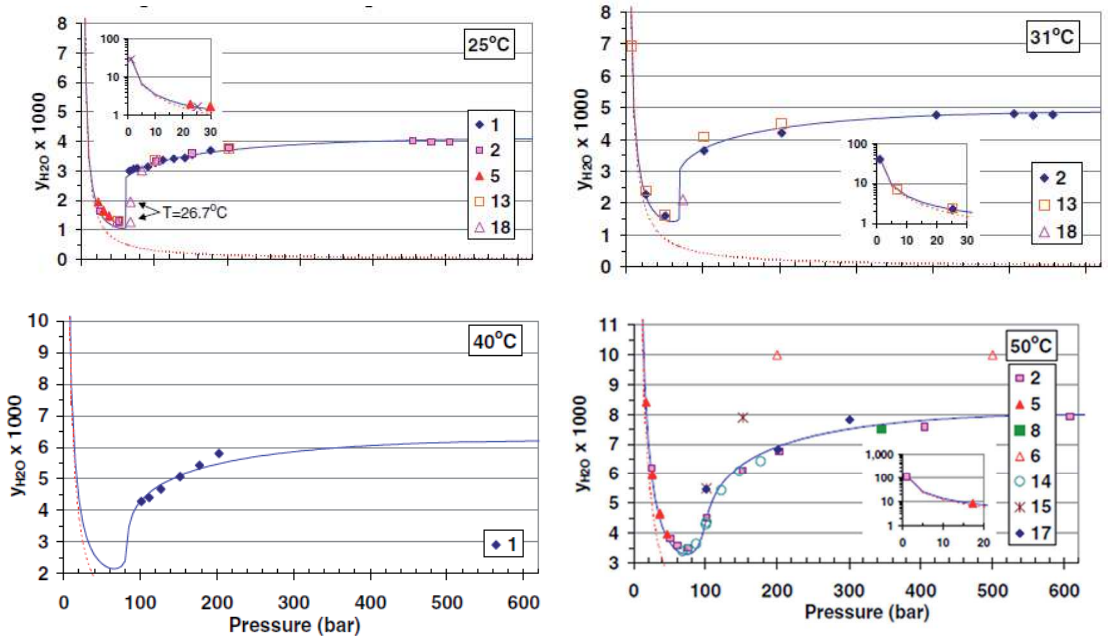

Fig. 4-20 *Water solubility in CO_2 rich phase for different operating conditions. From Spycher et al. [5].*

Additionally, during the CO_2 invasion process, the pressure distribution in the pore network leads to tremendous changes of water solubility. When the operating conditions are close to the critical point of CO_2, the sharp discontinuity in the water solubility is shifted to higher pressure with increasing temperatures. Hence, when the (p,T) range in which the sharp discontinuity in the water solubility occurs is included within the pressure distribution range inside micromodel, more water can precipitate out from the saturated CO_2 phase. This explains that water droplets distribute in different areas of the micromodel depending on temperature. In addition, the difference between the thermal conductivity of the horizontal (Pyrex) glass layer and (silicon) wafer substrate leads to a small (vertical) temperature gradient inside the pore network. Thus, the water droplet nucleation generally preferentially starts first on the top glass side.

During the CO_2 displacement experiments, the migration of the CO_2 plume is affected by two mechanisms: (i) at the front of the plume, drainage and capillary trapping and (ii) at the tail of the plume, imbibition and dissolution trapping. At the front of plume, CO_2 floods through the porous medium and occupies a fraction of the pore space. Water within the smaller pore space connects the hydrophilic surface of solids as a thin film. At the tail of the plume, the residual water dissolves into the fresh CO_2 phase and water droplets also displace CO_2 into the pore.

3.1.5 Conclusion

These studies performed for the first time at the p,T conditions of the geological formations were used to obtain qualitative visualizations of the CO_2-water displacement mechanisms and to capture, locally, some remarkable configurations of the two phase distributions. However, our microscopic visualization set up described in § 2.4 does not integrate all the CO_2 water interfaces with the required resolution at the full view of the complete micromodel. Therefore, it was not possible to implement an image analysis method giving access to the complete, two phase distributions and, consequently, the quantitative measurements on CO_2 saturation (water saturation,

respectively) were not provided in our present experimental status. In addition, we have already noted that the local flow velocity field is not measured, as the usual methods implemented in microfluidic, as for example the micro particle induced velocity (μPIV) technique, are still not available in microdevices working at high pressure. Finally, the only remaining quantitative parameters to perform preliminary analysis of the observed mechanisms were obtained mainly by the time responses of the pressure drop measurements across the microsystem, complemented by the time responses of the outlet water/CO_2 ratio production, both behaviors occuring from the initial time of the inlet CO_2 injection until the final time where the CO_2 full saturation of the micromodel occurs, as described in the next section.

3.2 Pressure drop response across the micromodel

3.2.1 Intrinsic pressure drop and CO_2 breakthrough time

We recall that our experiment ran are based on the pressure (and the concomitant flow rate) measurements performed at the pump levels (see Figs. 4-1 and 4-2), starting with the full free volume of the experimental setup saturated with water (or brine) and considering the external tube blow-off as two, time-separated, flow disturbances at the outlet pump level. Here, we have chosen as a typical example, the case of the liquid-like CO_2 injection within the saturated high-porosity micromodel, at 8 MPa, 25 °C, 50 μl/mn operating conditions.

Fig. 4-21 gives the typical time responses of the recorded pressures at both the inlet and the outlet pumps from the initial time of the liquid CO_2 injection to the time occurrence (t_s) of the so-called CO_2 steady state or the CO_2 full saturation (S_{CO2} =1 from Eq. 2-5) of the micromodel, where only the CO_2 is flowing across the micromodel. Therefore, Fig. 4-21 illustrates three (increasing, decreasing, quasi-constant) characteristic shapes, which infers three (t_b, t_w, and t_s) characteristic times defined from the following discussion.

The starting pressure is the same for both fluids, while the same ultimate ending pressure occurs due to the negligible viscous contribution of flowing CO_2 across the experimental setup (and across the micromodel, obviously). The inlet pressure keeps increasing during the initial period following the CO_2 injection. Simultaneously, the outlet pressure remains constant, while the outlet flow rate slightly increases (see Fig. 4-2). Indeed, when the injected CO_2 is pushed into the experimental setup (initially saturated with water), the outlet pump has to water back flow to maintain a constant pressure in the system (as the outlet pump is working in constant pressure mode). The increasing back flow rate is then a water flow, which corresponds to the first water flow disturbance due to the blow-off of the external inlet tube.

As previously mentioned, the CO_2 drainage process of interest occurs immediately after the first water flow disturbance and its initial short (a few seconds) period corresponds to the CO_2 invasion of the micromodel until CO_2 breaks throughout the outlet single channel of the micromodel. Now, the second water flow disturbance due to the blow-off of the external outlet tube starts, whose signature is a significant sharp peak of the back flow rate, which reflects the very fast blow-off of remaining water in the outlet tube by the fresh CO_2 flow where viscous effects are small. Indeed, water viscous effects are reduced due to the large inner diameter of the tube, while CO_2 viscous effects can be certainly negligible due to the CO_2 low viscosity, as already mentioned). Then, after the peak, the back flow rate, which can be constituted by a decreasing quantity of flowing water and an increasing quantity of CO_2 until the complete drying of the micromodel occurs, recover again the injection rate of CO_2 at steady value fixed by inlet pump (*i.e.* 50 $\mu L \cdot min^{-1}$, here).

Consequently, using the time variation of the pressure drop, $\Delta p(t) = p_i(t) - p_o$, we defined the ***intrinsic pressure drop*** $\Delta p_0 = \Delta p(t=t_b)$ as the maximum of $\Delta p(t)$ at CO_2 ***breakthrough time*** $t=t_b$. The accurate determination of the CO_2 breakthrough time was obtained as the concomitant time where the abrupt decreasing response of the pressure dropt measured by the inlet pump and the abrupt increasing response of the flow rate measured by the outlet pump were starting.

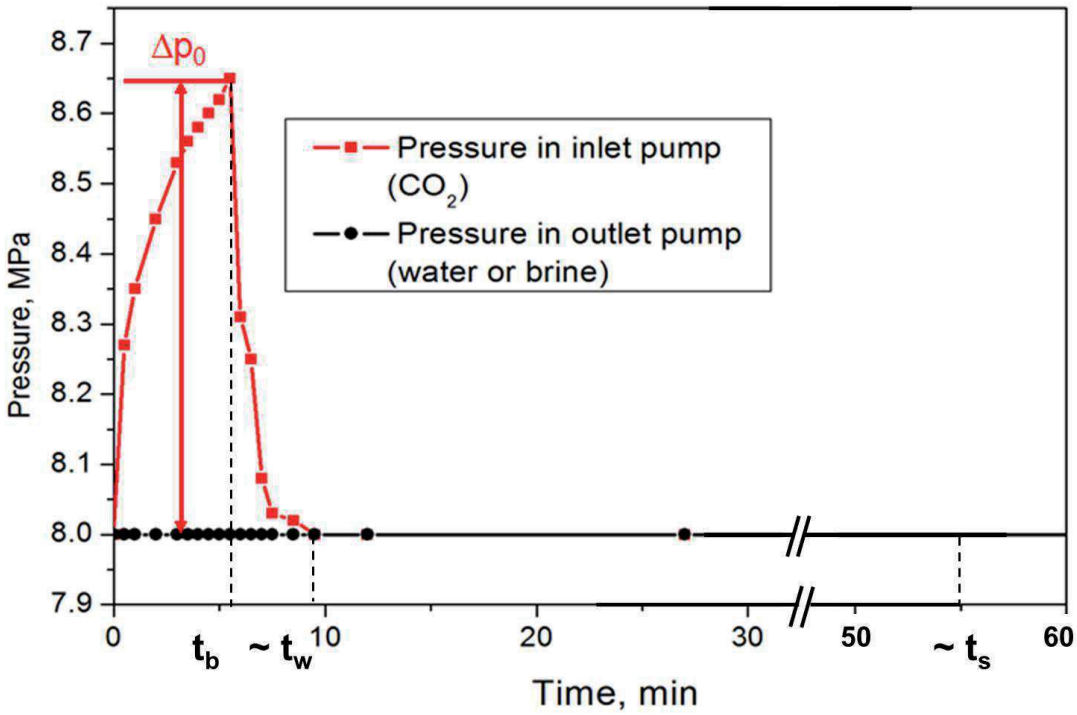

Fig. 4-21 *Fluid pressure (inlet and outlet) measurements versus time for liquid-like CO_2 injection at operating conditions, 8 MPa -25 ºC -50 µL·min^{-1} (H-type micromodel). Δp_0 is the intrinsic pressure drop, t_b is the breakthrough time, t_s is the time to full saturation and t_w is the time to primary water displacement (see text).*

3.2.2 CO_2 invasion and CO_2 drainage processes

For convenience, the CO_2 flowing mechanisms involved during the time period $t \leq t_b$ where $\Delta p_i(t)$ increases until Δp_0 was called the CO_2 ***invasion process***, while the ones during $t \geq t_b$ where $\Delta p_i(t)$ decreases from Δp_0 to zero was called the CO_2 ***drainage process***. Obviously, the increase of the pressure drop during the CO_2 invasion process is caused mainly by the viscous forces due to the water displacement and probably accounts for capillary effects related to the formation and displacements of the CO_2/ water interfaces. Therefore Δp_0 appears as the measured parameter which reflects the intrinsic driving force to displace viscous water in the micromodel. Obviously, when the objective is the comparison between the CO_2 sweep efficiency of the liquid, supercritical, and gas CO_2 injection, the viscosity ratio M defined by Eq. 2-4 appears as the natural parameter involved in the analysis of the observed

behaviors due to the viscous effects (see also the discussion below). Moreover, at the CO_2 breakthrough time, the residual water saturation in the micromodel takes probably a significant value before that the CO_2 drainage process starts. Indeed, the captured pictures of the CO_2/water phase configurations at the early times following the CO_2 breakthrough time, clearly shown that the residual water occupies a significant part of the free volume of the pore network, as the forms of pools, bridges or domes (see previous Figs. 4-9 to 4-19).

Simultaneously, the outlet flow rate exhibits firstly a sharply increase because the CO_2 phase pushes the viscous water outside the micromodel just after the CO_2 breakthrough time, before being secondly quickly brought back to a lower constant value when the main flow of water pushed by CO_2 stops. During this initial time period (generally of the order of a few minutes and lower than 12 mn for all the experiments considered in this work), the mutual CO_2/water dissolution effects are assumed to have an increasing, but small contribution in the observed mechanisms and are thus ignored in the so-called primary water displacements. Introducing the phenomenological ***time of primary water displacement*** $\mathbf{t_w}$ ~ 6-12 min (subscript w recall for water), the ***primary water displacement*** during the time period ranging from t_b to t_w is a process involving a fraction of water, saturating the pore volume initially, which flushes out when CO_2 flows through the porous medium.

3.2.3 Primary water displacements and water drying mechanisms

Due to the fast mass transfer at the pore scale within the micromodels, the capillary trapping and dissolution trapping cannot be clearly distinguished from the recorded images, except if we use our previous phenomenological time separation around t_w ~ 10 mn, assuming that the initial primary water displacements during $t_w - t_b$ are mainly governed by viscous, capillary and CO_2 saturations effects, and are thus followed by the water drying mechanisms ($t_s - t_w$), where capillary and mutual dissolution effects become dominating.

Finally, the ultimate stage of the CO_2 drainage process from t_w until the ***time to full CO_2 saturation*** $\mathbf{t_s}$ – with expected long duration compared to t_b (and/or t_w) - corresponds thus to the ***drying mechanism*** of the remaining residual water inside the micromodel, only monitored by the optical local observations of the increasing (decreasing) CO_2 (water) saturation S_{CO2} (S_{water}) (see Eq. 2-5). We note that t_s is thus a time estimation indicative of the fading and/or disappearance of the isolated water droplets, the water bridges and the water domes within the pore network (the disappearance of the water bridges cannot be optically resolved). Obviously mutual dissolution of the CO_2/water components and capillary number (see Eq. 2-3 and discussion in section 3.2.3 below) are probably the main essential parameters involved in the analysis of the observed behaviors due to capillary, drying and dissolution effects during this ultimate stage.

Despite the non-measurable CO_2 (or water) saturations, we can thus admit that the CO_2 flows are conform to the Darcy regime where the initial decrease of the pressure drop, when $t > t_b$, reflects the increase of the relative permeability (k_{ri}), due to the water/CO_2 phase distribution (neglecting the mutual CO_2/water dissolution effects). k_{ri} is one of the most important parameters during the CO_2 drainage process in presence of CO_2 saturation. In such a hypothetic situation, it appears then possible to estimate the relative permeability of the pore network, as shown in the next section 3.2.4.

3.2.4 Relative permeability during the early time of the CO_2 drainage process

Here, we are concerned by the time period $t_b < t < t_w$, i.e., the early time of the CO_2 drainage process following the CO_2 breakthrough time. According to the Darcy law of Eq. (2-8), the relative permeability (k_{rCO2}) is a function of the CO_2 flow rate and pressure drop Δp_D across the pore network:

$$k_{rCO2} = \frac{\mu_{CO2} \times L_{p(eq)} \times u}{K \times \Delta p_D} = \frac{\mu_{CO2} \times u}{K} \times \frac{L_{tot}}{\Delta p} \qquad \text{Eq. 4-9}$$

where μ_{CO2} is the CO_2 viscosity of displacing fluid (Pa·s), $L_{p(eq),HL}$ is equivalent length of porous medium (m), L_{tot} is total equivalent length (m), K is the pore network permeability (m^2), Δp_D is the pressure drop across the pore network, Δp is the measured pressure drop across the micromodel, and u is the Darcy mean velocity of the injected fluid ($m \cdot s^{-1}$).

Table 6 gives the values obtained for both the pressure drop and the relative permeability over time. Note that the values of relative permeability after 3 min are not reliable due to the quasi-zero values of $\Delta p(t-t_b)$, which are within the uncertainty range (±0.01 MPa) of the pressure measurements.

Table 6 *Summary of the pressure drop and relative permeability data after the CO_2 breakthrough time operating the H-type micromodel (porosity Φ = 0.6, permeability K = 1.14×10^{-11} m^2) at 8 MPa-25 ℃-50 $\mu L \cdot min^{-1}$.*

$t-t_b$ (min)	Pressure drop (MPa)	Relative permeability
0	0.65	0.0742
0.5	0.31	0.1555
1	0.25	0.1928
1.5	0.08	0.6026
2	0.02	0.92
3	~0.01	Not reliable
4	~0.01	Not reliable

Once CO_2 floods into the porous medium, as the saturation of CO_2 increases, the pressure drop decreases until to zero at steady state. The relative permeability of CO_2 increases, and as noted above, the relative permeability value is not reliable after reaching $t - t_b > 2.5$ min, i.e., a time comparable to the phenomenological time t_w. For convenience, in term of our previous discussion when $t > t_w$, we have arbitrarily

modified the value of the relative permeability to unity after $t_w \sim 10$ min. Figure 4-22 gives the relative permeability and pressure drop versus time.

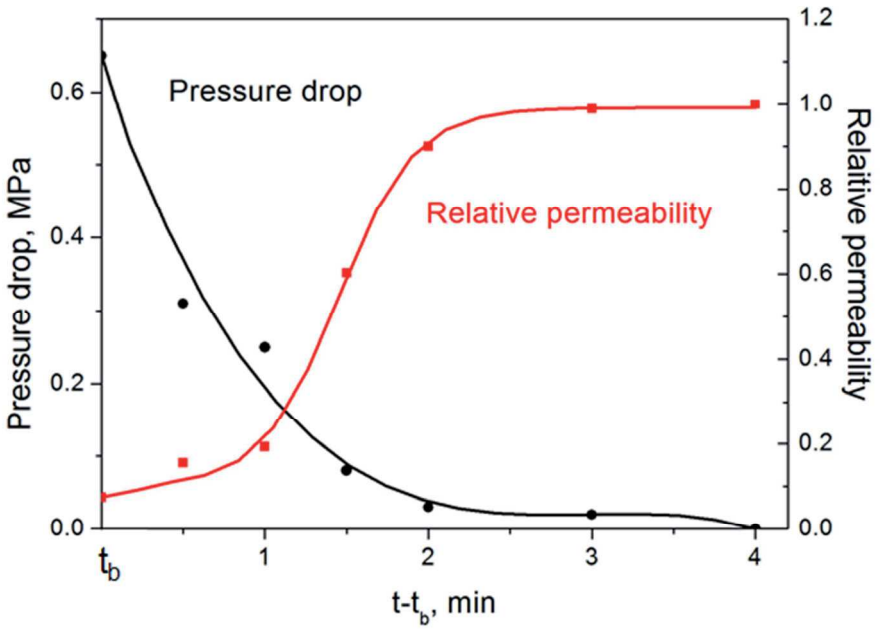

Fig. 4-22 *Relative permeability and pressure drop curves as a function of time after CO_2 breaks through a H-type micromodel (8 MPa - 25 ºC - 50µL·min^{-1}).*

The main conclusive remark of this simplified Darcy description of the CO_2 flows across the micromodel is the following: As the Darcy pressure drops Δp_D decreases during the CO_2/water displacement process, the saturation and the relative permeability of CO_2 increase. We can then already anticipate some essential features of the discussion of section 3.3 where, compared to gas and supercritical CO_2 cases, the selected liquid CO_2 case has probably a higher sweeping force during the primary drainage. Similarly, the intrinsic pressure drop for the lower porosity micromodel (which results from a higher capillary pressure at the smaller pore scale), is probably higher than the one for the present higher porosity micromodel. Thus the porous medium with low porosity requires a higher injection pressure for CO_2 breakthrough. In addition, wettability of the micromodel also has a probable great influence on Δp_0. Indeed, the hydrophobic surface generates a higher driving force for CO_2 drainage,

while a better sweeping efficiency is achieved when working with CO_2 wetting micromodels.

3.2.3 Time duration of the CO_2 drainage process to obtain CO_2 full saturation of the micromodel

As a consequence of the previous phenomenological time separation introducing t_w, the following discussion refers to the ultimate time period $t_w < t < t_s$, where $t_s - t_b$ is the total time duration of the CO_2 drainage process to obtain the CO_2 full saturation (making reference to t_b). The main characteristic mechanism of this latter period is governed by the residual water slowly dissolving into the flowing CO_2 veins across the pore network. The objective is to characterize the efficiency of capillary trapping and dissolution trapping considering the experimental conditions and the results reported in Table 7, where, as already mentioned, it is noticeable that t_s is not easy to estimate with precision from the pictures of the CO_2 full saturation of the micromodel.

Indeed, the mutual solubility of CO_2 and water (or brine) depends on the operating temperature and pressure. The increasing pressure and decreasing temperature lead generally to a higher CO_2 solubility in water. Simultaneously, it is also noted that the contact angle increases with the mutual dissolution of water and CO_2, which results in a decreasing capillary pressure and more easily pore invasion by CO_2. Therefore, the CO_2 solubility in water can cause a decrease of the capillary effects, which leads to a shorter time to CO_2 full saturation. To check this result we have introduced the corresponding values of the capillary number Ca defined by Eq. 2-3, which cover the typical range $(0.6 - 8.5)\times10^{-5}$. As shown in Table 7, the time $t_s - t_b$ to CO_2 full saturation decreases with an increasing capillary number at constant temperature. Please note that the Ca values also increases as the injection flow rate and/or as the temperature increases at constant pressure). At higher Ca, the saturation of residual water is smaller and less fresh dry CO_2 is needed to dissolve it. Above the critical temperature, the solubility of water in CO_2 phase increases with temperature and

pressure. Below the critical temperature, the solubility decreases before critical pressure and then increases with an increasing pressure. Finally, when the experiments conditions are located above the critical point, i.e., corresponding to the supercritical CO_2 injection, the increasing pressure is beneficial to the full saturation.

In addition, the density of the injected CO_2 also strongly affects the full saturation process. At 6 MPa - 50 ºC - 50 $\mu L \cdot min^{-1}$ and 8 MPa - 75 ºC - 50 $\mu L \cdot min^{-1}$, the times to CO_2 full saturation are much shorter relative to their low breakthrough saturation. When the injected CO_2 from the inlet channel at room temperature entered into the heated microsystem (50 ºC / 75 ºC), the density decreases dramatically. Thus the higher flow rate can take out more residual water from the pore network.

A final remark can be added noting that our present experiments were performed injecting so-called *dry* CO_2 in the saturated micromodel, which also needs to perform similar experiments in the future, thus injecting so-called *wet* CO_2 in the saturated micromodel, to provide better understanding of the water/CO_2 dissolution effects.

Table 7 *Time to CO_2 fully saturated micromodels after CO_2 breakthrough time. $^{(*)}$ indicates the selected typical example of liquid-like CO_2 injection corresponding to Fig. 4.21.*

p MPa	T ºC	injection rate µl/min	10^5 Ca	Time, min		
				H-type water wetting	L-type water wetting	L-type Non-water wetting
8	25	100	8.511	< 6.5	5.8	< 7
8	25	50	4.256	44.5$^{(*)}$	33	20.2
8	25	25	2.133	> 120	-	-
8	50	100	2.366	26.5	25.9	25.5
8	50	50	1.183	71.5	77.5	29.2
8	50	25	0.592	< 120		150.5
8	75	50	1.17	4	-	-
6	50	50	0.891	24.5	11.5	-

3.2.4 Concluding remark

In this section we have analyzed the variations of the characteristic data - Δp_0, t_b, t_w, k_r and t_s – as functions of the operating conditions and the observed water/CO_2 displacements within the micromodel. In spite of the absence of direct measurement of the effective CO_2 saturation S_{CO2} of Eq. 2-6, we have also shown that its qualitative behavior can be accounted for from the pressure drop time response, especially during the CO_2 drainage process leading to the final CO_2 full saturation. We have also included the role of the viscosity ratio and the capillary number in the relative importance of the residual (or capillary) and dissolution trapping mechanisms. As also briefly mentioned, the CO_2 sweep efficiency was strongly affected by the operation conditions and the micromodel characteristics. The more specific influence of these main parameters is now detailed hereafter.

3.4 Summarizing the operating parameters effects

In the following discussion we illustrate the "*geological laboratory on chip* (GloC) *concept*" based on the transparent micromodels developed in this work, which combined optical observation with monitored operating conditions especially considering the CO_2 (residual/capillary and dissolution) trapping mechanisms on the geological formations. Indeed, we combine the previous optical captures of the remarkable configurations of the CO_2/water phase distribution with the following changes of i) the *in situ* thermodynamic conditions (temperature, pressure and injection rate), ii) the CO_2 and water properties (viscosity, density and solubility), iii) the properties of the porous matrix (porosity and wettability), as all these essential operating parameters can have significant effects on the CO_2 flow patterns and CO_2 saturation levels in the true heterogeneous geological formations.

3.4.1 Effects of injection rate

In order to examine the effect of the injection rates, some experiments were performed at constant pressure (8 MPa) and constant temperature (50 ºC), while injection rate varies from 25 to 100 µL·min^{-1}. The pressure drop variations over time were plotted in Fig. 4-23. The intrinsic pressure drop Δp_0 is increasing (while the CO_2 breakthrough time t_b is decreasing) with an increasing injection rate, due to the viscous forces associated to the water displacement.

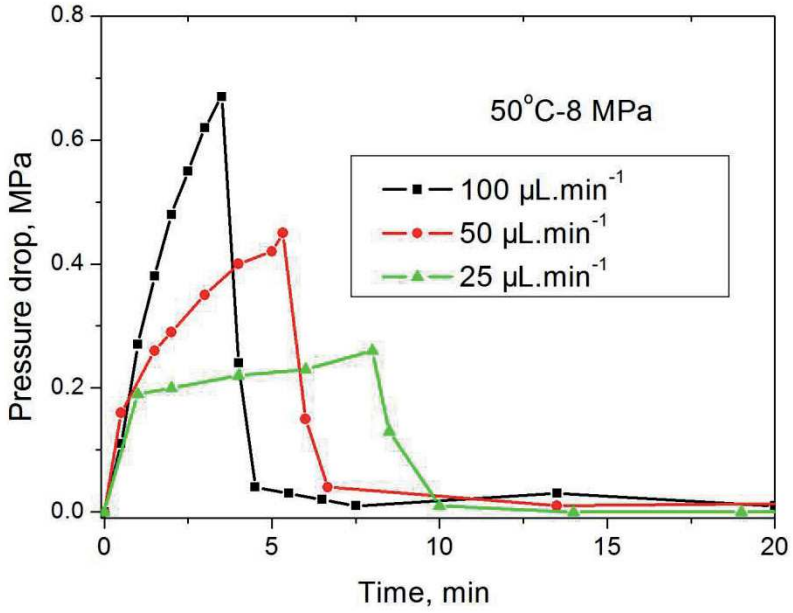

Fig. 4-23 *Pressure drop across the micromodel as a function of time for various injection flowrates at p = 8 MPa and T = 50 ºC.*

Such a behavior can be understood from the three pictures of Fig. 4-24, which show that the preferential flow paths of CO_2 depend on the injection rates. At low injection rate (q_i = 25 µL·min^{-1}), CO_2 creates a small flow path through the water and formed a continuous stream with a large amount of residual water. Oppositely, for higher injection rates (q_i = 100 µL·min^{-1}), CO_2 floods through the porous medium and occupied most of the pore space. CO_2 almost fully saturates the pore space near the

inlet and only left a thin water film around the silicon pillars, which rapidly dissolved into the later CO_2 stream.

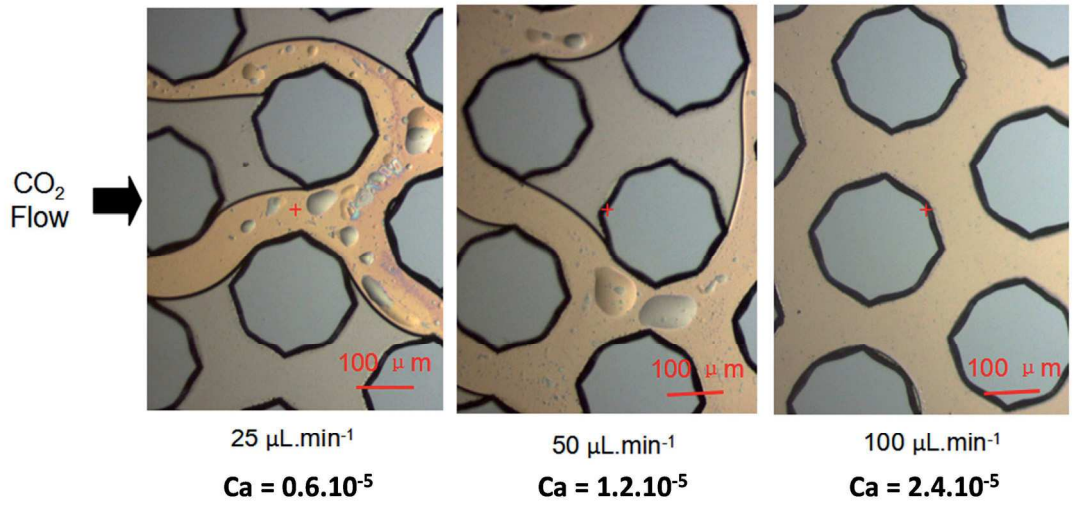

Fig. 4-24 *Images of CO_2 flow paths in the water media in hydrophilic micromodel at different injection rates. CO_2 flow directions are given by the black arrow.*

Therefore, the distribution patterns of CO_2 at lower injection rate show dominant features of capillary force effect with preferential long veins of flowing CO_2 and then, finally, lower CO_2 saturation during the CO_2 drainage. At higher injection rates, CO_2 completely flows into the pore volumes since the increasing injection rate results in a sufficient displacement driving force. More sweep efficiency at high injection rate can drive more water out and lead to an increasing CO_2 saturation, as expected in geological CO_2 storage. This can be directly linked to an increasing capillary number (see Fig. 4-24 and Table 2).

3.4.2 Effects of temperature and pressure

We also investigated the effects of temperature and pressure on water displacement by injecting liquid CO_2 (with high viscosity), $scCO_2$ (with moderate viscosity), and CO_2 gas (with low viscosity), respectively, into the micromodels at a constant

injection rate (50 $\mu L \cdot min^{-1}$). As show in Fig. 4-25, the pressure drop during CO_2 injection decreases from the liquid-like nature (full black squares) to the gas-like nature (open blue reverse triangle) of the injected CO_2. Simultaneously, it can be noticed that CO_2 breaks through the micromodel at the same time, as the flow rate is constant whatever the p, T operating conditions. Introducing thus the viscosity ratio $M=\mu_{CO2}/\mu_{H2O}$, as previously defined by Eq. 2.4, and using the related values ranging from 0.07542 and 0.03272, as reported in Table 5, the intrinsic pressure drop Δp_0 caused by the water and the CO_2 viscous forces increases with an increasing viscosity ratio. Obviously, injecting gas-like CO_2 at p = 6 MPa and T = 50°C exhibits the most unfavorable water displacement.

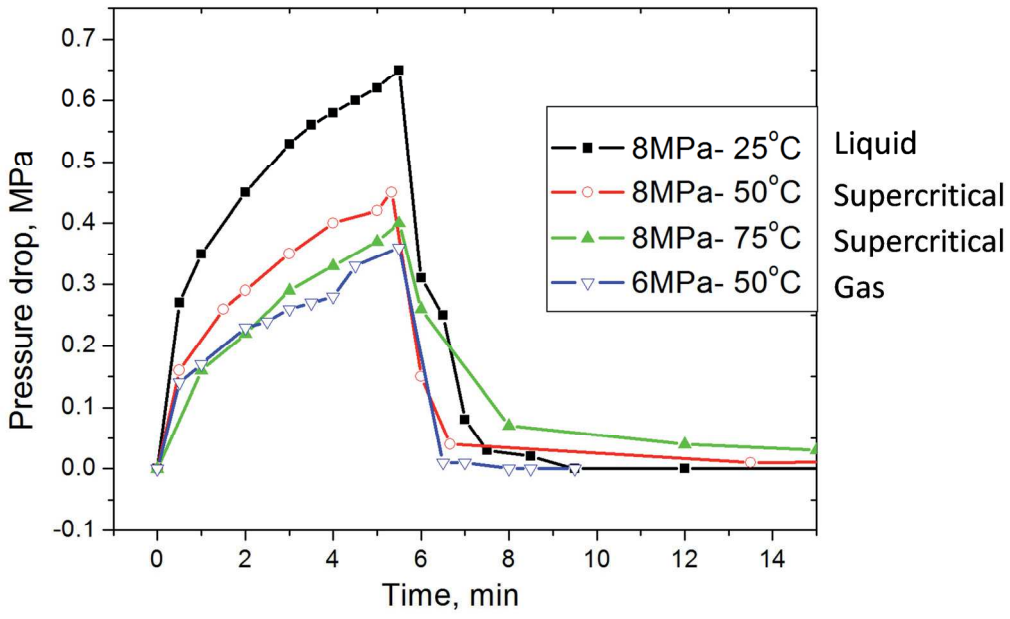

Fig. 4-25 *Pressure drop through the micromodels versus time during the CO_2 injection in a water-saturated micromodel at different pressures and temperatures.*

However, the above account for the viscosity ratio effects related to the change of the p,T operating conditions is probably not complete as, for the two intermediate cases at two different temperatures (50°C and 75°C) and same pressure (8 MPa), the pressure drop as well as Δp_0 show a small decrease (open red circles to full green

triangles) as the viscosity ratio slightly increases (0.03721 to 0.05266, see Table 5). The latter relative behavior is reversed during the CO_2 drainage process. Now, the viscous ratio effect analysis can be complemented by the interfacial effects related to the formation and the displacement of the interfaces between CO_2 and water. Indeed, it is worth noticing that the capillary pressure effects also vary due to the change of the interfacial tension (and probably the contact angle) if the dissolution effects are accounted for as functions of the temperature and pressure changes. First, the interfacial tension of water/CO_2 decreases strongly with an increasing pressure below the CO_2 critical pressure, then levels off and decreases slightly with temperature [6]. Secondly, the contact angle variations are the consequence of the dissolution of CO_2 in water, as above mentioned. Therefore, the capillary entry pressure decreases with increasing temperature and pressure leading to the assumption that injecting "cold" $scCO_2$ exhibits the most unfavorable water displacement than injecting "hot" $scCO_2$, due to the increase of the capillary effects.

Finally, the pressure drop during CO_2 injection appears mainly governed by the injection rate and the viscosity ratio, as the latter property well-accounts for the significant contrast from liquid-like CO_2 to gas-like CO_2 in terms of water displacements limited by the viscous effects. However, the contributions of the interfacial tension and the contact angle variations due the p,T operating conditions cannot be ignored, especially injecting $scCO_2$, which balance between viscosity ratio and interfacial property changes can reverse the unfavorable/favorable nature of the water displacements.

3.4.3 Effects of porosity

As above mentioned, CO_2 saturations in the primary drainage process are different in H and L type micromodels (see Table 7 for example). Here, Fig. 4-26 shows the relative changes for the pressure drop time responses during the CO_2 invasion process followed by the primary drainage process within H and L type (water wetting) micromodels, at the same operating conditions (8 MPa, 50°C, 50 µl/mn). The curves

exhibit lower intrinsic pressure drop Δp_0 and CO_2 breakthrough time t_b in the H-type micromodel than the corresponding ones in the L-type micromodel. In addition, we have already noted that the CO_2 breakthrough saturation is higher in the H-type than the CO_2 breakthrough saturations in the L-type. Therefore, the pressure drop increases while the CO_2 saturation decreases with a decreasing porosity, in agreement with previous works [2]. Here the porosity difference is only due to the pore shape and size differences (see Fig. 4-4 (a)). The increase of Δp_0 reflects then the increase of both viscous and capillary effects from the larger to the smaller pore spaces between the solid plots.

However, the initial relative increase of the pressure drop appears paradoxical since the relative position of the curves in Fig. 4-26 exhibits lower pressure drop in the low porosity case than in the high porosity case. The relative difference is small and difficult to explain only using viscous and capillary effects. The difference in the CO_2 saturations during the early time of the CO_2 invasion process remains one among the probable causes to these pressure drop behaviors (the latter explanation was not confirmed as our observations of the CO_2 saturation was only partial).

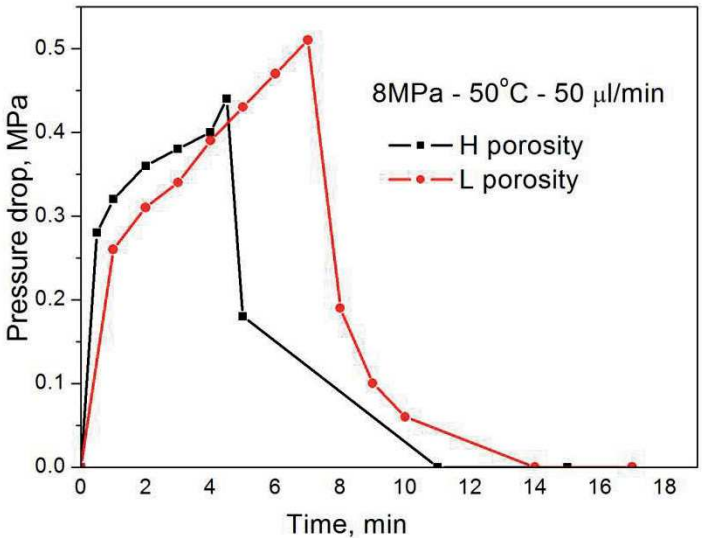

Fig. 4-26 *Comparison of pressure drops during the CO_2 injection within H, L micromodels.*

Finally, the comparison between these two micromodels demonstrates that, during CO_2 invasion and drainage processes of heterogeneous porous media, CO_2 preferentially occupies the larger pores and is blocked out of the smaller pores, while the related CO_2 saturation can be also probably modified by the heterogeneities. Moreover, our previous remark of § 3.1.3 considering the remarkable distributions of the CO_2/water phases during the CO_2 drainage of a squared pore network can be also used to support the above analysis.

3.4.4 Effects of wettability

Wettability is the ability of one fluid to spread on or adhere to a solid surface. It affects the displacement mechanisms and determines the fluid distribution in the porous medium. To quantify the effects of wettability on the injectivity rate at the pore scale, we used a surface modification procedure through Self-Assembly Monolayer (SAM) grafting. Octadecyltri-chlorosilane (OTS) was the silane molecule used to modify the wettability of a L-type micromodel from hydrophilic to hydrophobic. After flowing 45 min the SAM solution (OTS + toluene) through the micromodel in a glove box, the silica surface changed from water wetting to CO_2 wetting (for more details about the surface modification procedure, see Chapter 2).

Fig. 4-27 shows an increase of the intrinsic pressure drop and a slightly earlier CO_2 breakthrough within the CO_2 wetting micromodels. Note, however, that the steady state in CO_2 wetting microsystems need more time to be reached. The finite contact angle results in a decreasing capillary resistance, therefore enabling the CO_2 stream to breaks through the porous medium earlier. Therefore, the comparison of the CO_2 injection into either the hydrophobic or the hydrophilic micromodel, results in a higher pressure drop, a better sweep efficiency and a slightly longer CO_2 breakthrough time in the hydrophobic case. These results are well consistent with previous simulation works at the core scale [7].

The above discussion means that the two phase displacement process in the porous media is going to be considerably more efficient if the wetting phase displaces the non-wetting phase. In the case of CO_2 injection in an aquifer, the injected CO_2 could easily breaks into a low permeable porous material with hydrophobic surfaces, which can turns out to be risky for geological CO_2 sequestration as CO_2 leakage through the caprock is possible.

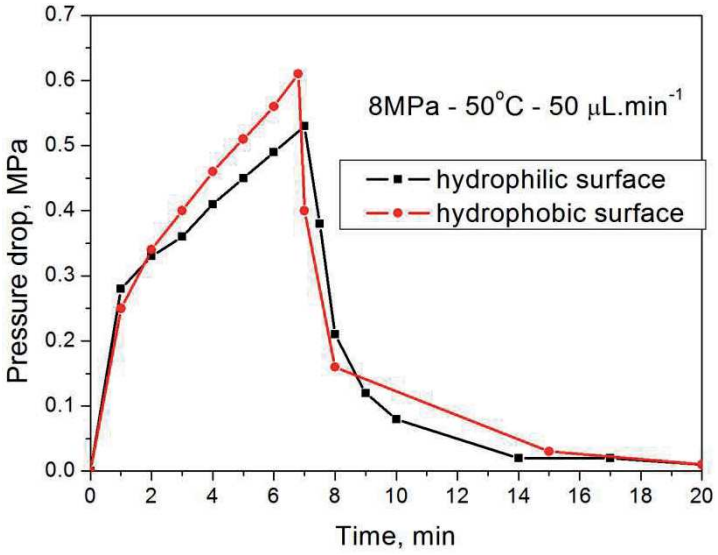

Fig. 4-27 *Pressure drops during the whole CO_2 injection at different wettabilities in a L-type micromodel.*

3.4.5 Conclusive remarks

The optical capture of the local two-phase distributions was combined with the time control of the operating conditions (temperature, pressure and injection rate) and with the change of the two main characteristics properties (porosity and wettability) of the pore network. In such a situation, the qualitative behaviors of the CO_2 sweep efficiency and the CO_2 saturation can be analyzed in terms of the fluids properties (viscosity, density and solubility), in spite of the absence of direct quantitative estimation of these two essential parameters. As the p,T experimental conditions were representative of the ones encountered within the real geological formations, we can

already formulate the three following preliminary conclusive remarks related to the residual (or capillary) and dissolution trapping mechanisms:

i) The increasing viscosity ratio leads to an increasing driving force for CO_2 to break through,

ii) The CO_2 breakthrough saturations increase when the capillary effects increase.

iii) High porosity and hydrophobic surfaces result in a high CO_2 saturation and a better sweep efficiency during CO_2 displacement.

3.5 Carbonate precipitation

After the residual and dissolution trapping mechanisms observed during the initial stages of the CO_2 geological storage, the mineral trapping mechanism is the ultimate and the most secure stage. However, it is only available when considering long timescale, due to the slow reaction kinetic of such a process at the reservoir scale. The dissolved CO_2 in the aqueous phase can form bicarbonate and carbonate ions, which can react with the metals, alkali-metals or alkali-earth metals cations from the reservoir rocks, leading to the precipitation of solid carbonate minerals.

The long time scale for such an event to occur is the biggest challenge for experimental mineral precipitation studies. Therefore, optical micromodels coupled to the use of cations aqueous solutions have been developed in this work to perform carbonate precipitation experiments. Such new experiments operated at the p,T conditions of the geological formation take advantage of the fast mass transfers at the pore scale to provide direct local observations of the reactant products during the CO_2 drainage, similarly to our previous capture of CO_2/water phase distributions.

Here, we investigated the mechanism of carbonate precipitation at pore scale by injecting CO_2 into a buffered calcium chloride solution in the hydrophilic and hydrophobic micromodels, under different flow conditions. The enhanced role of the aqueous phase was expected from the modification of the water-wetting property of the micromodel. The buffered solution (pH = 10) consisting of calcium chloride and NaOH-glycine added to the brine. The buffered solution can slow down the pH

decrease induced by the CO_2 dissolution in the aqueous phase, therefore increasing the bicarbonate and carbonate concentrations in the brine.

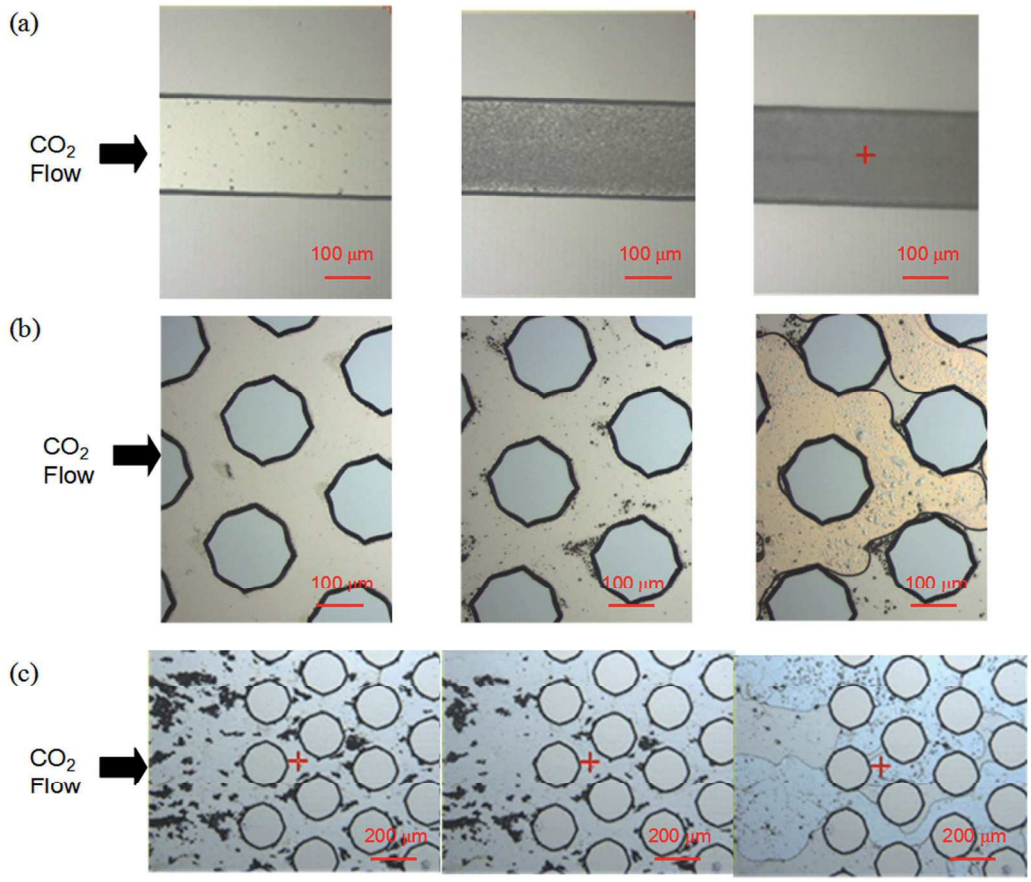

Fig. 4-28 *Images of carbonates precipitation at different conditions: (a) precipitation process in the inlet feeding microchannel; (b) carbonates precipitation at 0.1 mol·l^{-1} $CaCl_2$ solution, 8 MPa - 25 °C - 50 µL·min^{-1}, water-wetting micromodel; (c) carbonates precipitation at 1 mol·l^{-1} $CaCl_2$ solution, 8 MPa - 25 °C - 50 µL·min^{-1}, CO_2-wetting. CO_2 flow directions are given by the black arrows.*

Fig. 4-28 shows the carbonate precipitation process in the micromodel during CO_2 injection. We noted that the process occurs even before CO_2 enters the pore network, as shown in Fig. 4-28 (a), where it can be seen that salts precipitate from the solution inside the inlet feeding microchannels due to a fast CO_2 dissolution into the brine (as expected from the use of the buffered solution). Indeed, during the CO_2 invasion of

the inlet channel upstream the pore network, this dissolution mechanism can exist at the moving CO_2/brine interface. The dissolved CO_2 produced HCO_3^- or CO_3^{2-} anions, which can react with the divalent cations Ca^{2+} to form calcite ($CaCO_3$).

Within the pore network, this dissolution mechanism also exists at the CO_2/brine interface (Fig. 4-28 (b) and (c)). In the water-wetting micromodel case of Fig. 4-28 (b), calcium carbonate precipitates at the front side of the silica pillars along the injection, since the pillars can offer wetted surfaces for heterogeneous precipitation. After CO_2 breaks through, the precipitation process stops because the dissolved CO_2 destabilized the buffered solution, therefore turning somewhat more acidic. Most of the formed calcite stayed in the residual brine phase around the silica pillars.

Since carbonates mainly form and remain within the aqueous phase, there were little carbonate precipitates to be observed after CO_2 floods through the hydrophobic micromodel case of Fig. 4-28(c). In such a hydrophobic wettability, flowing CO_2 displaces more easily the aqueous medium in the pore network

The carbonate precipitates in the residual water turn out to be pure calcite, which was characterized by Raman spectrometer (Fig. 4-29). As shown in the Raman spectra reported in the left part of the figure, the characteristic peak for calcite stays at ～ 1100 cm^{-1}.

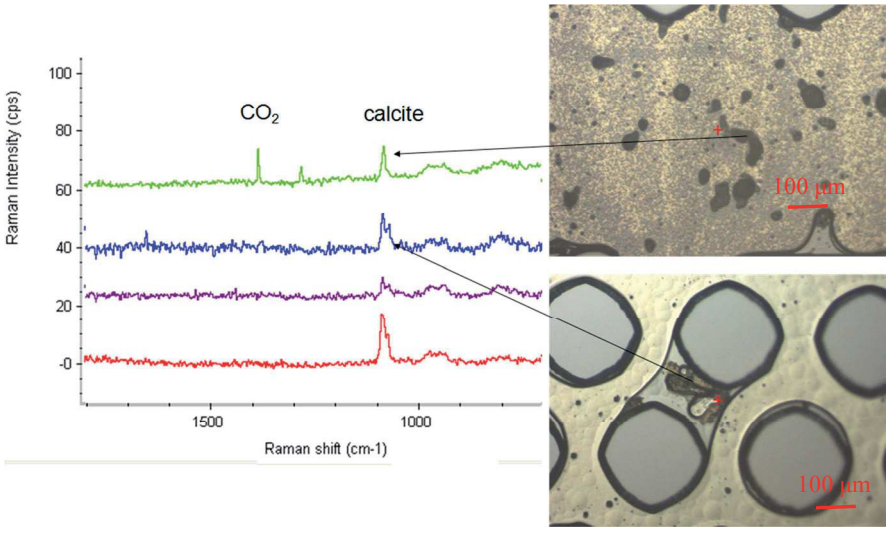

Fig. 4-29 *Raman scattering spectra of $CaCO_3$ precipitates formed in the micromodel in the CO_2 phase (top) and the brine phase (bottom).*

Note, that the reverse mechanism - *i.e.,* dissolution of the $CaCO_3$ minerals - was hardly observed in our present study since pH values remained too high to initiate such a dissolution process.

In our observations, the precipitation only occurred at the CO_2 injection fronts for high $CaCl_2$ concentration, high temperature and pressure. The $CaCO_3$ precipitation rate increases with an increasing temperature. At p = 6 MPa, no precipitation occurred. The results from this study indicate that mineral precipitation reactions are determined by the pH of the fluid formation. The precipitation is usually accompanied by the salting out process, which will decrease the concentration of divalent cations and change the pH. Our experiments also demonstrate that the carbonate formation is a precipitation mechanism in the aqueous phase, which can decrease the porosity and permeability of porous media, therefore increasing the difficulty for CO_2 to break through.

4. Conclusion

A serie of experiments were conducted at subcritical and supercritical CO_2 conditions within three high-pressure two-dimensional silicon / Pyrex micromodels with:

(i) high porosity and hydrophilic pore surface,
(ii) low porosity and hydrophilic pore surface, and
(iii) low porosity and hydrophobic pore surface, respectively.

The experiments simulate reservoir conditions with different, wettability and pore sizes.

When injecting CO_2 in saturated micromodels, some typical features of the water/pore distributions were observed: water pools, water bridges, water domes and water droplets. Various displacement mechanisms were captured in both wetting and non-wetting pore network configurations, as exemplified in Figure 4-30:

1) CO_2 breaks through the pore network and occupies a number of pores (water pool formations) during drainage.
2) Water droplets precipitate from CO_2 phase (crying mechanism) at some cases.
3) In the case of CO_2 / ionic brine system, carbonate precipitation occurs even before CO_2 enters the pore.
4) Over time, the residual water dissolved into the CO_2 stream, which reaches the full saturation of CO_2 (drying mechanism).

Based on these micromodel observations, we established qualitatively that CO_2 saturation generally increases with increasing capillary number Ca and viscosity ratio M, especially for the $scCO_2$ injection. In addition, high porosity and CO_2 wetting porous medium lead to higher CO_2 saturations.

We noted that, at pore scale, the pressure drop magnitude across the microsystem is mainly dependent of the viscosity ratio and proportional to the injection rate. It is also strongly affected by the pore size and the change of the wetting conditions in the porous medium. The larger pore size allows a small entry pressure and an early CO_2 breakthrough. CO_2 wetting micromodels are more efficient for the CO_2 drainage process. It results in high intrinsic pressure drops and CO_2 early breakthroughs.

The time to CO_2 full saturation is determined by the capillary trapping and solubility trapping. Thus, it is affected by the CO_2 saturation and the mutual solubilities of CO_2 and water.

We also observed the so-called *crying* mechanism within the micromodels at high temperature (low CO_2 density). The water droplets precipitated as the form of *tears* out from CO_2 phase depending on the CO_2 density and the H_2O solubility in CO_2 with the temperature and pressure changes along the micromodel during CO_2 invasion. The droplets in the upstream CO_2 flow dissolved into the fresh CO_2 and disappeared. The ones in the downstream CO_2 flow grew up and merged with the neighboring residual water. The imbibition of water reduces the saturation of CO_2.

In the observations of CO_2 / ionic brine system, the carbonate precipitation occurred at the CO_2 injection front at high $CaCl_2$ concentrations, high temperature and pressure. Carbonates can only precipitated before CO_2 breaks through due to the change of pH in the brine. The residual carbonate acts as solids in the pore network, which can affect the displacement process and the CO_2 distribution in the porous medium.

All the above results summarized in Figure 4-30 highlight the great interest of the GLoC concept for laboratory studies of the basic pore-scale mechanisms involved in the CO_2 geological storage.

Displacement mechanisms	Water wetting	Non water wetting
Initially saturated with water or brine	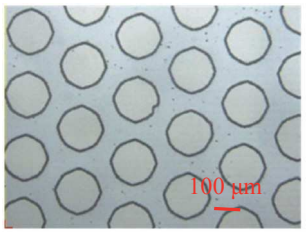	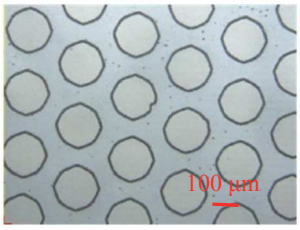
Drainage (wetted/dewetted water pools and water domes)	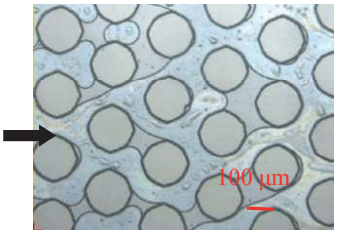 Wetted pools 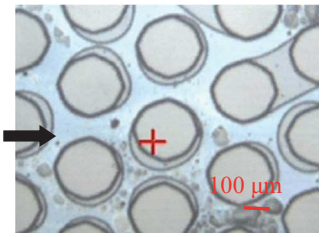 Water domes	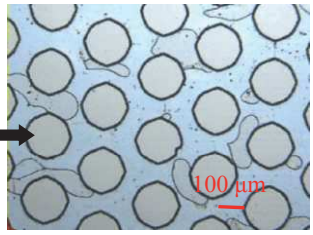 Dewetted pools
Crying mechanism (isolated droplets)	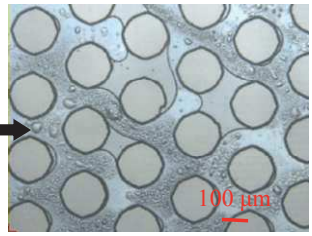	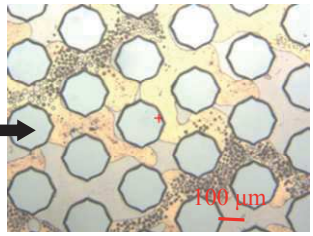
Carbonate precipitation	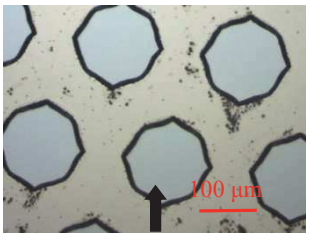	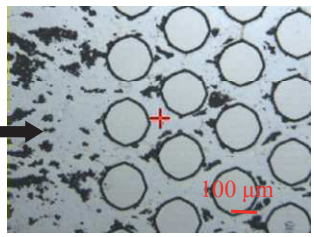
Drying mechanism (full saturated with CO_2)	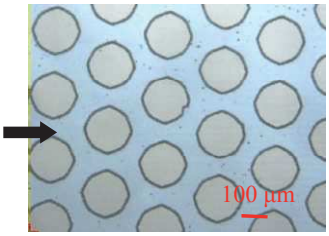	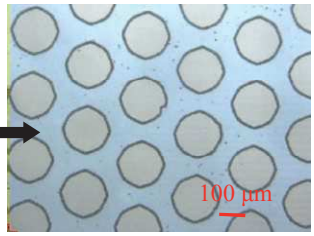

Fig. 4-30 *Observed displacement mechanisms during CO_2 flooding into micromodels (water wetting and non-water wetting). CO_2 flow directions are given by the black arrows.*

References

1 P. Chiquet, J.-L. Daridon, D. Broseta, S. Thibeau, Energy Convers. Manage. 48 (2007a) 736-744.

2 Y. Roig, PhD thesis, Université de Bordeaux, 2012.

3 N.S.K. Gunda, J. Joseph, A. Tamayol, M. Akbari, S.K. Mitra, Microfluid Nanofluid 14 (2013) 711-721.

4 P. Chiquet, J.-L. Daridon, D. Broseta, S. Thibeau, Energy Convers. Manage. 48 (2007a) 736-744.

5 N. Spycher, K. Pruess, J. Ennis-King, Geochimica et Cosmochimica Acta 67 (2003) 3015-3031.

6 L.C. Nielsen, I.C. Bourg, G. Sposito, Geochimica et Cosmochimica Acta 81 (2012) 28-38.

7 C. Chalbaud, M. Robin, S. Bekri and P. Egermann, Proceedings of the International Symposium of the Society of Core Analysts, Calgary, Canada, 10-12 Sept (2007), Paper SCA2007-09.

General Conclusion

This dissertation is the first contribution to the pore-scale studies in p,T geological conditions of overall fields related to CO_2 injection into deep saline aquifers, involving CO_2 solubility, CO_2 drainage process, and carbonate precipitation. The introductive Chapter discussed the review of the potential methods for the sustainable management of the anthropic CO_2 production, for which the CO_2 deep underground geological storage in deep saline aquifers is a proposed remediation solution. The adequate scientific experimental knowledge at the laboratory scale is required for better understanding the storage mechanisms in the geological formations. Such a challenge, where the observations of two phase flows in porous media can bring valuable insights into pore-scale studies of CO_2 storage in deep saline aquifers, was successfully treated in Chapter 2, from the microfabrication of quasi-2D high pressure silicon/Pyrex micromodels designed to mimic the actual storage conditions encountered in real geological reservoirs.

The studies presented in Chapter 3 detail the novel interest of the high pressure micromodels (silicon/Pyrex) for the investigations of the solubility of CO_2 in water and salt water at real reservoir conditions. In order to determine the viability of the silicon/Pyrex micromodels to replicate the reservoir conditions, CO_2 solubility studies have been first performed using microreactors probed by confocal Raman spectroscopy. The calibration curves for CO_2 to relate band height ratios (the dissolved CO_2 bands are referenced to the O-H stretching band of water) to solubility were plotted in a wide range of temperature, pressure and salinity. This study proved that the use of pressurized microreactors, combined with the Raman measurement technique, is viable in the laboratory and can be extended to high CO_2 concentration ranges. More importantly, this method drastically reduces the experiment time.

The studies presented in the final Chapter 4 of the dissertation assess the *Geological Lab on a Chip* (GLoC) concept using our silicon/Pyrex micromodels for capturing the key mechanisms of the CO_2 invasion processes related to CO_2 underground storage at reservoir conditions. After performing the analysis and the analogy modeling of the water viscous flow in our experimental setup to overcome the deficiencies in the exact knowledge of the local velocity field, the 2D porous networks were used to directly visualize the pore-scale fluid phases distributions, the relative fluid phases displacements and the CO_2-brine-mineral reactions during the CO_2 invasion at the geological reservoir conditions. We observed the capillary trapping during CO_2 drainage process, the drying mechanisms due to the H_2O solubility in CO_2 phase, the water bridges interconnecting the neighboring hydrophilic silica pillars, the water films surrounding isolated hydrophilic silica pillars, the "crying" mechanism when H_2O solubility sharply decreases along the micromodel and the carbonates precipitation in the residual brine phase. This chapter reports the preliminary discussions concerning the effects of pressure, temperature, capillary number, viscosity ratio, porosity, wettability and brine composition on displacement mechanisms (viscous fingering and capillary fingering), CO_2 breakthrough saturations, sweep forces, CO_2 full saturation time and carbonates precipitation at pore scale.

The innovations in this dissertation involve:

1. The development of a novel and fast method to measure CO_2 solubility in water and brine using silicon-Pyrex microreactors coupled to confocal Raman spectroscopy.

2. The first time investigation and characterization of the key mechanisms of the CO_2 invasion within a micro porous medium at pore scale in real p,T conditions.

3. New pore-scale studies of reactions among CO_2, brine and minerals developed in real p,T conditions to investigate the pore-scale mineral trapping mechanisms.

Finally, this thesis paves the new route for developing more realistic 2D pore network designs of pressurized microporous media. It is possible to fabricate heterogeneities in permeability or/and wettability to investigate the heterogeneity effects. A gap in the pore network can be used to mimic cracks and fractures in the real porous media (see Fig. 1).

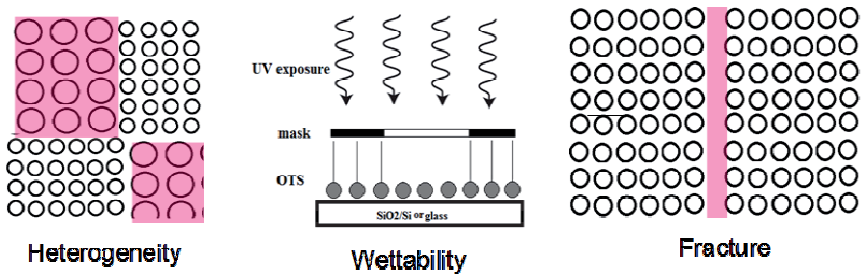

Fig. 1 *New 2D pore network designs: Heterogeneity, one micromodel with different permeabilities and wettabilities; A gap in the pore network to mimic the fracture in the real porous media.*

There is also an increasing need for image analysis techniques and local flow velocity measurement to obtain the CO_2 saturation and local velocity for better understanding the displacements mechanisms at pore scale. For instance, two unstable displacements (viscous fingering and capillary fingering) were not observed in this work due to the limitations of analysis techniques and operating conditions (see Fig. 2). Therefore, it is necessary to extend the range of capillary number Ca and viscous ratio M to better understand these two unstable displacements.

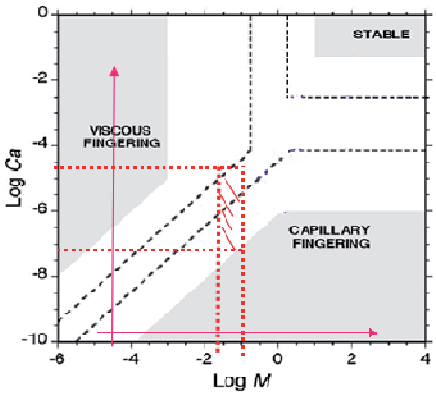

Fig. 2 *Stability diagram resulting from the displacement experiments [from* C. Y. Zhang, et al., Environ. Sci. Technol. 41 (2007) 3672-3678*] (the red zone is the operating area in this work).*

Additionally, future work will be also dedicated to numerical simulations developments in order to validate the assumptions made in Chapter 4, and more generally to provide information concerning the local velocity fields and the related water – CO_2 saturations. The envisioned CFD tools will be based on commercial codes (PHOENIC type), with laminar flows and Eulerian - Eulerian 2 fluids methods to follow the two-phase distribution in 3D configurations.

Ultimately, the final objective for CO_2 geological storage is to reach the 3D-pore filling micromodel with reactive / non-reactive packed bed in the microchannels to compare the geochemical effects and hydrodynamics effects during CO_2 injection (see Fig. 3). The difficulty of 3D micromodels is the visualization setup due to their random and multilayers structures. Confocal microscopy coupled with X-Ray spectroscopy and tomography could be used for deeply examining the effects of the porous matrix properties.

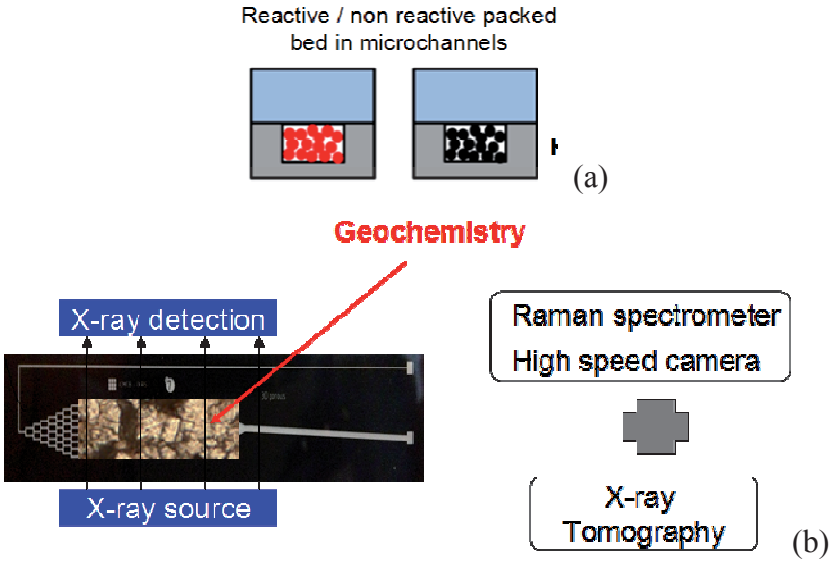

Fig. 3 *(a) Scheme of the 3D microchannel designs with reactive / non-reactive particles packed bed; (b) Scheme of new analysis methods for 3D micromodels.*

These future GLoCs are expected of primary importance for Laboratory understanding and real simulations of the CO_2 sequestration in deep saline aquifers needed for the sustainable management of the anthropogenic CO_2 in the near future.

Titre : **Microfluidique supercritique pour la compréhension des systèmes CO_2 / eau sous pression et en température : Application à la gestion durable de la filière CO_2.**

Résumé :

Le stockage géologique du CO_2 est une stratégie prometteuse pour limiter la concentration de CO_2 anthropique dans l'atmosphère. Les aquifères salins (AS) ont été identifiés comme des options viables car ils possèdent de grandes capacités potentielles de stockage. Toutefois, les processus relatifs au piégeage du CO_2 souffrent d'un manque de connaissances fondamentales car il existe peu de méthodes d'expérimentation rapides et reproductibles, travaillant dans les conditions du stockage géologique. Ainsi, nous avons développé des microréacteurs haute pression, véritables laboratoires géologiques sur puce (GLoCs), recréant les conditions de porosité et de perméabilité des AS pour :

(i) Mesurer la solubilité du CO_2 dans l'eau et les saumures *via* un couplage microsystèmes / spectroscopie Raman ;
(ii) Etudier les mécanismes d'invasion du CO_2 dans les formations géologiques, incluant notamment les écoulements diphasiques en milieux poreux, les séparations de phases et la précipitation des carbonates.

Mots-clés:

- Stockage géologique du CO_2
- Laboratoires géologiques sur puce
- Micromodèles hautes pression et température
- Saturation en milieux poreux

Title : **Supercritical Microfluidics for understanding CO_2 / water systems under pressure and temperature : Application to the sustainable management of the anthropogenic CO_2.**

Summary :

CO_2 geological storage is a promising strategy to control the anthropogenic CO_2 concentration in the atmosphere. Deep saline aquifers (DSA) were identified as viable options since they exhibit large storage capacity. However, processes inherent to CO_2 trapping suffer from a lack of fundamental knowledge, since there are too few fast and reproducible experimental approaches able to work at geological storage conditions. Therefore, to address these limitations, we have developed high pressure microreactors, so-called "geological labs on a chip" - GloCs – allowing mimicking porosity and permeability conditions of DSA for:

(i) Measuring solubility of CO_2 in water and brine through the combination of microsystems and confocal Raman spectroscopy,
(ii) Studying invasion mechanisms of CO_2 in geological formations, including in particular biphasic flows in porous media, phase separation and carbonates precipitation.

Keywords:

- CO_2 geological storage
- Geological Labs on a Chip
- High pressure and temperature micromodels
- Porous media saturations